Benjamin Geisler

Transition Metals and Silicon:

Magnetic Properties of Thin Films, Impurities, and Heusler Alloys on the Atomic Scale

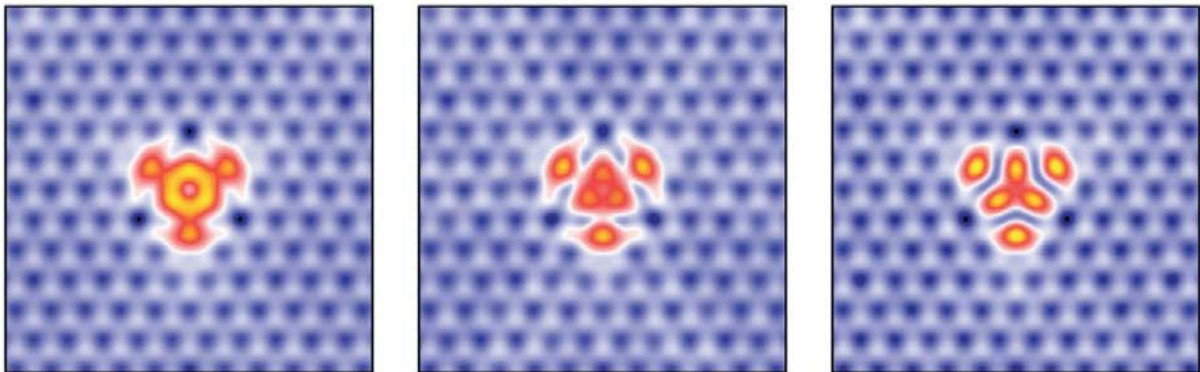

Cuvillier Verlag Göttingen
Internationaler wissenschaftlicher Fachverlag

Transition Metals and Silicon:
Magnetic Properties of Thin Films, Impurities,
and Heusler Alloys on the Atomic Scale

Dieses Werk ist copyrightgeschützt und darf in keiner Form vervielfältigt werden noch an Dritte weitergegeben werden.
Es gilt nur für den persönlichen Gebrauch.

Dieses Werk ist copyrightgeschützt und darf in keiner Form vervielfältigt werden noch an Dritte weitergegeben werden.
Es gilt nur für den persönlichen Gebrauch.

Transition Metals and Silicon: Magnetic Properties of Thin Films, Impurities, and Heusler Alloys on the Atomic Scale

Dissertation

zur Erlangung des akademischen Grades

doctor rerum naturalium
(Dr. rer. nat.)

von

Benjamin Geisler

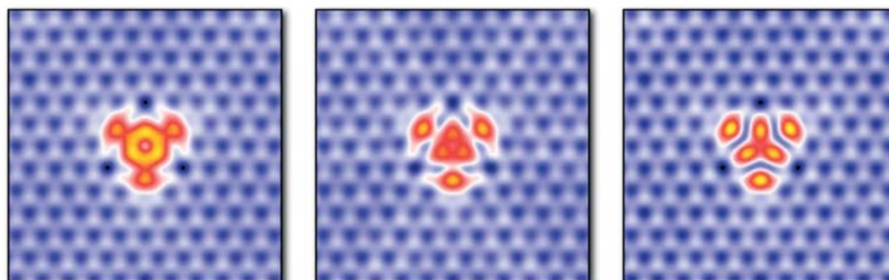

der Fakultät für Physik
der Universität Duisburg-Essen
vorgelegt im September 2014

Dieses Werk ist copyrightgeschützt und darf in keiner Form vervielfältigt werden noch an Dritte weitergegeben werden.
Es gilt nur für den persönlichen Gebrauch.

Bibliografische Information der Deutschen Nationalbibliothek
Die Deutsche Nationalbibliothek verzeichnet diese Publikation in der Deutschen Nationalbibliografie; detaillierte bibliografische Daten sind im Internet über http://dnb.d-nb.de abrufbar.
1. Aufl. - Göttingen: Cuvillier, 2015
Zugl.: Duisburg-Essen, Univ., Diss., 2014

Gutachter: Prof. Dr. Peter Kratzer
Gutachter: Prof. Dr. Friedhelm Bechstedt
Gutachter: Prof. Dr. Peter Entel
Prüferin: Prof. Dr. Rossitza Pentcheva
Prüfer: Prof. Dr. Heiko Wende

Termin der Disputation: 4. Februar 2015

© CUVILLIER VERLAG, Göttingen 2015
Nonnenstieg 8, 37075 Göttingen
Telefon: 0551-54724-0
Telefax: 0551-54724-21
www.cuvillier.de

Alle Rechte vorbehalten. Ohne ausdrückliche Genehmigung des Verlages ist es nicht gestattet, das Buch oder Teile daraus auf fotomechanischem Weg (Fotokopie, Mikrokopie) zu vervielfältigen.
1. Auflage, 2015
Gedruckt auf umweltfreundlichem, säurefreiem Papier aus nachhaltiger Forstwirtschaft.

ISBN 978-3-95404-944-8
eISBN 978-3-7369-4944-7

Dieses Werk ist copyrightgeschützt und darf in keiner Form vervielfältigt werden noch an Dritte weitergegeben werden.
Es gilt nur für den persönlichen Gebrauch.

Abstract

Rational materials design for future spintronics devices requires a thorough, detailed understanding of materials properties. Modern experimental methods like scanning tunneling microscopy allow for investigations on the atomic scale, where contact can be made to atomistic simulations employing the methods of state-of-the-art computational physics. This provides an understanding on a fundamental, quantum-mechanical, *ab initio* level.

This thesis addresses several topics related to magnetism on the atomic scale in the field of spintronics, such as ferromagnetic thin films, dilute magnetic semiconductors, or magnetic tunnel junctions. As a common theme of all topics, the technologically important semiconductor Si is combined in different ways with 3*d* transition metals. The systems are investigated by performing large-scale, state-of-the-art *ab initio* calculations on massively parallel high-performance computers. Special attention is paid to a close relation between theory and experiment and to the reliability of the employed computational methods.

First, the growth mode and the atomic, electronic, and magnetic structure of epitaxial 3*d* transition metal silicide films on the Si(111) surface are studied. It is shown how biaxial strain as well as quantum confinement and/or interface/surface effects modify their magnetic properties. The atomic structure of different MnSi/Si(111) surface reconstructions is revealed in cooperation with high-resolution scanning tunneling microscopy, and a dependence of the MnSi film atomic structure on the growth protocol is found.

Second, a new experimental strategy to detect *bulklike* properties of magnetic impurities in semiconductors and insulators, e.g., Cr, Mn, and Fe in Si, on the atomic scale with *surface* methods is suggested and demonstrated by *ab initio* simulations. The approach involves spin-polarized scanning tunneling microscopy and passivated surfaces. It can image the extension of wave functions, the anisotropy of the induced spin polarization in the host material, and the exchange coupling between neighboring impurities. It is also possible to study two-dimensional structures like clusters or δ layers.

Third, the electronic transport and spincaloric properties of epitaxial magnetic tunnel junctions with half-metallic Co_2MnSi Heusler electrodes and MgO tunneling barriers are investigated. A new approach to spincaloric properties is presented that circumvents the linear response approximation inherent in the Seebeck coefficient. The influence of phonons and interface magnons on the tunnel magnetoresistance ratio is discussed.

Dieses Werk ist copyrightgeschützt und darf in keiner Form vervielfältigt werden noch an Dritte weitergegeben werden.
Es gilt nur für den persönlichen Gebrauch.

Dieses Werk ist copyrightgeschützt und darf in keiner Form vervielfältigt werden noch an Dritte weitergegeben werden.
Es gilt nur für den persönlichen Gebrauch.

Kurzfassung

Ein durchdachtes Materialdesign für zukünftige Spintronik-Bauelemente setzt ein detailliertes Verständnis der Materialeigenschaften voraus. Experimentelle Verfahren wie die Rastertunnelmikroskopie erlauben es heutzutage, Untersuchungen auf atomarer Skala durchzuführen. Hier kann eine Brücke zur modernen Computerphysik geschlagen und so ein Verständnis auf einer fundamentalen, quantenmechanischen Ebene erlangt werden.

Die vorliegende Dissertation behandelt verschiedene Themen aus dem Bereich der Spintronik, die mit Magnetismus auf der atomaren Skala zusammenhängen: ferromagnetische dünne Schichten, semimagnetische Halbleiter und magnetische Tunnelkontakte. Stets wird der technologisch wichtige Halbleiter Si auf unterschiedliche Weise mit $3d$-Übergangsmetallen kombiniert. Die Systeme werden mit zeitgemäßen *ab-initio*-Verfahren untersucht, wobei massiv-parallele Hochleistungsrechner zum Einsatz kommen. Besonderes Augenmerk liegt dabei auf dem engen Verhältnis zwischen Theorie und Experiment sowie auf der Zuverlässigkeit der eingesetzten numerischen Verfahren.

Zuerst werden das Wachstum und die strukturellen, elektronischen und magnetischen Eigenschaften von epitaktischen $3d$-Übergangsmetallsilizidschichten auf der Si(111)-Oberfläche untersucht. Es wird gezeigt, wie biaxiale Verspannung sowie Grenz- und Oberflächeneffekte den Magnetismus beeinflussen. Zusammen mit der Rastertunnelmikroskopie wird die atomare Struktur verschiedener Oberflächenrekonstruktionen von MnSi/Si(111) aufgeklärt und ein Zusammenhang mit den Wachstumsbedingungen nahegelegt.

Danach wird ein neuer Ansatz vorgeschlagen, der es ermöglicht, die Eigenschaften von magnetischen Defekten in Halbleitern und Isolatoren auf der atomaren Skala zu beobachten. Entscheidend dabei ist, dass *Volumenmaterial*-Eigenschaften abgebildet werden, obwohl mit der spinpolarisierten Rastertunnelmikroskopie eine Methode der *Oberflächenphysik* zum Einsatz kommt. Das Verfahren ist in der Lage, die räumliche Ausdehnung von Wellenfunktionen, die Anisotropie der im Wirtsmaterial induzierten Spinpolarisation und die Austauschkopplung benachbarter Defekte sichtbar zu machen. Darüber hinaus können auch zweidimensionale Strukturen wie Cluster oder δ-Lagen beobachtet werden.

Abschließend werden die Transport- und Spinkalorikeigenschaften epitaktischer, magnetischer Tunnelkontakte mit halbmetallischen Co_2MnSi-Heuslerelektroden und MgO-Tunnelbarrieren untersucht. Dafür wird ein neuer Ansatz vorgestellt, bei dem kein Seebeckkoeffizient berechnet wird. Der Einfluss von Phononen und Grenzflächenmagnonen auf das Tunnelmagnetowiderstandsverhältnis wird diskutiert.

Dieses Werk ist copyrightgeschützt und darf in keiner Form vervielfältigt werden noch an Dritte weitergegeben werden.
Es gilt nur für den persönlichen Gebrauch.

Dieses Werk ist copyrightgeschützt und darf in keiner Form vervielfältigt werden noch an Dritte weitergegeben werden.
Es gilt nur für den persönlichen Gebrauch.

Contents

Page

1 Introduction **9**

2 Methodology **15**
2.1 The electronic structure . . . 16
2.2 Density functional theory . . . 19
2.3 Scanning tunneling microscopy . . . 38
2.4 Ballistic quantum transport . . . 42

3 Transition metal silicide thin films on Si(111) **47**
3.1 Introduction and overview . . . 48
3.2 Properties of bulk Si and of the Si(111) surface . . . 49
3.3 Bulk properties of 3d transition metal monosilicides . . . 59
3.4 The effect of epitaxial strain . . . 74
3.5 Correlation effects in MnSi and FeSi . . . 84
3.6 Growth mode and atomic structure of MnSi/Si(111) . . . 86
3.7 Magnetic properties of MnSi/Si(111) thin films . . . 107
3.8 Interface and surface properties of Mn_5Si_3/Si(111) . . . 112

4 Transition metal impurities in Si **121**
4.1 Introduction and overview . . . 122
4.2 The H/Si(111) and H/GaAs(110) surfaces and surface states . . . 123
4.3 Transition metal impurities in bulk Si . . . 127
4.4 Wave function imaging of H/Si(111) subsurface impurities . . . 137
4.5 Two-dimensional subsurface impurity layers and clusters . . . 150
4.6 Subsurface doping with organic molecules . . . 158

5 Magnetic tunnel junctions with Heusler electrodes **167**
5.1 Introduction and overview . . . 168
5.2 Properties of Co_2MnSi and MgO . . . 169
5.3 Phonon influence on the half-metallic gap . . . 174
5.4 Magnetic tunnel junctions . . . 177

6 Summary and Outlook **193**

A Computational details **199**

Dieses Werk ist copyrightgeschützt und darf in keiner Form vervielfältigt werden noch an Dritte weitergegeben werden.
Es gilt nur für den persönlichen Gebrauch.

List of Figures **205**

List of Tables **209**

List of Abbreviations **211**

References **213**

Danksagungen **231**

Dieses Werk ist copyrightgeschützt und darf in keiner Form vervielfältigt werden noch an Dritte weitergegeben werden.
Es gilt nur für den persönlichen Gebrauch.

Chapter 1

Introduction

Since the invention of the universal programmable computer in the 1940s, solid state physics has contributed tremendously to the development of computer hardware. Nevertheless, a quite unphysical separation has occurred: It was soon realized in practical computer engineering that electric and magnetic phenomena, which are known to depend on each other and are described in a combined theory, each have their own advantages and disadvantages. Electricity, on the one hand, is fast, but volatile. Magnetism, on the other hand, that arises in condensed matter as a macroscopic quantum effect, is slower, but persistent. Consequently, electric charges and capacitors are used nowadays for information processing and temporary data storage, while magnetism is used almost exclusively in reliable long-term storage devices.

The field of spintronics [1–3], which emerged some years ago, attempts to recombine electricity and magnetism, which both originate from electrons: While the former is a result of the electron charge, the latter is mostly a consequence of the electron spin. It should therefore be possible to exploit the electron spin as a carrier of information in addition to its charge. Fundamental and continuously investigated topics in the field of spintronics are the injection, transport, manipulation, storage, and detection of spin-polarized carriers [3–5]. The vision is to devise a new electronics, with new devices for information processing and data storage.

Metal-based spintronics devices already play an important role in our everyday life. The 2007 Nobel Prize in Physics was awarded to A. Fert and P. Grünberg for the discovery of the giant magnetoresistance effect, which is used in read heads of hard discs. Another device belonging to this field is the magnetoresistive random access memory (MRAM), which is based on the tunnel magnetoresistance (TMR) effect and already commercially available. In a MRAM module, the capacitive storage used in conventional dynamic random access memory (DRAM) is replaced by a form of magnetic storage that employs magnetic tunnel junctions (MTJs). A considerable advantage of MRAM is the persistence of the stored information, even if the energy supply of the device is removed. This is clearly not the case in DRAM modules, since they constantly need energy for refreshing the stored information [6]. Consequently, MRAM is more energy efficient. Moreover, it is cost effective to integrate, has an unlimited endurance, and provides fast (≈ 5 ns) random access [6,7]. Another suggested concept aims at overcoming the rigidity of the present hardware by creating logic devices, based on MTJs, that are reprogrammable at run-time (so-called “chameleon” processors [8]).

Dieses Werk ist copyrightgeschützt und darf in keiner Form vervielfältigt werden noch an Dritte weitergegeben werden.
Es gilt nur für den persönlichen Gebrauch.

Semiconductor spintronics, on the other hand, offers a possible direction towards devices that perform logic, communication, and storage within the same materials technology [9]. A drawback of metal-based spintronics is that metals have no band gap; therefore, the carrier density cannot be as precisely controlled as in semiconductors (by doping, electrostatic gating, or band gap engineering). Moreover, the room-temperature spin relaxation times in nonmagnetic semiconductors are three orders of magnitude longer than in nonmagnetic metals [9]. Semiconductor spintronics devices compare favorably in speed and efficiency to electronic devices [10]. They could further reduce the power consumption by staying out of equilibrium for a long time (of the order of the spin relaxation time) instead of undergoing frequent equilibration (energy dissipation) [9]. Magnetic transistors could combine nonvolatility and reprogrammability with amplification [9]. Moreover, this technology could open a door towards quantum computation [9].

An interesting subtopic of semiconductor spintronics is Si spintronics [5], not least for technological and economical reasons: Si is an abundant material, the de-facto standard semiconductor, and our industry and technology is highly optimized for Si processing. In addition, the Si crystal structure has inversion symmetry, and its isotopes ^{28}Si (92%) and ^{30}Si (3%) have no nuclear spin [5]. Consequently, the spin relaxation in Si is dominated by the Elliott-Yafet mechanism (in contrast to the D'yakonov-Perel' mechanism, which plays an important role in III-V semiconductors like GaAs [11]), a combined action of momentum scattering, e.g., by phonons or impurities, and spin-orbit interaction, which is small in Si [5]. From an analysis of the Elliott and Yafet processes it has been shown recently that the phonon-induced spin relaxation time τ of the conduction electrons in bulk Si behaves as $\tau \sim T^{-3}$, reaching large values of 1 μs for $T = 60$ K and around 10 ns for $T = 300$ K [12]. Conventional doping reduces the spin relaxation time due to a more frequent impurity scattering [5]. Room-temperature spin injection, spin manipulation, and spin detection in Si has been demonstrated recently [13] as well as the nonlocal detection of a spin accumulation [14].

Rational materials design for future spintronics devices requires a thorough, detailed understanding of materials properties and their interdependence in various fields; for instance, (i) the dependence of structural properties on the growth protocol, (ii) the interplay of structural, electronic, and magnetic properties, (iii) the interactions between the different constituents of the material, e.g., between a semiconductor host and magnetic impurities embedded therein, and (iv) the dependence of transport and spincaloric properties on the electronic and magnetic structure. Modern experimental methods allow for an investigation of these points on the atomic scale. Therefore, contact can be made to state-of-the-art computational physics, which provides detailed insight on the same length scale. This enables one to analyze systems on a fundamental, quantum-mechanical, *ab initio* level, far beyond phenomenological approaches.

In this spirit, the present thesis addresses several topics related to magnetism on the atomic scale in the fields of semiconductor and metal-based spintronics, such as ferromagnetic thin films, dilute magnetic semiconductors (DMS), or MTJs with half-metallic electrodes. As a common theme of all topics, the semiconductor Si is combined in different ways with the abundant and "magnetic" 3*d* transition metals (TMs).

The present thesis is organized as follows: After this introduction (**Chapter 1**), the employed numerical methods are presented (**Chapter 2**), e.g., spin-polarized density functional theory (DFT) within the plane wave framework, ultrasoft pseudopotentials, semilocal and hybrid exchange-correlation functionals, on-site electronic correlation, the simulation of spin-

Dieses Werk ist copyrightgeschützt und darf in keiner Form vervielfältigt werden noch an Dritte weitergegeben werden.
Es gilt nur für den persönlichen Gebrauch.

polarized scanning tunneling microscopy (SP STM) images from the DFT electronic structure in the spirit of the Tersoff-Hamann approximation, and ballistic quantum transport in the Landauer-Büttiker formalism. Other methods like *ab initio* thermodynamics, Monte Carlo simulations, or the Sivan-Imry approach to spincaloric properties are described later in this thesis. Subsequently, the results are discussed in three different chapters. Each of these chapters begins with a more profound introduction, which provides an integration of the results into the current state of research.

One possible route to fabricate a spin injector (or a spin detector) is by growing a ferromagnetic thin film of TMs on a semiconductor substrate (e.g., Si). The high reactivity of the Si surfaces leads to the immediate formation of TM silicides. **Chapter 3** treats several topics concerning different 3*d* TM silicides as bulk material and as film structure of different thickness grown epitaxially on the Si(111) surface. Structural, electronic, and magnetic properties of bulk 3*d* TM monosilicides, which largely crystallize in the complex B20 structure, are presented. In particular, the band gap, which is known to exist for FeSi, is shown to be a universal property of this class of materials. It is linked to the B20 crystal structure and separates two opposing groups of bands with different predominant TM 3*d* orbital character. MnSi and FeSi are also studied in the rock-salt and zinc-blende crystal structures. The validity of the present theoretical description of these materials, which exhibit nontrivial electronic correlations, and the applicability of *ab initio* thermodynamics is assessed.

Calculations for bulk 3*d* TM silicides under biaxial strain provide materials properties in the limit of thick (e.g., several hundred monolayers) epitaxial films on Si(111). For MnSi, a strain-induced volume expansion, increased magnetic moments and Curie temperature, and a phonon softening are found. FeSi makes a surprising transition from a nonmagnetic semiconductor to an almost half-metallic ferromagnet if matched epitaxially to Si(111), which means that it displays a finite density of states at the Fermi energy only in one spin channel. These findings make MnSi and FeSi especially interesting. On the other hand, it is explicitly demonstrated for MnSi/Si(111) heterostructures that the magnetic behavior of thin (e.g., just a few monolayers) 3*d* TM silicide films can deviate significantly from that of thicker films due to quantum confinement and/or interface/surface effects.

Subsequently, the growth mode, the atomic, and the magnetic structure of epitaxial MnSi thin films on Si(111) are analyzed in more detail. Interface properties are presented for MnSi/Si(111) and FeSi/Si(111). The atomic structure of the recently observed $\sqrt{3} \times \sqrt{3}$ and 3×3 surface reconstructions of MnSi films is revealed by combining experimental atomic-resolution STM imaging and first-principles simulations. A comparison of results for films grown by different techniques provides evidence that their internal stacking depends on the growth protocol. Since the magnetic properties of MnSi films are closely related to their atomic structure, the occurrence of different stacking sequences implies that strict control of the growth conditions is required to reproducibly fabricate MnSi films with specified properties. Finally, it is shown that the competing formation of Mn_5Si_3 can be excluded in the present experiments.

A second route towards new materials for spintronics is the doping of semiconductors or insulators with magnetic impurities. The systematic, reliable investigation of these DMS systems is a highly problematic and nontrivial task due to the many possible pitfalls. An example shall be given: Since high doping concentrations ($\sim 1\,\%$) of magnetic impurities are necessary, DMS samples can suffer from clustering and segregation of the impurities. This makes it hard (or impossible) for conventional experimental methods to isolate the different

Dieses Werk ist copyrightgeschützt und darf in keiner Form vervielfältigt werden noch an Dritte weitergegeben werden.
Es gilt nur für den persönlichen Gebrauch.

types of magnetic interactions present in the sample (e.g., impurity-host interactions of isolated impurities vs. impurity-impurity interactions of impurity pairs or clusters; moreover, signals from segregated bulk phases of the impurity material). First-principles simulations, on the other hand, can suffer from the band gap problem or a deficient energy level ordering. **Chapter 4** introduces a new strategy to study experimentally the unbiased, *bulklike* impurity-host and impurity-impurity interactions of magnetic impurities in semiconductors and insulators on the atomic scale by using *surface* methods like SP STM in conjunction with passivated host surfaces. This strategy can lead to new insights on a fundamental, atomic level in the field of DMS.

The proof of principle is given by large-scale *ab initio* computer simulations for 3*d* TM impurities in Si, but the suggested approach is generalizable to other DMS systems like Co-doped ZnO. Different structural, electronic, and magnetic properties of interstitial and substitutional Cr, Mn, and Fe impurities in bulk Si and below the H/Si(111) surface are explained. Kinetic considerations concerning the injection and migration of subsurface impurities are made. It is demonstrated how SP STM in conjunction with passivated host surfaces can be used to image and measure the extension of impurity wave functions, the anisotropic spin polarization induced in the host electronic structure, and, *quantitatively*, the exchange coupling constants between neighboring impurities. This provides, for instance, a visual explanation why a ferromagnetic coupling is more difficult to achieve in Si than in GaAs. It is shown that semilocal and state-of-the-art hybrid exchange-correlation functionals lead to similar electronic and magnetic structures, with the exception of the substitutional Fe impurity. It is demonstrated how the latter can be used as a benchmark for the applicability of hybrid functionals in DMS simulations.

The new technique can also be applied to impurity δ layers and two-dimensional impurity clusters, which are studied afterwards. In particular, it is found that (111) δ layers of interstitial Cr impurities in Si exhibit a strong ferromagnetic interaction and are half-metallic. More generally, Cr-doped Si seems to be an interesting candidate material for a DMS. Moreover, it is shown how a ferromagnetic semiconductor could be constructed from two-dimensional Fe clusters embedded in Si.

The last part of the chapter is devoted to the experimentally motivated question whether or not it is possible to generate subsurface Fe impurities by deposition of organic molecules (e.g., iron phthalocyanine, FePc) on the H/Si(111) surface. It is concluded that the implantation is possible, but the necessary steps in the reaction are quite improbable due to the high binding energy of Fe in FePc. Gas phase calculations of phthalocyanine molecules with different TM centers employing different exchange-correlation functionals underline that these high binding energies are reasonable. It is shown that van-der-Waals corrections to semilocal DFT are very important for the correct description of the FePc adsorption on H/Si(111). Besides, silicon phthalocyanine is found to be an interesting example of d_0 magnetism in molecules.

Magnetic materials containing Si can be synthesized in many ways. Instead of diluting Si with TMs, one can also add Si to an alloy of TMs. An example is the Heusler alloy Co_2MnSi, which is a half-metallic ferromagnet. **Chapter 5** focuses on electronic transport and spincaloric properties of epitaxial MTJs with half-metallic Co_2MnSi Heusler electrodes and MgO tunneling barriers. Such heterostructures can be employed in a suggested "thermo-MRAM" module, which uses the magneto-Seebeck effect to read out the magnetic state of a MTJ without an applied voltage or a flowing charge current. Moreover, a Co_2MnSi/MgO/se-

Dieses Werk ist copyrightgeschützt und darf in keiner Form vervielfältigt werden noch an Dritte weitergegeben werden.
Es gilt nur für den persönlichen Gebrauch.

miconductor setup in conjunction with an applied voltage or a temperature gradient can be used as spin injector that avoids the conductivity mismatch problem.

Given that the Co_2MnSi electrodes are ferromagnetic half-metals, the relative magnetization of the two electrodes has striking consequences for the transport properties of the MTJ. For the case of parallel electrode magnetization, electronic transport, spincaloric properties, and the dependence of both on the interface atomic structure are analyzed. In addition to conventionally obtained, approximate Seebeck coefficients, a more general route to spincaloric properties is presented that directly provides the response of the system (current or voltage) to arbitrary thermal gradients. It is demonstrated that the conventional Seebeck coefficient can be understood as first-order Taylor expansion coefficient of the voltage response. Thermal variations of the chemical potential in the leads and finite-bias effects can be readily included in this method. It is shown that a targeted growth control of the MTJs can be used to tailor their spincaloric properties (e.g., magnitude and sign of the thermally induced voltage).

In contrast, an antiparallel magnetization of the half-metallic electrodes should ideally prevent any electronic transport. Nevertheless, a parasitic current flows in room-temperature experiments that reduces the TMR ratio. It is shown by using a statistical approach to the electron-phonon interaction involving randomly distorted structures that the excitation of phonons has no relevant effect on the electronic structure of Co_2MnSi at room temperature and therefore cannot account for the strong decrease of the TMR ratio. On the other hand, it is argued that inelastic tunneling involving thermally activated interface magnons is among the most probable explanations for the observed behavior. First-principles calculations reveal that such interface magnons are much more easy to excite than bulk magnons.

Finally, **Chapter 6** summarizes the contents of this thesis and provides perspectives for future investigations.

Dieses Werk ist copyrightgeschützt und darf in keiner Form vervielfältigt werden noch an Dritte weitergegeben werden.
Es gilt nur für den persönlichen Gebrauch.

Publications

Parts of this thesis have been published:

- B. Geisler, P. Kratzer, T. Suzuki, T. Lutz, G. Costantini, and K. Kern, *Growth mode and atomic structure of MnSi thin films on Si(111)*, Phys. Rev. B **86**, 115428 (2012), Ref. [15]
- B. Geisler and P. Kratzer, *Strain stabilization and thickness dependence of magnetism in epitaxial transition metal monosilicide thin films on Si(111)*, Phys. Rev. B **88**, 115433 (2013), Ref. [16]
- T. Suzuki, T. Lutz, B. Geisler, P. Kratzer, K. Kern, and G. Costantini, *Surface morphology of MnSi thin films grown on Si(111)*, Surf. Sci. **617**, 106 (2013), Ref. [17]

Some publications are in preparation:

- B. Geisler and P. Kratzer, *Atomic-scale detection of magnetic impurity interactions in bulk semiconductors*, submitted to Phys. Rev.
- B. Geisler and P. Kratzer, *Spincaloric properties of epitaxial $Co_2MnSi/MgO/Co_2MnSi$ magnetic tunnel junctions*
- B. Geisler and P. Kratzer, *Cr-doped Si as novel dilute magnetic semiconductor*
- B. Geisler and P. Kratzer, *Physi- and chemisorption of organic molecules on H/Si*(111)

Further publications that are related to this thesis:

- B. Geisler, P. Kratzer, and V. Popescu, *Interplay of growth mode and thermally induced spin accumulation in epitaxial $Al/Co_2TiSi/Al$ and $Al/Co_2TiGe/Al$ contacts*, Phys. Rev. B **89**, 184422 (2014), Ref. [18]
- D. Comtesse, B. Geisler, P. Entel, P. Kratzer, and L. Szunyogh, *First-principles study of spin-dependent thermoelectric properties of half-metallic Heusler thin films between platinum leads*, Phys. Rev. B **89**, 094410 (2014), Ref. [19]

Dieses Werk ist copyrightgeschützt und darf in keiner Form vervielfältigt werden noch an Dritte weitergegeben werden.
Es gilt nur für den persönlichen Gebrauch.

Chapter 2

Methodology

Contents

2.1 The electronic structure **16**
- 2.1.1 The many-particle problem in quantum mechanics 16
- 2.1.2 The adiabatic approximation 17
- 2.1.3 Bloch's theorem 18

2.2 Density functional theory **19**
- 2.2.1 The theorems of Hohenberg and Kohn 20
- 2.2.2 The Kohn-Sham scheme 20
- 2.2.3 Exchange and correlation 24
- 2.2.4 Plane waves and pseudopotentials 31
- 2.2.5 Different and complementary approaches 37

2.3 Scanning tunneling microscopy **38**
- 2.3.1 Basic experimental principles 38
- 2.3.2 STM images from DFT: The Tersoff-Hamann approximation 39
- 2.3.3 Spin-polarized STM 41

2.4 Ballistic quantum transport **42**

Dieses Werk ist copyrightgeschützt und darf in keiner Form vervielfältigt werden noch an Dritte weitergegeben werden.
Es gilt nur für den persönlichen Gebrauch.

2.1 The electronic structure

Almost every result that will be presented in this thesis is based on the electronic structure of a certain physical system. This system can be an infinitely extended solid, an isolated impurity in a host material, a molecule, or just a single atom. All relevant physical properties of this system are determined, or significantly influenced, by its electronic structure: The quantum-mechanical many-particle behavior of electrons in the potential of the nuclei.

2.1.1 The many-particle problem in quantum mechanics

On the atomic scale, condensed matter physics is governed by the Schrödinger equation,

$$\mathrm{i}\hbar \frac{\partial}{\partial t} |\psi_t\rangle = \hat{H} |\psi_t\rangle \,, \tag{2.1}$$

where $\hat{H}$ is the Hamilton operator ("Hamiltonian") of the system under consideration and the vector $|\psi_t\rangle$ denotes the quantum-mechanical state the system is in at time t. Solving Eq. (2.1) is equivalent to finding the stationary solutions and their energies, that is, eigenstates (or, similarly, eigenvectors) $|\psi_i\rangle$ and eigenenergies E_i of $\hat{H}$,

$$\hat{H} |\psi_i\rangle = E_i |\psi_i\rangle \,,$$

since the time evolution of the quantum system can be expressed (for time-independent Hamiltonians) by decomposing an arbitrary initial state $|\psi_0\rangle$ into the eigenbasis of $\hat{H}$:

$$|\psi_t\rangle = \sum_j \exp\left\{-\frac{\mathrm{i}}{\hbar} E_j t\right\} \left\langle \psi_j | \psi_0 \right\rangle \left| \psi_j \right\rangle .$$

While a molecule consists of only few atoms, solids usually contain about 10^{23} atoms per cm^3. Each atom consists of a nucleus and several electrons. The full Hamiltonian of such a system, neglecting relativistic effects, external magnetic fields, and quantum electrodynamics, reads:

$$\hat{H} = \hat{T}_\mathrm{n} + \hat{T}_\mathrm{e} + \hat{V}_\text{n-n} + \hat{V}_\text{e-e} + \hat{V}_\text{e-n} \,,$$

with kinetic energy operators (in position representation) for nuclei (n) and electrons (e),

$$\begin{aligned} \hat{T}_\mathrm{n} &= \sum_I^{N_\mathrm{n}} \frac{\hat{P}_I^2}{2M_I} = -\sum_I^{N_\mathrm{n}} \frac{\hbar^2}{2M_I} \nabla^2_{\vec{R}_I} \,, \\ \hat{T}_\mathrm{e} &= \sum_i^{N_\mathrm{e}} \frac{\hat{p}_i^2}{2m} = -\sum_i^{N_\mathrm{e}} \frac{\hbar^2}{2m} \nabla^2_{\vec{r}_i} \,, \end{aligned}$$

and Coulomb interaction potential operators,

$$\begin{aligned} \hat{V}_\text{n-n} &= +\frac{1}{2} \sum_{I \neq J}^{N_\mathrm{n}} \frac{e^2}{4\pi\varepsilon_0} \frac{Z_I Z_J}{|\vec{R}_I - \vec{R}_J|} \,, \\ \hat{V}_\text{e-e} &= +\frac{1}{2} \sum_{i \neq j}^{N_\mathrm{e}} \frac{e^2}{4\pi\varepsilon_0} \frac{1}{|\vec{r}_i - \vec{r}_j|} \,, \\ \hat{V}_\text{e-n} &= -\sum_{i,I}^{N_\mathrm{e},N_\mathrm{n}} \frac{e^2}{4\pi\varepsilon_0} \frac{Z_I}{|\vec{r}_i - \vec{R}_I|} \,, \end{aligned}$$

Dieses Werk ist copyrightgeschützt und darf in keiner Form vervielfältigt werden noch an Dritte weitergegeben werden.
Es gilt nur für den persönlichen Gebrauch.

where the factor 1/2 eliminates double counting. Relativistic effects (like mass modifications or the electron spin) can be included later. The full many-particle wave functions Φ_i depend on the coordinates of all electrons and nuclei and are solutions of

$$\hat{H}\,\Phi_i(\vec{r}_1,\ldots,\vec{r}_{N_\mathrm{e}};\,\vec{R}_1,\ldots,\vec{R}_{N_\mathrm{n}}) = E_i\,\Phi_i(\vec{r}_1,\ldots,\vec{r}_{N_\mathrm{e}};\,\vec{R}_1,\ldots,\vec{R}_{N_\mathrm{n}}). \tag{2.2}$$

It is needless to say that, in general, such a system can be solved neither algebraically nor numerically. Even simple many-particle systems like a He atom or the H_2 molecule cannot be described exactly (although very good approximate results can be achieved here). Therefore, several well-chosen approximations are necessary that will be discussed in this chapter.

2.1.2 The adiabatic approximation

First of all, the motion of the nuclei can be decoupled from the motion of the electrons due to their highly different masses ($m/M \approx 10^{-3}$). This procedure is known as the "adiabatic approximation" (or Born-Oppenheimer approximation [20]). Generally, any many-particle wave function Φ can be decomposed according to

$$\Phi(\{\vec{r}_i,\,\vec{R}_I\}) = \sum_\nu \Psi_\nu(\{\vec{r}_i\}:\{\vec{R}_I\})\;\Xi_\nu(\{\vec{R}_I\}), \tag{2.3}$$

with electronic wave functions $\Psi_\nu(\{\vec{r}_i\}:\{\vec{R}_I\})$ and nucleonic wave functions $\Xi_\nu(\{\vec{R}_I\})$. Considering m/M as a small quantity, the kinetic energy of the nuclei $\hat{T}_\mathrm{n}$ can be regarded as a perturbation to the electronic part of the Hamiltonian $\hat{H}_\mathrm{e}$:

$$\hat{H} = \hat{H}_\mathrm{e} + \hat{T}_\mathrm{n}\,, \qquad \hat{H}_\mathrm{e} = \hat{T}_\mathrm{e} + \hat{V}_\text{n-n} + \hat{V}_\text{e-e} + \hat{V}_\text{e-n}\,.$$

Note that $\hat{H}_\mathrm{e}$ contains no differential operators with respect to the nucleonic positions $\vec{R}_I$. Inserting the wave function $\Phi(\{\vec{r}_i,\,\vec{R}_I\})$ as given in Eq. (2.3) into Eq. (2.2) and using the electronic part of the equation,

$$\hat{H}_\mathrm{e}\;\Psi_\nu(\{\vec{r}_i\}:\{\vec{R}_I\}) = \epsilon_\nu(\{\vec{R}_I\})\;\Psi_\nu(\{\vec{r}_i\}:\{\vec{R}_I\}), \tag{2.4}$$

leads, after multiplication with $\Psi^*_{\nu'}(\{\vec{r}_i\})$ and integration over the electron coordinates $\vec{r}_i$, to the still exact expression

$$(\hat{T}_\mathrm{n} + \epsilon_\nu(\{\vec{R}_I\}))\;\Xi_\nu(\{\vec{R}_I\}) + \sum_{\nu'} A_{\nu,\nu'}\;\Xi_{\nu'}(\{\vec{R}_I\}) = E\;\Xi_\nu(\{\vec{R}_I\}).$$

The adiabatic approximation [21, 22] corresponding to the limit $m/M \to 0$ consists of neglecting the transition matrix elements $A_{\nu,\nu'}$ (which contain the electronic wave functions). It leads to a complete separation of electronic and nucleonic dynamics. The equation for the nucleonic wave functions then reads:

$$(\hat{T}_\mathrm{n} + \epsilon_\nu(\{\vec{R}_I\}))\;\Xi_\nu(\{\vec{R}_I\}) = E\;\Xi_\nu(\{\vec{R}_I\}). \tag{2.5}$$

Thus, the problem is separated into two Schrödinger-like equations (2.4) and (2.5). The electronic equation (2.4) depends only parametrically on the positions of the nuclei. Hence, one can study the interacting electrons in a fixed, "external" potential generated by the nuclei. The central idea behind the adiabatic approximation is that the electron system responds instantaneously to changes of the nucleonic positions due to the mass difference,[1]

[1] Typical time scales for the electrons (nuclei) are femtoseconds (picoseconds).

Dieses Werk ist copyrightgeschützt und darf in keiner Form vervielfältigt werden noch an Dritte weitergegeben werden.
Es gilt nur für den persönlichen Gebrauch.

and that there are no excitations of the electronic system (transitions $\nu \to \nu'$) due to nucleonic dynamics, so that the electrons remain in their (ground) state [22].

In most cases, speaking of "nucleonic wave functions" is exaggerated, since normally no Schrödinger-like equation, e.g., Eq. (2.5), is solved for the nuclei. Instead, they move on trajectories following classical dynamics, acted upon by forces calculated from the quantum-mechanical electron system (e.g., Hellmann-Feynman forces [23], which are used in this thesis for optimizations, i.e., relaxations, of the different atomic structures). For heavy atoms, this approximation is very good. Although nothing else than this is done in this thesis, it should be mentioned here that there exist other approaches, especially in modern research. For instance, *ab initio* path-integral molecular dynamics can be done, in which both the electrons and the nuclei are treated as quantum particles [24, 25].

2.1.3 Bloch's theorem

The complexity of a quantum many-particle problem is a consequence of the Coulomb interaction between the particles. However, even if the particles are assumed to be "noninteracting" (despite, e.g., some effective, mean-field-like interaction or the inclusion of the Pauli exclusion principle for electrons) and only the electronic parts of the wave functions are considered (for fixed nuclei), the question arises how a solid bulk system of 10^{23} atoms can be described efficiently. The key observation is that the potential generated by the nuclei is invariant under certain translations in a bulk crystal. Therefore, the whole (ideal and infinite) crystal can be constructed from a single unit cell by using translational operations. Bloch's theorem, which is well known in mathematics as Floquet's theorem, states that eigenfunctions of the electronic Hamiltonian $\hat{H}$ of the crystal can be chosen such as to possess the same translational invariance, modulated by a phase factor.[2] It is of fundamental importance in the field of electronic structure theory of solids.

Consider a periodic lattice in three dimensions which is described by real space lattice vectors $\vec{R} = n_1\vec{a}_1 + n_2\vec{a}_2 + n_3\vec{a}_3$. Since a translation operator $\hat{T}_{\vec{R}}$, which is defined by

$$\hat{T}_{\vec{R}}\, f(\vec{r}) = f(\vec{r} - \vec{R})$$

for arbitrary functions f, commutes with an electronic, single-particle Hamiltonian[3] in the case of a periodic potential,

$$\hat{H} = -\frac{\hbar^2\nabla^2}{2m} + V(\vec{r}), \qquad V(\vec{r} + \vec{R}) = V(\vec{r}) \quad \forall\vec{R},$$

the eigenstates of $\hat{H}$ can be chosen such that they are simultaneously eigenstates of all possible translation operators $\hat{T}_{\vec{R}}$. The translation operators are unitary; thus, they have complex eigenvalues with unit norm that can consequently be written as $\mathrm{e}^{-\mathrm{i}\vec{k}\vec{R}}$, which introduces the real vector $\vec{k}$. This can equivalently be deduced from their group properties. The eigenvalue equation,

$$\hat{T}_{-\vec{R}}\, \psi_{n\vec{k}}(\vec{r}) = \psi_{n\vec{k}}(\vec{r} + \vec{R}) = \mathrm{e}^{\mathrm{i}\vec{k}\vec{R}}\, \psi_{n\vec{k}}(\vec{r}),$$

turns out to be Bloch's theorem already. It is common to make a Bloch-like wave function *ansatz*,

$$\psi_{n\vec{k}}(\vec{r}) = \mathrm{e}^{\mathrm{i}\vec{k}\vec{r}} u_{n\vec{k}}(\vec{r}) \quad \text{with} \quad u_{n\vec{k}}(\vec{r} + \vec{R}) = u_{n\vec{k}}(\vec{r}), \tag{2.6}$$

[2] Note that this does not mean that *every* wave function of the crystal has translational invariance.

[3] We will be using single-particle equations and wave functions later in the Kohn-Sham context, e.g., Eq. (2.10).

Dieses Werk ist copyrightgeschützt und darf in keiner Form vervielfältigt werden noch an Dritte weitergegeben werden.
Es gilt nur für den persönlichen Gebrauch.

since

$$\psi_{n\vec{k}}(\vec{r}+\vec{R}) = \mathrm{e}^{\mathrm{i}\vec{k}(\vec{r}+\vec{R})} u_{n\vec{k}}(\vec{r}+\vec{R}) = \mathrm{e}^{\mathrm{i}\vec{k}\vec{R}} \mathrm{e}^{\mathrm{i}\vec{k}\vec{r}} u_{n\vec{k}}(\vec{r}) = \mathrm{e}^{\mathrm{i}\vec{k}\vec{R}} \psi_{n\vec{k}}(\vec{r}).$$

If we insert the Bloch-like wave function *ansatz* into a Schrödinger-like equation,

$$\hat{H}\psi_{n\vec{k}}(\vec{r}) = \left[-\frac{\hbar^2\nabla^2}{2m} + V(\vec{r})\right] \mathrm{e}^{\mathrm{i}\vec{k}\vec{r}} u_{n\vec{k}}(\vec{r}) = \varepsilon_{n\vec{k}}\, \mathrm{e}^{\mathrm{i}\vec{k}\vec{r}} u_{n\vec{k}}(\vec{r}) = \varepsilon_{n\vec{k}}\, \psi_{n\vec{k}}(\vec{r}),$$

apply the operator in brackets and cancel the phase, we end up with the following partial differential equation for the $u_{n\vec{k}}$:

$$\left[\frac{\hbar^2}{2m}(\vec{k} - \mathrm{i}\nabla)^2 + V(\vec{r})\right] u_{n\vec{k}}(\vec{r}) = \varepsilon_{n\vec{k}}\, u_{n\vec{k}}(\vec{r}). \tag{2.7}$$

As we see, $\vec{k}$ enters the equation as a parameter; thus, we can solve it separately for each $\vec{k}$ we are interested in. Since the $u_{n\vec{k}}$ have to fulfill the lattice periodicity constraint, solving Eq. (2.7) becomes a boundary value problem on one single unit cell spanned by the vectors $\vec{a}_i$. Therefore, the energies $\varepsilon_{n\vec{k}}$ will be discrete. The index n labels the different solutions for a given $\vec{k}$ and is usually referred to as band index.

It is possible to restrict $\vec{k}$ to the first Brillouin zone. Since the reciprocal lattice vectors $\vec{G} = m_1\vec{b}_1 + m_2\vec{b}_2 + m_3\vec{b}_3$ fulfill (or can be defined via) $\mathrm{e}^{\mathrm{i}\vec{R}\vec{G}} = 1$, any $\vec{k}$ can be folded back to the first Brillouin zone by using an appropriate $\vec{G}$ without inducing any changes. This means that the problem of solving the Schrödinger equation for an infinite crystal reduces to the study of a single unit cell for different $\vec{k}$. As a consequence of the periodic boundary conditions, the number of $\vec{k}$ points in the first Brillouin zone is identical to the number of unit cells in the crystal volume that is considered. In the limit of an infinite system, the eigenvalues $\varepsilon_{n\vec{k}}$ become quasi-continuous functions of $\vec{k}$ and form bands.

2.2 Density functional theory

In the previous section it was shown how large periodic crystals can be described efficiently using Bloch's theorem, which states that the electronic structure of the infinite solid can be derived from calculations of single unit cells containing a small atomic basis. Single atoms and medium-sized molecules like porphyrins or phthalocyanines are not periodic, but contain a comparable number of electrons which move in an external potential given by the fixed nuclei. Unfortunately, already these small quantum systems are far too complicated to be solved directly. A possible alternative is the extremely successful density functional theory (DFT), for which W. Kohn received the 1998 Nobel Prize in Chemistry. Even though DFT was introduced nearly fifty years ago, there is still ongoing research concerning fundamental aspects. Its applications are extremely widespread. DFT is the quantum-theoretical method of choice for systems that are too large to be treated by the more exact quantum-chemical methods like configuration interaction or coupled cluster (small molecules), but still small enough to be in range for modern high-performance computers. Nowadays, systems containing around 1000 atoms can be handled.[4] Very large biomolecules or polymers

[4] See, for example, Refs. [26, 27]. Note that actually the number of *electrons*, not the number of atoms, is the decisive factor. Thus, the feasibility of a system depends on the involved elements, the basis set (localized vs. delocalized), whether an all-electron or a pseudopotential approach is used, the necessary quality of the Brillouin zone sampling (metallic/insulating/isolated system), etc.

Dieses Werk ist copyrightgeschützt und darf in keiner Form vervielfältigt werden noch an Dritte weitergegeben werden.
Es gilt nur für den persönlichen Gebrauch.

with several thousands of atoms are beyond DFT and can only be described by empirical methods like classical molecular dynamics employing so-called force fields.

Density functional theory is closely related to the Thomas-Fermi method which was already proposed in 1927 and employs the charge density $n(\vec{r})$ as its basic variable. However, it is more sophisticated in its mathematical foundation and the treatment of kinetic energy, exchange, and correlation of the interacting particles.

2.2.1 The theorems of Hohenberg and Kohn

Density functional theory is based on two mathematical theorems published by Hohenberg and Kohn in 1964 [28]. They can be applied to any system of N interacting particles in an external potential $V_{\text{ext}}(\vec{r})$, thus also (and especially) to interacting electrons in a potential given by the nuclei.

1. The external potential $V_{\text{ext}}(\vec{r})$ is, except for a constant shift, a unique functional of the ground state density $n_0(\vec{r}) = \langle \Psi_0 | \sum_{i=1}^{N} \delta(\vec{r} - \vec{r}_i) | \Psi_0 \rangle$. Since the external potential determines the Hamiltonian $\hat{H}$ completely, all properties (observables) of the system follow from $n_0(\vec{r})$.

2. The ground state density $n_0(\vec{r})$ minimizes the total energy functional

$$E[n] = F_{\text{HK}}[n] + E_{\text{ext}}[n] = F_{\text{HK}}[n] + \int \mathrm{d}^3 r \; n(\vec{r}) \; V_{\text{ext}}(\vec{r}), \tag{2.8}$$

   where $F_{\text{HK}}[n] = T[n] + E_{\text{e-e}}[n]$ is a *universal* functional (independent of any external potential) as defined by Hohenberg and Kohn [28]. $T[n]$, $E_{\text{e-e}}[n]$, and $E_{\text{ext}}[n]$ account for the kinetic energy, the electron-electron potential energy, and the electron-nucleus potential energy, respectively.

The astonishingly simple proof normally assumes a system with nondegenerate ground state, but can be extended to the degenerate case [22, 29]. The alternative, more general foundation of DFT proposed by Levy and Lieb [30, 31] already comprises this aspect. It is important to note here that these theorems found DFT as an *exact* many-particle theory without approximations, even though the coordinate space dimension is reduced from $3N$ to 3 for N particles in three dimensions.

In summary, the theorems of Hohenberg and Kohn imply that if we have found the global minimum n_0 of $E[n]$ by using, for example, the variational principle, we know the exact ground state energy $E[n_0] = \langle \Psi_0 | \hat{H} | \Psi_0 \rangle$ and all other properties we are interested in of the interacting many-body system.

2.2.2 The Kohn-Sham scheme

The next step, which turned DFT into the successful technique in electronic structure theory it is nowadays, was made by Kohn and Sham (KS) in 1965 [32]. They replaced the many-body problem of interacting electrons and nuclei by an auxiliary single-electron system that leads to the same ground state density $n_0(\vec{r})$ as the real system.

Dieses Werk ist copyrightgeschützt und darf in keiner Form vervielfältigt werden noch an Dritte weitergegeben werden.
Es gilt nur für den persönlichen Gebrauch.

The Kohn-Sham equations

The task is to minimize the energy functional (2.8). From occupied, fermionic single-particle wave functions $\psi_i(\vec{r})$ building up a Slater determinant Ψ the density can be derived as

$$n(\vec{r}) = \sum_{i=1}^{N} \langle \Psi | \delta(\vec{r} - \vec{r}_i) | \Psi \rangle = \sum_{i=1}^{N} |\psi_i(\vec{r})|^2.$$

The kinetic energy of such a system is, in Hartree units,[5]

$$T = \langle \Psi | \left[-\frac{1}{2} \sum_{i=1}^{N} \nabla_i^2 \right] | \Psi \rangle = \sum_{i=1}^{N} \int \mathrm{d}^3 r \; \psi_i^*(\vec{r}) \left[-\frac{1}{2} \nabla^2 \right] \psi_i(\vec{r}) = \frac{1}{2} \sum_{i=1}^{N} \int \mathrm{d}^3 r \left| \vec{\nabla} \psi_i(\vec{r}) \right|^2,$$

where in the last step integration by parts has been used, omitting the surface term. We can also calculate a Hartree term which arises from the "classical" Coulomb interaction of an electron density $n(\vec{r})$:

$$E_\mathrm{H} = \frac{1}{2} \int \mathrm{d}^3 r_1 \int \mathrm{d}^3 r_2 \, \frac{n(\vec{r}_1)\, n(\vec{r}_2)}{|\vec{r}_1 - \vec{r}_2|}.$$

The universal part of the energy functional (2.8) can now been written as

$$F_\mathrm{HK}[n] = T + E_\mathrm{H}[n] + E_\mathrm{xc}[n],$$

which defines formally the so-called exchange-correlation functional, one of the most important components in DFT:

$$E_\mathrm{xc}[n] = F_\mathrm{HK}[n] - T - E_\mathrm{H}[n] = (T[n] - T) + (E_\text{e-e}[n] - E_\mathrm{H}[n]).$$

It contains the difference between the original kinetic energy functional and the single-particle kinetic energy defined above, which is presumably small [29], and the nonclassical part of the electron-electron interaction. The total energy functional now reads:

$$E[n] = T + E_\mathrm{H}[n] + E_\mathrm{xc}[n] + E_\mathrm{ext}[n]. \tag{2.9}$$

By minimizing this functional with respect to the density n, the Kohn-Sham equations can be derived. The constraint $\int \mathrm{d}^3 r \; \psi_i^*(\vec{r}) \psi_j(\vec{r}) = \delta_{ij}$ of orthonormal single-particle wave functions has to be included via Lagrange multipliers ε_{ij}:

$$\Omega[n] = E[n] - \sum_{i,j=1}^{N} \varepsilon_{ij} \left(\int \mathrm{d}^3 r \; \psi_i^*(\vec{r}) \psi_j(\vec{r}) - \delta_{ij} \right).$$

The variational equation (minimization condition) leads to

$$\begin{aligned} 0 \stackrel{!}{=} \frac{\delta \Omega[n]}{\delta \psi_i^*(\vec{r})} &= \frac{\delta T}{\delta \psi_i^*(\vec{r})} + \left[\frac{\delta E_\mathrm{H}}{\delta n(\vec{r})} + \frac{\delta E_\mathrm{xc}}{\delta n(\vec{r})} + \frac{\delta E_\mathrm{ext}}{\delta n(\vec{r})} \right] \frac{\delta n(\vec{r})}{\delta \psi_i^*(\vec{r})} - \sum_{j=1}^{N} \varepsilon_{ij} \psi_j(\vec{r}) \\ &= -\frac{1}{2} \nabla^2 \psi_i(\vec{r}) + [V_\mathrm{H} + V_\mathrm{xc} + V_\mathrm{ext}]\, \psi_i(\vec{r}) - \sum_{j=1}^{N} \varepsilon_{ij} \psi_j(\vec{r}), \end{aligned}$$

[5] Hartree units: $e = \hbar = m = (4\pi\varepsilon_0)^{-1} = 1$ vs. Rydberg units: $e^2/2 = \hbar = 2m = 1$

Dieses Werk ist copyrightgeschützt und darf in keiner Form vervielfältigt werden noch an Dritte weitergegeben werden.
Es gilt nur für den persönlichen Gebrauch.

where the chain rule has been used. Unitary transformation of the ψ_i [29] leads to the well-known form of the Kohn-Sham equations,

$$\left[-\frac{1}{2}\nabla^2 + V_{\mathrm{KS}}(\vec{r})\right]\psi_i(\vec{r}) = \varepsilon_i\psi_i(\vec{r}), \tag{2.10}$$

where the effective Kohn-Sham potential is given by

$$V_{\mathrm{KS}} = V_{\mathrm{H}} + V_{\mathrm{xc}} + V_{\mathrm{ext}}. \tag{2.11}$$

These eigenvalue equations are partial differential equations of the Schrödinger type and are much easier to handle than the original many-particle system. They describe the movement of a single electron in an effective potential generated by the other electrons (through their charge density) and the nuclei. This is the common mean-field interpretation of the Kohn-Sham equations. In the case of periodic boundary conditions, Bloch's theorem can be applied, which leads to equations like Eq. (2.7).

Solving the Kohn-Sham equations: The self-consistency scheme

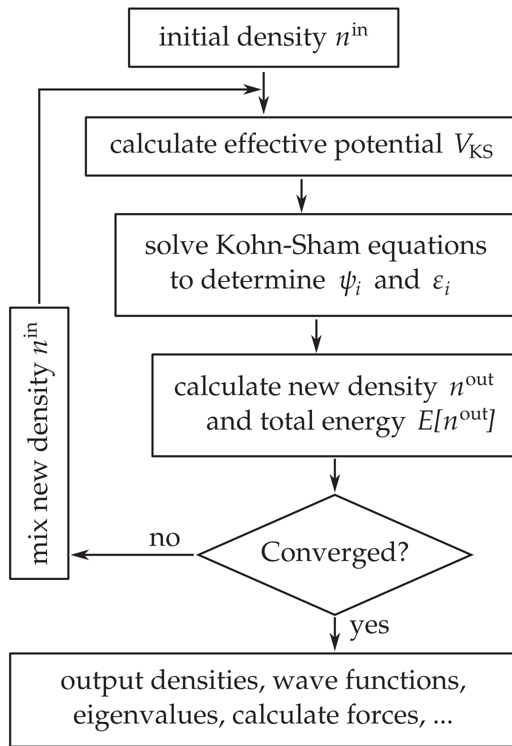

Figure 2.1 – DFT-SCF flowchart for solving the Kohn-Sham equations.

The effective Kohn-Sham potential V_{KS} depends via the Hartree potential,

$$V_{\mathrm{H}}(\vec{r}) = \frac{\delta E_{\mathrm{H}}}{\delta n(\vec{r})} = \int \mathrm{d}^3 r' \, \frac{n(\vec{r}\,')}{|\vec{r}-\vec{r}\,'|} \ ,$$

on the density n and thus on the wave functions ψ_i, which again depend on V_{KS}. Thus, the Kohn-Sham equations (2.10) have to be solved iteratively, as outlined in Fig. 2.1.

Starting from an initial density n_1^{in} (calculated, for example, from superimposed atomic orbitals), the ψ_i are determined as solutions of Eqs. (2.10). From these wave functions a new density n_1^{out} is derived. By using some mixing algorithm, a density n_2^{in} is generated from n_1^{out} and (several) old densities, and Eqs. (2.10) are solved again. This *self-consistent field* (SCF) loop is repeated until the density n (and the corresponding energy $E[n]$) is converged.[6]

Converging the density is, in principle, a chapter of its own. Several mixing algorithms exist, like simple linear mixing,

$$n_{i+1}^{\mathrm{in}} = \beta n_i^{\mathrm{out}} + (1-\beta) n_i^{\mathrm{in}},$$

or the more elaborate (and in most cases faster converging) Broyden mixing, a Krylov-like method that uses data of several preceding densities and will be employed predominantly in

[6] "Converged" means that the following density changes are only small; for instance, the norm of the difference of two subsequent densities is below a chosen threshold.

Dieses Werk ist copyrightgeschützt und darf in keiner Form vervielfältigt werden noch an Dritte weitergegeben werden.
Es gilt nur für den persönlichen Gebrauch.

this thesis. Linear mixing with $\beta = 1$ corresponds to the naive case where one only uses the new density, a strategy that mostly fails. Other common schemes are Pulay mixing, which works similarly to the Broyden method, and Kerker mixing.

Spin-polarized systems

For a spin-polarized system with collinear magnetic moments, the effective Kohn-Sham potential can be written as

$$\begin{aligned} V_{\mathrm{KS}}^{\sigma}(\vec{r}) &= V_{\mathrm{ext}}(\vec{r}) + V_{\mathrm{H}}(\vec{r}) + V_{\mathrm{xc}}^{\sigma}(\vec{r}) \\ &= V_{\mathrm{ext}}(\vec{r}) + \frac{\delta E_{\mathrm{H}}}{\delta n^{\sigma}(\vec{r})} + \frac{\delta E_{\mathrm{xc}}}{\delta n^{\sigma}(\vec{r})}, \end{aligned}$$

where $\sigma \in \{\uparrow, \downarrow\}$. The generalization of density and kinetic energy expressions is very simple, since just an additional summation over the two spin states σ has to be performed. In addition, a spin density can be defined:

$$m(\vec{r}) = n^{\uparrow}(\vec{r}) - n^{\downarrow}(\vec{r}).$$

The Hartree potential,

$$V_{\mathrm{H}}(\vec{r}) = \frac{\delta E_{\mathrm{H}}}{\delta n^{\sigma}(\vec{r})} = \int \mathrm{d}^3 r' \, \frac{n^{\uparrow}(\vec{r}\,') + n^{\downarrow}(\vec{r}\,')}{|\vec{r} - \vec{r}\,'|} = \int \mathrm{d}^3 r' \, \frac{n(\vec{r}\,')}{|\vec{r} - \vec{r}\,'|} \qquad \forall \sigma,$$

is spin-independent. The extension of Eq. (2.7) to the spin-polarized, collinear case is straightforward:

$$\left[\frac{1}{2}(\vec{k} - \mathrm{i}\nabla)^2 + V_{\mathrm{KS}}^{\sigma}(\vec{r})\right] u_{n\vec{k}}^{\sigma}(\vec{r}) = \varepsilon_{n\vec{k}}^{\sigma} \, u_{n\vec{k}}^{\sigma}(\vec{r}). \tag{2.12}$$

Here one simply has two sets of effective potentials V_{KS}^{σ}, energy eigenvalues $\varepsilon_{n\vec{k}}^{\sigma}$, and wave functions $u_{n\vec{k}}^{\sigma}$. The spin index σ in the latter two quantities is often absorbed in n or in $\vec{k}$ by a doubling of the bands or the $\vec{k}$ points, respectively.

Interpretation of the Kohn-Sham eigenvalues

It is tempting to interpret the Kohn-Sham eigenvalues ε_i as energy levels of the studied system. In fact, this is actually the common procedure. However, care has to be taken. First of all, they arise only as auxiliary quantities in the Kohn-Sham scheme, and at first sight there is no obvious reason why any connection to physical observables should exist. However, by using the adiabatic connection concept it is possible to show that differences of Kohn-Sham eigenvalues can be interpreted as well-defined "zeroth-order" approximations to excitation energies in the interacting system [33], which means that they can be compared, for example, to results from angle-resolved photoemission spectroscopy (ARPES) experiments. One exception that allows for a rigorous statement is the highest occupied energy eigenvalue in a *finite* system, which can be shown to be equal to minus the ionization energy [22, 34], a statement that is similar to Koopmans' theorem in Hartree-Fock theory. Problematic are the facts that (i) the electron-electron interaction is in general not small, which weakens the perturbative statement above, and (ii) the exact exchange-correlation functional is not known (see below).

Dieses Werk ist copyrightgeschützt und darf in keiner Form vervielfältigt werden noch an Dritte weitergegeben werden.
Es gilt nur für den persönlichen Gebrauch.

These remarks need to be kept in mind in the discussion of the well-known DFT band gap problem for semiconductors. The failure of DFT should not be directly deduced from the too small energy gap in the Kohn-Sham spectrum [see also Eq. (2.13) on page 27]. Nevertheless and more importantly, problems in, e.g., the simulation of impurities in semiconductors can arise if the energy level sequence is predicted falsely. We will come back to this point later in this thesis.

It is possible to improve the energy levels, especially the Kohn-Sham band gaps in semiconductors, by the many-body quasiparticle *GW* approximation [35] or by hybrid exchange-correlation functionals which also calculate the Fock exchange. The latter case will be discussed below. The drawback is that both types of calculations are extremely demanding with respect to computational resources, and for that reason they are not applicable to large systems.

Even with the Kohn-Sham approach, DFT is still exact, and if the correct expression for the exchange-correlation functional were known, the calculated Kohn-Sham ground state density would be the ground state density of the fully-interacting system. Unfortunately, the exact expression for $E_{\mathrm{xc}}[n]$ is *not* known, and approximate formulations are necessary. Some of them will be discussed below. The separation of the total energy functional into independent-particle kinetic energy, long-range Hartree energy, and exchange-correlation energy turns out to be a clever strategy, since only in this case the latter can be approximated in a local (or semilocal) way. This leads us to the next section, which describes several common approximations for the exchange-correlation functional.

2.2.3 Exchange and correlation

The central problem in the energy functional (2.9) is that the exchange-correlation part $E_{\mathrm{xc}}[n]$ is simply not known, which makes approximations inevitable. From this point on, Kohn-Sham DFT is no longer exact.

As the name already suggests, the constituents of the exchange-correlation functional have a clear physical background. The term “exchange” refers to the indistinguishability of electrons and to the Pauli exclusion principle, which forces two electrons (fermions) in the same spin state not to occupy the same region in space and is accounted for by a wave function that behaves antisymmetric under particle exchange. The term “correlation”, on the other hand, conveys the idea that the motion of one electron is correlated with the position and motion of the other electrons.

In the course of time, many different approximations for the exchange-correlation functional have been proposed. In all prominent examples, the homogeneous electron gas, which can be solved exactly, is of fundamental importance.

Homogeneous electron gas

The homogeneous electron gas is a model of an interacting free electron gas without external potential, but with a constant background charge to ensure charge neutrality. It is often referred to as “jellium model” and usually studied analytically in textbooks to demonstrate the Hartree-Fock approximation.

Dieses Werk ist copyrightgeschützt und darf in keiner Form vervielfältigt werden noch an Dritte weitergegeben werden.
Es gilt nur für den persönlichen Gebrauch.

In Hartree atomic units the Hamiltonian reads:

$$\hat{H} = -\frac{1}{2}\sum_i \nabla_i^2 + \frac{1}{2}\sum_{i\neq j}\frac{1}{|\vec{r}_i - \vec{r}_j|} - \frac{1}{2}\left(\frac{N}{V}\right)^2 \int_V \mathrm{d}^3r\, \mathrm{d}^3r' \frac{1}{|\vec{r} - \vec{r}'|} ,$$

and contains the kinetic energy of the electrons, the *full* electron-electron interaction, and the difference of electron-background and background-background interaction in a volume V. The Hamiltonian is well defined, since the different divergent Coulomb interactions cancel each other. (No $q = 0$ component arises in Fourier space.)

The homogeneous electron gas model can be solved *without* approximations numerically via Quantum Monte Carlo (QMC) simulations. The important point here is that fits of QMC solutions for different densities $n(\vec{r})$ and, if necessary, different spin polarizations,

$$\zeta(\vec{r}) = \frac{n^{\uparrow}(\vec{r}) - n^{\downarrow}(\vec{r})}{n^{\uparrow}(\vec{r}) + n^{\downarrow}(\vec{r})} ,$$

are the basis for the local density approximation explained below.

Local density and generalized gradient approximations: LDA and GGA

Already Kohn and Sham realized [32] that the way from the homogeneous electron gas to an approximate expression for the exchange-correlation functional is not far. The following form corresponds to the local density approximation (LDA):

$$E_{\mathrm{xc}}^{\mathrm{LDA}}[n] = \int \mathrm{d}^3r\; n(\vec{r})\, \varepsilon_{\mathrm{xc}}^{\mathrm{hom}}(n(\vec{r})).$$

Here one simply assumes at all positions $\vec{r}$ that the exchange-correlation energy density is the same as in a homogeneous electron gas with the same density $n(\vec{r})$. The exchange-correlation energy density can be divided into exchange and correlation contributions,

$$\varepsilon_{\mathrm{xc}}^{\mathrm{hom}}(n) = \varepsilon_{\mathrm{x}}^{\mathrm{hom}}(n) + \varepsilon_{\mathrm{c}}^{\mathrm{hom}}(n),$$

where the exchange term can be given analytically and is proportional to $-n^{1/3}$ [29]. The correlation term can be fitted to QMC data of the homogeneous electron gas [36,37].

In the spin-polarized case, the local spin density approximation (LSDA) is often used:

$$E_{\mathrm{xc}}^{\mathrm{LSDA}}[n,\zeta] = \int \mathrm{d}^3r\; n(\vec{r})\, \varepsilon_{\mathrm{xc}}^{\mathrm{hom}}(n(\vec{r}),\zeta(\vec{r})).$$

Again, an exact expression for the exchange part can be derived [38]. The correlation term can be approximated to scale analogously to the exchange part [39] or it can be fitted to QMC data [37].

From these definitions it becomes already clear that the L(S)DA is expected to work best in very homogeneous systems like nearly-free-electron metals and worst in highly inhomogeneous systems like atoms, molecules, or solids with highly varying densities.

The overall performance of the LDA is surprisingly good. One of the most probable reasons is that it obeys some exact properties; for example, the spatial integral over the exchange-correlation hole around an electron is exactly -1 ("sum rule"). Furthermore, there is a delicate error cancellation between exchange and correlation parts [29].

Dieses Werk ist copyrightgeschützt und darf in keiner Form vervielfältigt werden noch an Dritte weitergegeben werden.
Es gilt nur für den persönlichen Gebrauch.

Common shortcomings of the LDA are overbinding effects arising in many cases (too large binding or cohesive energies, especially in van-der-Waals (vdW) systems; too small lattice constants [40]; too large bulk moduli). Moreover, magnetic properties are often predicted erroneously, a prominent example being the ground state of bulk Fe [which is nonmagnetic (NM) hcp in LDA instead of ferromagnetic (FM) bcc].

An improvement for several situations is the inclusion of the magnitude of the density gradient $|\nabla n|$. Already Kohn and Sham suggested such a "gradient expansion approximation" (GEA) [32]. The low-order expansion of the exchange and correlation expressions is actually known [41]. Nevertheless, it has been shown that the GEA does not lead to a consistent improvement of the LDA; instead, it often produces even less accurate results [42]. This behavior can be traced back to the too large gradients in real materials. Furthermore, the exchange-correlation hole does not fulfill the aforementioned sum rule.

It turned out to be fortunate to deviate from an exact gradient expansion form for the functional. The generalized gradient approximation (GGA) allows for more freedom, and consequently many suggestions for functionals have been made in the past. One of the most prominent functionals is the one proposed by Perdew and Wang in 1991 (PW91, Refs. [43, 44]). Perdew, Burke, and Ernzerhof suggested in 1996 a similar functional with a much simpler form (PBE, Ref. [45]), which is nowadays maybe the most important GGA functional used in DFT. Although PBE is often considered to be equivalent to PW91, it has been shown that significant differences can arise in calculated results, e.g., Pt monovacancy formation energies or surface energies [46]. In this thesis, the PBE functional will be used predominantly. It can be written as

$$E_{\mathrm{xc}}^{\mathrm{PBE}}[n^{\uparrow},n^{\downarrow}] = E_{\mathrm{x}}^{\mathrm{PBE}}[n^{\uparrow},n^{\downarrow}] + E_{\mathrm{c}}^{\mathrm{PBE}}[n^{\uparrow},n^{\downarrow}],$$

where the exchange term fulfills the spin-scaling relation

$$E_{\mathrm{x}}^{\mathrm{PBE}}[n^{\uparrow},n^{\downarrow}] = \frac{1}{2}\left(E_{\mathrm{x}}^{\mathrm{PBE}}[2n^{\uparrow}] + E_{\mathrm{x}}^{\mathrm{PBE}}[2n^{\downarrow}]\right).$$

Thus, it is sufficient to calculate the fully spin-polarized exchange contribution,

$$E_{\mathrm{x}}^{\mathrm{PBE}}[n] = \int \mathrm{d}^3r\; n(\vec{r})\, \varepsilon_{\mathrm{x}}^{\mathrm{hom}}(n(\vec{r}))\, F_{\mathrm{x}}(s(\vec{r}))\,, \qquad s(\vec{r}) = \frac{1}{2(3\pi^2)^{1/3}} \frac{|\nabla n(\vec{r})|}{n(\vec{r})^{4/3}}\,,$$

with the dimensionless exchange enhancement factor F_{x} and the reduced density gradient s. The factor $F_{\mathrm{x}}(s)$ is the crucial difference to the LDA and characterizes the different GGA functionals. A plot of $F_{\mathrm{x}}(s)$ comparing different GGA functionals can be found in Ref. [22], which makes clear that (i) all GGA functionals lead to similar results for small s and (ii) $F_{\mathrm{x}}(s) \geq F_{\mathrm{x}}^{\mathrm{LDA}}(s) = 1$ for all s in the case of PBE, which results in lower exchange energies compared to LDA and corrects the LDA overbinding, especially in atoms and small molecules [45]. The correlation term, on the other hand, is

$$E_{\mathrm{c}}^{\mathrm{PBE}}[n^{\uparrow},n^{\downarrow}] = \int \mathrm{d}^3r\; n(\vec{r})\, \left[\varepsilon_{\mathrm{c}}^{\mathrm{hom}}(n(\vec{r}), \zeta(\vec{r}))\, F_{\mathrm{c}}(r_s(\vec{r}), \zeta(\vec{r}), t(\vec{r}))\right],$$

with $r_s = (3/4\pi n)^{1/3}$, $t \sim |\nabla n|/\phi n^{7/6}$, and $\phi = \frac{1}{2}\left[(1+\zeta)^{2/3} + (1-\zeta)^{2/3}\right]$. Details of the actual parametrization of F_{x} and F_{c} are given in Ref. [45]. Even though the whole construction might appear far-fetched at first sight, the PBE functional is the essence of seven

Dieses Werk ist copyrightgeschützt und darf in keiner Form vervielfältigt werden noch an Dritte weitergegeben werden.
Es gilt nur für den persönlichen Gebrauch.

plausible and physical conditions which it fulfills. Among these are the sum rule for the exchange-correlation hole (see above), the Lieb-Oxford bound [47] for the exchange energy,

$$E_{\mathrm{x}}^{\mathrm{PBE}}[n^{\uparrow}, n^{\downarrow}] \geq E_{\mathrm{xc}}^{\mathrm{PBE}}[n^{\uparrow}, n^{\downarrow}] \geq -1.679 e^2 \int \mathrm{d}^3 r \; n(\vec{r})^{4/3},$$

the cancellation of exchange and correlation gradient corrections in the slowly varying limit ($s \to 0$), and a vanishing correlation term in the rapidly varying limit ($t \to \infty$). Apart from the fitted QMC results for the homogeneous electron gas, *all* parameters entering the functional are fundamental constants.

Characteristic for the semilocal PBE functional, along with the aforementioned LDA overbinding correction, is a frequent underbinding of the valence electrons, which leads to overestimated lattice constants of solids and bond lengths of molecules [40]. Bulk moduli are often too low, and also surface energies tend to be lower in PBE than in LDA, which is certainly a consequence of the underbinding. A further important aspect is the correct determination of the magnetic ground state of bcc-Fe, which is a strong argument to employ GGA functionals in studies of transition metal (TM) compounds.

The computational cost of GGA functionals is only slightly higher than for the LDA. However, the inclusion of gradients leads to some numerical difficulties. In particular, a numerically well-chosen expression for the exchange-correlation potential V_{xc} is required [22].

Hybrid functionals

For semiconductors and insulators, the (semi-)local LDA and GGA exchange-correlation functionals usually predict too small energy gaps in the Kohn-Sham band structure. For example, LDA leads to a value of about 0.51 eV (0.00 eV) for Si (Ge), while PBE gives a value of about 0.67 eV (0.00 eV). The experimental band gap is 1.17 eV (0.74 eV) at low temperature [48]. The situation is similar for the insulator MgO (7.90 eV experimentally [49]), where LDA and PBE predict only 4.90 and 4.35 eV, respectively. Note that for Ge actually *no* gap opens at all.

One can sometimes find the statement that there is no band gap issue, since DFT is a ground state theory, and the spacing between valence band (VB) and conduction band (CB) states is a matter of excitations. However, the band gap is a well-defined ground state property that can be calculated from ground state total energies of differently charged systems,

$$\varepsilon_{\mathrm{G}} = (E_{N+1} - E_N) - (E_N - E_{N-1}) = -A + I, \tag{2.13}$$

where A is the electron affinity and I is the ionization energy. This method to determine the band gap is sometimes referred to as ΔSCF and superior to the usual procedure of calculating the difference between Kohn-Sham valence band maximum (VBM) and conduction band minimum (CBM). However, it still shows in practice that LDA-/GGA-DFT does not give the correct band gap.

One of the state-of-the-art strategies to solve this problem are hybrid functionals, even though the idea is not new [50]. In a hybrid functional, exact nonlocal Fock exchange is included in the total energy expression, thus discarding the concept of (semi-)locality. A common example is the PBE0 hybrid functional [51], which is based on PBE:

$$E_{\mathrm{xc}}^{\mathrm{PBE0}} = E_{\mathrm{c}}^{\mathrm{PBE}} + \alpha E_{\mathrm{x}}^{\mathrm{HF}} + (1 - \alpha) E_{\mathrm{x}}^{\mathrm{PBE}},$$

Dieses Werk ist copyrightgeschützt und darf in keiner Form vervielfältigt werden noch an Dritte weitergegeben werden.
Es gilt nur für den persönlichen Gebrauch.

where $\alpha = 1/4$ is determined from perturbation theory. Obviously, a fraction of the PBE exchange is replaced by exact nonlocal Fock exchange from Hartree-Fock (HF) theory,

$$E_{\mathrm{x}}^{\mathrm{HF}} = -\frac{1}{2}\sum_{i,j}\int \mathrm{d}^3 r_1 \int \mathrm{d}^3 r_2 \, \frac{\psi_i^*(\vec{r}_1)\psi_j^*(\vec{r}_2)\psi_j(\vec{r}_1)\psi_i(\vec{r}_2)}{|\vec{r}_1 - \vec{r}_2|}, \tag{2.14}$$

where the ψ_i are occupied Kohn-Sham wave functions. The evaluation of this expression is computationally *extremely* demanding, since $O(M^2)$ numerical integrations are necessary, where M is the number of occupied states times the number of $\vec{k}$ points. As one can see, a hybrid exchange-correlation functional containing Fock exchange is no longer just a functional of the particle density, and the Kohn-Sham formalism has to be generalized. Furthermore, the error cancellation of exchange and correlation that arises in the LDA and GGA functionals is partially sacrificed.

An additional refinement is a screening of the Coulomb potential for the exchange interaction, which leads to a hybrid functional that is usually called HSE (Heyd-Scuseria-Ernzerhof [52–54]):

$$E_{\mathrm{xc}}^{\mathrm{HSE}} = E_{\mathrm{c}}^{\mathrm{PBE}} + \alpha E_{\mathrm{x}}^{\mathrm{HF,\,SR}}(\omega) + (1-\alpha)E_{\mathrm{x}}^{\mathrm{PBE,\,SR}}(\omega) + E_{\mathrm{x}}^{\mathrm{PBE,\,LR}}(\omega).$$

The Coulomb potential is split into a short-range (SR) and a long-range (LR) part,

$$\frac{1}{r} = \frac{1-\mathrm{erf}(\omega r)}{r} + \frac{\mathrm{erf}(\omega r)}{r},$$

and the parameter ω controls the screening. For $\omega = 0$, HSE is equal to PBE0, and for $\omega \to \infty$ it asymptotically reaches PBE. A reasonable, empirically justified choice is $\omega \approx 0.2$ Å^{-1}. The mixing parameter is again set to $\alpha = 1/4$. HSE with this parameter set is known as HSE06 [53, 54]. For Si, Ge, and MgO, HSE06 predicts band gaps of 1.22, 0.54, and 6.40 eV, respectively, which is clearly an improvement over LDA and PBE. The lattice constants are also improved or at least of similar quality. While LDA, in general, tends to give too small lattice constants and PBE usually too large ones, HSE06 lies in between, with a slight tendency towards PBE values [48].

In principle, hybrid functionals can also be applied to metallic systems. However, convergence problems are a common issue. Furthermore, calculations of metallic systems require many $\vec{k}$ points for an accurate Brillouin zone integration, which makes the evaluation of the Fock operator even more time consuming, since the computational time scales with the second power of the number of occupied wave functions $\psi_{\nu\vec{k}}$ (see above).

The DFT+U method

For some solids, usually referred to as "strongly correlated" materials, conventional LDA or GGA fails to predict even basic properties. Common examples are TM oxides, which play an important role in the area of high-T_{C} superconductivity. Instead of a Mott insulating ground state, a metallic behavior is predicted, for example, in FeO and CoO [55, 56]. The common belief is that an improved description of electronic correlation effects is necessary to open the band gap in this case [57].

A computationally cheap technique to address this issue is the LDA+U or GGA+U approach, which was originally suggested by Anisimov *et al.* [58–62] and has undergone several refinements over the years. It consists of an energy correction E_U which is added to the usual

Dieses Werk ist copyrightgeschützt und darf in keiner Form vervielfältigt werden noch an Dritte weitergegeben werden.
Es gilt nur für den persönlichen Gebrauch.

energy functional and leads to a correction of the Kohn-Sham potential. The physical motivation behind E_U is an improved many-body treatment of localized $3d$ and $4f$ electrons in the spirit of a Hubbard model with on-site Coulomb repulsion U and exchange interaction J. Frequently used is the rotationally invariant formulation with effective $U_{\text{eff}} = U - J$ [57, 63], which will be described in the following.

Starting from the usual LDA or GGA, the total energy functional is extended as

$$E_{\text{GGA}+U} = E_{\text{GGA}} + E_{\text{Hubbard}} - E_{\text{DC}} = E_{\text{GGA}} + E_U,$$

where E_{Hubbard} is derived from a Hubbard-like Hamiltonian and E_{DC} is a double counting correction term which accounts for the averaged correlation energy already included in E_{GGA}.[7] After choosing some set of orbitals $\{\phi_m^I\}$, which are localized at atom I, one defines projection operators,

$$\hat{P}^I_{mm'} = |\phi^I_m\rangle\langle\phi^I_{m'}|.$$

Now, the occupation matrices $n^{I\sigma}_{mm'}$ can be constructed,

$$n^{I\sigma}_{mm'} = \sum_{\nu\vec{k}} f^{\sigma}_{\nu\vec{k}} \left\langle \psi^{\sigma}_{\nu\vec{k}} \middle| \hat{P}^I_{mm'} \middle| \psi^{\sigma}_{\nu\vec{k}} \right\rangle,$$

where m and m' index the localized orbitals, I runs through all atoms in the unit cell, and σ is the spin index. The projection operators act on the Kohn-Sham wave functions. The weight factors $f^{\sigma}_{\nu\vec{k}}$ denote the respective occupations. Projectors associated with different sites I do not have to be orthogonal. The matrices $\mathbf{n}^{I\sigma}$ are diagonal in the spin index.

The choice of the localized manifold (and thus of the projectors $\hat{P}^I_{mm'}$) is not unique. It is equally legitimate to project onto normalized atomic orbitals or Wannier functions, or to use Mulliken populations or spherical integrals around the atoms over angular-momentum-decomposed charge densities [57]. However, it is typically constructed from the five d (in the case of TM compounds) or the seven f atomic orbitals (for rare earths and actinides) localized at the respective atoms. If a plane wave/pseudopotential technique is used, the radial part of these orbitals is typically taken from the pseudopotential files. The angular dependence is given by the fixed orbital angular momentum quantum number l and the corresponding magnetic quantum number m.

By using the occupation matrices, E_U can be written as [57]:

$$E_U = E_{\text{Hubbard}} - E_{\text{DC}} = \frac{U}{2} \sum_{I,m,\sigma} \left\{ n^{I\sigma}_{mm} - \sum_{m'} n^{I\sigma}_{mm'} n^{I\sigma}_{m'm} \right\} = \frac{U}{2} \sum_{I,\sigma} \mathrm{Tr} \left[\mathbf{n}^{I\sigma}(1 - \mathbf{n}^{I\sigma}) \right].$$

The trace is invariant under unitary transformations in the space of the localized orbitals and is thus equivalent to a sum over occupation matrix eigenvalues $\lambda^{I\sigma}_i$:

$$E_U = \frac{U}{2} \sum_{I,i,\sigma} \left\{ \lambda^{I\sigma}_i (1 - \lambda^{I\sigma}_i) \right\}.$$

Since $0 \leq \lambda^{I\sigma}_i \leq 1$, the term E_U can obviously be interpreted as an energy penalty favoring empty ($\lambda^{I\sigma}_i = 0$) or full ($\lambda^{I\sigma}_i = 1$) occupation of the involved localized orbitals and counteracting an even distribution of charge among the different orbitals.

[7] The actual form of E_{DC} is point of vivid discussion in the literature. In the method presented here the so-called "atomic limit" is used.

Dieses Werk ist copyrightgeschützt und darf in keiner Form vervielfältigt werden noch an Dritte weitergegeben werden.
Es gilt nur für den persönlichen Gebrauch.

An interesting physical justification for the inclusion of such a Hubbard correction can be given [57]. In LDA or GGA, the total energy of an atom in contact with an electron reservoir is a continuously differentiable, parabola-shaped function of the (fractional) number of electrons in the system, connecting the values for integer electron number E_{N-1}, E_N, E_{N+1}, etc. This is related to the spurious self-interaction of the fractional electron. Actually, such a situation with fractional electron number $N < N + \eta < N + 1$ has to be described by a statistical mixture, and the real shape of the total energy graph would then be piecewise linear:

$$E_{N+\eta} = (1 - \eta)E_N + \eta E_{N+1}.$$

Without the approximations made for the exchange-correlation functional, DFT would be capable of describing this behavior correctly [64]. The correction E_U should be constructed such as to eliminate the erroneous curvature from the LDA/GGA total energy curve. This provides a criterion to determine the value of U consistently.

By recalling the fact that in Kohn-Sham theory the derivative of the total energy with respect to a chosen wave function occupation gives the respective energy eigenvalue,

$$\varepsilon_i = \frac{\partial E_{\mathrm{GGA}}}{\partial n_i},$$

which is sometimes referred to as Janak's theorem [65], one can see that in the presence of U the eigenvalues are modified according to

$$\varepsilon_{i,\sigma} = \frac{\partial E_U}{\partial n_{i,\sigma}} = \sum_{I,j} \frac{\partial \lambda_j^{I\sigma}}{\partial n_{i,\sigma}} \frac{\partial E_U}{\partial \lambda_j^{I\sigma}} \quad \text{with} \quad \frac{\partial E_U}{\partial \lambda_j^{I\sigma}} = \frac{U}{2}(1 - 2\lambda_j^{I\sigma}),$$

which means that they are lowered (elevated) in energy if the corresponding localized orbitals are occupied (unoccupied). This potentially leads to a metal-insulator transition, for example in the FeO compound [57], but also the description of molecules can benefit from a Hubbard-U, e.g., porphyrins with a TM center [66, 67]. The method has also been applied to TM-doped semiconductors like Si [68] or TM-based compounds like half-metallic Heusler alloys [69]. In this thesis, the influence of U is studied for TM silicides and TM-doped Si (chapters 3 and 4).

It should be noted, however, that such an inclusion of on-site electronic correlation does not automatically lead to improved results. Instead, the performance of the method has to be benchmarked by comparison with experiment, even though the value of U can be calculated in a consistent manner by a method based on a linear response approach [57]. Since U can also depend on the site I, different values of U can be used in a system simultaneously, e.g., for compounds containing different TMs. Moreover, the value of U and the projection method are strongly related. It is not possible to give a general value for U in a specific case, since different DFT programs may use different projection methods. If atomic orbitals taken from pseudopotentials are used, the projection can even differ from pseudopotential to pseudopotential.

The DFT+U method can lead to comparable results as hybrid functionals do, but with much less effort. However, since correlation is not exchange in the DFT context, this is only sometimes the case.[8]

[8] Example: For the organic molecule iron phthalocyanine (FePc), the symmetry of the orbitals around the Fermi energy [HOMO (highest occupied molecular orbital), LUMO (lowest unoccupied molecular orbital), HOMO−1, LUMO+1]

Dieses Werk ist copyrightgeschützt und darf in keiner Form vervielfältigt werden noch an Dritte weitergegeben werden.
Es gilt nur für den persönlichen Gebrauch.

2.2.4 Plane waves and pseudopotentials

In a numerical implementation of the Kohn-Sham formalism, the charge and spin densities n, m and the Kohn-Sham wave functions ψ have to be expanded in a basis.

The plane wave basis set

A very convenient basis set choice, especially for periodic systems, are plane waves,

$$\langle\vec{r}|\vec{G}\rangle = \mathrm{e}^{\mathrm{i}\vec{G}\vec{r}}, \qquad \langle\vec{G}'|\vec{G}\rangle = \int \mathrm{d}^3r\ \mathrm{e}^{\mathrm{i}(\vec{G}-\vec{G}')\vec{r}} = \delta_{\vec{G},\vec{G}'} \quad ,$$

where $\vec{G}$ are reciprocal lattice vectors. Since the $u_{\nu\vec{k}}(\vec{r})$ in Eq. (2.6) are lattice periodic, they can be expanded into these plane waves,

$$u_{\nu\vec{k}}(\vec{r}) = \sum_{\vec{G}} u_{\nu,\vec{k},\vec{G}}\ \mathrm{e}^{\mathrm{i}\vec{G}\vec{r}} = \sum_{\vec{G}} u_{\nu,\vec{k}+\vec{G}}\ \mathrm{e}^{\mathrm{i}\vec{G}\vec{r}} \quad \text{with} \quad \sum_{\vec{G}} |u_{\nu,\vec{k}+\vec{G}}|^2 = 1,$$

and the Bloch-like wave functions then read

$$\psi_{\nu\vec{k}}(\vec{r}) = \sum_{\vec{G}} u_{\nu,\vec{k}+\vec{G}}\ \mathrm{e}^{\mathrm{i}(\vec{k}+\vec{G})\vec{r}},$$

where the spin index σ has been suppressed and ν can be interpreted as a combined spin and band index.

Inserting these Fourier-transformed wave functions into the Kohn-Sham equations (2.10) leads to an eigenvalue problem with explicit dependence on $\vec{k}$, similar to Eq. (2.12):

$$\sum_{\vec{G}'} \left[\frac{1}{2}|\vec{k}+\vec{G}|^2 \delta_{\vec{G},\vec{G}'} + V_{\mathrm{H}}(\vec{G}-\vec{G}') + V_{\mathrm{xc}}(\vec{G}-\vec{G}') + V_{\mathrm{ext}}(\vec{k}+\vec{G},\vec{k}+\vec{G}') \right] u_{\nu,\vec{k}+\vec{G}'} = \varepsilon_{\nu\vec{k}}\, u_{\nu,\vec{k}+\vec{G}}. \tag{2.15}$$

This equation can be read as matrix-vector multiplication.[9] While V_{H} and V_{xc} only depend on the difference $\vec{G}-\vec{G}'$, the matrix element of the external potential,

$$V_{\mathrm{ext}}(\vec{k}+\vec{G},\vec{k}+\vec{G}') = \int \mathrm{d}^3r\ \mathrm{e}^{-\mathrm{i}(\vec{k}+\vec{G})\vec{r}}\ V_{\mathrm{ext}}(\vec{r})\ \mathrm{e}^{+\mathrm{i}(\vec{k}+\vec{G}')\vec{r}},$$

can depend on $\vec{k}$ if V_{ext} is replaced by a nonlocal expression.

The tremendous advantage of plane waves is that the expansion described above is actually a Fourier transformation. A very fast algorithm exists, the fast Fourier transformation (FFT), which can be used to efficiently transfer functions from real space to Fourier space and vice versa. Moreover, the quality of the basis set (the number of basis functions) can be systematically improved in a very simple way: In principle, an infinite number of plane waves with different $\vec{G}$ would be necessary to represent all wave functions perfectly. Since

deviates between (semi-)local DFT (PBE, LDA) and hybrid functional results (B3LYP, PBE0, HSE06) according to the author's calculations (all-electron and pseudopotentials). Qualitative agreement (energy ordering and occupation of these orbitals) can be achieved by using the much faster PBE+U approach with $U = 3$ eV. However, this does not always work: For CuPc, qualitative agreement between B3LYP and PBE+U can be achieved for the HOMO$-$1 and HOMO orbitals only. A reversed ordering remains for the LUMO and LUMO+1 orbitals, which are entirely unaffected by U up to 5 eV even though one of them has Cu 3d character.

[9] The matrix consists of diagonal elements with mostly kinetic energy origin and off-diagonal elements that arise due to the potentials.

Dieses Werk ist copyrightgeschützt und darf in keiner Form vervielfältigt werden noch an Dritte weitergegeben werden.
Es gilt nur für den persönlichen Gebrauch.

this is not possible, some truncation condition has to be introduced. Usually, the size of the basis set is limited by a cutoff energy (here for the wave functions),

$$\frac{1}{2}|\vec{k}+\vec{G}|^2 < E^{\text{cut}}_{\text{wfc}},$$

so by simply increasing $E^{\text{cut}}_{\text{wfc}}$ the basis set becomes more and more complete. In general, the charge and spin densities need a higher cutoff energy $E^{\text{cut}}_{\text{dns}}$ in their expansion. For each material, convergence tests have to be performed to determine appropriate values for $E^{\text{cut}}_{\text{wfc/dns}}$.

The disadvantage, on the other hand, is that the plane wave basis set is "universal" and not optimized for a certain problem. Thus, many basis functions are required to provide an accurate expansion of wave functions and densities. The atom with the most complex wave function structure (tight orbitals) determines the lowest acceptable value for the cutoff energies. Especially, the description of core states, which are bound closely to the nuclei and exhibit tight peaks or oscillations in the radial part of the wave functions, is not feasible. Valence states can have strong oscillations due to the orthogonality with the core states. Consequently, many Fourier components would be necessary for an accurate description. This is why a plane wave basis set has to be accompanied by the pseudopotential technique.

The pseudopotential technique

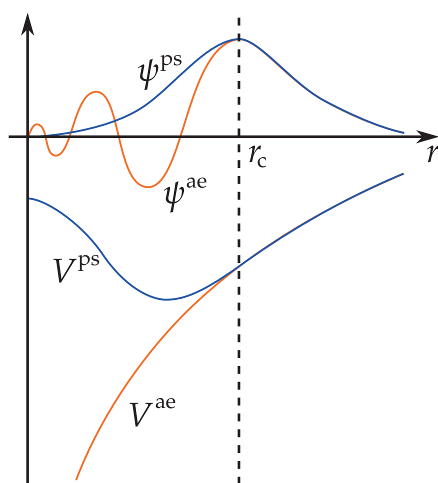

Figure 2.2 – Illustration of the pseudopotential principle.

A common strategy to reduce the numerical effort in a DFT calculation is the replacement of the real atoms by so-called pseudoatoms. A pseudoatom schematically consists of the real atom's valence electrons orbiting a static core formed by the real atom's nucleus and core electrons. Core electrons belong to "inner" (closed shell) atomic orbitals with a relatively large energetic distance to the valence electrons and are therefore assumed to be chemically inert. Their wave functions can be approximated to be fixed ("frozen core approximation") and are not updated during the SCF iterations. Thus, the number of "dynamic" electrons is considerably reduced, which lowers the computer time and memory requirements, since the number of bands that have to be calculated in each SCF iteration depends on the number of electrons.

Mathematically, a pseudoatom is represented by a pseudopotential. Pseudopotentials model the interaction of the valence electrons with the ionic core (nucleus and core electrons). In Fig. 2.2 a sketch of a pseudopotential is shown to illustrate the working mechanism. A rapidly oscillating wave function ψ^{ae} belonging to the full potential $V^{\text{ae}}(r) \sim -Z/r$ is replaced by a pseudo wave function ψ^{ps} which equals the original wave function ψ^{ae} beyond a certain radial cutoff r_{c}, but replaces its oscillations close to the core by a nodeless, smooth behavior which makes ψ^{ps} easier to represent in a plane wave basis than ψ^{ae}: Less Fourier components are necessary, that is, a much lower wave function cutoff energy can be chosen. Subsequently, an

Dieses Werk ist copyrightgeschützt und darf in keiner Form vervielfältigt werden noch an Dritte weitergegeben werden.
Es gilt nur für den persönlichen Gebrauch.

appropriate pseudopotential V^{ps} is constructed from this ψ^{ps} by inversion of the Schrödinger equation.

A pseudopotential is usually generated for an isolated atom and sometimes optimized for certain applications. Due to the frozen core approximation it is not clear that it leads to results of similar quality in different chemical environments. If a pseudopotential *does* reproduce all-electron results with similar quality for different materials, it is said to be "transferable". The quality of a peudopotential can be estimated (i) by comparison of pseudopotential calculation results with values obtained from all-electron calculations (all-electron energy levels vs. pseudo energy levels and their spacings; structural and magnetic properties), and (ii) by checking whether the logarithmic derivatives at some diagnostic radius $r_{\text{diag}} \gtrsim r_{\text{c}}$, $\delta(\varepsilon) = \partial_r \ln \psi(r;\varepsilon)|_{r=r_{\text{diag}}}$, of all-electron and pseudo radial wave functions agree in the different angular momentum channels over the energy range of interest.

Norm-conserving pseudopotentials

In 1979, Hamann, Schlüter, and Chiang (HSC, Ref. [70]) presented a scheme to generate transferable pseudopotentials. An important aspect of their concept was that the pseudo wave functions were created such that they have the same norm as the all-electron wave functions:

$$\int_0^{r_{\text{c}}} \mathrm{d}r\, r^2\, |\psi^{\text{ps}}(r)|^2 = \int_0^{r_{\text{c}}} \mathrm{d}r\, r^2\, |\psi^{\text{ae}}(r)|^2. \tag{2.16}$$

This constraint implies that the electrostatic properties are correct outside the cutoff radius r_{c}. Furthermore, it guarantees that the logarithmic derivatives of the pseudo wave functions and the all-electron wave functions agree beyond r_{c} in value and slope (first energy derivative) around some reference energies (eigenvalues of the orbitals the pseudopotential was constructed for). This is important for the scattering properties and the transferability.

Such a norm-conserving pseudopotential (NCPP) is generated as follows. At first, the all-electron Kohn-Sham equations are solved for an isolated atom to obtain atomic orbitals $\psi_i^{\text{ae}}(r)$. (Note that only the radial part is of importance here.) The oscillations of the valence orbitals are removed by constructing valence pseudo wave functions $\psi_l^{\text{ps}}(r)$, one for each angular momentum channel l ("pseudization"), which agree with the corresponding $\psi_l^{\text{ae}}(r)$ for all $r \geq r_{\text{c}}$, but exhibit a chosen, smooth behavior for $r < r_{\text{c}}$ while still fulfilling the norm-conserving constraint Eq. (2.16). Now, additional potentials $V_l(r)$ are introduced for each angular momentum channel l, which are corrections to a local potential $V_{\text{loc}}(r)$. They vanish for $r \geq r_{\text{c}}$. For $r < r_{\text{c}}$, their value can be calculated from inverting the pseudopotential Kohn-Sham equations. This is possible since the $\psi_l^{\text{ps}}(r)$ have no nodes inside the core region. $V_{\text{loc}}(r)$ is equal to the full potential beyond r_{c} and can be chosen arbitrarily (but ideally smooth) inside the core region.

Improvements concerning the hardness (required plane wave cutoff energy) of HSC pseudopotentials were made, for example, by Rappe, Rabe, Kaxiras, and Joannopoulos [71] as well as by Troullier and Martins [72]. Moveover, Kleinman and Bylander [73] suggested a fully nonlocal and separable form of the pseudopotential, which leads to a linear scaling of the calculations with the number of basis functions. This is a significant advantage over the semilocal HSC potentials, where the scaling is quadratic. The drawback is the possible occurence of so-called "ghost states" (wrong ordering of energy eigenstates) which have to be avoided carefully by generating the pseudopotential appropriately.

Dieses Werk ist copyrightgeschützt und darf in keiner Form vervielfältigt werden noch an Dritte weitergegeben werden.
Es gilt nur für den persönlichen Gebrauch.

Ultrasoft pseudopotentials

Some chemical elements like Al, Si, or P can be accurately described by quite "soft" NCPPs.[10] This is due to their slowly varying pseudo wave functions in real space. Other chemical elements are more demanding: Second-row elements like O, N, or F possess sharp, contracted p orbitals, and TMs (as studied in this thesis) are intricate because of their quite localized d orbitals. In this case, very "hard" NCPPs would be necessary.[11] This is especially inconvenient if one wants to study a system containing only a few hard elements among lots of soft elements (like an isolated TM impurity in a large cell of bulk Si): Due to the delocalized nature of plane waves, the numerical effort necessary to achieve a certain accuracy depends on the hardest element in the system, as already mentioned above.

In 1990, D. Vanderbilt introduced a new concept [74] of *ultrasoft* pseudopotentials (USPPs), leading to drastically lowered plane wave cutoff energies. Here the charge density n is split up into two summands: a soft part (derived from smooth orbitals) and a hard part (augmented charge). USPPs are generated in a fully nonlocal, separable form (like Kleinman-Bylander) *directly* from the pseudo wave functions instead of first creating a HSC-type pseudopotential and subsequently casting it into Kleinman-Bylander form. Moreover, the norm-conserving constraint Eq. (2.16) is relaxed, which allows one to describe also tight orbitals efficiently. The price is that the eigenvalue problem (2.15) has to be generalized (see below).

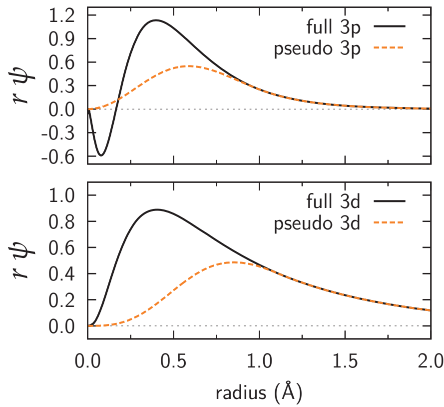

Figure 2.3 – Two selected all-electron and pseudo wave functions of a Mn USPP. The cutoff radii (Å) are $r_c^p = 1.06$ and $r_c^d = 1.16$.

Since almost all pseudopotentials used in the scope of this thesis have been generated by the author, the methodology is presented in more detail, following Refs. [74, 75]. This also provides more insight into the working mechanisms of USPPs.

At first, a usual all-electron calculation for a free atom is carried out (in the framework of Kohn-Sham DFT). This leads to a screened all-electron Kohn-Sham potential $V_{\mathrm{KS}}^{\mathrm{ae}}(r)$. Cutoff radii have to be chosen for the local potential r_c^{loc} and for wave functions in different angular momentum channels r_c^l. A smooth local potential $V_{\mathrm{loc}}(r)$ is constructed that agrees with $V_{\mathrm{KS}}^{\mathrm{ae}}(r)$ beyond r_c^{loc}. It can be generated such as to automatically reproduce the logarithmic derivative at some reference energy in a certain angular momentum channel. For all pseudopotentials used in the scope of this thesis, $rV_{\mathrm{loc}}(r) \to 0$ for $r \to 0$.

Then, by using the self-consistently acquired all-electron potential, the Schrödinger equation can be solved for each angular momentum channel l and usually one to three *arbitrary* energies $\varepsilon_{l\tau}$, $\tau \in \{1,2,3\}$, which cover the energy range over which good scattering properties are desired:

$$\left[\hat{T} + V_{\mathrm{KS}}^{\mathrm{ae}}(r)\right] \psi_i^{\mathrm{ae}}(\vec{r}) = \varepsilon_i \psi_i^{\mathrm{ae}}(\vec{r}),$$

where $i = \{l,m,\tau\}$ and $\hat{T} = -\nabla^2/2$ is the kinetic energy operator. The solutions ψ_i^{ae} are *not* determined self-consistently and are, in general, not normalizable. Nevertheless, one writes

[10] A plane wave cutoff energy of 20 Ry should be sufficient.
[11] A plane wave cutoff energy of 70 Ry or more is needed to achieve converged results.

Dieses Werk ist copyrightgeschützt und darf in keiner Form vervielfältigt werden noch an Dritte weitergegeben werden.
Es gilt nur für den persönlichen Gebrauch.

formally

$$\left(\hat{T} + \hat{V}_{\text{KS}}^{\text{ae}} - \varepsilon_i\right)|\psi_i^{\text{ae}}\rangle = 0$$

in the usual bra-ket notation, although scalar products will be ill defined. For each ψ_i^{ae} one can generate a pseudized version ψ_i^{ps} that joins smoothly with its all-electron counterpart at r_{c}^l (cf. Fig. 2.3). No norm-conserving constraint is mandatory here, which leads to the additional "ultrasoft" behavior of ψ_i^{ps} for $r < r_{\text{c}}^l$ that can clearly be seen in Fig. 2.3, especially for the $3d$ orbitals, where no nodes need to be removed. By using the smooth potential $V_{\text{loc}}(r)$, one constructs auxiliary local orbitals,

$$|\chi_i\rangle = \left(\varepsilon_i - \hat{T} - \hat{V}_{\text{loc}}\right)\left|\psi_i^{\text{ps}}\right\rangle,$$

and the consequently well-defined quantities

$$B_{ij} = \langle\psi_i^{\text{ps}}|\chi_j\rangle,$$

which are then used to define the projector functions,

$$|\beta_i\rangle = \sum_j (B^{-1})_{ij}\,|\chi_j\rangle.$$

They are confined to the core region and vanish outside, exactly like the augmentation functions:

$$Q_{ij}(\vec{r}) = \psi_i^{\text{ae}}(\vec{r})^*\psi_j^{\text{ae}}(\vec{r}) - \psi_i^{\text{ps}}(\vec{r})^*\psi_j^{\text{ps}}(\vec{r}),$$

which are formed by the atomic orbitals. Note that $\sum_i \int Q_{ii}$ is the density difference between the all-electron and the pseudopotential case. The Q functions themselves can be pseudized inside a sphere of radius r_{in}, which reduces the number of Fourier components and consequently lowers the density cutoff $E_{\text{dns}}^{\text{cut}}$. Outside, they match the original Q functions. The pseudization is performed in such a way that the electrostatic potential beyond r_{in} remains unchanged. Further information about this pseudization procedure can be found in Ref. [75].

The last step is a descreening of the local potential,

$$V_{\text{loc}}^{\text{ion}}(r) = V_{\text{loc}}(r) - V_{\text{H}}(r) - V_{\text{xc}}(r),$$

with atomic Hartree and exchange-correlation potentials, and of the projector coefficients,

$$D_{ij}^{(0)} = (B_{ij} + \varepsilon_j q_{ij}) - \int \mathrm{d}^3r\; n(\vec{r})\, V_{\text{loc}}(\vec{r}),$$

where

$$q_{ij} = \int \mathrm{d}^3r\; Q_{ij}(\vec{r}).$$

Integration is possible here (despite the nonnormalizable wave functions in the Q_{ij}), since the difference between all-electron and pseudo wave function vanishes beyond some distance from the core. In summary, an USPP is fully characterized by the four quantities $V_{\text{loc}}^{\text{ion}}(r)$, $D_{ij}^{(0)}$, $Q_{ij}(\vec{r})$, and $\beta_i(\vec{r})$.

Let us now assume a cell with atoms centered at different sites $\vec{R}_I$. For simplicity, the formalism is shown only for the case of a single atomic species in the unit cell. Otherwise, different pseudopotentials have to be used at different sites I. The total energy functional (2.9) of the electron system is slightly modified [75,76]:

$$E = \sum_i \langle\psi_i|\hat{T} + \hat{V}_{\text{NL}}|\psi_i\rangle + E_{\text{H}}[n] + E_{\text{xc}}[n] + \int \mathrm{d}^3r\; n(\vec{r})\, V_{\text{loc}}^{\text{ion}}(\vec{r}). \tag{2.17}$$

Dieses Werk ist copyrightgeschützt und darf in keiner Form vervielfältigt werden noch an Dritte weitergegeben werden.
Es gilt nur für den persönlichen Gebrauch.

Obviously, the simple, local external potential $V_{\text{ext}}(\vec{r})$ has been replaced by a different local potential, and an additional nonlocal term has been introduced, which acts on the Kohn-Sham wave functions ψ_i:

$$V_{\text{loc}}^{\text{ion}}(\vec{r}) = \sum_I V_{\text{loc}}^{\text{ion}}(|\vec{r} - \vec{R}_I|), \qquad \hat{V}_{\text{NL}} = \sum_I \sum_{nm} D_{nm}^{(0)} |\beta_n^I\rangle\langle\beta_m^I|.$$

These two terms represent the pseudopotential. The β functions are projectors, localized at the atom positions (as described above):

$$\langle\vec{r}|\beta_n^I\rangle = \beta_n^I(\vec{r}) = \beta_n(\vec{r} - \vec{R}_I).$$

The expression for the density is also modified:

$$n(\vec{r}) = \sum_i f_i \left[|\psi_i(\vec{r})|^2 + \sum_I \sum_{nm} Q_{nm}^I(\vec{r}) \langle\psi_i|\beta_n^I\rangle\langle\beta_m^I|\psi_i\rangle \right],$$

with the occupations f_i and

$$Q_{nm}^I(\vec{r}) = Q_{nm}(\vec{r} - \vec{R}_I).$$

In addition to the usual square of the absolute value of Kohn-Sham wave functions ψ_i, an augmentation charge is included.

As a consequence of the relaxed norm-conserving constraint, the Kohn-Sham wave functions obey *generalized* orthonormality conditions:

$$\langle\psi_i|\hat{S}|\psi_j\rangle = \delta_{ij},$$

with the Hermitian overlap operator

$$\hat{S} = 1 + \sum_I \sum_{nm} q_{nm} |\beta_n^I\rangle\langle\beta_m^I|.$$

If this is accounted for, variational minimization of the total energy, Eq. (2.17), leads to the modified Kohn-Sham equations:

$$\hat{H}|\psi_i\rangle = \varepsilon_i \hat{S}|\psi_i\rangle, \qquad \hat{H} = \hat{T} + \hat{V}_{\text{KS}} + \sum_I \sum_{nm} D_{nm}^I |\beta_n^I\rangle\langle\beta_m^I|, \tag{2.18}$$

with the Kohn-Sham effective potential in position representation,

$$V_{\text{KS}}(\vec{r}) = V_{\text{H}}(\vec{r}) + V_{\text{xc}}(\vec{r}) + V_{\text{loc}}^{\text{ion}}(\vec{r}).$$

The expressions for V_{H} and V_{xc} are as usual, cf. Eq. (2.11). The screened version of the projector coefficients,

$$D_{nm}^I = D_{nm}^{(0)} + \int \mathrm{d}^3r\, Q_{nm}^I(\vec{r}) V_{\text{KS}}(\vec{r}),$$

depends on the Kohn-Sham potential (and thus on the wave functions and the charge density) and has to be updated constantly during the SCF cycle.

Dieses Werk ist copyrightgeschützt und darf in keiner Form vervielfältigt werden noch an Dritte weitergegeben werden.
Es gilt nur für den persönlichen Gebrauch.

Nonlinear core correction

A final important aspect that shall be mentioned briefly in the context of pseudopotentials is the so-called "nonlinear core correction" (NLCC, Ref. [77]). One problem within the pseudopotential approximation is related to the fact that the density n entering Eq. (2.17), especially the exchange-correlation functional E_{xc}, is generated only from the (pseudo) valence states. Hence, the (nonlinear) exchange-correlation interaction between core and valence electrons is accounted for only in a *linearized* form as included in the pseudopotential. This can be overcome by storing a (partial) core density $\tilde{n}$ in the pseudopotential, which is added to the valence density during the descreening of the pseudopotential and in Eq. (2.17) in such a way that $E_{\mathrm{xc}}[n] \rightarrow E_{\mathrm{xc}}[n+\tilde{n}]$. The inclusion of a partial core density instead of the full core density is sufficient (and saves Fourier coefficients in the representation of $\tilde{n}$), since the correct description of the charge density in a radial interval where core and valence densities of comparable magnitude overlap is sufficient to warrant transferability [77].

The NLCC is primarily needed for atoms with few valence electrons (like alkali metals) and more and more as the atomic number Z increases, i.e., the farther the upper core orbitals extend into the tail of the valence density. If the so-called "semicore" electrons (filled electron subshells that are energetically close to the valence states) are dynamically treated like the valence electrons (e.g., $3p$ electrons in the TM elements), NLCC becomes less important. It is very helpful for spin-polarized systems and eliminates the need for separate spin-up and spin-down ionic pseudopotentials. One finds that magnetic properties (magnetic moments and total energies of different magnetic configurations) are very sensitive to the actual choice of the partial core. Thus, the latter can be used to additionally optimize the pseudopotential with respect to all-electron results.

2.2.5 Different and complementary approaches

The technique presented above resides on a plane wave basis set and (ultrasoft) pseudopotentials and is one of many possible numerical realizations of DFT. It is used predominantly in this thesis (via the Quantum ESPRESSO code [78]), but not exclusively. The reason is that different approaches have different advantages (like accuracy vs. performance). Here a short overview of different methods used in this work is given.

A very popular technique using a plane wave basis set is the so-called projector augmented wave (PAW) method [79]. Its formalism and the accuracy of the results are very similar to that of the USPP method [80]. It is realized, for instance, in the Vienna *ab initio* simulation package (VASP), which is probably the most popular DFT program nowadays [81]. Instead of USPPs, it uses so-called PAW datasets. VASP is used in this thesis mainly for calculations with hybrid exchange-correlation functionals. However, the calculation of the Fock exchange energy (2.14) is not very efficient in a plane wave basis (see below).

In such plane wave pseudopotential methods, the core electrons are static and incorporated into the pseudopotential, as has been described in the previous sections. Only a chosen set of valence electrons is treated dynamically in the SCF cycle. This is an additional approximation (frozen core approximation, see above) which is *in principle* not necessary in DFT, but convenient in order to save computational resources (and, thus, it is often *practically* necessary).

If one aims instead for a more accurate all-electron treatment, which can be used, for example, as reference to assess the quality of the pseudopotential approach, the problem arises

Dieses Werk ist copyrightgeschützt und darf in keiner Form vervielfältigt werden noch an Dritte weitergegeben werden.
Es gilt nur für den persönlichen Gebrauch.

that the inner electron wave functions are hard to describe by plane waves: Many basis functions (a very high cutoff energy) are required. The plane wave basis is simply inadequate for this task. However, it is perfectly suited for the description of the "outer parts" of the wave functions (beyond the nodes) in the interstitial region between the atoms. For the core regions, a different approach is necessary. One possibility is to define spheres of certain radii (the so-called muffin-tin radii, which are typically chosen around 1 Å, depending on the size of the atoms) centered at the atom positions $\vec{R}_I$, and to use different, more atom-like basis sets inside these spheres that match the plane waves in the interstitial regions. This is done, for instance, within the full-potential linearized augmented plane-wave plus local-orbital method (referred to as LAPW in the following), which is implemented in the WIEN2k code [82].

It is also possible to abandon the concept of plane waves entirely and to work with a completely localized basis set, for example, with numeric atom-centered orbitals. Such a basis set is used in the FHI-aims code [83]. Due to their local nature, the calculation of the Fock exchange energy (2.14) can be done very efficiently with such basis functions. Moreover, isolated systems like gas phase molecules can be described accurately with a comparatively small basis set.[12]

All methods mentioned so far are based on wave functions, which are numerically represented by basis set expansion coefficients. An entirely different approach is to work with Green's functions, which is done, for instance, in the Korringa-Kohn-Rostocker (KKR) method. This technique is quite popular (especially in the transport theory community), but is not used in this thesis (and is therefore mentioned at this point only for the sake of completeness). A recent review on the calculation of condensed matter properties with the KKR method can be found in Ref. [84].

2.3 Scanning tunneling microscopy

A considerable part of this thesis is devoted to the theoretical analysis of scanning tunneling microscopy (STM) images and to new concepts that involve STM. Therefore, a basic overview of this technique shall be given in the following.

2.3.1 Basic experimental principles

The STM was developed in the early 1980s by G. Binnig and H. Rohrer [85–87] from IBM, who were awarded the Nobel Prize in Physics for their invention already in 1986. The STM is a noninvasive method for scanning surfaces with atomic resolution and provides information about the topography and the electronic structure of a surface. For this, it exploits the quantum-mechanical tunneling process: The surface is laterally scanned by a small probe tip (ideally with a single atom at the end) hovering a few Å above the surface, as illustrated in Fig. 2.4(a). If a small voltage is applied between surface and tip (typically $V \in [-2, +2]$ V), electrons will tunnel from the tip into the sample or vice versa [Fig. 2.4(b)], and the tunneling current I can be measured. The exponentially decaying nature of wave functions in vacuum, and thus of the tunneling current, leads to the situation that the foremost tip atom strongly

[12]In most plane wave codes, one has to model such a system with a large cell containing the molecule and a quite spacious vacuum region, which is necessary in order to eliminate the spurious interaction between periodic images. Since the number of plane waves is proportional to the cell volume, this is highly inefficient.

Dieses Werk ist copyrightgeschützt und darf in keiner Form vervielfältigt werden noch an Dritte weitergegeben werden.
Es gilt nur für den persönlichen Gebrauch.

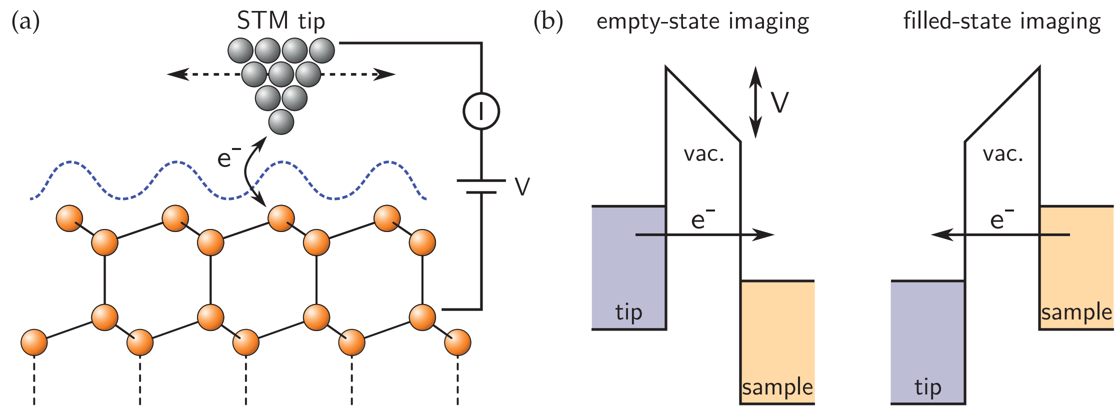

Figure 2.4 – (a) Working principle of the STM with atomic resolution. (b) Depending on the sign of the bias voltage V, electrons tunnel with a higher rate from the tip to the sample (negative bias, empty states) or from the sample to the tip (positive bias, filled states).

dominates the tunneling process. This provides the key for the atomic resolution that can be achieved with the STM.

The STM can be operated primarily in two modes: (i) a constant height mode, in which the tip scans the surface without vertical adjustment, and variations in the tunneling current $I(x,y)$ are recorded; (ii) in a constant current mode, in which the tip is vertically adjusted during the scan by a feedback circuit and a piezoelectric crystal, thus keeping the tunneling current I at a constant value. In the latter mode, the height of the tip $z(x,y)$ is recorded.

One advantage of the constant current mode, which is more commonly used, is that the probe tip will (in principle) not crash into the surface by accident. A disadvantage is that the scan is slower than in the constant height mode, since the feedback circuit limits the scan speed. Thus, for the study of fast surface processes, the constant height mode is used, which, on the other hand, requires higher effort in the experimental setup to provide a long-term stability comparable to the constant current mode.

The atomic-resolution capability and its sensitivity to the *electronic* structure of surfaces make the STM a remarkable experimental technique. Among the most stunning applications are certainly the "quantum corrals", where individual atoms are arranged (also by STM) on a metal surface, e.g., in a circle, and subsequently scanned. This images directly the quantum-mechanical wave nature of electrons [88]. Modern developments in the field include photon emission due to inelastic tunneling processes [89–93] and sensitivity to the magnetic properties of the sample by using magnetic tips [94]. The latter will be of importance in this thesis.

2.3.2 STM images from DFT: The Tersoff-Hamann approximation

The electron tunneling between the STM tip and the sample can be described theoretically. Within the formalism introduced by J. Bardeen [95], the tunneling current I can be expressed in first-order perturbation theory as [94]:

$$I = \frac{2\pi e}{\hbar} \sum_{\mu,\nu} \Big\{ f(\varepsilon_\mu)\,[1 - f(\varepsilon_\nu + eV)] - f(\varepsilon_\nu + eV)\,\big[1 - f(\varepsilon_\mu)\big] \Big\} |M_{\mu,\nu}|^2\, \delta(\varepsilon_\mu - \varepsilon_\nu).$$

Dieses Werk ist copyrightgeschützt und darf in keiner Form vervielfältigt werden noch an Dritte weitergegeben werden.
Es gilt nur für den persönlichen Gebrauch.

In this formula, f is the Fermi distribution function and V is the applied voltage between tip and sample. The index μ (ν) labels the electronic states of the tip (sample). The δ function ensures energy conservation. The matrix elements,

$$M_{\mu,\nu} = \frac{\hbar^2}{2m} \int \mathrm{d}\mathbf{S} \left(\psi_\mu^* \nabla \psi_\nu - \psi_\nu \nabla \psi_\mu^* \right),$$

have to be evaluated by integrating over any surface within the vacuum region between tip and sample. For small applied voltages, the expression for the current can be approximated as:

$$I = \frac{2\pi e}{\hbar} eV \sum_{\mu,\nu} |M_{\mu,\nu}|^2 \, \delta(\varepsilon_\mu - E_\mathrm{F}) \, \delta(\varepsilon_\nu - E_\mathrm{F}).$$

The difficulty here is that the actual atomic structure of the STM tip is usually not known. Therefore, the electronic states of the tip ψ_μ cannot be calculated. The idea of Tersoff and Hamann was to model the tip as simple as possible. They assumed an s-type (spherical) wave function at the tip apex [96, 97],

$$\psi_\mu = \mathrm{e}^{-\kappa R}/R,$$

with a radius R and an inverse decay length κ. This assumption is reasonable, since usual STM tips are made from normal metals which have s states at their Fermi energy that dominate the tunneling current. With this Tersoff-Hamann approximation the current in linear response further simplifies to:

$$I \sim V \mathrm{e}^{-2\kappa R} \sum_\nu |\psi_\nu(\vec{r})|^2 \, \delta(\varepsilon_\nu - E_\mathrm{F}).$$

Here $\vec{r}$ denotes the center of the effective, spherical tip. Thus, the central quantity is the expression

$$\sum_\nu |\psi_\nu(\vec{r})|^2 \, \delta(\varepsilon_\nu - E_\mathrm{F}),$$

which is the so-called local density of states (LDOS).

Consequently, the simulation of STM images in the spirit of Tersoff and Hamann from the electronic structure (once obtained) is quite straightforward. In this thesis, the *integrated* local density of states (ILDOS) is used, which is derived from DFT sample states $\psi_{n\vec{k}}$ in a given energy interval around the Fermi energy of the sample determined by the applied bias voltage V and thus provides a better approximation beyond linear response:

$$\varrho(\vec{r}) = \left| \int_0^{eV} \mathrm{d}\varepsilon \sum_{n\vec{k}} |\psi_{n\vec{k}}(\vec{r})|^2 \, \delta(\varepsilon - \varepsilon_{n\vec{k}} + E_\mathrm{F}) \right| = \sum_{n\vec{k}} w_{n\vec{k}} \, |\psi_{n\vec{k}}(\vec{r})|^2. \tag{2.19}$$

The weights $w_{n\vec{k}}$ are nonzero only in a certain energy window around the Fermi energy E_F given by the bias voltage V:

$$w_{n\vec{k}} = \begin{cases} w_{\vec{k}} & \text{for } (\varepsilon_{n\vec{k}} - E_\mathrm{F}) \in [0,\, eV] \\ 0 & \text{otherwise.} \end{cases}$$

The $\vec{k}$-point weights $w_{\vec{k}}$ are those used in the Brillouin zone integration. Actually, states outside (but close to) the energy interval are not entirely rejected, but included with a rapidly decaying weight.

Dieses Werk ist copyrightgeschützt und darf in keiner Form vervielfältigt werden noch an Dritte weitergegeben werden.
Es gilt nur für den persönlichen Gebrauch.

When comparing simulated and experimental STM images one has to keep in mind the approximate nature of Kohn-Sham DFT and the Tersoff-Hamann approach. Nevertheless, we will see several examples throughout this thesis where the agreement of simulated and experimental STM images is remarkable. The reason for this lies in the fact that the images are *integrated* quantities and often depend more strongly on "topological", i.e., structural aspects than on details of the electronic structure. In addition, there is no interest in a one-to-one correspondence between experimental and theoretical bias voltage V: In the experiment, sample and tip act as additional resistors, and consequently the actual voltage drop in the vacuum region is often unknown. Finally, one can check the electronic structure in advance.

Possible improvements of the Tersoff-Hamann approximation are the inclusion of non-spherical tip approximations [98, 99], or even using the Bardeen formula with realistic tip DFT wave functions [100]. Moreover, Landauer-Büttiker-type transport calculations could be done at each xy point (substrate and tip material as leads, surface and tip as scattering region). However, in the literature, the Tersoff-Hamann approximation is mostly used in its plain form, which combines results of sufficient accuracy with low computational cost.

Numerical realization

In most publications, simulated STM images are simply plots of the (integrated) LDOS $\varrho(x,y,z)$ at a suitably chosen height z, which corresponds roughly to the constant height mode. In this thesis a different approach is used, mimicking the constant current mode.

After the determination of the electronic structure within DFT, the ILDOS [Eq. (2.19)] is constructed for several bias voltages V. Subsequently, z_c with $\varrho(z_\mathrm{c}) = \varrho_\mathrm{c}$ is determined for each pair (x,y), where the critical densities ϱ_c typically range from 10^{-5} to 10^{-7} / bohr^3. Since all wave functions and densities are stored on a discrete grid with a certain finite spacing in each direction, a linear interpolation is used to find the optimal z_c:

$$\varrho_1 := \varrho(z_1) < \varrho_\mathrm{c}, \quad \varrho_2 := \varrho(z_2) > \varrho_\mathrm{c}, \quad z_\mathrm{c}(\varrho_\mathrm{c}) = z_1 + \frac{\varrho_\mathrm{c} - \varrho_1}{\varrho_2 - \varrho_1}(z_2 - z_1) \qquad \forall\ (x,y).$$

Here z_1 is the z closest to the surface still fulfilling $\varrho(z_1) < \varrho_\mathrm{c}$, and z_2 is the z furthest away from the surface still fulfilling $\varrho(z_2) > \varrho_\mathrm{c}$. Afterwards, $z_\mathrm{c}(x,y)$ is plotted. This provides an isosurface plot for a constant density. Since the tunneling current is proportional to the density in the Tersoff-Hamann approximation, this corresponds to the constant current mode.

2.3.3 Spin-polarized STM

Since the focus of this thesis lies on the magnetic properties of different systems, the question arises whether it is possible to resolve these properties on an atomic scale with the STM. Indeed, one can exploit the spin polarization and spin-dependent tunneling in magnetic STM tips. The tunneling current depends on the relative orientation of tip and surface magnetization. This experimental method is referred to as spin-polarized STM (SP STM). Pioneering work in this field has been done by Wiesendanger *et al.* in 1990 [101], who used a FM CrO_2 tip to study the alternately magnetized Cr(001) terraces separated by monatomic steps.[13] Nowadays, Cr tips are frequently used, since the antiferromagnetic (AFM) nature of

[13] Interestingly, bulk CrO_2 is actually half-metallic, i.e., metallic (semiconducting) in the majority (minority) spin channel.

Dieses Werk ist copyrightgeschützt und darf in keiner Form vervielfältigt werden noch an Dritte weitergegeben werden.
Es gilt nur für den persönlichen Gebrauch.

Cr leads to a spin polarization at the foremost tip atom and simultaneously avoids the disturbing influence of long-range magnetic stray fields [94]. The ideal tip material for SP STM would be a half-metallic antiferromagnet [102] that exhibits a perfect spin filtering in addition to the absence of stray fields.

In this thesis, SP STM images are simulated from the DFT electronic structure by applying the aforementioned approach, Eq. (2.19), separately to the two spin channels. Thus, a spin-polarized ILDOS is used. Subsequently, the two images (height profiles) can be subtracted to get a magnetic-contrast image: $z(x,y) = z^{\uparrow}(x,y) - z^{\downarrow}(x,y)$. This procedure corresponds to the case of *maximal contrast*: Normally, the spin filtering will be subject to imperfections like spin fluctuations, misaligned tip-sample spins, and other effects which lower the contrast. Moreover, without a half-metallic tip, the contrast will always be reduced. For small bias voltages, one can write [94]:

$$I \sim \left\{ (D_{\mathrm{t}}^{\uparrow} + D_{\mathrm{t}}^{\downarrow})(D_{\mathrm{s}}^{\uparrow} + D_{\mathrm{s}}^{\downarrow}) + (D_{\mathrm{t}}^{\uparrow} - D_{\mathrm{t}}^{\downarrow})(D_{\mathrm{s}}^{\uparrow} - D_{\mathrm{s}}^{\downarrow}) \cos(\theta) \right\},$$

where $D_{\mathrm{t/s}}^{\sigma}$ is the density of states (DOS) at the Fermi energy for the tip/sample and θ is the angle between tip and sample magnetization. If either tip or sample is NM, or if their magnetizations are orthogonal, the latter term vanishes, and the tunneling current behaves as in the Tersoff-Hamann approximation. With a magnetic tip, $D_{\mathrm{t}}^{\uparrow} \neq D_{\mathrm{t}}^{\downarrow}$, the current is modulated to some degree by the relative magnetization. Finally, for a half-metallic tip and (anti)parallel spin alignment one can write, for instance, $D_{\mathrm{t}}^{\downarrow} = 0$ and $\cos(\theta) = \pm 1$, and thus it follows that

$$I \sim D_{\mathrm{t}}^{\uparrow} \left\{ (D_{\mathrm{s}}^{\uparrow} + D_{\mathrm{s}}^{\downarrow}) \pm (D_{\mathrm{s}}^{\uparrow} - D_{\mathrm{s}}^{\downarrow}) \right\} \quad \curvearrowright \quad I^{\uparrow\uparrow} \sim 2 D_{\mathrm{t}}^{\uparrow} D_{\mathrm{s}}^{\uparrow}, \quad I^{\uparrow\downarrow} \sim 2 D_{\mathrm{t}}^{\uparrow} D_{\mathrm{s}}^{\downarrow},$$

which means that exclusively one spin channel of the sample is probed, and thus the magnetic contrast is maximal.

2.4 Ballistic quantum transport

The ballistic transport properties of systems on the atomic scale [e.g., nanowires, molecules, or magnetic tunnel junctions (MTJs)] can show interesting quantum effects. They can be calculated within the Landauer-Büttiker approach, which connects the conductance through such a system to the quantum-mechanical transmission probability.

The Landauer-Büttiker approach

Theoretical modeling can be done in the following way (cf. Fig. 2.5): Assuming an open quantum system, in which the current I propagates in one dimension (z), one starts by defining left (L, $z < 0$) and right (R, $z > L$) semi-infinite leads (electron reservoirs) with chemical potentials μ_{L} and μ_{R}. These two leads are connected by a scattering region (S, $0 < z < L$). An external bias voltage V can be applied, which shifts the chemical potentials of the leads according to

$$\mu_{\mathrm{L}} - \mu_{\mathrm{R}} = eV.$$

The current I, and thus the conductance $G = I/V$, can be calculated with the Landauer-Büttiker formula [103, 104],

$$I = \frac{e}{h} \int \mathrm{d}E \left[f_{\mu_{\mathrm{L}}}(E) - f_{\mu_{\mathrm{R}}}(E) \right] T(E), \tag{2.20}$$

Dieses Werk ist copyrightgeschützt und darf in keiner Form vervielfältigt werden noch an Dritte weitergegeben werden.
Es gilt nur für den persönlichen Gebrauch.

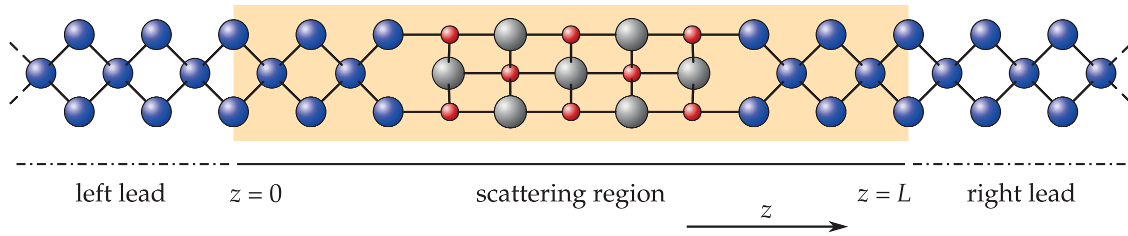

Figure 2.5 – Ballistic conductance setup, consisting of left and right semi-infinite leads and the scattering region. This example shows an Fe/MgO/Fe MTJ.

where $T(E)$ is the energy-dependent total transmission and $f_\mu(E)$ is the Fermi distribution function in the leads. It is obvious here that all important information resides in $T(E)$. For zero temperature, Eq. (2.20) becomes

$$I = \frac{e}{h} \int_{\mu_\mathrm{R}}^{\mu_\mathrm{L}} \mathrm{d}E \; T(E),$$

and for infinitesimal voltages (linear response regime) it further simplifies to the well-known expression

$$I = \frac{e^2}{h} T(E_\mathrm{F}) V = G_0 T(E_\mathrm{F}) V \quad \curvearrowright \quad G = G_0 \, T(E_\mathrm{F}),$$

where $G_0 = e^2/h$ is the conductance quantum per spin and E_F is the Fermi energy of the system in equilibrium. The remaining (and much more demanding) task is the calculation of $T(E)$.

Implementation in a plane wave framework

H. J. Choi and J. Ihm described a method to calculate the ballistic conductance through the outlined setup (cf. Fig. 2.5) in an *ab inito* framework with norm-conserving Kleinman-Bylander pseudopotentials [105]. This method was consequently not well-suited for systems with localized (d) orbitals and thus generalized by A. Smogunov, A. Dal Corso, and E. Tosatti to the case of magnetic systems described by USPPs [106].

One starts with DFT calculations for fully periodic unit cells to obtain their effective Kohn-Sham potentials. The electrode unit cells are usually very small and provide $V_\mathrm{KS}^\mathrm{L,R}$. The unit cell describing the scattering region is much larger in general (cf. Fig. 2.5) and provides V_KS^S. It has to be chosen in such a way that its potential at the left and the right boundaries matches the potential of the bulk electrode cells. Thus, the scattering region usually includes several layers of electrode material, as illustrated in Fig. 2.5.

The transmission $T(E)$ can be derived from the scattering states Ψ of the system at energy E, which are, in the USPP formalism, solutions of

$$E\hat{S}\,|\Psi\rangle = \left[\hat{T} + \hat{V}_\mathrm{KS} + \sum_I \sum_{nm} D^I_{nm}\,|\beta^I_n\rangle\langle\beta^I_m|\right]|\Psi\rangle\,,$$

an equation similar to Eq. (2.18). However, since E enters the equation not as solution, but as an external parameter, it can be rewritten conveniently as

$$E\,|\Psi\rangle = \left[\hat{T} + \hat{V}_\mathrm{KS} + \sum_I \sum_{nm} \tilde{D}^I_{nm}\,|\beta^I_n\rangle\langle\beta^I_m|\right]|\Psi\rangle\,,$$

Dieses Werk ist copyrightgeschützt und darf in keiner Form vervielfältigt werden noch an Dritte weitergegeben werden.
Es gilt nur für den persönlichen Gebrauch.

where the USPP overlap operator $\hat{S}$ has been incorporated in $\tilde{D}^I_{nm} = D^I_{nm} - Eq_{nm}$. In this form, the equation is similar to the norm-conserving case, so that the method of Choi and Ihm can be applied [105, 106]. The solutions have to fulfill Bloch's theorem in xy direction,

$$\Psi_{\vec{k}_\perp}(\vec{r}_\perp + \vec{R}_\perp, z) = \mathrm{e}^{\mathrm{i}\vec{k}_\perp \vec{R}_\perp} \Psi_{\vec{k}_\perp}(\vec{r}_\perp, z),$$

where the $\vec{R}_\perp$ are lateral supercell lattice vectors. The wave functions can be represented in reciprocal space,

$$\Psi_{\vec{k}_\perp}(\vec{r}_\perp, z) = \sum_{\vec{G}_\perp} \Psi_{\vec{k}_\perp}(\vec{G}_\perp, z)\, \mathrm{e}^{\mathrm{i}(\vec{k}_\perp + \vec{G}_\perp)\vec{r}_\perp},$$

individually classified by $\vec{k}_\perp$ vectors from the two-dimensional Brillouin zone (2D-BZ). The number of $\vec{G}_\perp$ vectors included in the calculation (which is limited by a specified cutoff, similar to Sec. 2.2.4) determines the accuracy (and the necessary computation time).

For a given set $\{E, \vec{k}_\perp\}$ one can subsequently construct the scattering state originating from each rightward propagating electrode wave function ψ_j at this energy:

$$\Psi_j = \begin{cases} \psi_j + \sum_{i \in \mathrm{L}} r_{ij} \psi_i & \text{for} \quad z < 0, \\ \sum_n c_n \phi_n + \sum_{Im} c_{Im} \phi_{Im} & \text{for} \quad 0 < z < L, \\ \sum_{i \in \mathrm{R}} t_{ij} \psi_i & \text{for} \quad z > L. \end{cases}$$

The sum over $\{Im\}$ denotes a sum over all projectors β^I_m in the corresponding cell (L, S, or R).[14]

The wave functions in the electrodes, ψ_i, also fulfill Bloch's theorem in xy direction. However, since the translational symmetry in z direction is lost, one writes

$$\psi_j(\vec{r}_\perp, z + d) = \mathrm{e}^{\mathrm{i}kd} \psi_j(\vec{r}_\perp, z),$$

where d is the unit cell length of the corresponding electrode bulk cell in z direction and k is usually a complex number. States with $\mathrm{Im}(k) = 0$ are propagating, whereas states with $\mathrm{Im}(k) \neq 0$ are growing or decaying. All of them form the complex band structure of the electrode. In the electrode unit cell one can decompose

$$\psi_j(\vec{r}) = \sum_n c_{n,j} \phi_n(\vec{r}) + \sum_{Im,j} c_{Im,j} \phi_{Im}(\vec{r}),$$

where ϕ_n are linearly independent solutions of a homogeneous equation and ϕ_{Im} is a particular solution of an inhomogeneous equation (using the appropriate electrode Kohn-Sham potential):

$$0 = \left[-\nabla^2/2 + V_{\mathrm{KS}}(\vec{r}) - E\right] \phi_n(\vec{r}),$$
$$0 = \left[-\nabla^2/2 + V_{\mathrm{KS}}(\vec{r}) - E\right] \phi_{Im}(\vec{r}) + \sum_{\vec{R}_\perp} \mathrm{e}^{\mathrm{i}\vec{k}_\perp \vec{R}_\perp} \beta^I_m(\vec{r} - \vec{R}_I - \vec{R}_\perp).$$

The same procedure can be applied to the unit cell describing the scattering region.

[14]The reader will certainly not confuse the current I with the atom index I.

Dieses Werk ist copyrightgeschützt und darf in keiner Form vervielfältigt werden noch an Dritte weitergegeben werden.
Es gilt nur für den persönlichen Gebrauch.

Heading for the coefficients $\{c_n, c_{Im}, r_{ij}, t_{ij}\}$, which describe Ψ_j completely, one solves

$$c_{Im,j} + \sum_i r_{ij} c_{Im,i} = c_{Im} \quad \text{and} \quad \sum_i t_{ij} c_{Im,i} = c_{Im}$$

for spheres intersecting the plane $z = 0$ (between left lead and scattering region) and for spheres intersecting the plane $z = L$ (between right lead and scattering region), respectively. An additional set of linear algebraic equations is provided by the usual matching conditions on the wave function and its z derivative on the planes $z = 0$ and $z = L$. Subsequently, the transmission $T(E,\vec{k}_\perp)$ follows from the coefficients t_{ij}.

Summarizing, the following steps have to be made:

1. Perform DFT calculations of electrode and scattering region bulk cells to obtain the effective Kohn-Sham potentials $V_{\text{KS}}^{\text{L,R,S}}$.
2. Choose E and a grid of $\vec{k}_\perp$ and perform the following:
   a) Calculate the complex band structure in both electrodes using $V_{\text{KS}}^{\text{L,R}}$ and determine the rightward (in positive z direction) propagating wave functions ψ_j.
   b) Construct the corresponding scattering states Ψ_j using V_{KS}^{S} and thus determine t_{ij}.
   c) Calculate $(\mathbf{T})_{ij} = T_{ij} = \sqrt{I_i/I_j}\, t_{ij}$, where I_j is the probability current of the rightward propagating state ψ_j (see Ref. [106] for details on the calculation of I_j).
   d) Calculate $T(E,\vec{k}_\perp) = \text{Tr}[\mathbf{T}^\dagger \mathbf{T}] = \sum_{ij} |T_{ij}|^2 = \sum_i T_i$, where T_i are the eigenvalues of the Hermitian matrix $\mathbf{T}^\dagger \mathbf{T}$ (eigenchannel transmissions).
3. Calculate $T(E) = \sum_{\vec{k}_\perp} w_{\vec{k}_\perp} T(E,\vec{k}_\perp)$ with Brillouin zone weight factors $w_{\vec{k}_\perp}$.

Note that the spin is assumed to be conserved in this formalism, so transmission takes place only between states of equal spin.

Parallelization

The method is tailor-made for parallelization over $\vec{k}_\perp$. The author of this thesis implemented such a parallelization scheme employing the Message Passing Interface (MPI). The scaling is almost linear due to negligible overhead, and the program was run successfully on more than four thousand CPU cores in parallel on a Cray machine. The program generates a Monkhorst-Pack [107] grid of $\vec{k}_\perp$ points at the beginning and reduces it to the irreducible Brillouin zone given by the symmetry of the whole system. The reduced $\vec{k}_\perp$ points are subsequently distributed to several small pools of four CPU cores each, which calculate parts of the transmission $T(E)$. Finally, the whole Brillouin zone is restored for a more instructive visualization of $T(E,\vec{k}_\perp)$.

Dieses Werk ist copyrightgeschützt und darf in keiner Form vervielfältigt werden noch an Dritte weitergegeben werden.
Es gilt nur für den persönlichen Gebrauch.

Dieses Werk ist copyrightgeschützt und darf in keiner Form vervielfältigt werden noch an Dritte weitergegeben werden.
Es gilt nur für den persönlichen Gebrauch.

Chapter 3

Transition metal silicide thin films on Si(111)

Contents

3.1 Introduction and overview . . . 48
3.2 Properties of bulk Si and of the Si(111) surface . . . 49
3.2.1 Properties of bulk Si . . . 49
3.2.2 The Si(111) surface . . . 54
3.3 Bulk properties of 3d transition metal monosilicides . . . 59
3.3.1 The B20 crystal structure . . . 59
3.3.2 Monte Carlo simulations on the trillium sublattice . . . 60
3.3.3 Structural properties . . . 63
3.3.4 Electronic properties, magnetic properties, and the band gap . . . 65
3.3.5 MnSi and FeSi in different crystal structures . . . 70
3.4 The effect of epitaxial strain . . . 74
3.4.1 The strained bulk material as limit of thick epitaxial films . . . 74
3.4.2 Phonon spectrum of MnSi under the influence of biaxial strain . . . 80
3.5 Correlation effects in MnSi and FeSi . . . 84
3.6 Growth mode and atomic structure of MnSi/Si(111) . . . 86
3.6.1 Different MnSi(111) surfaces . . . 87
3.6.2 The MnSi/Si(111) and FeSi/Si(111) interfaces . . . 89
3.6.3 Coexisting $\sqrt{3} \times \sqrt{3}$ surfaces of MnSi/Si(111) . . . 91
3.6.4 The 3×3 reconstruction of MnSi/Si(111) . . . 103
3.7 Magnetic properties of MnSi/Si(111) thin films . . . 107
3.8 Interface and surface properties of Mn_5Si_3/Si(111) . . . 112
3.8.1 Bulk properties of Mn_5Si_3 . . . 113
3.8.2 Surfaces and Mn_5Si_3/Si(111) heterostructures . . . 114
3.8.3 STM analysis of Mn_5Si_3/Si(111) surfaces . . . 118

Dieses Werk ist copyrightgeschützt und darf in keiner Form vervielfältigt werden noch an Dritte weitergegeben werden.
Es gilt nur für den persönlichen Gebrauch.

3.1 Introduction and overview

One way of fabricating a spintronics device [1,2] is by growing a FM thin film electrode (ideally with small conductivity mismatch) on a semiconductor substrate with a well-defined, atomically sharp interface. From a technological point of view, the involved materials should be “established” and the fabrication process itself should be kept as simple as possible. The “magnetic” 3*d* TMs (like Cr, Mn, Fe, Co, and Ni) and Si are obvious choices for constructing such a heterostructure, since the former are known to react strongly (exothermic) with a Si surface. Hence, just by codeposition of TM and Si atoms on a Si surface and moderate annealing one can form TM silicide films of high structural and interfacial quality on top of the semiconductor [108–110]. The drawback is that such silicides are often non- or only weakly magnetic in their ground state crystal structure, even those one would expect to be promising due to the high magnetic moment of the constituents, like CrSi, MnSi, or FeSi. Also, $CrSi_2$, CoSi, $CoSi_2$, and NiSi are of no interest in this context [111]. However, structural modifications induced by epitaxial growth can possibly improve this situation. Several theoretical studies based on *ab initio* thermodynamical arguments concerning TM (silicide) thin films on Si have been published in the last years. The focus lay on the technologically relevant Si(100) surface, on which films of different TM monosilicides in B2 (CsCl) structure have been investigated [112]. Mn was found to be most promising [113]. Later, also thin Mn monosilicide films on the Si(111) surface have been studied, comparing the B2 to the B20 structure [114]. The advantage of Si(111) is that it is compatible to both the MnSi-B20 and MnSi-B2 structures, the lattice constant fitting better to MnSi-B20. The competition between thin film growth and island nucleation has also been discussed [114]. It was found that MnSi on Si(100) tends to form 3D islands instead of thin films. The situation is better on the Si(111) surface where thin film formation is more probable since island nuclei need to be larger.

This chapter is about epitaxial growth of TM silicide films of different stoichiometry and thickness on Si(111) and the influence of epitaxial strain, surfaces, interfaces, and quantum confinement on their structural, electronic, and magnetic properties on the atomic scale. FeSi and especially MnSi are discussed in more detail, including different surfaces and interfaces to Si(111). Moreover, the reliability of *ab initio* calculations in this field is carefully assessed. This is of importance due to the electronic correlations present in B20 compounds like FeSi and MnSi [115, 116]. The chapter starts with a presentation of the substrate material Si, which plays an important role throughout the whole thesis, followed by a comprehensive theoretical study of TM monosilicides in B20 structure. After a detailed discussion of biaxial strain and correlation effects, the interplay of different growth protocols and the resulting atomic (and thus magnetic) structure of the TM silicide films is analyzed in close cooperation between theory and experiment. It is demonstrated how one can discriminate between different internal layer stacking sequences in MnSi/Si(111) epitaxial films on the basis of atomic-resolution STM images. Such knowledge is required in order to reproducibly fabricate MnSi films with specified magnetic properties. The chapter closes with a discussion of Mn_5Si_3/Si(111) heterostructures, since Mn_5Si_3 is the competitive phase in MnSi/Si(111) film growth and thus has to be excluded prior to finding a structural model based on MnSi in B20 structure.

Dieses Werk ist copyrightgeschützt und darf in keiner Form vervielfältigt werden noch an Dritte weitergegeben werden.
Es gilt nur für den persönlichen Gebrauch.

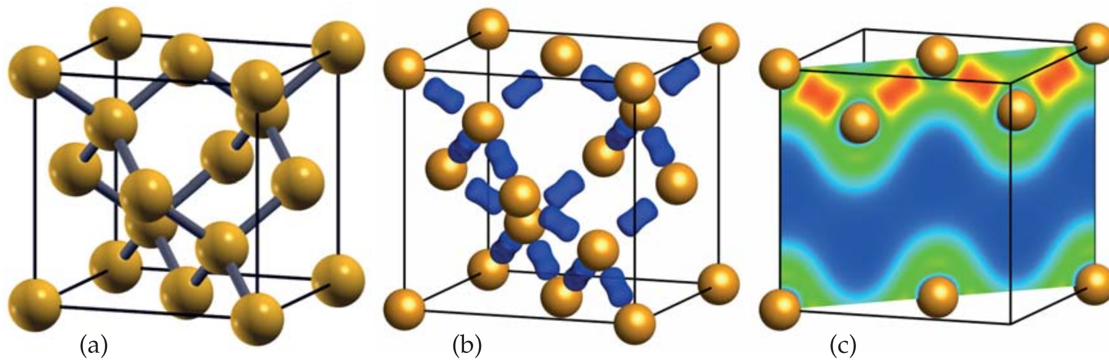

Figure 3.1 – (a) Atomic model of bulk Si in diamond structure, showing the fourfold nearest-neighbor coordination (bonding). (b) Isosurfaces of the valence charge density calculated with DFT-PBE. (c) Section along a (110) plane showing atoms and the valence charge density along the Si-Si bonds. The color shifts from blue to red with increasing density.

3.2 Properties of bulk Si and of the Si(111) surface

3.2.1 Properties of bulk Si

Si is a member of group IV (the carbon group) of the periodic table of elements and the *de facto* standard semiconductor that is predominantly used in modern electronics.

Structural properties

Its ground state crystal structure is the diamond structure, which can be regarded as a special case of the zinc-blende structure. Consequently, bulk Si can be described by a fcc Bravais lattice with an atomic basis consisting of two Si atoms at $(0,0,0)\,a_0$ and $(1,1,1)\,a_0/4$ in Cartesian coordinates, where a_0 is the lattice constant. In this structure, each Si atom has fourfold coordination, which is optimal in conjunction with the sp^3 hybridization of the valence orbitals.

Figure 3.1 shows Si in its diamond structure and the covalent bonding, the valence charge density being concentrated between two adjacent Si atoms. In Table 3.1, structural properties calculated with different exchange-correlation functionals and different methods are summarized and compared to experimental values and previous theoretical results. The values have been derived from DFT calculations by performing a least-squares fit of several total energy values (as a function of the lattice constant or, equivalently, the volume) to the Murnaghan equation of state [122],

$$E(V) = E(V_0) + \frac{B_0 V_0}{B_0'} \left\{ \frac{(V_0/V)^{B_0'-1}}{B_0'-1} + \frac{V}{V_0} \right\} - \frac{B_0 V_0}{B_0'-1}. \tag{3.1}$$

Here $V_0 \sim a_0^3$ is the equilibrium volume, B_0 is the bulk modulus, and B_0' is its derivative with respect to the pressure. Reference [120] reports all-electron results, calculated with the LAPW method. All other theoretical values have been derived within a pseudopotential approach. The GGA exchange-correlation functionals are worst for the lattice constant, with a deviation of 0.7 % from the experimental value for PBE, while LDA and HSE06 deviate only by -0.4 % and 0.2 %, respectively. By taking a zero-point anharmonic expansion correction

Dieses Werk ist copyrightgeschützt und darf in keiner Form vervielfältigt werden noch an Dritte weitergegeben werden.
Es gilt nur für den persönlichen Gebrauch.

Table 3.1 – Structural properties of bulk Si, calculated with different approximations of the exchange-correlation functional and compared to previous results from the literature. LAPW denotes all-electron results, while NCPP, USPP, and PAW are different pseudopotential approximations. Experimental values follow Refs. [117–119] and the references therein. The zero-point anharmonic expansion (ZPAE) corrected value has been taken from Ref. [40].

		a_0 (Å)	B_0 (GPa)	B_0'	E_{coh} (eV/f.u.)
PBE (this work)	USPP	5.47	88	4.28	4.62
PBE (Ref. [120])	LAPW	5.47	88	4.25	4.59
PBE+vdW (this work)	USPP	5.41	97	4.54	4.84
PW91 (this work)	USPP	5.46	88	4.31	4.63
PW91 (Ref. [121])	NCPP	5.45	92	–	–
LDA (this work)	USPP	5.40	96	4.27	5.35
LDA (Ref. [120])	LAPW	5.41	95	4.25	5.26
HSE06 (this work)	PAW	5.44	97	4.10	–
Exp. (Refs. [117–119])		5.43	99	4.09	4.63
Exp. with ZPAE (Ref. [40])		5.42			

into account [40], these values change to 0.9%, −0.2%, and 0.4%, respectively. The PBE bulk modulus is significantly smaller than the experimental result; the same holds for the PW91 value. Again, LDA provides better results, and especially the advanced hybrid functional HSE06 leads to improved values. The cohesive energy, on the other hand, is described very well by the two GGA functionals, the LDA value being far too high. These results reflect the well-known LDA overbinding, which leads to underestimated lattice constants and overestimated cohesive energies.

A first assessment of the quality of the pseudopotential approach in this case can be done by comparing the all-electron LAPW and USPP results listed in Table 3.1. Obviously, the agreement for the lattice constant, the bulk modulus, its derivative, and the cohesive energy is very good, especially for the PBE values.

For consistency reasons in later calculations (cf. Sec. 4.6.2 on page 162), an additional set of structural parameters has been derived including an empirical vdW energy correction to the PBE functional, also known as "dispersive forces" or DFT-D [123, 124]. The lattice constant is reduced to the LDA value, and the bulk modulus is also improved. The cohesive energy, which is already excellent in PBE, increases a bit, but stays clearly below the LDA value.

Electronic properties

Si in diamond structure is a NM (that is, only diamagnetic) semiconductor with an indirect band gap of around 1.17 eV at low temperatures. While the VBM is located at the Γ point, one finds the CBM along the Δ symmetry line, close to the X point. Figure 3.2(a) compares an all-electron band structure of Si in diamond structure to the result of an USPP calculation. The agreement is excellent. Note that this is *not* the consequence of some pseudopotential fitting procedure; in contrast, it underlines the validity of the pseudopotential approach and the quality of the generated pseudopotential.[1]

[1]It should be noted that Si is one of the most easy elements concerning pseudopotential generation.

Dieses Werk ist copyrightgeschützt und darf in keiner Form vervielfältigt werden noch an Dritte weitergegeben werden.
Es gilt nur für den persönlichen Gebrauch.

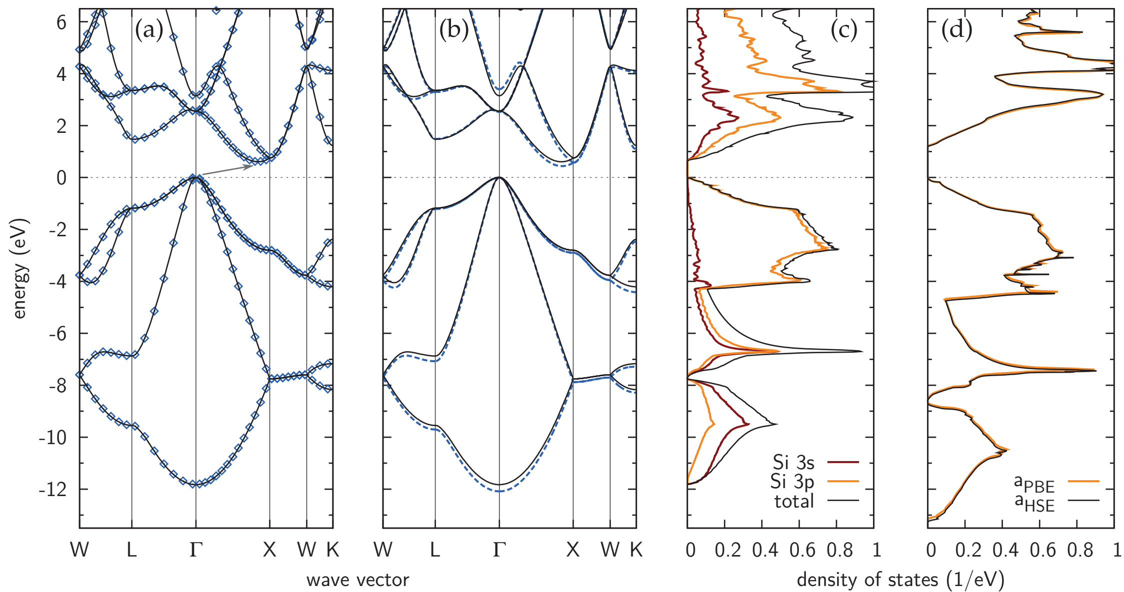

Figure 3.2 – Electronic Kohn-Sham band structures and DOS (per f.u.) for Si in diamond structure. The different VBM have been aligned at zero energy. (a) Comparison of all-electron LAPW (blue diamonds) and USPP (black lines) band structures for PBE, showing perfect agreement. The arrow indicates the indirect band gap. (b) Comparison of USPP band structures for PBE (solid black lines) and LDA (dashed blue lines). (c) USPP-PBE total DOS (black lines) together with projections onto different Si orbitals. (d) Total DOS derived from a HSE06 calculation. The larger Kohn-Sham band gap can clearly be seen. Using the PBE lattice constant (orange lines) instead of the HSE06 value (black lines) has obviously no relevant influence on the DOS.

The influence of the exchange-correlation functional is demonstrated in Fig. 3.2(b), where PBE and LDA are compared. The LDA VBs are stretched to slightly lower energies. (Note that the VBM is shifted to zero energy for both functionals.) The band gap is smaller in LDA; the CBs around the X point are below those for PBE, while at the Γ point they tend to lie slightly above the latter. Over all, these electronic differences are minor, especially if one keeps in mind that the band gap is by far too small in either case.

The four VBs of Si shown in Fig. 3.2 are derived from the Si-Si-bonding sp^3-hybridized versions of the single 3s and the three 3p orbitals of Si. (Consequently, the CB consists of the antibonding states.) Figure 3.2(c) shows a decomposition of the total DOS into these 3s and 3p parts. The energetically lowest region (-12 eV to -8 eV) is dominated by 3s character, especially at the Γ point (lowest part). With increasing energy, the 3p character becomes more pronounced and dominates from -4 eV to 0 eV, again especially at the Γ point close to the Fermi energy (VBM). The lower part of the CB has both 3s and 3p character.

Obviously, the Kohn-Sham band gap $\varepsilon_G = \varepsilon_{CBM} - \varepsilon_{VBM}$ at the Fermi energy is too small. As already mentioned in the previous chapter, there are different ways to improve this situation. Table 3.2 compares Kohn-Sham band gaps (*not* determined with the ΔSCF approach described in Sec. 2.2.3 on page 27) calculated with different exchange-correlation functionals. Moreover, recent results from Ref. [125] are cited, where many-body quasiparticle band gaps have been calculated within the G_0W_0 approximation and a self-consistent GW approach: While the initial wave functions ψ_i are kept fixed to the PBE results, the energy eigenvalues ε_i are updated in a self-consistency cycle, correcting the Green's function G and the

Dieses Werk ist copyrightgeschützt und darf in keiner Form vervielfältigt werden noch an Dritte weitergegeben werden.
Es gilt nur für den persönlichen Gebrauch.

Table 3.2 – Width of the Kohn-Sham band gap ε_G of bulk Si, calculated with different approximations of the exchange-correlation functional and compared to previous results from the literature. a_0 denotes the lattice constant used in the calculation. Experimental values follow Ref. [48] and the references therein. The deviations are given with respect to the experimental low-temperature value.

		a_0 (Å)	Band gap (eV)	
PBE (this work)	USPP	5.47	0.61	(−48%)
PBE (this work)	LAPW	5.47	0.61	(−48%)
PBE (Ref. [125])	PAW	5.43	0.62	(−47%)
PBE (Ref. [48])	Gaussian	5.48	0.67	(−43%)
PBE + G_0W_0 (Ref. [125])	PAW	5.43	1.12	(−4%)
PBE + GW (Ref. [125])	PAW	5.43	1.28	(+9%)
LDA (this work)	USPP	5.40	0.44	(−62%)
LDA (this work)	LAPW	5.41	0.46	(−61%)
LDA (Ref. [126])	USPP	5.40	0.46	(−61%)
LDA (Ref. [48])	Gaussian	5.41	0.51	(−56%)
HSE06 (this work)	PAW	5.44	1.19	(+2%)
HSE06 (this work)	PAW	5.47	1.21	(+3%)
HSE06 (Ref. [48])	Gaussian	5.45	1.22	(+4%)
HSE03 (Ref. [127])	Gaussian	5.44	1.12	(−4%)
Exp., low temp. (Ref. [48])			1.17	(ref.)
Exp., room temp. (Ref. [48])			1.12	(−4%)

dielectric matrix of the screened potential W. As one can see, the G_0W_0 approach widens the band gap almost to the experimental low-temperature value, while the self-consistent GW already leads to a too large band gap. Note that, in general, the wave functions used in the GW procedure can have a significant influence on the result. This influence should be small for self-consistent GW; nevertheless, starting from hybrid functional results, for instance, could lead to further improvements. Especially, HSE-type functionals are already based on a screened Coulomb interaction, so the corrections that have to be made by the GW post-processing are probably much smaller in this case.

Figure 3.2(d) shows two DOS curves derived from HSE06 hybrid functional calculations of Si. The width of the Kohn-Sham band gap is considerably increased and agrees almost perfectly with the experimental value (cf. Table 3.2). The lattice constant used in the calculation has only minor influence on the band gap width; much more important is the actual parametrization of the functional (HSE06 vs. HSE03). The overall impression is that the hybrid functional scales up the DOS: The VB offset moves from −12 eV below the Fermi energy (PBE) to −13 eV (HSE06), and the peak at −7 eV shows a similar behavior. On the other hand, the CB peak at +2 eV moves to +3 eV, and only (roughly) half of this shift can be attributed to the larger band gap.

Dieses Werk ist copyrightgeschützt und darf in keiner Form vervielfältigt werden noch an Dritte weitergegeben werden.
Es gilt nur für den persönlichen Gebrauch.

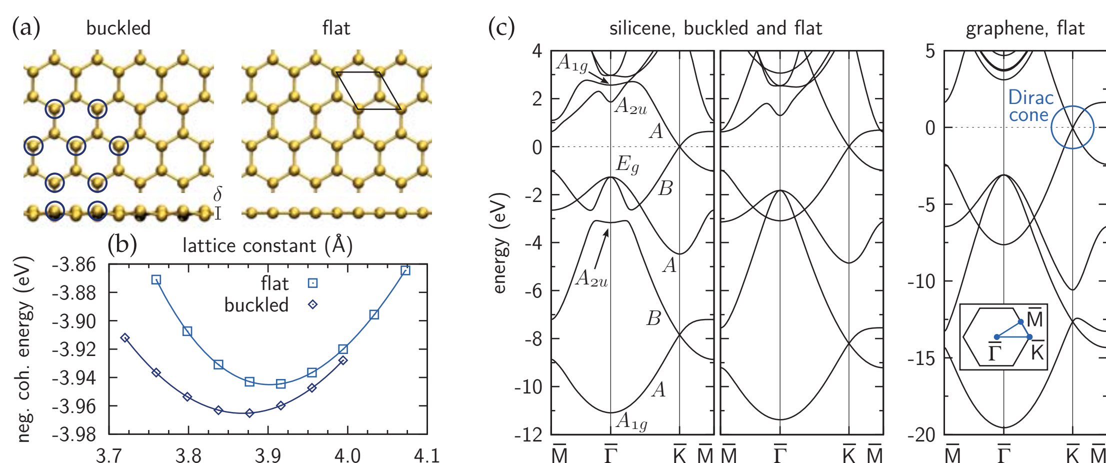

Figure 3.3 – Silicene, calculated with the PBE exchange-correlation functional. The low-buckled structure [$\delta > 0$; top and side views are shown in (a), and the buckling is partially indicated by blue circles] is energetically more stable than the flat one [since it has a higher cohesive energy, as shown in (b)]. The hexagonal unit cell is indicated by black lines. (c) Band structures of buckled and flat silicene. The graphene band structure is shown for comparison. The Dirac cone at the $\bar{K}$ point is clearly visible for all three systems. The labels at the bands refer to irreducible representations at $\bar{\Gamma}$ and along $\bar{\Gamma} - \bar{K}$ and underline that the bands, transforming according to different representations, really cross. The inset illustrates the chosen path in the hexagonal 2D-BZ.

GaAs: An alternative semiconductor

The popularity of Si in microelectronics is not unchallenged. GaAs, for example, has several advantages over Si: a higher electron mobility (high-frequency applications) and a direct band gap at the Γ point (efficient light-matter interaction for light emission and absorption). Thus, GaAs devices are frequently used in optoelectronics (one example being the vertical-cavity surface-emitting laser). Si, on the other hand, has a very high abundance in the Earth's crust and thus is relatively cheap. Furthermore, it provides a native oxide (SiO_2), which is used as insulator in the complementary metal oxide semiconductor (CMOS) technology. Unlike GaAs, it does not consist of poisonous elements; on the contrary, it is even present in the human body. Due to these reasons, and certainly because industrial processing is optimized to Si, alternatives have not yet reached a similar position.

Excursion: Silicene

In the course of the latest developments and events in the field of graphene (a flat, two-dimensional honeycomb arrangement of C atoms [128–130], for which A. K. Geim and K. S. Novoselov received the 2010 Nobel Prize in Physics), one can ask the interesting question whether a similar structure exists for other group-IV elements. Actually, this issue has been investigated theoretically already several years ago [131], but also very recently [132], where the Si equivalent to graphene has been termed "silicene". However, silicene does not seem to exist in nature, since Si strongly prefers the sp^3 hybridization. This is in contrast to C, which favors in its ground state the sp^2 hybridization due to its smaller atomic radius and thus forms graphite, a stack of graphene sheets held together by the vdW interaction, instead of diamond. Consequently, a two-dimensional Si structure is usually considered to be unstable. In fact, the PBE cohesive energy of Si in diamond structure is by 0.65 eV per f.u.

Dieses Werk ist copyrightgeschützt und darf in keiner Form vervielfältigt werden noch an Dritte weitergegeben werden.
Es gilt nur für den persönlichen Gebrauch.

higher (cf. Table 3.1 and Fig. 3.3). Thus, unlike graphene, silicene will not be flat, but will relax into a buckled structure with a corrugation of $\delta = 0.45$ Å, as displayed in Fig. 3.3. This value agrees with $\delta = 0.44$ Å calculated earlier by Cahangirov *et al.* within LDA [133]. The (negative) cohesive energy of silicene shows a second minimum in 1×1 unit cell calculations around $a \approx 2.71$ Å, corresponding to a high-buckled phase ($\delta \approx 2.1$ Å) which was reported to be unstable [133]. Here this phase has been calculated to possess a cohesive energy of 3.91 eV per f.u., so the low-buckled phase (3.97 eV per f.u.) is indeed more stable, as is even the flat phase. Despite these issues, the (with high probability successful) formation of silicene sheets on Ag(111) has been reported very recently [134], corroborated by STM and ARPES experiments. Ag has been chosen as substrate since it does not interact strongly with the deposited Si atoms.

Both the flat and the low-buckled silicene exhibit the linear π-π^* band crossing at the Fermi energy (the so-called "Dirac cone"), just as graphene does [cf. Fig. 3.3(c)]. Thus, one can expect the same interesting behavior: The charge carriers can behave like ultrarelativistic, massless Dirac fermions. The Fermi velocity around $\bar{K}$ has been estimated recently on the basis of first-principles calculations to be $v_F \approx 10^6$ m/s [133], which agrees perfectly with experimental results obtained from ARPES ($v_F \approx 1.3 \times 10^6$ m/s, Ref. [134]) and is comparable to the value measured for graphene ($v_F \approx 1.1 \times 10^6$ m/s, Ref. [135]). It should be noted, however, that the underlying Ag(111) substrate potentially opens a band gap; at least, a similar effect has been observed in graphene [136]. According to recent first-principles calculations, this interaction effect can be reduced by growing silicene on the passivated H/Si(111) surface, where only the weak vdW interaction plays a role [137].

3.2.2 The Si(111) surface

Cleavage of a Si crystal perpendicular to the [111] direction produces one of the Si(111) surfaces. Due to the diamond structure of Si, two possible surface terminations may exist already from the onset: the single dangling bond (SDB) and the triple dangling bond (TDB) termination (cf. Fig. 3.4). In the SDB case, the surface is terminated by a Si bilayer, so that three bonds are saturated and only one dangling bond remains (hence the name). The TDB termination, on the other hand, consists of an additional Si layer placed over the topmost Si atoms; in this case, three bonds of the additional Si layer remain unsaturated. (Equivalently, the topmost atomic layer of the Si bilayer can be removed, which leads to the same situation.)

Surface energies

In the scope of this work, surface energies γ are derived from first-principles calculations by using an *ab initio* thermodynamic approach [138]. The following expression relates to the case of a Si slab with two equivalent surfaces:

$$\gamma(T,p,\{\mu_i\}) = \frac{1}{2A}\Big\{G(T,p,\{N_i\}) - \sum_i N_i\mu_i\Big\} \quad \longrightarrow \quad \gamma = \frac{1}{2A}\Big\{E_{\text{slab}} - N_{\text{Si}}\mu_{\text{Si}}\Big\}. \tag{3.2}$$

Here A is the lateral area of the supercell containing the slab, E_{slab} is the calculated DFT total energy of the system, and N_{Si} is the number of Si atoms in the slab. The chemical potential of Si, μ_{Si}, is chosen to be equal to the energy of bulk Si in diamond structure in order to model thermodynamic equilibrium with the subsurface bulk material. In the case of a supercell with one surface and a passivated backside [a computational trick which can be used to

Dieses Werk ist copyrightgeschützt und darf in keiner Form vervielfältigt werden noch an Dritte weitergegeben werden.
Es gilt nur für den persönlichen Gebrauch.

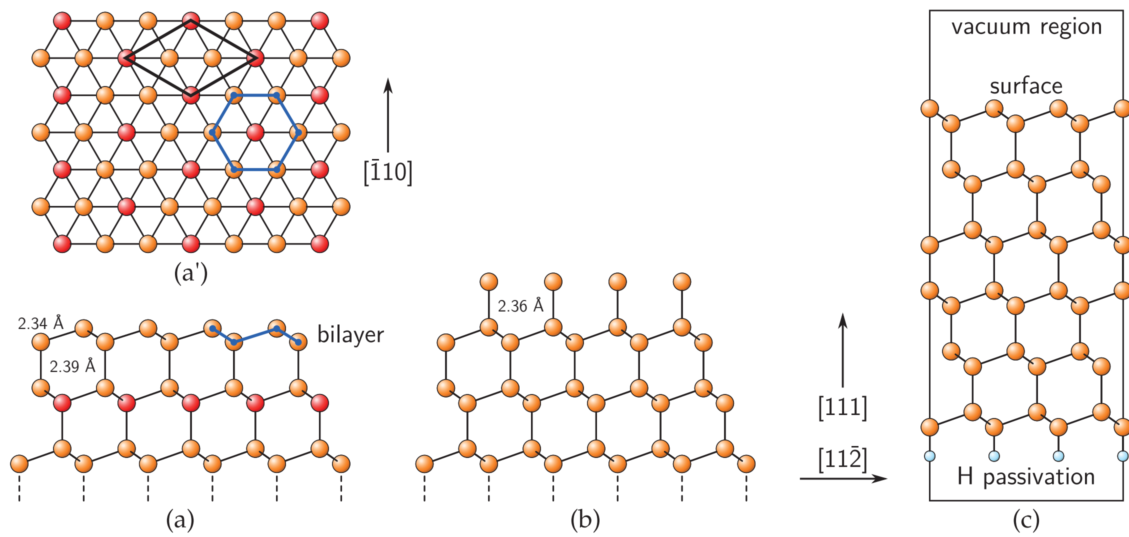

Figure 3.4 – Unreconstructed, but relaxed Si(111) surfaces. Side (a) and top (a') view of the single dangling bond (SDB) termination. The blue hexagon indicates one of the typical bilayer ring structures, which are centered around the Si atoms in the fourth layer (marked in red). The black rhombus indicates the 1×1 surface unit cell. The printed bond lengths display the deviations from the bulk value of 2.37 Å. (b) Side view of the triple dangling bond (TDB) termination. (c) Slab model, showing a Si surface and a H-passivated backside. The structure is periodic in all three spatial dimensions, but the spurious interaction between vertical replicas is suppressed by a vacuum region of approximately 20 Å.

mimic a semi-infinite bulk substrate, cf. Fig. 3.4(c)], the prefactor in Eq. (3.2) changes to $1/A$, and the surface energy of the passivation has to be subtracted. The latter two terms in the Gibbs free energy $G = E_{\text{slab}} + F_{\text{ph}} + pV$ can usually be neglected, even though the phonon contribution should be checked if statements for finite temperatures T are made.[2] Moreover, effects of configurational entropy can play a role via the usual free energy term $-TS$ in that case [139]. It is needless to say that Eq. (3.2) becomes less trivial in the case of more complex compounds consisting of several different elements. More precisely, the choice of the range of the different chemical potentials μ_i is an aspect one should assess carefully.

Already intuitively one can deduce that the surface energy γ of a TDB terminated Si(111) slab will be higher than that of a SDB terminated slab. However, it is not three times as high as the SDB value, but only about 1.84 times: The surface energies calculated in this work (using the PBE exchange-correlation functional) are 95 ± 1 meV/Å^2 for the relaxed, unreconstructed Si(111)-SDB surface and 175 ± 1 meV/Å^2 for the relaxed, unreconstructed Si(111)-TDB surface. The latter two values have been derived from several different calculations; for instance, different unit cells (1×1 vs. $\sqrt{3} \times \sqrt{3}$) have been used, and the Si slab in the supercell can have either two equivalent surfaces or one surface and a H-passivated backside. All procedures led to the same result. Reference [120] reports a TDB/SDB surface energy ratio of 1.75, calculated with the LAPW all-electron method, mainly due to a slightly larger value for the SDB case.

[2] The pV term is of the order 1 atm $\cdot$ 1 Å^3 $\approx 10^5$ Pa $\cdot$ 10^{-30} m^3 $= 10^{-25}$ J $\approx 10^{-3}$ meV and thus by far too small to be of relevance here. Phonon contributions mostly cancel if differences of surface energies of similar structures are considered.

Dieses Werk ist copyrightgeschützt und darf in keiner Form vervielfältigt werden noch an Dritte weitergegeben werden.
Es gilt nur für den persönlichen Gebrauch.

It is nevertheless tempting to pursue the following idea of a simple bond-cutting model: In the case of a SDB termination, one Si-Si bond is broken per 1×1 surface unit cell. From the bulk cohesive energy of fourfold coordinated Si given in Table 3.1 one can assign an energy of 2.308 eV to each Si-Si bond. By dividing this value by the area of the 1×1 surface unit cell (and keeping in mind that two surfaces are produced if the Si-Si bond is cut) one arrives at an estimate of 89.1 meV/Å^2 for the surface energy. Obviously, this value is already very close to the "correctly" calculated result, which validates the thought that the surface energy is simply the penalty energy for breaking a single covalent bond (at least for the SDB case).

Consequently, the surface energies should be larger for the overbinding LDA functional (which gives a by 16% larger Si bulk cohesive energy according to Table 3.1). By using a similar USPP approach as employed in this work, but the LDA for exchange and correlation, the authors of Ref. [126] arrived at surface energies of 113.6 and 108.6 meV/Å^2 for the unrelaxed (like cut bulk) and the relaxed (but unreconstructed) Si(111)-SDB surface. The latter value is indeed by 14% larger than the aforementioned PBE result calculated in the scope of this thesis. Analogously, they report 127.3 and 106.1 meV/Å^2 for unrelaxed and relaxed Si(110), respectively, and a value of 149.2 meV/Å^2 for both relaxed and unrelaxed Si(100).

Surface reconstructions

An important aspect in the field of surface science are surface reconstructions. A reconstruction is a rearrangement of surface atoms that leads to significant deviations from the expected atomic structure of the cleaved crystal. In contrast to a simple relaxation of the surface atoms, a reconstruction results in a larger surface unit cell and typically reduces the lateral symmetry.

The reason for these reconstruction phenomena is simply the broken periodicity of the infinite crystal due to the surface. It is possible to formulate a basic principle which governs the reconstruction processes: In general, the surface atoms will adopt the structure with the lowest surface free energy $\gamma(T, p, \{\mu_i\})$, provided that it is kinetically accessible from the chosen "starting configuration" under the preparation conditions $(T, p, \{\mu_i\})$. The latter part of the preceding sentence underlines that not necessarily only the most stable surface (corresponding to the *global* minimum of the surface free energy) is observed in the experiment; instead, local areas of different reconstructions can form, which correspond to *local* minima of the surface free energy.

In the field of semiconductor physics, this basic principle leads to three guidelines which explain reconstruction and relaxation. For electrically uncharged or autocompensated systems or absent space charge one can formulate [140]:

- minimize the number of dangling bonds by forming new bonds, and try to saturate the remaining dangling bonds;
- compensate charges;
- semiconductor surfaces tend to be insulating or semiconducting, not metallic.

Surface reconstructions are a common phenomenon of semiconductors, but can also be observed for certain metals: Au, Ir, and Pt are famous examples.

The Si(111) surfaces can exhibit several different reconstructions [141]: Cleavage in ultrahigh vacuum at moderate temperature ($T \lesssim 600$ K) produces a 2×1 structure of tilted,

Dieses Werk ist copyrightgeschützt und darf in keiner Form vervielfältigt werden noch an Dritte weitergegeben werden.
Es gilt nur für den persönlichen Gebrauch.

π-bonded zig-zag chains (either the so-called Pandey chains in the SDB case [142] or the Seiwatz chains in the TDB case [143]). Annealing this surface (heat treatment) above 603 K produces a 5×5 reconstruction, and above 873 K one ends up with the 7×7 reconstruction. There are also reports on $\sqrt{3}\times\sqrt{3}$, 2×2, $c2\times4$, 9×9, and 11×11 reconstructions [144].

The 7×7 reconstruction

The certainly most famous and most important reconstruction of the Si(111) surface is the 7×7 reconstruction. The widely accepted atomic structure model for this reconstruction has been presented by Takayanagi *et al.* [145]. This so-called dimer-adatom-stacking fault (DAS) model is shown in Fig. 3.5(a). Due to the large supercell size it has been very challenging in the past to calculate the electronic properties of this reconstruction on an *ab initio* level [146–148]. On modern computers, this task can be accomplished with moderate effort.[3]

The 7×7 surface unit cell is divided into a *faulted* and an *unfaulted* half. At the corners one finds *holes* with a central protruding atom. Along each of the triangle edges of the halves three Si-Si *dimers* are formed (dimer-row domain walls). Each of the halves contains three *rest atoms* and six exposed *adatoms*. There are three mirror planes defined by the $[111]$ and the $[11\bar{2}]$ axes (modulo an in-plane rotation by 120°) running through corner hole atoms. Furthermore, there are three C_3 rotational axes parallel to the $[111]$ direction and centered either at a corner hole atom or in the middle of one of the surface unit cell halves. These symmetries reduce the number of inequivalent "special" surface atoms to a single rest atom in both the faulted and the unfaulted half, two adatoms in both the faulted and the unfaulted half, and three dimer atoms.

The dimer atoms are fourfold coordinated, while the adatoms, the rest atoms, and the corner hole atoms are threefold coordinated [140]. The bond length hierarchy according to the PBE calculation is: Si bulk (2.37 Å), corner hole atoms (2.39 Å), rest atoms in the faulted and the unfaulted half (2.40 – 2.42 Å), dimer bonds (2.43 and 2.45 Å), and adatoms (2.46 – 2.50 Å). Thus, the latter are more weakly bound than the former.

Many surface states appear in the fundamental band gap of bulk Si (cf. Fig. 3.5(b) and Ref. [148]). In the projected density of states (PDOS), the rest atoms and the corner hole atoms show peaks 0.5 eV below the Fermi energy, which represent localized states. At the Fermi energy one finds only states which are derived from the adatoms. This underlines the less bound character of the latter, as mentioned above. Apart from negligible numerical noise, the Si dimers exhibit a large band gap around the Fermi energy. The shown unit cell has a magnetic moment of 1 μ_B. However, the energy difference between a spin-polarized and a NM calculation is only 5 meV per unit cell.

Figures 3.5(c) and 3.5(d) show simulated STM images (within the Tersoff-Hamann approximation, cf. Sec. 2.3.2 on page 39) for filled and empty states, respectively. The agreement with experimental images is very good (see, for instance, Refs. [149–151] or Fig. 3.35 on page 105).[4] For example, the differently pronounced structures in the faulted and unfaulted halves of the surface unit cell in the filled-state images are clearly reproduced, as are the protruding outermost adatoms in the faulted half. Since the rest atom states are covered by

[3] The accurately optimized atomic structure shown in in Fig. 3.5 is the result of a DFT-PBE-USPP calculation performed by the author, as are the details of the atomic and electronic structure mentioned in the following.

[4] Actually, the imaging of the Si(111)-(7×7) reconstruction was the first great success of the STM. Nowadays, this is a "finger exercise" for students in this field.

Dieses Werk ist copyrightgeschützt und darf in keiner Form vervielfältigt werden noch an Dritte weitergegeben werden.
Es gilt nur für den persönlichen Gebrauch.

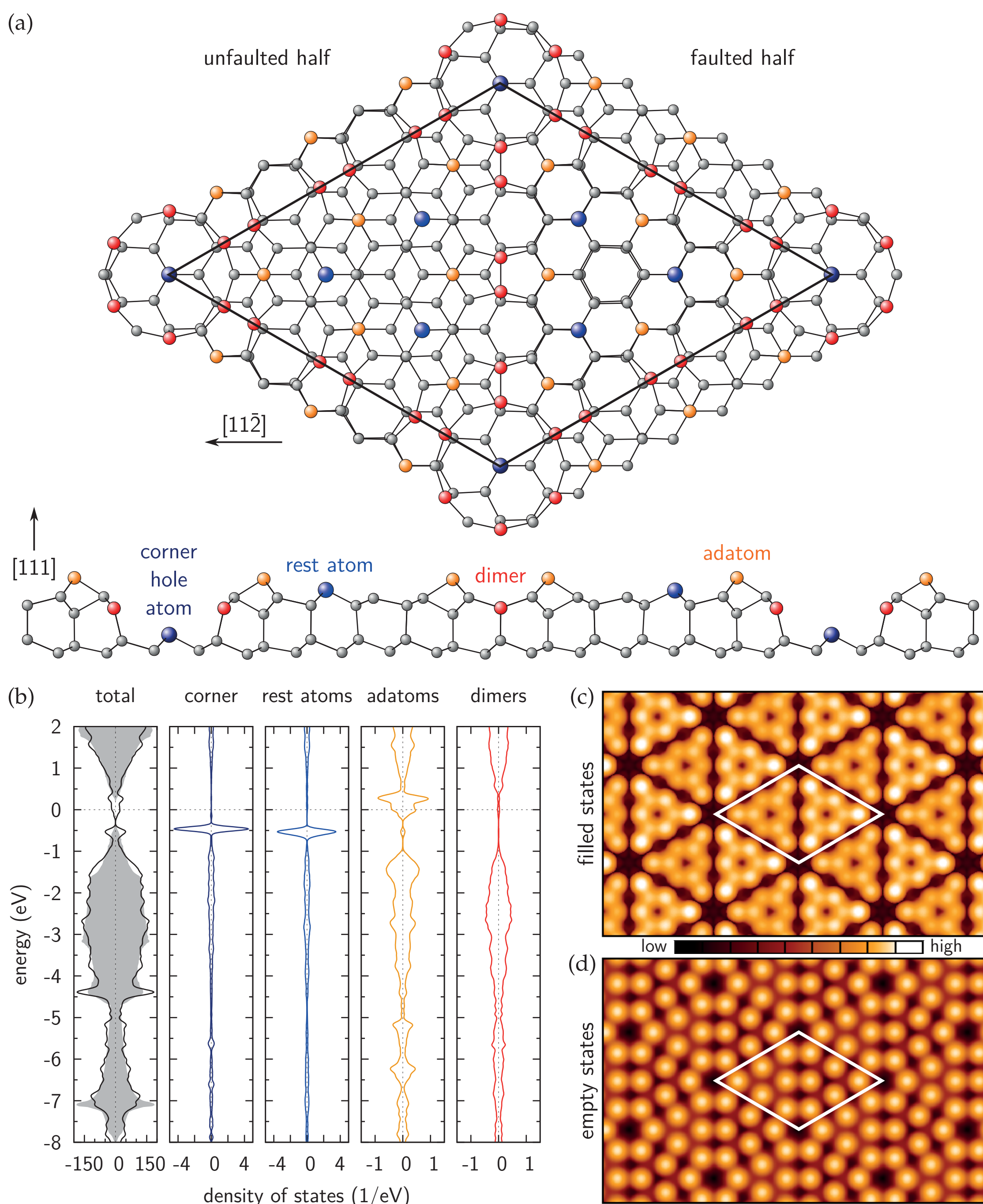

Figure 3.5 – Takayanagi dimer-adatom-stacking fault (DAS) model of the Si(111)-(7 × 7) surface reconstruction. (a) Top and side view of the optimized atomic structure. The small gray spheres represent "ordinary" Si atoms, while the colored spheres depict "special" Si atoms. The rhombus indicates the surface unit cell. (b) Total DOS and PDOS of different atom classes. A superposition of $3s$ and $3p$ states is shown in the PDOS. The gray shaded area shows the bulk DOS of Si for comparison. The pronounced peak at −4.4 eV is mostly an artifact of the H-passivated backside. Panels (c) and (d) show simulated filled- and empty-state STM images, respectively. The bias voltage is ∓0.8 V, and the critical density is 10^{-7} / bohr^3. The rhombus indicates the surface unit cell in analogy to (a).

Dieses Werk ist copyrightgeschützt und darf in keiner Form vervielfältigt werden noch an Dritte weitergegeben werden.
Es gilt nur für den persönlichen Gebrauch.

the energy integration interval, they also contribute to the structures.[5] The empty-state image looks clearly different, with strong, protruding adatoms and slightly more background in the unfaulted half than in the faulted half. The rest atoms are almost invisible now. These aspects also agree perfectly with experimental observations.[6] The corner holes can be seen clearly for both bias voltages.

Density functional theory is very successful in determining the most stable Si(111) surface reconstruction. The surface energy γ of the presented Si(111)-(7×7) reconstruction is indeed significantly lower than the aforementioned values of unreconstructed surfaces. In this work, a value of $\gamma = 76$ meV/Å^2 for PBE has been found. The LDA value is 84.9 meV/Å^2 (12% difference) [126]. The measured ordering (111), (100), and (110) according to Ref. [153] is correctly reproduced by DFT if all the respective reconstructions are taken into account [126]. This shows that the (111) surface is the cleavage face of Si. Moreover, this holds also for the other group-IV materials diamond (C) and Ge [140, 141]. The Si(111) surface shows large areas of similar height, so the distance between two steps is large when compared with other surfaces of Si.

3.3 Bulk properties of 3d transition metal monosilicides

3.3.1 The B20 crystal structure

The ground state crystal structure of many TM monosilicides like CrSi, MnSi, FeSi, and CoSi is the B20 structure. It can be described by a simple cubic unit cell containing four TM and four Si atoms sitting on the 4*a* Wyckoff positions:

$$(u_x, u_x, u_x),\ (-u_x + \frac{1}{2}, -u_x, u_x + \frac{1}{2}),\ (-u_x, u_x + \frac{1}{2}, -u_x + \frac{1}{2}),\ (u_x + \frac{1}{2}, -u_x + \frac{1}{2}, -u_x), \tag{3.3}$$

with $x \in \{\text{TM, Si}\}$, so different values for u have to be used for TM and Si atoms. Special cases are $u_{\text{TM}} = 1/4$ and $u_{\text{Si}} = 3/4$, which gives the rock-salt structure, and $u_{\text{TM}} = 0$ and $u_{\text{Si}} = 1/4$, which corresponds to the zinc-blende structure. For the mentioned TM monosilicides, one gets values for u_x that deviate significantly from these special cases; i.e., $0 < u_{\text{TM}} < 1/4$ and $3/4 < u_{\text{Si}} < 1$, which shows that the B20 structure can be interpreted in this case as a distorted form of rock-salt structure (cf. Fig. 3.6).

The rock-salt structure has space group $Fm\bar{3}m$. The B20 structure can be reached by a dimerizing-type displacement of TM and Si atoms along one of the [111] directions, which turns TM-Si neighbors along this direction in the rock-salt structure into TM-Si nearest neighbors in the B20 structure [154]. The TM-Si coordination is sevenfold: Each TM atom has one closest Si neighbor in the [111] direction, three Si neighbors at a slightly higher distance and three further Si neighbors at even higher distance. Beyond the Si neighbors, the TM-TM coordination is equidistant and sixfold. Thus, the coordination in the B20 structure is higher than in the rock-salt (sixfold) or in the zinc-blende (fourfold) structure. The implications of this fact on the band structure will be discussed below.

Another interesting special case is the so-called "ideal" B20 structure, which is characterized by $u_{\text{TM}} = 1/(4\tau) \approx 0.155$ and $u_{\text{Si}} = 1 - 1/(4\tau) \approx 0.845$, where $\tau = (1 + \sqrt{5})/2$ is the

[5] Early STM studies also provided filled-state images where only the rest atoms and the corner hole atoms are pronounced [149, 152].

[6] The agreement between theoretically simulated and experimentally recorded STM images is so striking in this case that they can hardly be distinguished. This underlines the quality of the Tersoff-Hamann approximation.

Dieses Werk ist copyrightgeschützt und darf in keiner Form vervielfältigt werden noch an Dritte weitergegeben werden.
Es gilt nur für den persönlichen Gebrauch.

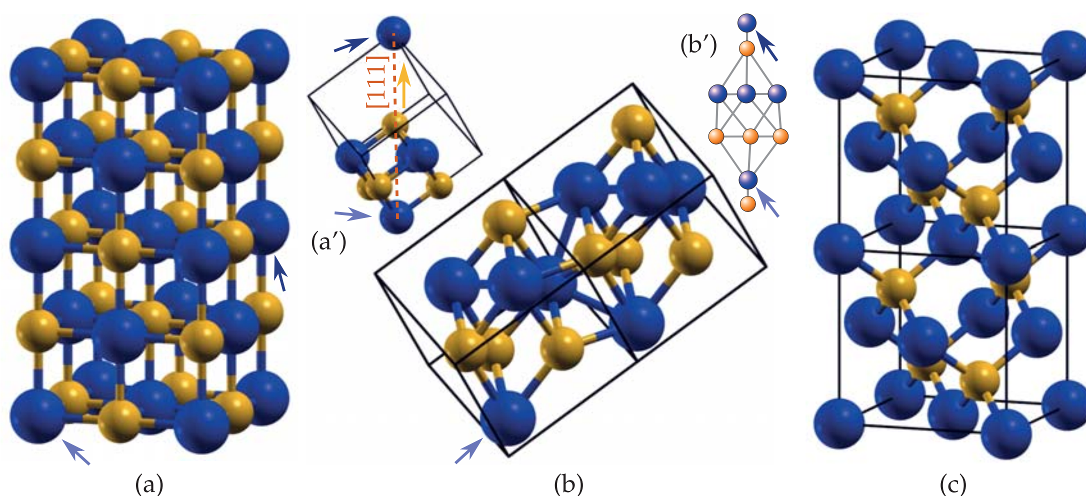

Figure 3.6 – Atomic models of the (a) rock-salt, (b) B20, and (c) zinc-blende structure. Each time, two simple cubic unit cells with a four-atom basis are shown. Bright orange (dark blue) spheres depict Si (TM) atoms. Structures (a) and (c) are shifted such that one of the TM atoms is centered at the origin. A fraction of the rock-salt structure (a′) shows how the dimerizing, rhombohedral distortion along the [111] direction leads to the B20 structure; i.e., the orange arrow indicates the displacement of the central Si atom, while the bright blue and the dark blue arrows mark TM atoms on the [111] axis. The small model (b′) shows the rhombohedral bonding in the B20 structure.

golden ratio [154, 155]. In this case, the inversion operation interchanges the TM and Si sites (by construction), since $u_{\mathrm{TM}} = 1 - u_{\mathrm{Si}}$. Each TM atom is then equidistantly coordinated to seven nearest Si neighbors, with a TM-Si distance of $a\sqrt{3}/(2\tau)$, where a is the simple cubic lattice constant.

Usually, the resulting space group is $P2_13$, which is nonsymmorphic. It contains twelve space group operations: identity (class E), three 180° rotations about the [100], [010], and [001] directions (each followed by a fractional translation, class C_2) and eight 120° rotations about the four $\langle 111 \rangle$ directions (some followed by a fractional translation, classes C_3 and C_3'). Most importantly, it does *not* contain the inversion operation, a fact which is crucial for the helical magnetism in MnSi, for example.

3.3.2 Monte Carlo simulations on the trillium sublattice

It is interesting to compare the sixfold coordinated TM-TM sublattice of the B20 structure (the so-called "trillium" lattice [156, 157]) to a simple cubic lattice which also exhibits sixfold coordination. The difference between both lattices becomes obvious if one tries to create closed loops of nearest neighbors (cf. Fig. 3.7). While in the simple cubic lattice each loop contains at least four atoms, a three-five segmentation can be observed in the trillium lattice. This implies that a perfect AFM spin ordering can be realized on the simple cubic lattice without problems, while significant frustration effects are expected for the trillium case.

Dieses Werk ist copyrightgeschützt und darf in keiner Form vervielfältigt werden noch an Dritte weitergegeben werden.
Es gilt nur für den persönlichen Gebrauch.

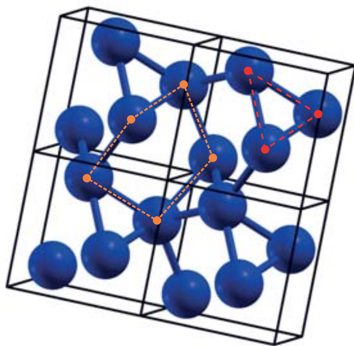

Figure 3.7 – Illustration of the three- and five-atom loops in the trillium lattice, which is a sublattice of the B20 crystal structure formed by the TM atoms.

In order to quantify the differences, one can perform classical Monte Carlo simulations of Heisenberg models on such lattices:[7]

$$H = \frac{1}{2} \sum_{i,j} J_{ij}\, \vec{S}_i \cdot \vec{S}_j \quad \text{with} \quad J_{ij} = \pm J \quad \text{and} \quad J > 0. \tag{3.4}$$

Here $\vec{S}_i$ are classical spins in three dimensions on N sites and J_{ij} are exchange coupling constants. The calculations have been restricted to nearest-neighbor interactions, thus $J_{ij} = 0$ if site j is not directly coordinated to site i. Positive (negative) J_{ij} correspond to AFM (FM) coupling. The factor $1/2$ eliminates double counting. Two system sizes have been considered: The smaller system contained $N = 864$ lattice sites, and the larger one $N = 6912$ lattice sites. For the simple cubic case, $12 \times 12 \times 6$ and $24 \times 24 \times 12$ lattices with one site per unit cell have been used. For the case of the trillium lattice, $6 \times 6 \times 6$ and $12 \times 12 \times 12$ lattices with four sites per unit cell have been used. All lattices were subject to periodic boundary conditions.

Interesting observables are the heat capacity and the magnetic susceptibility,

$$C_V(T) = \frac{\langle E^2 \rangle - \langle E \rangle^2}{k_\mathrm{B} T^2} \quad \text{and} \quad \chi(T) = \frac{\langle M^2 \rangle - \langle M \rangle^2}{k_\mathrm{B} T}, \tag{3.5}$$

where E is the energy of the system according to H and $M = |\sum_i^N \vec{S}_i|$ is its total magnetization. Both quantities reflect the fluctuations in the system and are especially noteworthy around the critical (Curie/Néel) temperature T_C.

The results can be seen in Fig. 3.8. First of all, both quantities show the well-known narrowing of the singularity around T_C with increasing system size due to the reduction of finite-size effects. The value of the critical temperature T_C in the FM case, estimated from the position of the singularities, is very similar for the trillium and the simple cubic lattice. For the latter, the singularities are located around $T_\mathrm{C}\, k_\mathrm{B}/J \approx 1/\ln(2)$, while for the former they are shifted to slightly lower values. This can be seen very clearly for χ. For $T \to 0$ or $T \to \infty$, both C_V and χ curves become asymptotically congruent for the different lattices.[8]

[7] The MPI-parallelized Monte Carlo program written by the author of this thesis can perform simulations on arbitrary lattices and employs the Metropolis algorithm [158] and the Mersenne twister pseudo random number generator [159]. In analogy to Ref. [157], the author used 2×10^5 Monte Carlo steps for equilibration and 1×10^6 Monte Carlo steps for measurements. Each Monte Carlo step consisted of N spin updates. The temperature T was gradually decreased.

[8] Note that even for the "simple cubic" Heisenberg model no exact expression for T_C is known. A value of $T_\mathrm{C}\, k_\mathrm{B}/J \approx 1/\ln(2) \approx 1.443$ has been put forward on the basis of Monte Carlo simulations [160].

Dieses Werk ist copyrightgeschützt und darf in keiner Form vervielfältigt werden noch an Dritte weitergegeben werden.
Es gilt nur für den persönlichen Gebrauch.

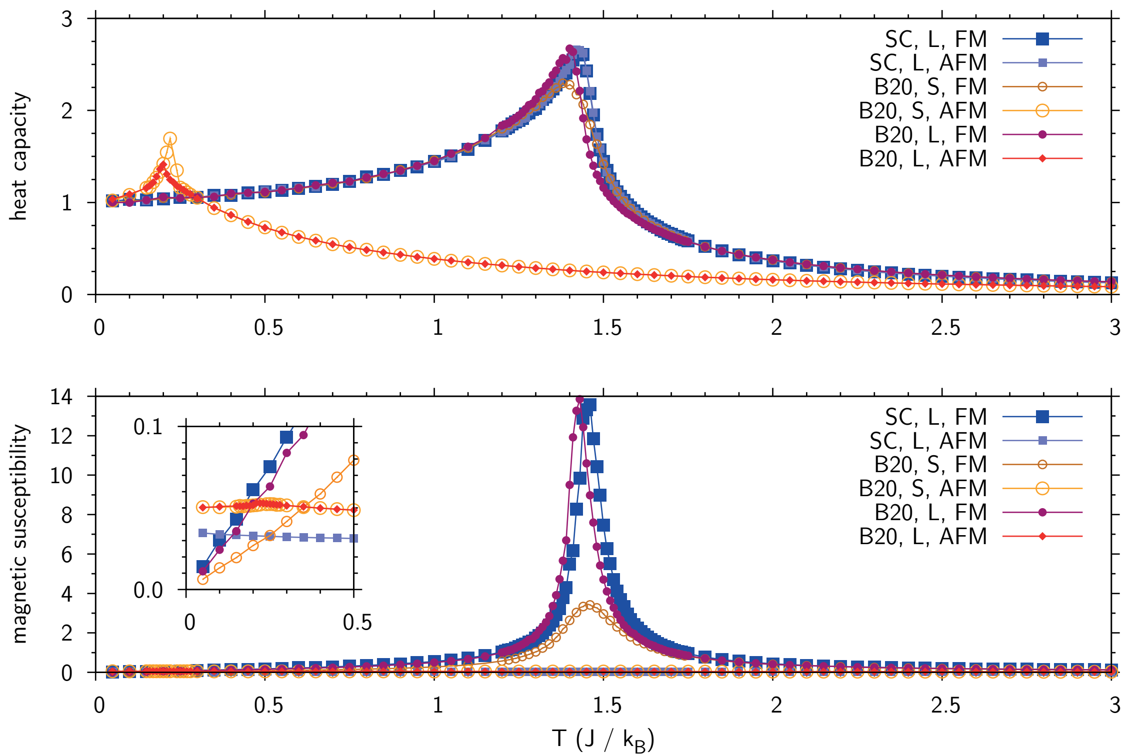

Figure 3.8 – Comparison of the heat capacity $C_V(T)/N$ (upper panel) and the magnetic susceptibility $\chi(T)/N$ (lower panel), defined in Eq. (3.5), for the trillium sublattice of the B20 structure (B20) and for the simple cubic lattice (SC), both with sixfold coordination. The results have been obtained by simulating a classical Heisenberg model. A smaller (S) and a larger (L) system have been considered.

A more significant difference between the two lattices arises for AFM coupling between adjacent sites. In this case, the critical temperature for the trillium lattice is located at much lower values ($T_C \approx 0.2\, J/k_B$) than for FM coupling. This value has already been reported very recently by S. V. Isakov, J. M. Hopkinson, and H.-Y. Kee [157]. In contrast, the singularity of the heat capacity for the simple cubic lattice is located at the same position for FM and AFM coupling. The AFM state is represented by a bipartition of the lattice, forming (111) planes of equal spin direction. Moreover, the FM and AFM C_V curves for the simple cubic lattice are congruent in the resolution provided by the statistical sampling, and only χ shows a strong difference.

This demonstrates that frustration effects become significant in the case of the AFM trillium lattice, although the local coordination is equivalent in both lattices. However, already in the FM case, differences between the two lattices can be seen around the critical temperature. The reason is probably the following: Since the correlation length diverges at the critical point, both C_V and χ (measuring fluctuations) become more sensitive to the bonding beyond the nearest-neighbor coordination (nonlocality) and thus to the different loop structures discussed above (cf. Fig. 3.7).

Dieses Werk ist copyrightgeschützt und darf in keiner Form vervielfältigt werden noch an Dritte weitergegeben werden.
Es gilt nur für den persönlichen Gebrauch.

Table 3.3 – Lattice constants a of different, completely relaxed TM silicides in B20 structure compared to literature: (†) Ref. [161], (‡) Refs. [162, 163]. $M_{\mathrm{calc}}^{\mathrm{PBE}}$ denotes the total magnetic moment per f.u. The magnetic moments localized at the TM atoms are given in parentheses.

	$a_{\mathrm{calc}}^{\mathrm{PBE}}$ (Å)	$a_{\mathrm{calc}}^{\mathrm{PW91}}$ (Å) †	a_{exp} (Å) ‡	$M_{\mathrm{calc}}^{\mathrm{PBE}}$ (μ_{B})
TiSi	4.972	–	–	0.00 (0.00)
VSi	4.735	4.739	–	0.00 (0.00)
CrSi	4.590	4.600	4.629	0.41 (0.45)
MnSi	4.516	4.519	4.558	1.00 (1.11)
FeSi	4.445	4.448	4.493	0.00 (0.00)
CoSi	4.430	4.442	4.447	0.00 (0.00)
NiSi	4.515	4.535	–	0.00 (0.00)

Table 3.4 – Bulk moduli $B_{\mathrm{calc}}^{\mathrm{PBE}}$ and Wyckoff parameters u for TM and Si atoms of different TM silicides in B20 structure. In parentheses, experimental values are given (Ref. [162]).

	$B_{\mathrm{calc}}^{\mathrm{PBE}}$ (GPa)	$u_{\mathrm{calc}}^{\mathrm{TM}}$	$1 - u_{\mathrm{calc}}^{\mathrm{Si}}$
TiSi	131	0.143	0.156
VSi	176	0.139	0.153
CrSi	188	0.137 (0.136)	0.152 (0.154)
MnSi	208	0.137 (0.138)	0.155 (0.154)
FeSi	215	0.136 (0.136)	0.160 (0.156)
CoSi	214	0.145 (0.14?)	0.157 (0.16?)
NiSi	173	0.149	0.154

3.3.3 Structural properties

The first important step after the preceding, more fundamental considerations is a theoretical determination of structural parameters like lattice constants, Wyckoff parameters, or bulk moduli, followed by a critical assessment of their quality by comparison with experimental values. The PBE exchange-correlation functional has been used in the following, mainly because it provided reasonable results in previous studies of different TM silicides [112–114]. A more critical assessment of this aspect is given later in Sec. 3.5. Noncollinear spin configurations, as they arise, for example, in MnSi, have been approximated to be collinear. This is reasonable since the wavelength of MnSi spin helices, for example, is much longer than the size of the systems considered in the following. Thus, any spin noncollinearity would just result in a *small* correction to the total energy.

Table 3.3 shows calculated lattice constants for all considered bulk TM monosilicides and compares them to recently calculated values, which were obtained using the PAW method and the PW91 exchange-correlation functional [161], as well as to experimental values [162, 163]. One can see that the agreement with Ref. [161] is almost perfect, especially when keeping in mind that different exchange-correlation functionals have been used. Compared to experimental values, the DFT-PBE lattice constants for CrSi, MnSi, FeSi, and CoSi are underestimated by only $-0.8\,\%$, $-0.9\,\%$, $-1.1\,\%$, and $-0.4\,\%$, respectively, which is also

Dieses Werk ist copyrightgeschützt und darf in keiner Form vervielfältigt werden noch an Dritte weitergegeben werden.
Es gilt nur für den persönlichen Gebrauch.

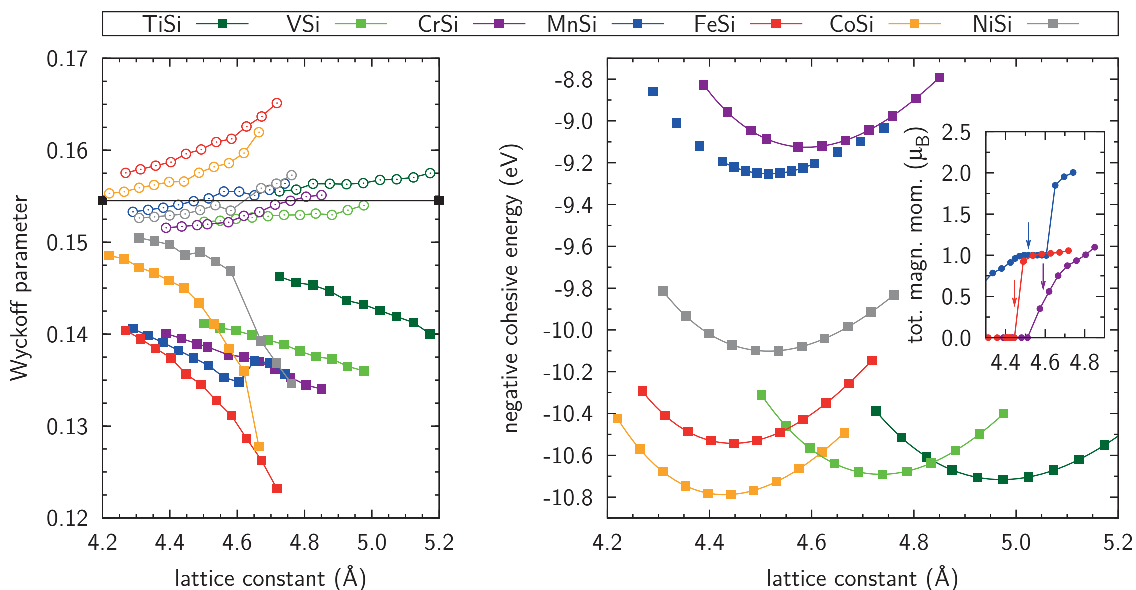

Figure 3.9 – Left: Wyckoff parameters u_{TM} (filled squares) and $1 - u_{Si}$ (open circles) of different TM silicides in B20 structure as functions of the lattice constant. The black horizontal line indicates the value for u_{TM} that corresponds to the ideal B20 structure. Right: Negative cohesive energies $-E_{coh}$ per f.u. and fits to the Murnaghan equation of state, Eq. (3.1). Inset: Total magnetic moments per f.u. The small arrows indicate the energy minima.

very good. Additionally, all-electron LAPW calculations have been performed to get an impression of the deviations caused by the pseudopotential approach. These were found to be small: For MnSi, a very good agreement of both the lattice constant (4.53 Å) and the bulk modulus (204 GPa) is achieved. The results for FeSi (4.46 Å, 228 GPa) and CrSi (4.60 Å, 187 GPa) are also good (cf. Tables 3.3 and 3.4).

As can be seen from Table 3.3, the equilibrium lattice constant is maximal for TiSi, reduces continuously until CoSi and goes up again for NiSi. The bulk modulus increases from TiSi to FeSi and CoSi and reduces again for NiSi. In the course of complete structural optimizations, the Wyckoff parameters u_{TM} and u_{Si} were also determined for each compound and several values of the lattice constant. The results can be seen in Fig. 3.9. Two trends can be deduced: First, u_{TM} tends to decrease as the lattice constant becomes larger, while $1 - u_{Si}$ increases. Second, this trend becomes more pronounced with increasing valency. Furthermore, one can see from Fig. 3.9 and Table 3.4 that all u_{TM} lie well below the ideal value $u_{TM} = 1/(4\tau) \approx 0.155$ for all considered lattice constants, even though they approach it as uniform (hydrostatic) pressure is applied; this general trend has already been predicted for the FeSi case [155]. For MnSi, the calculated energy difference between real and ideal B20 structure at their respective equilibrium lattice constant is 161 ± 5 meV per f.u. For FeSi, a value of 120 meV has been reported [155]. The deviation of the equilibrium Wyckoff parameter u_{TM} from its ideal value decreases from TiSi to FeSi, jumping up again for CoSi and NiSi (cf. Table 3.4).

The cohesive energies of the TM monosilicides, which describe the energy inclosed in the bonds,

$$E_{coh}^{TM\text{-}Si} = -(E_{tot}^{TM\text{-}Si} - E_{atom}^{TM} - E_{atom}^{Si}),$$

Dieses Werk ist copyrightgeschützt und darf in keiner Form vervielfältigt werden noch an Dritte weitergegeben werden.
Es gilt nur für den persönlichen Gebrauch.

are all in the range of 9 – 11 eV per f.u. (cf. Fig. 3.9). An all-electron value of $E_{\text{coh}} \approx 9.35$ eV has been reported for MnSi [120], calculated also with the PBE exchange-correlation functional, which is quite close to the value obtained here with the USPP approach. If the TM silicides are compared against each other, it turns out that the B20 compounds CoSi, TiSi, VSi, and FeSi are most strongly bound, followed by NiSi and the more weakly bound MnSi and CrSi. It should be noted, however, that all these values are already very high: For instance, calculated PBE values for FM bcc-Fe, α-Mn[9], AFM bcc-Cr, and diamond-Si are 4.93, 3.76, 3.93, and 4.62 eV per f.u., respectively. These values can be added appropriately and compared to Fig. 3.9. Equivalently, the zero-temperature formation energies (enthalpies) can be calculated, which are defined from bulk compound total energies as

$$\Delta H^{\text{TM-Si}} = E_{\text{tot}}^{\text{TM-Si}} - E_{\text{bulk}}^{\text{TM}} - E_{\text{bulk}}^{\text{Si}}. \tag{3.6}$$

The results are -0.576, -0.882, and -1.000 eV per f.u. for CrSi, MnSi, and FeSi, respectively, which means that they are far more stable and more strongly bound than the elemental solids of their constituents. Consequently, the formation of a TM silicide from its constituents in solid phase is a highly exothermic reaction. Again, Ref. [120] reports a theoretical value of -0.879 eV per f.u. for MnSi, which is in perfect agreement with the USPP value determined in this work. Experimental values at room temperature are -0.551, -0.629, and -0.797 eV per f.u. for CrSi, MnSi, and FeSi, respectively [166]. Obviously, the overall picture is given correctly by DFT-PBE. The deviations can be attributed to the PBE approximation on the one hand and to the influence of finite temperatures on the other hand.

The B20 structure is not the ground state for all TM monosilicides. For example, TiSi and NiSi prefer the B27 [167] and the B31 [166] structure, respectively. Both have the *Pnma* space group (like MnP). Full-optimization calculations (cell parameters a, b, c and all internal atom coordinates) for TiSi and NiSi led to NM solutions in both cases, with an energy spacing to the B20 phase of 570 meV and 177 meV per f.u., respectively. VSi preferred the B20 structure over aforementioned alternatives in test calculations and was NM. No data on VSi could be found in the literature, only for different stoichiometries (like VSi_2, V_3Si, V_5Si_3) [166, 168]. Presumably, this compound is unstable in nature. Despite these aspects, it is fruitful to include all three compounds, crystallized in an artificial B20 structure, in the following study.

3.3.4 Electronic properties, magnetic properties, and the band gap

Over the last years, two TM monosilicides have been discussed predominantly: MnSi and FeSi. For both, intense research is still ongoing, in particular because of their peculiar electronic and magnetic properties.

MnSi as bulk material is a chiral itinerant ferromagnet. Its complex magnetic structure is well studied: Several different magnetic phases exist, including a recently observed skyrmion phase [169] and a magnetic blue phase [170]. Without external magnetic field, MnSi shows a helical magnetic order of long wavelength (175 – 190 Å) below the critical temperature $T_C \approx 29.5$ K [171]. This helicity can be explained by the missing inversion symmetry of the crystal lattice, which results in a nonvanishing Dzyaloshinsky-Moriya (DM) term in the spin density expansion of the free energy [172, 173]. If an externally applied magnetic field

[9]One can construct the total energy of bulk α-Mn (which is the correct, but quite complicated ground state crystal structure of Mn) by calculating AFM γ-Mn (fcc structure) and correcting [164, 165] the resulting energy by -0.07 eV per f.u.

Dieses Werk ist copyrightgeschützt und darf in keiner Form vervielfältigt werden noch an Dritte weitergegeben werden.
Es gilt nur für den persönlichen Gebrauch.

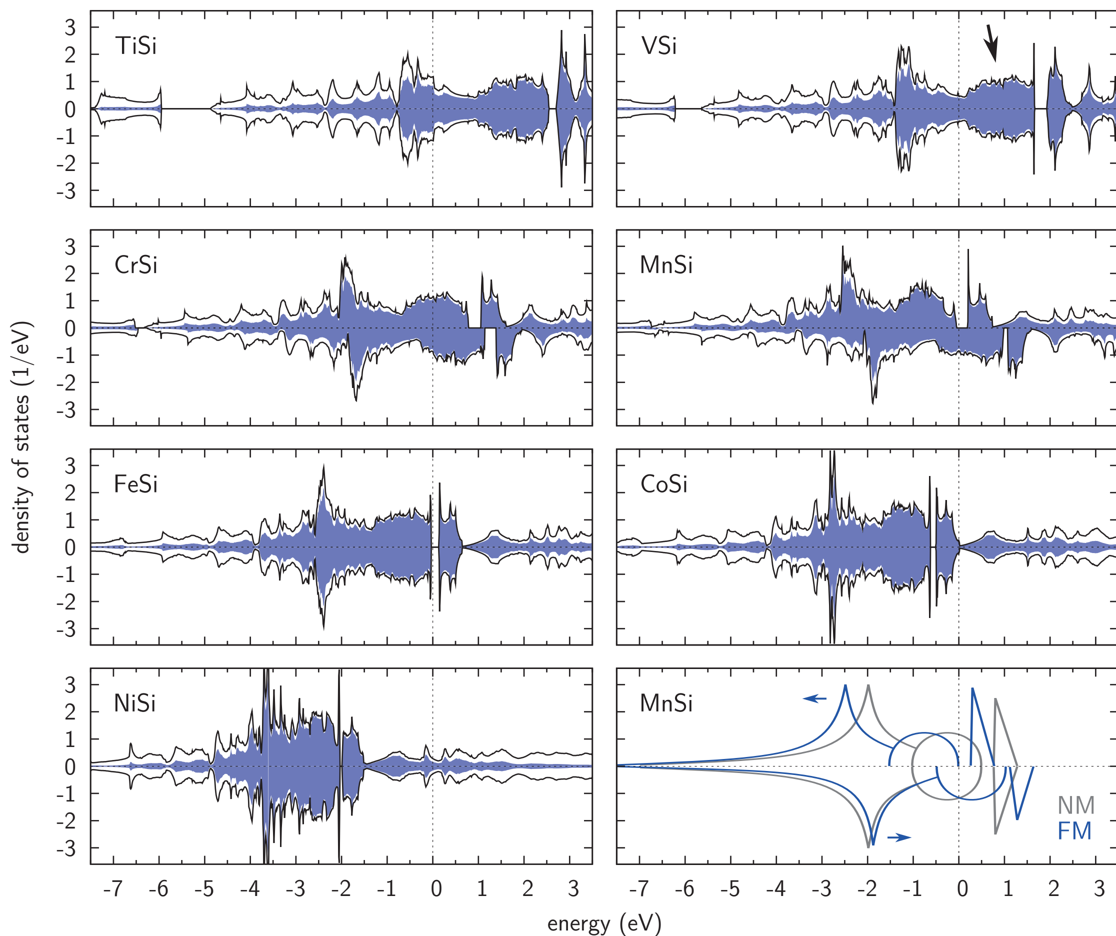

Figure 3.10 – Spin-resolved DOS for different TM monosilicides in B20 structure. The black lines indicate the total DOS per f.u., and the blue shaded areas correspond to the projection onto the TM 3*d* orbitals. The Fermi energy is chosen as reference energy. The black arrow in the VSi panel marks the "hill" referred to in the text. The bottom-right panel schematically indicates the origin of magnetism for MnSi.

exceeds $\mu_0 H_{C2} \approx 300 - 550$ mT, the DM contributions are overcome and the spins align ferromagnetically [169,174,175]. First-principles LDA calculations predicted a total magnetic moment of 1 μ_B per f.u. [154]. On the other hand, experiments report a saturation moment of 0.4 μ_B in the polarized phase at high external magnetic field, which strongly deviates from a moment of 2.27 μ_B according to a Curie-Weiss fit in the paramagnetic phase [176,177].

While MnSi is a metal also at low temperatures, FeSi has a NM, semiconducting ground state with a narrow band gap, but shows a transition to a metal around room temperature [178, 179]. The magnetic susceptibility rises exponentially up to 500 K and follows a Curie-Weiss temperature dependence at higher temperatures [180]. These unusual phenomena led to several model assumptions in the past, like FeSi being a *d*-electron Kondo insulator [178, 181, 182]. However, this view has been questioned recently by experimental [183] and theoretical [116] works which state that a correlated band insulator picture, where the 3*d* bands are renormalized due to electron-electron interactions, is more appropriate. Photoemission experiments measured a band gap width of around 60 meV at low

Dieses Werk ist copyrightgeschützt und darf in keiner Form vervielfältigt werden noch an Dritte weitergegeben werden.
Es gilt nur für den persönlichen Gebrauch.

temperatures [184, 185], while tunneling spectroscopy reported 50 meV [178]. Paschen *et al.* stated that the gap appears to be smaller in transport measurements (55 – 70 meV) than for charge or spin excitations (75 – 100 meV) [179]. Early LDA calculations reported a wider gap of 130 meV [186]. The gap closes quickly with increasing temperature [184, 185]. This is in agreement with recent theoretical estimates of the optical conductivity which showed no sign of a band gap above a temperature of 386 K [116].

From the densities of states for the bulk compounds shown in Fig. 3.10 it becomes obvious that the TM monosilicides in B20 structure follow a similar electron filling scheme as reported for the artificial zinc-blende structure [161]. The overall shape of the DOS is always the same, like in a rigid-band model (neglecting the exchange splitting for CrSi and MnSi for the moment), but a reduction of the $3d$ band width for the late TMs can be observed. The band gap, which has been studied experimentally for FeSi, can be observed somewhere in the DOS for *all* considered TM silicides and thus has to be already a consequence of the sevenfold atom coordination in the B20 crystal structure.[10] This universality of the band gap corroborates the aforementioned view of FeSi being "simply" a (correlated) band insulator.

One can inspect the character of the band gap in more detail for the representative case of FeSi. As in all studied TM-Si compounds (cf. Fig. 3.10), the TM $3d$ states dominate the DOS around the Fermi energy. From Fig. 3.11 one can see that the ubiquitous band gap separates actually two groups of bands which have predominantly either an Fe $3d_{x^2-y^2} + 3d_{xy}$ character (upper part of the VB) or an Fe $3d_{xz} + 3d_{yz}$ character (lower part of the CB), where the orientation of the $3d_{z^2}$ orbital has been chosen parallel to the $[111]$ direction of the cubic unit cell. The two opposing band groups can also be identified clearly in band structure plots with superimposed band character [cf. Fig. 3.11(c)]. How the difference between these two groups manifests itself in the crystal environment can be seen from sections through the ILDOS, which is defined as

$$I(\vec{r}) = \left| \int_0^E \mathrm{d}\varepsilon \sum_{n\vec{k}} |\psi_{n\vec{k}}(\vec{r})|^2 \, \delta(\varepsilon - \varepsilon_{n\vec{k}} + E_\mathrm{F}) \right| , \qquad (3.7)$$

with Kohn-Sham states $\psi_{n\vec{k}}$, energy eigenvalues $\varepsilon_{n\vec{k}}$, and the Fermi energy E_F. Here the author has used $E = +1$ eV ($E = -1$ eV), which covers the lowest CB (highest VB) states [cf. Fig. 3.11(b)]. The (111) lattice planes have been chosen such as to contain three Fe atoms forming a triangle (that is, a dense Fe layer; cf. Fig. 3.16 on page 74). These TM-TM triangles are characteristic for the B20 structure, since they build up the trillium lattice (see Ref. [156] for a more detailed description of this structural aspect). In addition to the expected localization around the Fe centers, the ILDOS shows that the highest VB orbitals point with one lobe into the centers of the Fe-Fe triangles, whereas the lobes of the lowest CB states point more or less along the triangle edges. This is in line with previous findings by Andersen *et al.*[11] It is reasonable to assume that this band and orbital structure carries over to all other B20 materials studied in this chapter.

According to Fig. 3.10, all considered materials in B20 structure are found to be metallic, except FeSi, which is correctly predicted to be a semiconductor at low temperatures. The

[10] Note that the author has checked that, for example, FeSi and MnSi in the sixfold coordinated rock-salt (B1) structure show *no* band gap in their DOS, even though the B20 structure is a distorted form of the rock-salt structure (cf. Fig. 3.14 on page 71). Moreover, MnSi in the eightfold coordinated CsCl (B2) structure also shows no band gap in its DOS [120], which has been confirmed by the author.

[11] O. K. Andersen, Max-Planck-Institut für Festkörperforschung, Stuttgart. Private communication.

Dieses Werk ist copyrightgeschützt und darf in keiner Form vervielfältigt werden noch an Dritte weitergegeben werden.
Es gilt nur für den persönlichen Gebrauch.

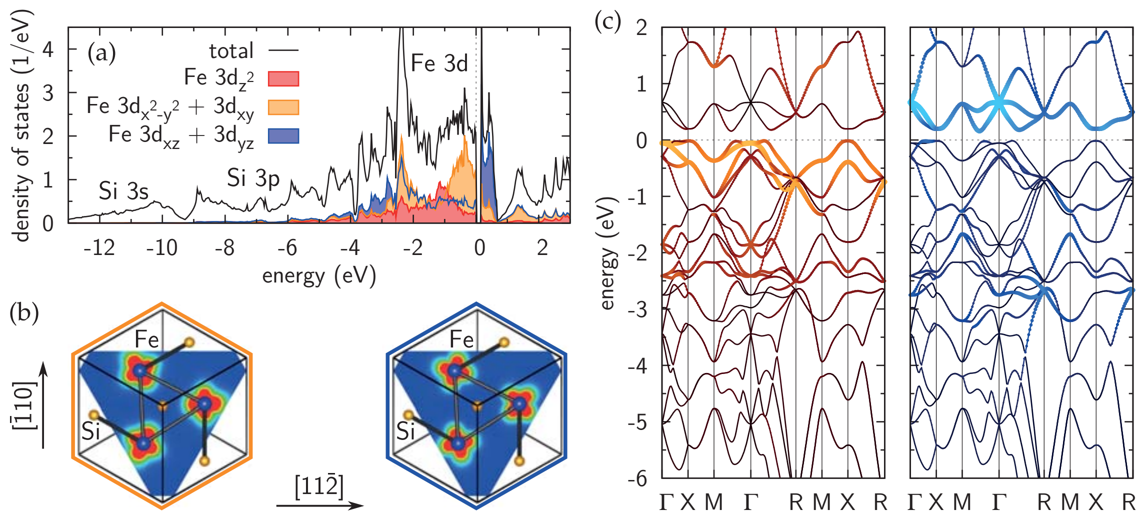

Figure 3.11 – Electronic structure of bulk FeSi in B20 structure. (a) DOS plot in which the black line indicates the total DOS per f.u. and the red, orange, and blue shaded areas correspond to projections onto the Fe $3d_{z^2}$, $3d_{x^2-y^2} + 3d_{xy}$, and $3d_{xz} + 3d_{yz}$ orbitals. The $3d_{z^2}$ orbital lies parallel to the [111] direction of the cubic unit cell. The Fermi energy is chosen as reference energy. (b) ILDOS sections along a characteristic (111) lattice plane in the cubic unit cell showing the spatial orientation of the topmost VB (left) and lowest CB (right) states in the crystal (cf. Figs. 3.6 and 3.16). As the ILDOS value increases, the plane color shifts from blue to red. (c) Band structure plots in which the band character is indicated by line color and line width. Please note especially the region around the Fermi energy. Thick bands with bright orange (bright blue) colors correspond to a strong $3d_{x^2-y^2} + 3d_{xy}$ ($3d_{xz} + 3d_{yz}$) band character.

DOS of CoSi exhibits only small values at the Fermi energy; consequently, CoSi is a metal with low conductivity. NiSi is also metallic in its actual ground state crystal structure B31 (cf. Fig. 3.12). These results agree with experimental observations [111]. For TiSi in B27 structure, DFT predicts a metallic behavior.

The author found a preference for the FM ground state for CrSi and MnSi. In this context, the origin of magnetism can be understood in a simple Stoner picture. By inspecting the DOS in Fig. 3.10 one can see that the “hill” (marked by a black arrow) between the position of the Fermi energy for VSi and the band gap (in which the Fermi energy for FeSi is located) can be filled with three electrons. For VSi, the hill is empty and the Fermi energy lies in a local minimum; an exchange splitting would not lead to a lowered total energy here. For CrSi and MnSi, the hill is partially filled with one or two electrons. In this situation, a NM solution is expected to be metastable. Indeed, in the case of CrSi, the exchange splitting shifts the bands such that the Fermi energy lies roughly in the center of the hill for the majority spins and slightly above the local minimum for the minority spins. For MnSi, the Fermi energy lies at 1/3 filling of the hill for the minority spins and in the band gap for the majority spins. The NM-FM transition for MnSi is schematically displayed in the bottom-right panel of Fig. 3.10, where the gray (blue) lines depict the initial NM (final FM) situation. Finally, for FeSi, the hill is filled completely and the Fermi energy lies in the band gap for both spin channels. For CoSi and NiSi, the Fermi energy is located in stable local minima again. Therefore, these materials are NM, in agreement with the experimental literature [111].

For CrSi, the energy splitting between the NM and the FM configuration at their respective equilibrium lattice constants is very small (only 1.6 meV per f.u.). This indicates a high

Dieses Werk ist copyrightgeschützt und darf in keiner Form vervielfältigt werden noch an Dritte weitergegeben werden.
Es gilt nur für den persönlichen Gebrauch.

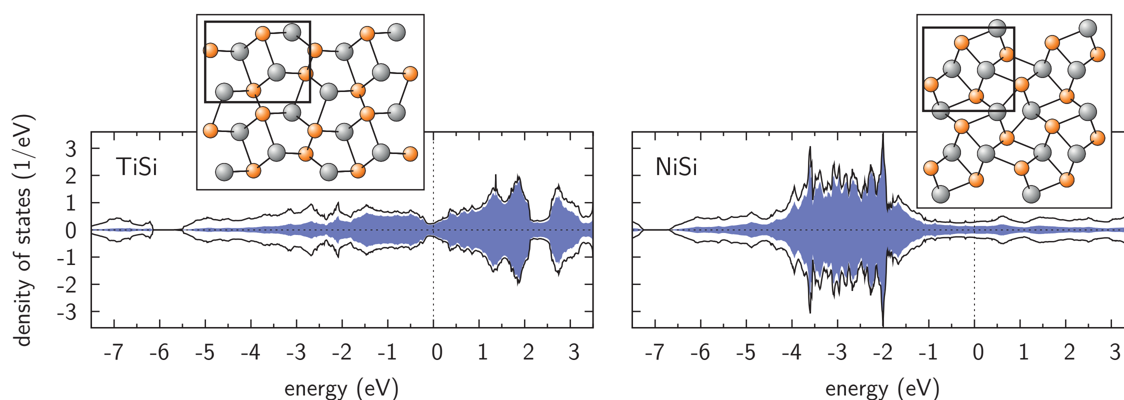

Figure 3.12 – TiSi in B27 structure (left) and NiSi in B31 structure (right). Shown are the total DOS (black lines), its projections onto the TM 3*d* orbitals (blue shaded areas), and characteristic views of the atomic structures. Gray circles depict the TM atoms, and smaller orange circles the Si atoms. The black rectangles indicate the orthorhombic unit cells.

fluctuability of the localized magnetic moments (0.45 μ_B per Cr in the FM phase) and agrees with the general view of CrSi as being a weak Pauli paramagnet [111, 177], especially at room temperature.

The FM phase in MnSi is found to be far more stable, with a NM-FM energy splitting of 61 meV per f.u. Interestingly, this compound is predicted to be half-metallic in this phase: In the majority spin channel, the Fermi energy lies in the small indirect band gap (0.23 meV calculated width in the DOS), close to the "VBM," while the minority spin channel behaves metallic. Consequently, the magnetic moment takes an integer value (1 μ_B per f.u.). This remains the case for lattice constants ranging from approximately 4.49 to 4.61 Å. For larger lattice constants, one finds a sudden transition to a higher spin state, in which the total magnetic moment approaches 2 μ_B per f.u. (cf. Fig. 3.9, inset).

FeSi is NM in the presented zero-temperature calculations, in agreement with previous theoretical work [116, 161, 186, 187]. It shows signs of ferromagnetism for increased lattice constants, but this magnetic configuration remains about 30 – 35 meV per f.u. higher in energy than the NM solution and thus is only metastable. It is difficult to extract the exact DFT energy of the FM state because of a NM-FM jump occurring very close to the equilibrium position (cf. Figs. 3.9 and 3.13; equivalently, Fig. 1(d) in Ref. [161]). For the same reason, it is only possible to give an upper bound for the magnetic moment of 0.92 μ_B per f.u. for the FM state (cf. Fig. 3.9). The band gap has a width of 0.16 eV according to the author's GGA calculations, which agrees roughly with previously reported LDA values [116, 186, 187], but is too large when compared to values derived from recent experiments [178, 179, 184, 185]. Note that usually band gaps are *underestimated* by conventional DFT. Dynamical correlations accounted for in LDA+DMFT (dynamical mean field theory) calculations reduce the width of the band gap by approximately a factor of 2 [116].

Since magnetic properties are a delicate issue and can significantly depend on the pseudopotential, the author checked the agreement of his CrSi, MnSi, and FeSi USPP results with LAPW calculations. For CrSi, a total magnetic moment of 0.44 μ_B per f.u. is found, which is in line with the pseudopotential result (cf. Table 3.3). As expected from the presence of the band gap, the integer magnetic moments for MnSi and FeSi are reproduced as well. Especially, the half-metallic character of MnSi is *no* artifact of the pseudopotential approach.

Dieses Werk ist copyrightgeschützt und darf in keiner Form vervielfältigt werden noch an Dritte weitergegeben werden.
Es gilt nur für den persönlichen Gebrauch.

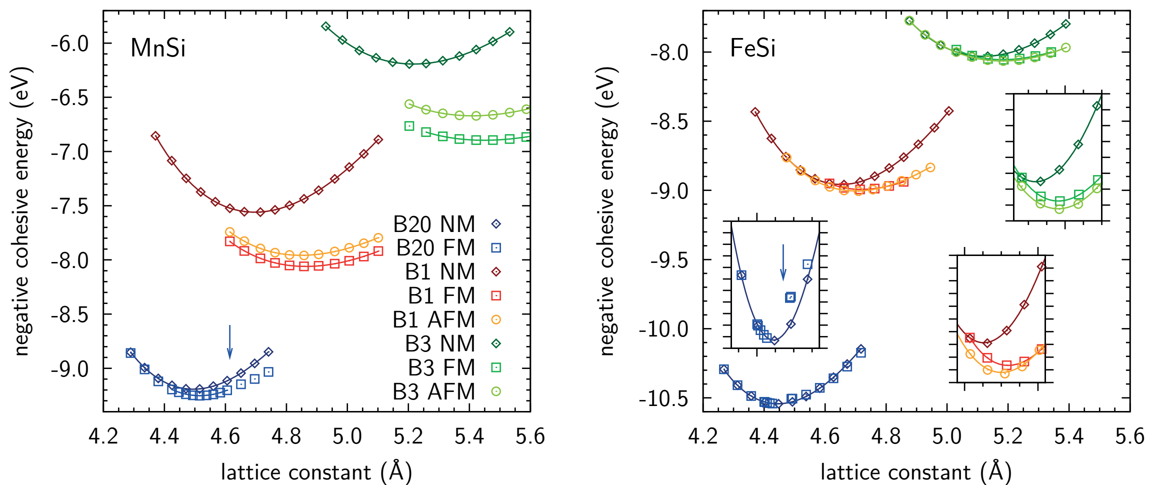

Figure 3.13 – Negative cohesive energies per f.u. as functions of the lattice constant for MnSi (left) and FeSi (right). Different structures [B20 structure, B1 (rock-salt structure) and B3 (zinc-blende structure)] are compared as well as different magnetic configurations (NM, FM, and AFM being represented by diamonds, squares, and circles, respectively). The insets show magnifications around the respective equilibrium lattice constant provided to clarify small energy differences. The arrows mark kinks in the B20-FM energy values, which arise because of spin transitions in DFT (cf. Fig. 3.9, inset, on page 64).

3.3.5 MnSi and FeSi in different crystal structures

In Ref. [120], calculated cohesive energies for bulk MnSi in different crystal structures have been presented. Among the studied structures it has been confirmed that the B20 structure indeed leads to the highest (that is, most stable) energy, followed by the CsCl (B2), the WC (tungsten carbide), the NiAs, and the rock-salt (B1) structures with decreasing stability.

In this section, the focus lies, in addition to the B20 structure, on the rock-salt and the zinc-blende (B3, not studied in Ref. [120]) structures. As mentioned above, both can be derived by using Eqs. (3.3) for special Wyckoff parameters: $u_{\mathrm{TM}} = 1/4$ and $u_{\mathrm{Si}} = 3/4$ give the rock-salt structure, while $u_{\mathrm{TM}} = 0$ and $u_{\mathrm{Si}} = 1/4$ correspond to the zinc-blende structure. The coordination is sevenfold, sixfold, and fourfold in the B20, B1, and B3 structure, respectively.

Figure 3.13 shows calculated negative cohesive energies for MnSi and FeSi in the three mentioned structures. Moreover, different magnetic configurations have been considered. For the B20 structure, the NM case and a FM spin alignment are shown, while for the B1 and B3 structures the results of an AFM configuration[12] are presented in addition. The different energy scales of structural and magnetic aspects become very clear from this figure, the latter being a small correction to the former.

For MnSi, the B20 structure with a FM spin alignment has the highest cohesive energy, followed by the NM case. The B1 structure is less stable, and the B3 structure is even less stable than the B1 structure. The equilibrium lattice constant increases from B20 over B1 to B3. For the latter two structures, a FM solution is most favorable, followed by the AFM ordering and the NM case. While the NM-FM energy difference is relatively small for the

[12] As an example, the AFM ordering between different (001) planes is shown. Note that in such cubic compounds several different AFM configurations are possible, like (110) or (111) planes. Moreover, no additional optimization of the cell parameter in z direction was performed.

Dieses Werk ist copyrightgeschützt und darf in keiner Form vervielfältigt werden noch an Dritte weitergegeben werden.
Es gilt nur für den persönlichen Gebrauch.

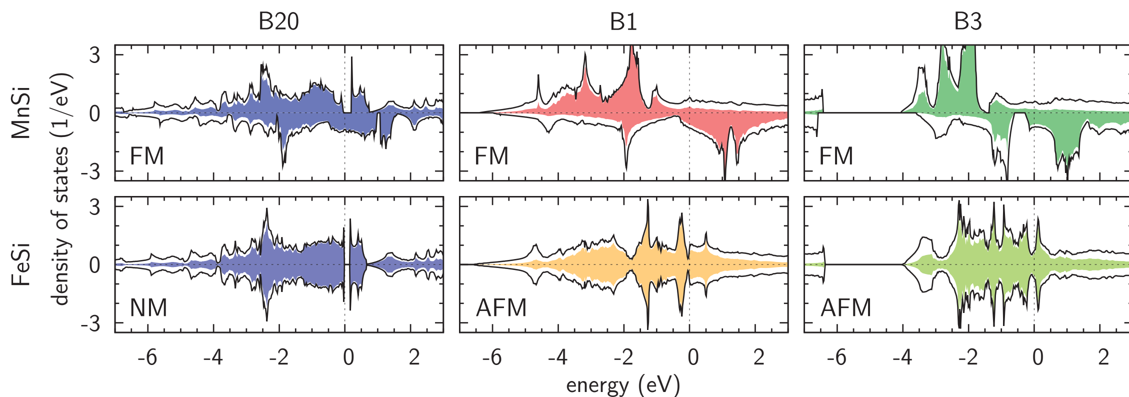

Figure 3.14 – Spin-resolved electronic structure of MnSi (upper row) and FeSi (lower row) in different crystal structures [B20, B1 (rock-salt structure) and B3 (zinc-blende structure)]. Black lines indicate the total DOS per f.u., while shaded areas indicate the projections onto the TM 3*d* orbitals. The colors refer to the curves in Fig. 3.13.

B20 structure, it is quite large for B1 and even larger for B3. Similarly, the AFM-FM energy difference increases from B1 to B3. The equilibrium lattice constant is found to be always smaller in the NM case than for solutions with finite magnetic moment, especially in the B1 and B3 structures.

For FeSi, the situation looks very similar at first sight. However, while the structural energy sequence is qualitatively the same, significant differences arise concerning the different magnetic cases. In the B20 structure, the NM solution has the highest stability. (Note that the leftmost FM data points in Fig. 3.13 also correspond to results with vanishing spin polarization.) In general, the NM-FM energy difference is much smaller than for MnSi; for all three structures, the magnetic moments vanish for lattice constants that are slightly smaller than the equilibrium lattice constant, and, consequently, the energy curves coincide. In contrast to MnSi, the AFM ordering is the most stable magnetic configuration in the B1 and B3 structures. Indeed, one expects a magnetic solution to become more and more beneficial (instead of vanishing magnetic moments, NM) for an increasing lattice constant, since the limiting case is an arrangement of isolated atoms with individual magnetic moments following Hund's rules.

The B20-FM energy data points for FeSi in Fig. 3.13 (right panel) clearly show a kink, which is related to a spin transition $0\ \mu_B \rightarrow 1\ \mu_B$ per f.u. in DFT (cf. Fig. 3.9, total magnetic moment curves, on page 64). A similar kink exists for MnSi, although it is not easy to see in Fig. 3.13, corresponding to the transition $1\ \mu_B \rightarrow 2\ \mu_B$ per f.u. The author confirmed the existence of the spin transition for MnSi by all-electron LAPW calculations, which proves that it is not an artifact of the pseudopotential approach. The kink in the energy curves can be inconvenient for the derivation of the bulk modulus, because a fitting beyond the transition point will lead to arbitrarily wrong results that strongly depend on the chosen lattice constant interval. This might appear trivial; however, for bcc-Fe the neglect of a similar spin-transition issue has lead to a large scatter of the published theoretical bulk moduli, a fact that was pointed out just recently [188].

The DOS for MnSi and FeSi in the three crystal structures are shown in Fig. 3.14. It is noteworthy that only the B20 structure manages to open the band gap. Especially, the experimentally measured band gap in FeSi does *not* arise for the rock-salt structure, neither

Dieses Werk ist copyrightgeschützt und darf in keiner Form vervielfältigt werden noch an Dritte weitergegeben werden.
Es gilt nur für den persönlichen Gebrauch.

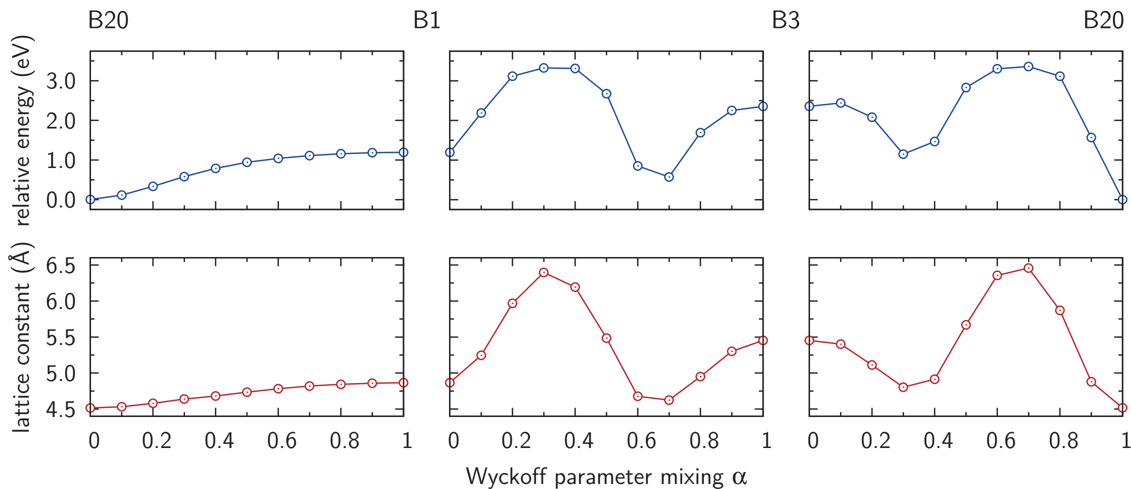

Figure 3.15 – Structural transformations between B20, B1 (rock-salt), and B3 (zinc-blende) structures in MnSi. Energy minima (upper row) and equilibrium lattice constants (lower row) for different structural mixing parameters α are shown. Only a FM spin alignment was considered (including possible NM situations), which is definitely the ground state at least for each $\alpha = 0$ and $\alpha = 1$. Energies are given per f.u. and relative to the B20 ground state energy.

in the shown AFM configuration, nor in the NM or the FM case, although there is a clear minimum in the DOS around the Fermi energy for the AFM and the NM case. It is therefore possible to conclude that the band gap is, in general, related to the sevenfold coordination arising in the B20 structure, an aspect that has already been mentioned above in the context of Fig. 3.10. The opening of the band gap at the Fermi energy is an additional driving force behind the distortion from the rock-salt structure to the B20 structure, at least for MnSi and FeSi, which are both particularly stable compounds (as one can see from their formation enthalpies on page 65).

The DOS for MnSi in zinc-blende structure agrees with results recently published by Zhang *et al.* [161]. One should note, however, that these authors missed the possibility of different magnetic configurations and discussed only FM spin alignments. As we can see here, FeSi, for example, prefers an AFM configuration if grown pseudomorphically in zinc-blende structure.

Structural transformation paths in MnSi

It has been mentioned above that the three cubic crystal structures B1, B3, and B20 can all be derived from Eqs. (3.3). This means, on the other hand, that there is a continuous, symmetry-conserving connection between these three structures.[13] Thus, one can define three linear paths for the Wyckoff parameters, controlled by a mixing parameter α, such that the resulting structures form a closed loop along B20 – B1 – B3 – B20:

$$u_x(\alpha) = \alpha\, u_x^{\mathrm{f}} + (1-\alpha)\, u_x^{\mathrm{i}} \,,$$

where u_x^{i} and u_x^{f}, $x \in \{\mathrm{Mn}, \mathrm{Si}\}$, are the aforementioned initial and final Wyckoff parameters for the different structures (cf. Sec. 3.3.1 on page 59).

[13] Both B1 and B3 crystal structures have a higher symmetry than the B20 crystal structure. The symmetry groups of the former contain that of the latter (cf. Table 3.5).

Dieses Werk ist copyrightgeschützt und darf in keiner Form vervielfältigt werden noch an Dritte weitergegeben werden.
Es gilt nur für den persönlichen Gebrauch.

Table 3.5 – Space and point groups of MnSi in different crystal structures. The image indicates the hierarchy of proper subgroups: $T \subset T_d \subset O_h$.

Structure	Space group	Point group (Schönflies)
B1	$Fm\bar{3}m$	O_h
B3	$F\bar{4}3m$	T_d
B20	$P2_13$	T (chiral)

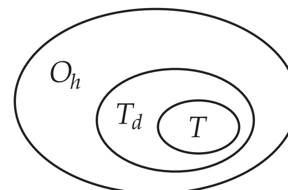

For several structures along these paths, equilibrium lattice constants and energy minima have been calculated for fixed atomic positions.[14] The results are shown in Fig. 3.15. The energies for $\alpha = 0$ and $\alpha = 1$ agree with those shown in Fig. 3.13. One can see that the transformation between the B20 and the B1 structure (i.e., the aforementioned distortion in [111] direction) is smooth and without kinetic hindrances: Energy and lattice constant are monotonic functions of the mixing parameter α. This is not the case for the paths B1 – B3 and B3 – B20, where energy barriers with heights of almost 3.5 eV per f.u. (relative to the energy of the B20 structure) block the linear transformation. Both maxima correspond to very open structures with only threefold coordination. Moreover, there are two local minima close to the B3 structure that correspond to intermediate, metastable structures with sevenfold (B1 – B3, $\alpha \approx 0.7$) and sixfold (B3 – B20, $\alpha \approx 0.3$) Mn-Si coordination. The total energy curves and the lattice constant curves have a similar shape. In conjunction with Fig. 3.13 one can conclude from these findings that MnSi (and also FeSi) obviously prefers a high coordination of its constituents, which is a typical behavior of metallic systems.[15] Furthermore, we see here that both B1 and B3 are not metastable, but even *unstable* structures, since the energy curves show no corresponding local minima. Thus, small atomic displacements will induce a structural transformation to the B20 ground state or to one of the aforementioned intermediate, metastable structures.

[14] The minimal values for each data point have been deduced from a total energy fit (using 11 different lattice constants) to the Murnaghan equation of state, Eq. (3.1). Cubic cells have been used.

[15] On the other hand, the sevenfold coordination marks the optimum: The even higher (i.e., eightfold) coordinated CsCl (B2) structure is slightly less stable than the B20 structure [120].

Dieses Werk ist copyrightgeschützt und darf in keiner Form vervielfältigt werden noch an Dritte weitergegeben werden.
Es gilt nur für den persönlichen Gebrauch.

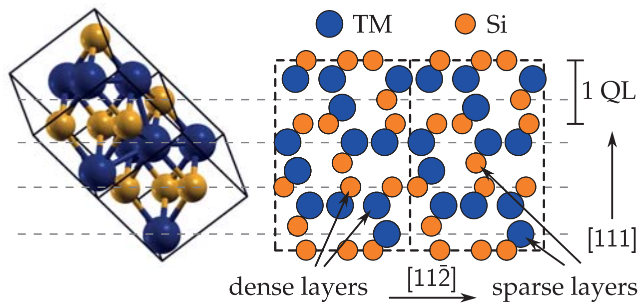

Figure 3.16 – Two simple cubic unit cells (left) showing the B20 structure and the buildup of the dense and sparse layers in [111] direction. The hexagonal cell (indicated to the right) contains 24 atoms and repeats itself after 12 layers (three QLs) in [111] direction. Small orange (big blue) spheres depict Si (TM) atoms.

3.4 The effect of epitaxial strain

In this section, we shall investigate the influence of biaxial strain on structural, electronic, and magnetic properties of bulk TM-Si compounds, focusing on expitaxial strain as induced by a Si(111) substrate. We will see that MnSi and FeSi respond most interestingly to biaxial strain: While the magnetic ordering temperature is raised considerably in the former, the latter undergoes a transition from a NM semiconductor to an almost half-metallic weak ferromagnet [16]. Moreover, a considerable phonon softening due to strain is found for MnSi.

3.4.1 The strained bulk material as limit of thick epitaxial films

For epitaxial films of about 20 nm thickness, a value typically used in experiments [108, 110, 189], surface, interface, and confinement effects are minor and the film properties are dominated by a strained-bulk behavior. Extensive research in the past[16] has established that epitaxial B20 TM monosilicide films on Si(111) will grow in [111] direction, since their hexagonal unit cell parameters a_{hex} fit closely the Si(111)-($\sqrt{3} \times \sqrt{3}$) surface lattice constant if Si[01$\bar{1}$] $\parallel$ TM-Si[11$\bar{2}$]. It will be distorted in the (111) (i.e., lateral) plane, and the small misfit strain is compensated by an accommodation of the unit cell height c_{hex} and of the atomic coordinates (relaxation).

The DFT-PBE Si(111)-(1 × 1) lattice constant calculated in this thesis (see also Table 3.1 on page 50) is 5.468 Å/$\sqrt{2}$ = 3.866 Å, deviating by +0.7% from the experimental value of 3.840 Å. This translates to a Si(111)-($\sqrt{3} \times \sqrt{3}$) lattice constant of $a_{\text{Si(111)}}^{\sqrt{3}\times\sqrt{3}} = 6.697$ Å (6.650 Å experimentally). The simple cubic unit cells of the TM monosilicides can be transformed to a hexagonal cell with the [111] direction pointing along the z axis (cf. Fig. 3.16): $a_{\text{hex}} = \sqrt{2}a_{\text{cub}}$, $c_{\text{hex}} = \sqrt{3}a_{\text{cub}}$. From Table 3.3 it follows that $a_{\text{hex}} = 6.491$ (6.546), 6.387 (6.446), and 6.286 (6.354) Å for CrSi, MnSi, and FeSi, respectively. (Experimental values are given in parentheses.) Thus, DFT-PBE overestimates the Si lattice constant while giving slightly underestimated TM-Si lattice constants. As a consequence, the lattice mismatch between the Si(111) substrate and a TM-Si film will be overestimated, and the in-plane tensile strain in the thin film will be higher in the calculations than in reality. The calculated (experimental) lattice mismatches are 3.2% (1.6%), 4.9% (3.2%) and 6.5% (4.7%) for CrSi, MnSi, and FeSi, respectively. To assess the significance of these deviations (for example, in how far the phenomena related to strain effects will also be overestimated), the author studied the influence of biaxial strain over a large lattice constant interval (see below).

[16] The reader is referred to a vast range of literature here; for instance, Refs. [108, 110, 114, 189–195].

Dieses Werk ist copyrightgeschützt und darf in keiner Form vervielfältigt werden noch an Dritte weitergegeben werden.
Es gilt nur für den persönlichen Gebrauch.

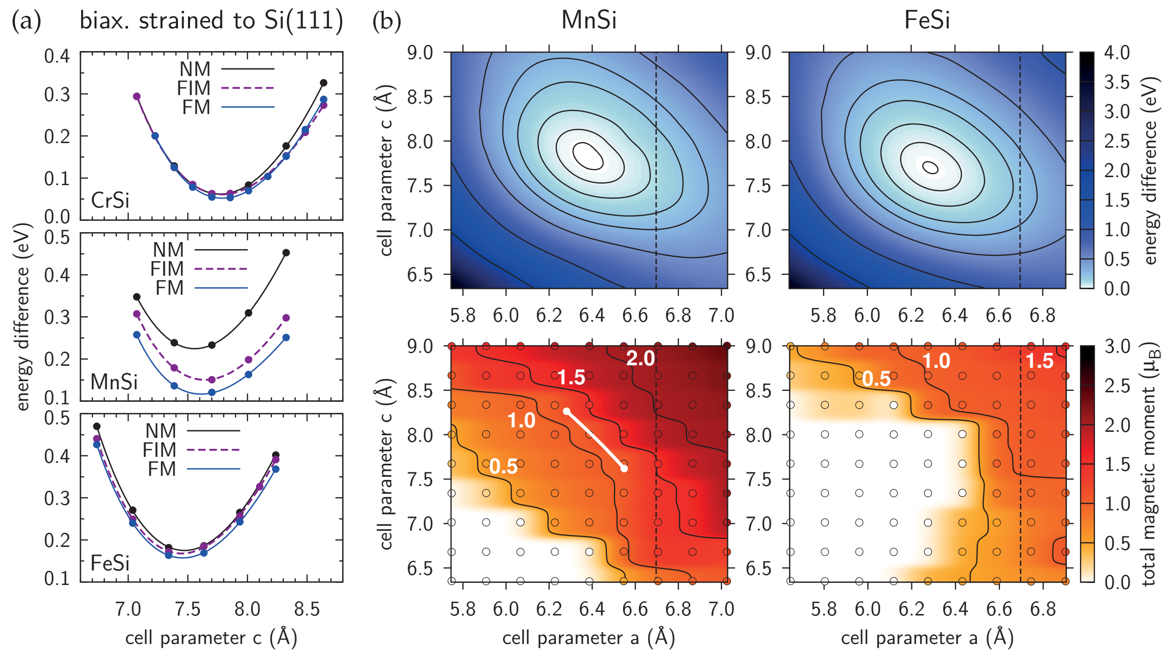

Figure 3.17 – (a) Total energy curves (per f.u.) of different magnetic configurations (NM, FIM with $q = \pi/3$, and FM) in CrSi, MnSi, and FeSi under biaxial strain as a function of the hexagonal unit cell height c. The lateral lattice constant has been chosen such as to fit the Si(111) surface. The energy values are differences with respect to the corresponding strain-free bulk structure. (b) Energetic and magnetic maps of MnSi and FeSi as functions of the hexagonal cell parameters a and c. Color encoded, the energy difference with respect to the corresponding strain-free bulk structure (upper row) and the total magnetic moment (lower row) per f.u. are shown. The black circles indicate the positions of calculated values and are filled with the corresponding color; the remaining area is interpolated. The vertical dashed lines mark the Si(111)-($\sqrt{3} \times \sqrt{3}$) lattice constant [cf. panels (a)]. The white curve in the MnSi magnetic moment map indicates the parameter range for the rhombohedral unit cell that has been used in Ref. [196] according to Eqs. (3.10), where the magnetic moment has been found to be constant (1 μ_B per f.u.).

In the hexagonal unit cell (cf. Fig. 3.16), the z axis coincides with the $[111]$ direction of the simple cubic unit cell. Along this direction, the structure is repeated after 12 individual layers. Four subsequent layers can be grouped into one quad-layer (QL), which then consists of a Si-dense, TM-sparse, Si-sparse, and TM-dense layer [114]. In the unstrained bulk material, atoms in sparse and dense layers are all symmetry equivalent.

The calculations which provided the results shown in Fig. 3.17 were carried out using such hexagonal unit cells. For each pair of cell parameters (a, c) a full relaxation of the internal atomic coordinates was performed. Figure 3.17(a) shows total energy curves for different values of the cell height c at fixed lateral cell parameter $a = a^{\sqrt{3}\times\sqrt{3}}_{\mathrm{Si}(111)}$ for CrSi, MnSi, and FeSi. In order to get an impression of the spin stiffness, the author studied different spin configurations within these hexagonal unit cells. It was assumed that the TM magnetic moments in one and the same layer are equal, while those of different layers were allowed to have a different magnitude and, possibly, an antiparallel orientation. This seems reasonable, since the application of strain lifts the symmetry equivalence between sparse and dense layers for TM and Si atoms. In addition to the NM case and the FM ordering, a partially compensating "ferrimagnetic" (FIM) pattern was investigated, which emerges from a cosinelike starting configuration of the TM magnetic moments,

Dieses Werk ist copyrightgeschützt und darf in keiner Form vervielfältigt werden noch an Dritte weitergegeben werden.
Es gilt nur für den persönlichen Gebrauch.

$$m^{\ell}_{\mathrm{TM}} = m^{0}_{\mathrm{TM}} \cos(q\ell), \tag{3.8}$$

where ℓ denotes the TM layer index, counting in [111] direction and starting with zero for a TM-sparse layer (cf. Fig. 3.16). For the moment, let us restrict the discussion to the case of $q = \pi/3$, for which the modulation fits into a single hexagonal unit cell. Note that this initial pattern actually *does* lead to a net total magnetic moment in practice, in contrast to a perfect AFM ordering, even though the mean of the cosine vanishes. The reason for this is simply that the cosine is superimposed by the sparse-dense layer structure, and, in addition to the different TM density, TM-sparse and TM-dense layers can bear different local magnetic moments, especially if biaxial strain is applied.

As one can see from Fig. 3.17(a), the FIM configuration ($q = \pi/3$) is always higher in energy than the FM configuration. An exception is CrSi at high vertical expansion, where the FIM ordering is lowest in energy. However, at the equilibrium height of the cell (c), the FM ordering is always lowest, even for CrSi. Especially, this means that the NM, semiconducting FeSi becomes a ferromagnet under epitaxial strain. The distances between NM, FIM, and FM curves and equilibrium energies are largest for MnSi and only small for CrSi (≈ 10 meV/f.u.) and FeSi (NM-FM 17.7 meV/f.u., FIM-FM 10.5 meV/f.u.). On this basis one can speculate that the Curie temperature will be very low for the latter two. The equilibrium heights of the hexagonal cells are 7.79, 7.61, and 7.46 Å for CrSi, MnSi, and FeSi in their FM phase, respectively. From this follows the height of a single QL to be about 2.4 – 2.6 Å in bulk, depending on the material. Thus, a thin film of 20 nm thickness consists of approximately 310 – 330 layers of the TM silicide.

On the basis of the preceding insights, MnSi and FeSi appear to be most interesting. For both of them, experimental data of samples with a high degree of structural quality exists in the literature. Hence, the discussion will be focused on MnSi and FeSi in the following. In Fig. 3.17(b), results for a wide range of planar lattice constants a and cell heights c are shown: Color-encoded maps display the total energy relative to the ground state without strain and the total magnetic moment (both per f.u.). The corresponding calculations have been carried out with considerable care: For each data point, a FM calculation has been compared to a NM calculation. Sometimes the FM calculations showed the tendency to converge to metastable solutions with finite magnetic moment, while the solution of the corresponding NM calculation was actually lower in energy. This has been taken into account by assigning a magnetic moment of zero to points with only metastable magnetic solutions. A further, similar complication was that for some points the calculated magnetic moments did not fit seamlessly into their neighborhood. In this case, additional calculations with reasonably constrained total moments have been performed, followed by calculations without constraints which started from the previously obtained potential. Usually, the new energy turned out to be smaller and the original result was replaced. However, this procedure did not work for all points; for example, the area around the small feature on the lower right side in the FeSi magnetic moment map was stable against all checks. The FIM configuration has been examined at some points, especially at the corners of the map and along $a^{\sqrt{3}\times\sqrt{3}}_{\mathrm{Si(111)}}$, and nowhere found to be lowest in energy.

In both energy maps, the minimum is consistent with the ground state cell parameters a_{hex} and c_{hex} given above. Obviously, there are no other local minima for $c(a)$ than the ground state (apart from metastable magnetic configurations). The magnetic maps in Fig. 3.17(b)

Dieses Werk ist copyrightgeschützt und darf in keiner Form vervielfältigt werden noch an Dritte weitergegeben werden.
Es gilt nur für den persönlichen Gebrauch.

Table 3.6 – Volume expansion $V^{\mathrm{PBE}}_{\mathrm{Si(111)}}$ and total magnetic moment $M^{\mathrm{PBE}}_{\mathrm{Si(111)}}$ of different TM monosilicide bulk structures laterally strained to the Si(111) surface lattice constant $a^{\sqrt{3}\times\sqrt{3}}_{\mathrm{Si(111)}}$. The strain-free volume $V^{\mathrm{PBE}}_{\mathrm{GS}}$ has been determined from Table 3.3. In parentheses, localized magnetic moments at the TM sparse/dense atoms are listed. All values are given per f.u.

	$V^{\mathrm{PBE}}_{\mathrm{GS}}$ (Å^3)	$V^{\mathrm{PBE}}_{\mathrm{Si(111)}}$ (Å^3)	$M^{\mathrm{PBE}}_{\mathrm{Si(111)}}$ (μ_B)
TiSi	30.73	31.51 (+2.5%)	0.00
VSi	26.54	26.54 (+0.0%)	0.00
CrSi	24.18	25.22 (+4.3%)	0.63 (0.64/0.72)
MnSi	23.03	24.63 (+7.0%)	1.50 (1.22/1.85)
FeSi	21.96	24.13 (+9.9%)	0.99 (0.57/1.30)
CoSi	21.73	23.84 (+9.7%)	0.00
NiSi	23.01	24.01 (+4.3%)	0.00

show that for compressive strain the magnetic moment tends to decrease, whereas for tensile strain it increases, obviously even beyond the value it takes on for the Si(111) surface lattice constant. The NM region is much larger for FeSi than for MnSi. For FeSi, the area with finite magnetic moment is sickle shaped. However, in the vicinity of the NM region, the energetic stability of these moments is very low. The maps demonstrate that the results are stable against small variations of the surface lattice constant; especially, using the experimental value for Si(111) would not lead to significant changes. Thus, the slightly overestimated lattice mismatch proves to be irrelevant.

Let us now compare the theoretical results to experimental data from the literature. As already mentioned, a FM ground state is predicted for biaxially strained FeSi, with a total magnetic moment of 0.99 μ_B per f.u. Since FeSi is semiconducting in the unstrained bulk case, a transition to a metallic, magnetic phase has to occur for a critical value of the biaxial tensile strain. Furthermore, one finds a volume expansion of 9.9% (cf. Table 3.6). Recently, the volume expansion in epitaxial FeSi thin films of 20 nm thickness on Si(111) was experimentally measured by Porter *et al.* [110]. Within the error bars, the authors found a volume difference between polycrystalline films, which they concluded to be a strain-free reference, and epitaxial films of approximately 10%. A similar effect was found for $Fe_{0.5}Co_{0.5}Si$, together with an increased Curie temperature (33%) and a higher saturation magnetization (cf. Fig. 4 in Ref. [110]). Their FeSi result agrees even quantitatively with those theoretically obtained within this thesis. Although the alloy $Fe_{0.5}Co_{0.5}Si$ has not been studied explicitly here, it is possible to deduce from the DFT results for FeSi and CoSi that the intermediate alloy will behave similarly with respect to the volume expansion. The electronic properties should be somewhere in between: CoSi is already weakly metallic without tensile strain and provides additional electrons to the distorted, metallic FeSi, so one can expect strained $Fe_{0.5}Co_{0.5}Si$ to be a metal as well. From their transport measurements on FeSi, where strained and unstrained material are being compared, one could deduce that the band gap prevails, although becoming narrower. However, the overall resistivity they observe is quite small. Older ultraviolet photoelectron spectroscopy studies of FeSi thin films on Si(111) were unable to resolve a gap and found a metallic state [197]. The DOS for epitaxial FeSi (cf. Fig. 3.18) indicates a metallic behavior with a high degree of spin polarization at the Fermi energy. For

Dieses Werk ist copyrightgeschützt und darf in keiner Form vervielfältigt werden noch an Dritte weitergegeben werden.
Es gilt nur für den persönlichen Gebrauch.

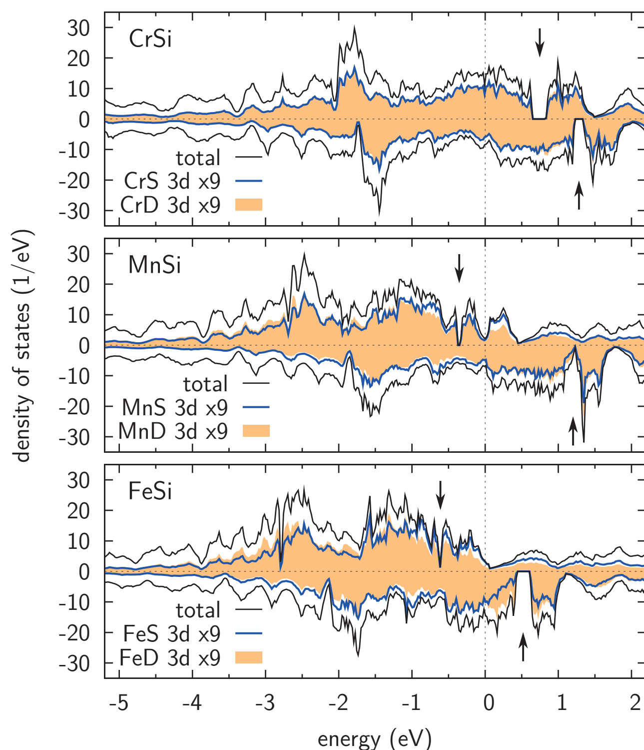

Figure 3.18 – Spin-resolved total DOS (black lines) per hexagonal unit cell for bulk CrSi, MnSi, and FeSi (from top to bottom) under the influence of biaxial strain as induced by the Si(111) surface. The orange shaded areas (blue lines) show projections onto sparse (dense) TM atoms. The respective Fermi energies have been chosen as reference in all three cases. The remnants of the characteristic B20 band gap are marked by the black arrows.

$Fe_{0.5}Co_{0.5}Si/Si(111)$, a metallic conductivity has been observed in experiment [110], which proves the correctness of the aforementioned expectation.

For MnSi, a volume expansion of 7% as well as an increase of the magnetic moment by 50% can be seen (cf. Fig. 3.17 and Table 3.6). Interestingly, one finds in addition a significant stabilization of the FM alignment: The energy splitting $E_{\text{FIM}} - E_{\text{FM}}$ between the FIM magnetic ordering ($q = \pi/3$) and the FM ordering is 18.5 meV in the case of bulklike, unstrained MnSi. Due to biaxial strain this value increases by 88% to 34.7 meV. The author also looked at a third configuration: It is possible to produce a perfectly compensating AFM ordering with vanishing total magnetic moment by flipping the moments with QL periodicity (two Mn layers up, two Mn layers down, etc.):

$$m^{\ell}_{\text{Mn}} = m^{0}_{\text{Mn}} \,\text{sgn}\{\cos[q(\ell - 1/2)]\}, \quad q = \pi/2. \tag{3.9}$$

In this case, however, a vertically enlarged hexagonal cell with 24 layers is necessary. The different magnetic configurations are visualized in Fig. 3.19. The energy splitting $E_{\text{AFM}} - E_{\text{FM}}$ between this QL AFM texture and the FM ground state is 33.2 meV per f.u., which means that it is more unfavorable than the FIM configuration. Under strain this value increases by 85% to 61.5 meV. Following the thought that roughly

$$T_{\text{C}} \sim |E_{\text{FM}} - E_{\text{AFM}}| \sim |E_{\text{FM}} - E_{\text{FIM}}|,$$

this means that the Curie temperature should show a significant increase. Indeed, Karhu *et al.* [108,109] observed such a trend in their MnSi/Si(111) films. While they found only a small increase of the saturation magnetization (maximally 8% according to Fig. 8(b) in Ref. [108]), they reported a value of $T_{\text{C}} \approx 43$ K for films of 10 nm thickness and above [108, 109]. This corresponds to an increase of about 46%. Thus, the DFT-PBE exchange-correlation functional

Dieses Werk ist copyrightgeschützt und darf in keiner Form vervielfältigt werden noch an Dritte weitergegeben werden.
Es gilt nur für den persönlichen Gebrauch.

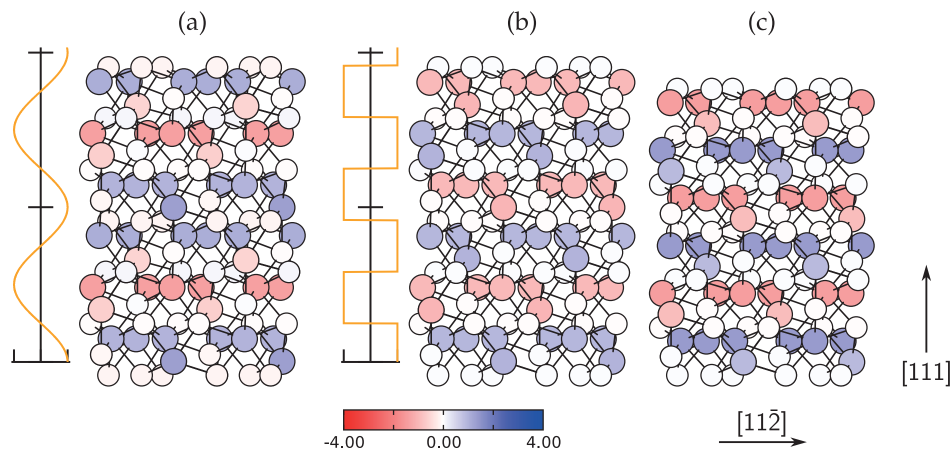

Figure 3.19 – Different metastable antiparallel magnetic configurations in MnSi. Small, almost white (big, colorful) spheres depict Si (Mn) atoms. The colors represent the local magnetic moment (in μ_B) at the different atoms. (a) Cosine-shaped pattern according to Eq. (3.8) for $q = \pi/3$ in strain-free MnSi. (b) Perfectly compensating AFM ordering with QL steps according to Eq. (3.9) in strain-free MnSi. (c) As (b), but for MnSi epitaxially strained to fit the Si(111) surface. Note the different magnetic moment magnitude for sparse and dense atoms, which reflects the strain-induced symmetry break.

is capable of predicting the correct trend, while one cannot expect quantitative agreement, since (i) nonlocal electronic correlations are not included and (ii) a precise calculation of T_C is beyond the scope of this thesis.

Another important consequence of this behavior is that MnSi obviously *cannot* be fully described as a simple Heisenberg ferromagnet with localized moments. Typically, the exchange constants in a Heisenberg model are decreasing functions of the interatomic distance; thus, an increased volume and increased average Mn-Mn distances should lead to a weaker magnetic coupling. However, this is in contrast to the theoretical results shown above and to the experimental findings, and points to the importance of the itinerant exchange for the magnetic ordering in MnSi.

As expected from the noninteger total magnetic moment, the Fermi energy has moved out of the half-metallic gap in which it is located for strain-free MnSi (cf. Fig. 3.18). Instead, it shifts to the next stable DOS valley in the majority channel, transferring $1/4$ electron per f.u. from the minority channel to the majority channel. The feature above the Fermi energy in the majority channel, which can take $1/2$ electron per f.u. and spin channel according to the FeSi and CoSi panels in Fig. 3.10 on page 66, is split and half filled. For strained FeSi, it is filled completely, and the Fermi energy sits at the same position in the majority channel as for strain-free CoSi. The DOS for strained CrSi shows only small differences compared to the strain-free case. Remnants of the band gap can still be seen for all three compounds in both spin channels.

It is interesting to look for a similar strain effect also in bulk TiSi, VSi, CoSi, and NiSi. However, these materials show no signs of FM order under biaxial strain, just like in the case of unstrained bulk. Hence, the respective values given in Table 3.6 have been derived using NM calculations. Furthermore, the author checked the presented USPP results for strained bulk material with all-electron LAPW calculations. The all-electron method gives total magnetic moments of 1.46 μ_B for MnSi and 1.00 μ_B for FeSi (cf. the USPP results in

Dieses Werk ist copyrightgeschützt und darf in keiner Form vervielfältigt werden noch an Dritte weitergegeben werden.
Es gilt nur für den persönlichen Gebrauch.

Table 3.6) and densities of states that are very similar to those shown in Fig. 3.18. Hence, one can confidently rule out that the theoretical observations are just pseudopotential artifacts: The strain-increased (strain-induced) magnetic moment is also seen in LAPW results for MnSi (FeSi).

The strain-induced symmetry break can be observed by looking at the localized magnetic moments, e.g., of the TM atoms, as listed in Table 3.6 or visualized for MnSi in Fig 3.19(c). For Si(111)-strained CrSi, MnSi, and FeSi, the localized moments at the sparse and dense atoms are not equal anymore and larger than those in the unstrained material. In particular, the magnetic moment at the dense atoms is larger than that at the sparse atoms. At the Si atoms, an antiparallel moment of approximately $-0.07\ \mu_B$, $-0.19\ \mu_B$, and $-0.12\ \mu_B$ is induced for CrSi, MnSi, and FeSi, respectively, which reduces the total magnetic moment. Such induced antiparallel moments already exist without strain and are a phenomenon that can be observed in other TM compounds as well, for example, in Heusler alloys [198]. The inequivalence can also be seen in the structural properties, e.g., in the distances between the TM atoms, which, neglecting the Si atoms, form a trillium lattice [156] of sixfold coordination, as mentioned above. In the unstrained case, all TM-TM distances are the same: 2.77 Å for MnSi and 2.73 Å for FeSi. For MnSi (FeSi) subject to epitaxial strain as induced by a Si(111) substrate one finds: dense-dense intralayer 3.01 Å (2.92 Å); dense-dense interlayer 2.68 Å (2.66 Å); sparse-dense, crossing a Si-sparse layer 2.83 Å (2.84 Å); and sparse-dense, crossing a Si-dense layer 2.81 Å (2.85 Å). The behavior is very similar for MnSi and FeSi: All TM-TM distances increase, except the dense-dense interlayer distance. As a consequence, four different coupling constants are necessary if one wants to model this system by a nearest-neighbor Heisenberg Hamiltonian.

Karhu *et al.* studied the effect of biaxial strain on the uniaxial anisotropy in MnSi by using DFT (full-potential local-orbital method) and a rhombohedral unit cell with different values for the rhombohedral angle Ξ around $\pi/2$ [196]. They found no deviations of the total magnetic moment from the usual bulk value of 1 μ_B per f.u. This seems to be contradictory to the presented results at first sight. The equations

$$\begin{aligned} a_{\text{hex}}(\Xi) &= a_{\text{cub}}^{\text{MnSi}} \sin(\Xi) \sqrt{\frac{2\sqrt{3}}{\sqrt{[1+2\cos(\Xi)]^2 + 2\sin(\Xi)^2}}}, \\ c_{\text{hex}}(\Xi) &= a_{\text{cub}}^{\text{MnSi}} \sqrt{[1+2\cos(\Xi)]^2 + 2\sin(\Xi)^2}, \end{aligned} \tag{3.10}$$

with the MnSi lattice constant $a_{\text{cub}}^{\text{MnSi}} = 4.556$ Å used by these authors make it possible to connect their results to those discussed above. Their parameter range is displayed as a white line in the magnetic moment map of MnSi in Fig. 3.17(b) on page 75. Indeed, there is a complete agreement between both calculations: Around the white line, the magnetic moment is constant. The reason for this is the half-metallic gap predicted by DFT, in which the Fermi energy can move for some time due to biaxial strain before the total magnetic moment starts to change (cf. Fig. 3.10 on page 66).

3.4.2 Phonon spectrum of MnSi under the influence of biaxial strain

Studying the phonon spectrum of a material is not only interesting in itself, but also provides information on the dynamical stability of the studied structure. For instance, it is imaginable that a simulated material appears to be most stable in a certain crystal structure only because

Dieses Werk ist copyrightgeschützt und darf in keiner Form vervielfältigt werden noch an Dritte weitergegeben werden.
Es gilt nur für den persönlichen Gebrauch.

of external boundary conditions, like a fixed Bravais lattice or symmetry. In a larger supercell with more degrees of freedom, a different, more stable crystal structure might emerge. Such "instabilities" can become obvious from phonon calculations, since $\vec{q}$ vectors aside from the Γ point probe the relative motion of atoms in adjacent unit cells, especially for the acoustic phonon branches.

Here we will mainly look at the influence of epitaxial strain on the phonon spectrum of MnSi and the dynamical stability of the strained bulk structure. The results will certainly be transferable to the case of real film structures, although additional surface and interface phonons will arise in this case.

The phonon dispersion relations of MnSi single crystals in B20 structure have been measured very recently by Lamago *et al.* with inelastic neutron scattering [199]. They compared their experimental results to DFT-PBE calculations and found that the agreement improves if the calculations are carried out with a FM spin polarization.

In the calculations of the phonon band structures shown in the following, the density functional perturbation theory (DFPT) has been employed [200]. DFPT is a linear response approach to determine the dynamical matrices: The required Hessian of the Born-Oppenheimer energy surface (the so-called "matrix of interatomic force constants") is calculated from the ground state electron charge density $n(\vec{r},\{\vec{R}_I\})$ and from its linear response to distortions of the crystal geometry $\partial n(\vec{r},\{\vec{R}_I\})/\partial \vec{R}_J$. These quantities can be derived from a single unit cell. A different, very common technique to calculate the phonon spectrum of a solid is the so-called "frozen phonon" method, in which the frequencies of selected phonon modes are determined from energy differences arising in a perfectly equilibrated crystal structure due to explicit, small, periodic displacements of few atoms in supercells of different size.

The simple cubic unit cell of MnSi contains eight atoms and thus gives rise to 24 phonon modes. For the strained material, the author used a distorted rhombohedral unit cell, adapted to the optimized cell parameters given in the preceding section, with the same number of atoms. The dynamical matrices were calculated on a $4\times4\times4$ $\vec{q}$-point grid.[17] Subsequently, the phonon dispersions were derived using Fourier interpolation. It is possible to define phonon band characters from the eigenvectors $\vec{U}_s$ (the so-called "displacement patterns") of the dynamical matrix, for example,

$$\chi_s(\nu,\vec{q}) = \sum_\alpha U_s^\alpha(\nu,\vec{q})^2, \qquad 1 = \sqrt{\sum_{s,\alpha} U_s^\alpha(\nu,\vec{q})^2} \qquad \forall\ (\nu,\vec{q}),$$

where s labels the atoms and α the three spatial directions. These quantities indicate which atoms participate in the lattice vibration if a certain phonon mode is excited.

The results of the MnSi phonon calculations are shown in Fig. 3.20. The displayed band characters $\chi(\nu,\vec{q})$ have been summed up over atoms of the same element. The reason is simply that although all Mn atoms, for instance, are symmetry equivalent in the strain-free case, the displacement patterns for an arbitrary $\vec{q}$ are *not* equal for all Mn atoms. The band characters indicate an equal partitioning between Mn and Si atoms for the acoustic branches, just as expected: All atoms in one and the same unit cell vibrate in phase. Moreover, one can see that the phonon bands with dominating Mn character are lower in energy (and

[17] This is a very time-consuming process: Although it is sufficient to work with a single, small unit cell (in contrast to the large supercells arising in the frozen phonon approach), each irreducible phonon mode representation at each $\vec{q}$ point requires a *very* precisely converged SCF run. Symmetry reduces the $\vec{q}$-point grid used in this case to 11 $\vec{q}$ points. This leads to 208 SCF runs in total, and most of them are very hard to converge to the necessary accuracy.

Dieses Werk ist copyrightgeschützt und darf in keiner Form vervielfältigt werden noch an Dritte weitergegeben werden.
Es gilt nur für den persönlichen Gebrauch.

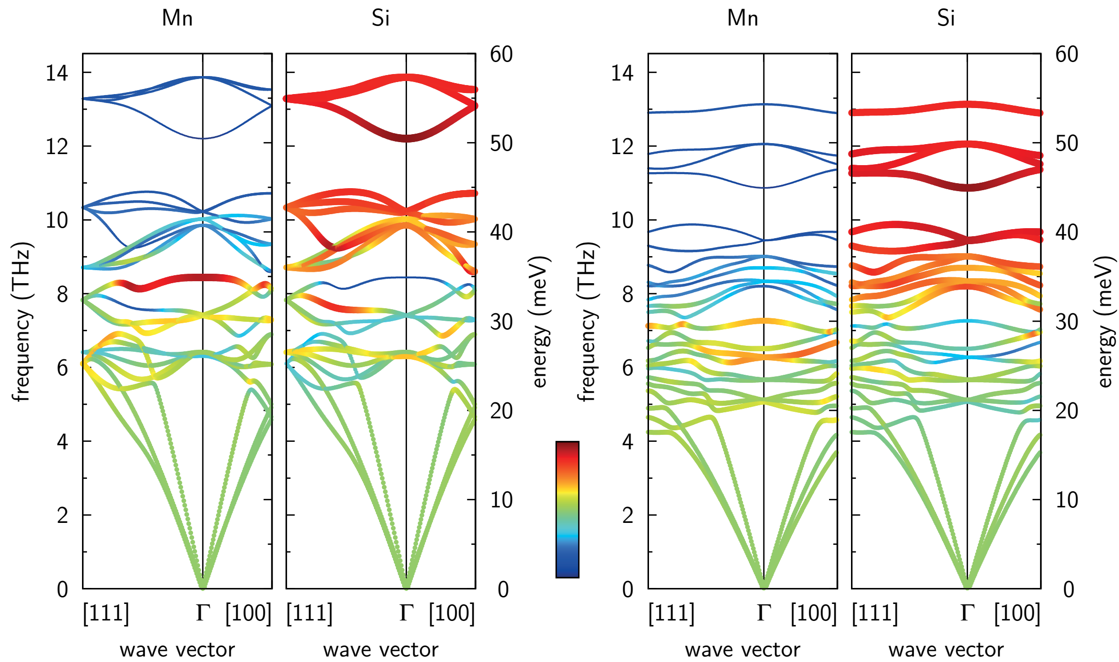

Figure 3.20 – Calculated phonon dispersion relations of bulk MnSi (left) and of bulk MnSi under biaxial strain as induced by a Si(111) substrate (right). In square brackets, the directions of the $\vec{q}$ wave vector in the reciprocal space of the simple cubic lattice are given. The coloring and width of the bands correspond to the band character $\chi(\nu, \vec{q})$ and indicate how intensely Mn (left panels) or Si (right panels) atoms are vibrating if the respective phonon is excited [thin blue (thick red) bands correspond to the minimum (maximum)].

thus, frequency) than those with dominating Si character, which form the topmost group of bands. This can be understood from the harmonic oscillator (or the linear chain), where the resonance frequency (phonon dispersion prefactor) scales like $1/\sqrt{m}$ with the particle mass m. Particles with higher mass vibrate with lower frequencies.

As one can further see from Fig. 3.20, the biaxial strain induced by a hypothetical Si(111) substrate leads to a considerable phonon softening in the silicide: The phonon states are pushed (rescaled) to lower energies. Hence, they can be excited more easily. Moreover, the degeneracy of different bands at the Brillouin zone edges is lifted. Most importantly, no imaginary (displayed as negative) frequencies arise in both the unstrained and the strained material, which proves the dynamical stability of the unstrained and strained B20 bulk structure.

The thermalized phonon system can be modeled by using a canonical ensemble with a heat bath at temperature T. The usual expression for the (Helmholtz) free energy is:

$$F = -k_\mathrm{B} T \ln(Z) = \int_0^\infty \mathrm{d}\varepsilon\, g(\varepsilon) \left(k_\mathrm{B} T \ln(1 - \mathrm{e}^{-\varepsilon/k_\mathrm{B} T}) + \frac{\varepsilon}{2} \right),$$

where Z is the canonical partition function and $g(\varepsilon)$ denotes the DOS (phonon modes), which can be calculated—analogously to the band structure—by using Fourier interpolation. It is normalized in such a way that

$$\int_0^\infty \mathrm{d}\varepsilon\, g(\varepsilon) = 3N = 24,$$

Dieses Werk ist copyrightgeschützt und darf in keiner Form vervielfältigt werden noch an Dritte weitergegeben werden.
Es gilt nur für den persönlichen Gebrauch.

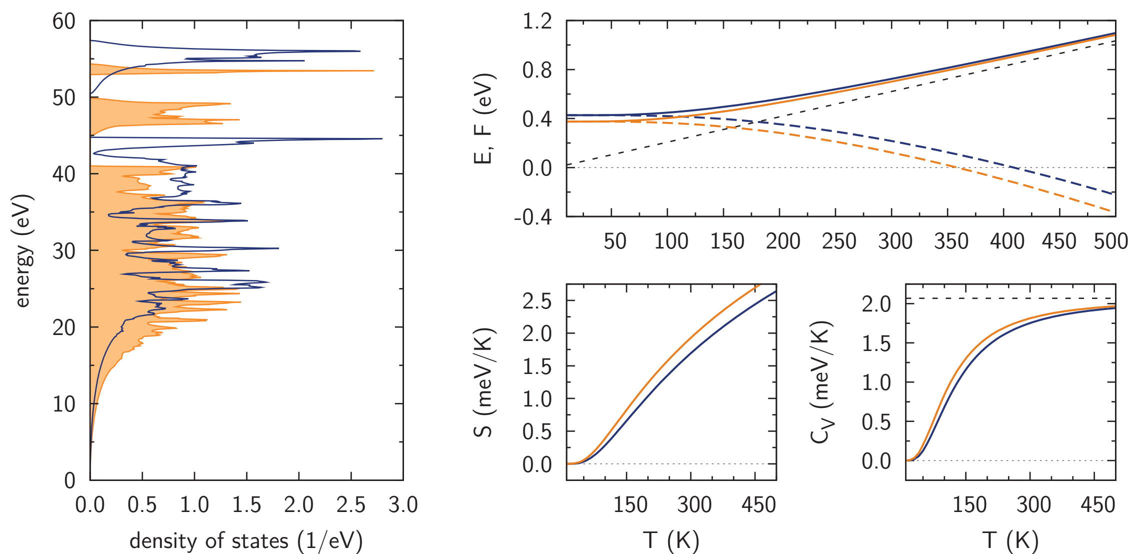

Figure 3.21 – Phonon DOS $g(\varepsilon)$ (left) and related thermodynamic quantities as functions of the heat bath temperature T (right) for MnSi (blue) and MnSi under biaxial strain as induced by a Si(111) substrate (orange). The solid (dashed) lines in the top-right panel represent the internal energy E (free energy F). The black dashed line indicates the asymptotic behavior $E = 3Nk_BT$. The two bottom-right panels show the entropy S and the heat capacity C_V; in the latter case, the black dashed line marks $C_V = 3Nk_B$ (Dulong-Petit law). All values correspond to a single unit cell (four formula units).

with $N = 8$ being the number of atoms in the unit cell. The expectation value of the (internal) energy, on the other hand, is ($\beta = 1/k_BT$):

$$E = -\frac{\partial}{\partial\beta}\ln(Z) = k_BT^2\frac{\partial}{\partial T}\ln(Z) = \int_0^\infty d\varepsilon\,\varepsilon\,g(\varepsilon)\left(\frac{1}{e^{\varepsilon/k_BT}-1}+\frac{1}{2}\right).$$

The corresponding entropy can be derived by using the common relation $F = E - TS$,

$$S = \frac{1}{T}(E-F) = \frac{1}{T}\int_0^\infty d\varepsilon\,g(\varepsilon)\left(\frac{\varepsilon}{e^{\varepsilon/k_BT}-1} - k_BT\ln(1-e^{-\varepsilon/k_BT})\right),$$

or, equivalently, from

$$S = k_B\int_0^\infty d\varepsilon\,g(\varepsilon)\left\{[n(\varepsilon)+1]\ln[n(\varepsilon)+1] - n(\varepsilon)\ln[n(\varepsilon)]\right\},$$

with the Bose distribution function[18] $n(\varepsilon) = (e^{\varepsilon/k_BT}-1)^{-1}$. The quantum statistics is done correctly here, accounting for the phonon bosonic character. On the other hand, the density of phonon modes is assumed to be independent of T. One can imagine that a thermalized electron system might lead to slightly different force constants and thus to a slightly different phonon spectrum.

The thermodynamic quantities E, F, S, and C_V are shown in Fig. 3.21, together with the phonon DOS $g(\varepsilon)$ for the strained and the strain-free system. For high temperatures T, the

[18] Actually, it is a Bose distribution function (as arising in the grand canonical ensemble) without μ, which can also be called Planck distribution function; see, for instance, Ref. [201].

Dieses Werk ist copyrightgeschützt und darf in keiner Form vervielfältigt werden noch an Dritte weitergegeben werden.
Es gilt nur für den persönlichen Gebrauch.

energy mean should behave asymptotically as $E = 3Nk_\mathrm{B}T$, which is obviously fulfilled with and without biaxial strain.[19] For $T \to 0$, F and E converge to the same value:

$$\lim_{T\to\infty} F = \lim_{T\to\infty} E = \frac{1}{2}\int_0^\infty \mathrm{d}\varepsilon\, \varepsilon\, g(\varepsilon).$$

The difference between E and F is clearly larger for the strained system than for the strain-free case. Consequently, the entropy S is also larger. The heat capacity of the phonon system can be derived from the aforementioned quantities via

$$C_V = \frac{\partial}{\partial T}E = T\frac{\partial}{\partial T}S$$

and is shown in Fig. 3.21. It approaches the classical limit $C_V = 3Nk_\mathrm{B}$, also known as Dulong-Petit law, for high temperatures T. For temperatures below 500 K, the heat capacity of the strained system is larger than that of the strain-free system, which is simply due to the faster increasing entropy in the former case.

3.5 Correlation effects in MnSi and FeSi

Throughout the previous sections it has been demonstrated that conventional GGA-type exchange-correlation functionals like PBE are capable of providing a qualitatively correct description of many of the phenomena observed in TM monosilicides. Nevertheless, it could be fruitful to explore the effect of on-site electronic correlation in FeSi and MnSi. For example, the relative stability of low-spin and high-spin states that have been calculated within the GGA could be sensitive to such a type of correlation. Already some years ago it was argued by Anisimov *et al.* that the inclusion of a Hubbard-U term operating in the vicinity of the Fe atoms could stabilize a magnetic moment of around 1 μ_B in FeSi for a value of $U > 4.6$ eV [187]. Moreover, the inclusion of on-site correlation may lead to a better description of excitations, either for comparison with spectroscopic experiments or for estimating the contributions of Stoner excitations to the magnetic susceptibility.

Recent ARPES experiments on FeSi required an empirically determined self-energy shift to account for the correct position of the bands, but the overall DFT band structure was found to be in qualitative agreement with the experiment [183]. Experiments on MnSi using x-ray absorption, photoemission, and fluorescence led to the conclusion that the Mn atoms are in a mixed valence state, which points to some role of electron correlation in this material [115]. On the other hand, it was also concluded that the on-site electronic correlation is apparently not strong enough to lead to a localization of the magnetic moments. Hence, a description of MnSi as an itinerant ferromagnet is appropriate (and also consistent with the theoretical findings under strain, which have been discussed in the previous section). This view of the origin of magnetism in MnSi is also corroborated by measurements of the magnetic susceptibility: From a fit of the paramagnetic susceptibility above the Curie temperature (between 120 and 300 K) to a Curie-Weiss law, one would arrive at a magnetic moment of 2.27 μ_B, which is a much higher value than the magnetic moment of 0.4 μ_B found in saturation magnetization at low temperatures [176]. Thus, the Rhodes-Wohlfarth parameter [202] of MnSi

[19] In the E integral, the exponential function in the denominator of the Bose factor has to be expanded up to second order. Subsequent use of the geometric series cancels the $+1/2$ term and gives the well-known classical limit $E = 3Nk_\mathrm{B}T$, independent of $g(\varepsilon)$. Application of $\partial/\partial T$ leads to the Dulong-Petit law.

Dieses Werk ist copyrightgeschützt und darf in keiner Form vervielfältigt werden noch an Dritte weitergegeben werden.
Es gilt nur für den persönlichen Gebrauch.

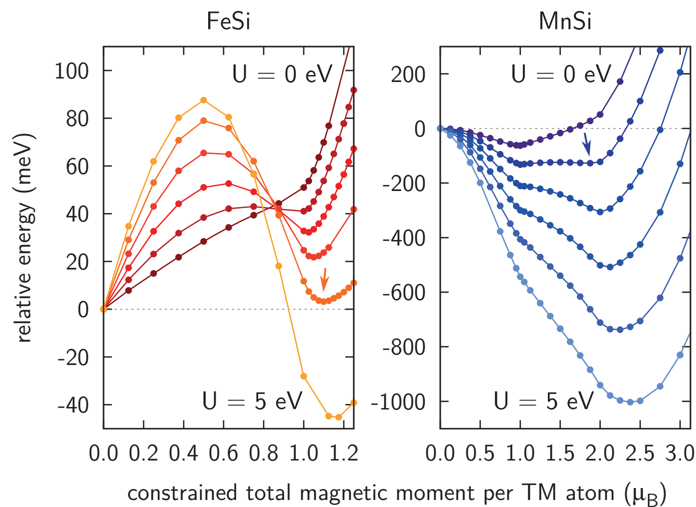

Figure 3.22 – Total energy curves as functions of the constrained total magnetic moment, both per f.u., from DFT+U calculations with varying U between 0 and 5 eV in steps of 1 eV. The energy value for zero moment has been chosen as reference for each curve. A second local minimum (small arrows) can be stabilized at a higher magnetic moment by inclusion of on-site electronic correlation.

is much larger than unity, a behavior typical for itinerant, weakly FM materials. The large magnetic moment derived from the Curie-Weiss fit could point to the existence of high-spin Stoner excitations.

In order to explore these topics, the author performed constrained total magnetic moment calculations for different values of U, keeping the cell size and atomic positions fixed for simplicity. The rotationally invariant formulation of the DFT+U scheme described in Sec. 2.2.3 (pages 28 ff.) has been used. The basic exchange-correlation functional was PBE. The results for FeSi shown in Fig. 3.22 reproduce quite accurately the previous results of Anisimov *et al.*, in particular, the stabilization of a magnetic moment near 1 μ_B for high U values (marked by an arrow). Minor differences with respect to Ref. [187] can be attributed to the different exchange-correlation functional (GGA vs. LDA) and a probably slightly different cell size.

For MnSi, a second magnetic state stabilizes around 2 μ_B already for $U \approx 1$ eV, as can be seen in Fig. 3.22. For higher values of U, the original minimum at 1 μ_B becomes unstable and the second minimum moves to higher magnetic moments. Thus, the inclusion of on-site electronic correlation does not lead to an improved agreement between the measured (via the saturation magnetization) and the calculated magnetic moment in MnSi. It is rather likely that the deviation is due to strong quantum-dynamical spin fluctuations that reduce the moment obtained in DFT, as already suggested earlier by Karhu *et al.* and Moriya [196, 203]. The conclusion here is that the correct description of the ground state of MnSi (FeSi) is in conflict with a value of U exceeding 1 eV (4 eV). However, the flat energy minimum observed for MnSi at $U \approx 1$ eV between 1 and 2 μ_B could be physically relevant, as it allows for energetically low-lying excitations of the Mn atom into a high-spin state, which is compatible with the large increase of the paramagnetic susceptibility near T_C (see Refs. [176, 204] for measured curves).

As a side track, the author found that optimizing the crystal structure in the presence of U adversely affects the calculated lattice constant. With increasing U, the equilibrium lattice constant a of MnSi also increases (4.58, 4.60, and 4.66 Å for 1, 2, and 3 eV, respectively), and the magnetic moments at the respective equilibrium lattice constants are even higher than those indicated in Fig. 3.22. Already for $U = 1$ eV, 2 μ_B is the ground state magnetic moment, at a lattice constant that is overestimated by a similar percentage as the Si lattice constant is overestimated by PBE (cf. Table 3.1).

Dieses Werk ist copyrightgeschützt und darf in keiner Form vervielfältigt werden noch an Dritte weitergegeben werden.
Es gilt nur für den persönlichen Gebrauch.

Consequently, no significant increase of the total magnetic moment arises anymore if the FM calculations of Si(111)-strained bulk MnSi, which have been discussed in the previous section, are repeated with $U = 1$ eV. The NM-FM energy difference increases from roughly 110 meV (without U) to 276 meV, and the FIM-FM energy difference, 57 meV, is also somewhat higher than the value derived without U. This indicates a further stabilization of the high-spin FM ground state due to on-site electronic correlation. For FeSi, calculated with $U = 4$ eV, a higher total magnetic moment of about 1.5 μ_B is found in the FM phase, and the NM-FM energy difference raises to 300 meV. However, the FIM configuration is suddenly more stable than the FM phase, with an energy difference of 47 meV. The total magnetic moment in this FIM phase is 0.33 μ_B.[20] This, and the DOS of this configuration, which is not shown here, still indicate a metallic character instead of a band gap at the Fermi energy. Thus, no qualitative difference is achieved by inclusion of on-site electronic correlation in this respect. In order to shed more light on this issue, careful measurements of the magnetic properties in future experiments on FeSi/Si(111) systems would certainly be very helpful.

From the preceding observations the author draws the conclusion that for the type of electronic correlations present in FeSi and MnSi the Coulombic on-site repulsion plays only a minor role, and a DFT+U scheme is not superior to standard GGA-type exchange-correlation functionals, although it offers a possible interpretation of the high magnetic moments derived from paramagnetic susceptibility fits. For similar reasons one cannot expect improvements from the use of hybrid functionals such as HSE06. As a possible outlook, it could rather be interesting to investigate the effect of strain in TM-Si compounds within the framework of DMFT. For simple bulk FeSi, this method shows a renormalization of the bands close to the Fermi energy, in agreement with experimental findings [116]. Hence, such an approach could possibly be illuminating for MnSi as well.

3.6 Growth mode and atomic structure of MnSi/Si(111)

In the previous sections we have seen that MnSi (and certainly FeSi) exhibits the most interesting behavior among the different 3*d* TM monosilicides, especially under epitaxial strain. Therefore, it suggests itself to study the growth of this material on a Si(111) substrate. As has been pointed out above, MnSi will grow in [111] direction in this case.

Several experimental studies on such heterostructures have been carried out in the past. For instance, increased ordering temperatures have been reported, as already discussed above [108, 189]. Furthermore, studies of the magnetic anisotropy and the magnetic texture under epitaxial strain have been performed [109, 196]. Other experimental work focused on structural, growth, and surface electronic properties [192–195,206]. However, due to the complexity of the B20 crystal structure, the atomic structure of the films and their dependence on the growth parameters have remained vague for a long time, and a thorough *theoretical* investigation has been called for [192, 193, 195, 206]. Moreover, it has been pointed out recently by Karhu *et al.* that structural and magnetic properties of MnSi films are closely related to each other [109]. Hence, knowledge about the interplay between the growth conditions and the atomic structure is required to reproducibly fabricate MnSi films with specified magnetic properties.

This section will present the results of such a theoretical investigation. They are interwoven with (and supported by) observations from further experimental STM studies, which have

[20] Note that all values here are given per f.u.

Dieses Werk ist copyrightgeschützt und darf in keiner Form vervielfältigt werden noch an Dritte weitergegeben werden.
Es gilt nur für den persönlichen Gebrauch.

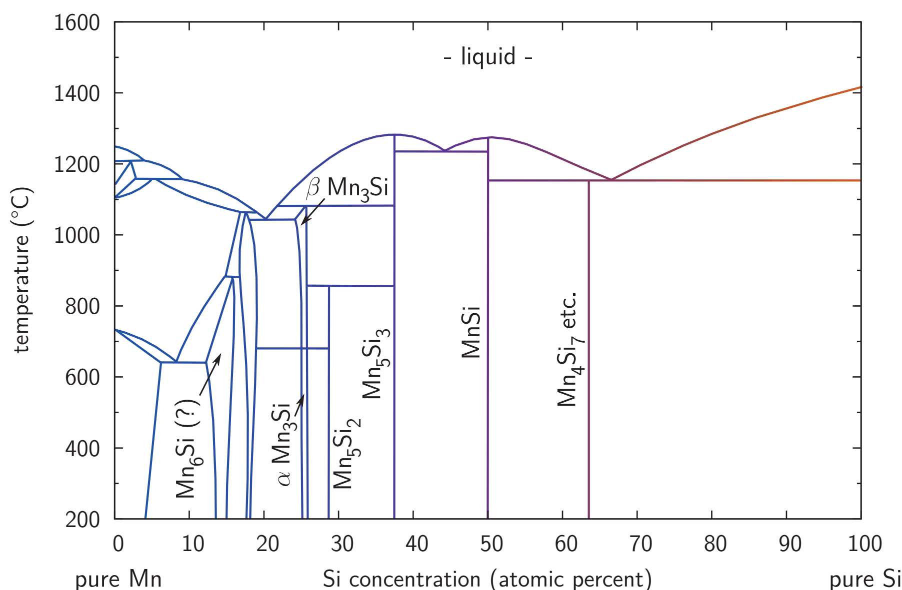

Figure 3.23 – Sketch of the Mn-Si phase diagram (according to Refs. [168, 205]).

been carried out by T. Suzuki, T. Lutz, and G. Costantini in the group of K. Kern at the Max-Planck-Institut für Festkörperforschung in Stuttgart, Germany.

As one can see from the alloy phase diagram shown in Fig. 3.23, pure MnSi is found only in a very small composition range. For thin film growth on Si(111) it is not clear *a priori* which phase will form. Therefore, low-energy electron diffraction (LEED) or comparable techniques have to be used to check the surface periodicity of the films [192–195]. However, using this as a sole indicator for MnSi growth can be misleading if silicides with a different stoichiometry exhibit a similar surface periodicity. For this reason, the author additionally studied Mn_5Si_3 films on Si(111), which will be discussed later in this chapter.

3.6.1 Different MnSi(111) surfaces

In order to understand the atomic structure of the epitaxial MnSi films on Si(111), knowledge about the surface terminations and the interface structure is necessary. It is helpful to begin with energetic, atomic, and magnetic properties of the different (111) surfaces of MnSi *without* biaxial strain.

Since MnSi has no inversion symmetry in its ground state B20 crystal structure, the (111) and $(\bar{1}\bar{1}\bar{1})$ surfaces are not equivalent. In conjunction with the four individual dense and sparse layers of Mn and Si atoms (cf. Fig. 3.16 on page 74) this leads to eight inequivalent surfaces. The relaxed atomic structure of these surfaces is shown in Fig. 3.24. The inequivalence is obvious: Already the subsurface layer is a different one for the (111) and the $(\bar{1}\bar{1}\bar{1})$ surfaces.

Figure 3.24 also shows the local magnetic moments at the different atoms. Nearly all (sub-) surface Mn magnetic moments are much larger than the bulk value (1.11 μ_B, cf. Table 3.3). Only the subsurface Mn atoms in the case of the (111) Si-dense termination bear significantly smaller values. Although these effects can be explained by the reduced coordination of the

Dieses Werk ist copyrightgeschützt und darf in keiner Form vervielfältigt werden noch an Dritte weitergegeben werden.
Es gilt nur für den persönlichen Gebrauch.

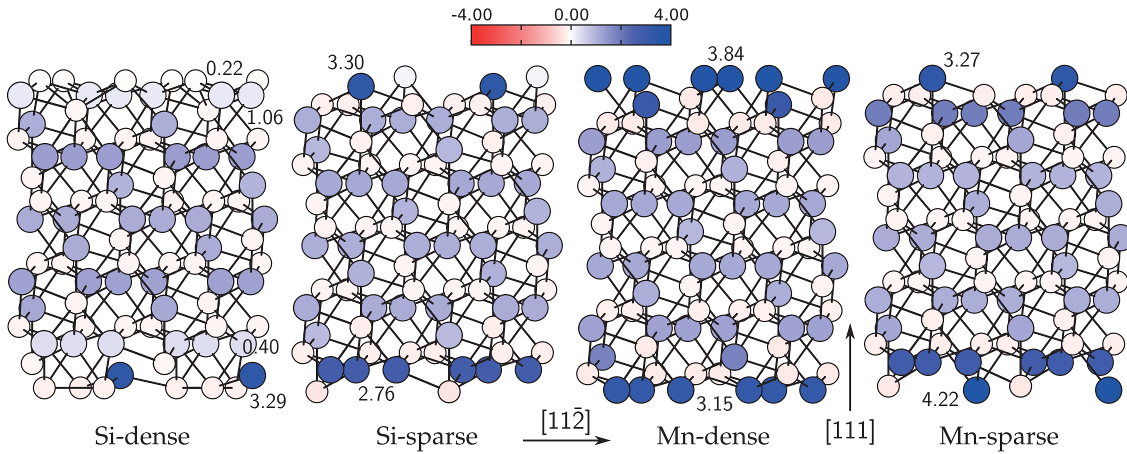

Figure 3.24 – Optimized atomic structures of the different MnSi(111) and ($\bar{1}\bar{1}\bar{1}$) surfaces. Color encoded, the local magnetic moments (in μ_B) are given; the values for Mn atoms close to the surfaces are printed explicitly.

atoms near the surfaces and are the expected behavior, this last case shows that a reduced coordination does not necessarily lead to increased magnetic moments.

In analogy to Eq. (3.2) one can calculate the surface energies $\gamma(\mu_{\mathrm{Si}})$, assuming that the surface is in thermodynamic equilibrium with the subsurface MnSi bulk material:

$$\gamma(\mu_{\mathrm{Si}}) = \frac{1}{2A}\Big\{E_{\mathrm{slab}} - (N_{\mathrm{Si}} - N_{\mathrm{Mn}})\mu_{\mathrm{Si}} - N_{\mathrm{Mn}}E_{\mathrm{MnSi}}\Big\}.$$

This equation follows from Eq. (3.2) under the equilibrium condition $E_{\mathrm{MnSi}} = \mu_{\mathrm{Mn}} + \mu_{\mathrm{Si}}$, which is used to eliminate the variable μ_{Mn}. E_{slab} and E_{MnSi} are the DFT total energies of the slab structure (including two surfaces and vacuum) and MnSi bulk material, respectively; the N_i are the different numbers of atoms in the structure, and A is the surface area of the slab structure. The chemical potential of Si, μ_{Si}, can take on values between E_{Si} (the DFT total energy of Si bulk in diamond structure) and $E_{\mathrm{Si}} + \Delta H^{\mathrm{MnSi}}$. The formation enthalpy ΔH^{MnSi} of MnSi is negative [see Eq. (3.6) on page 65]. Beyond this interval, the segregation into bulk Mn and bulk Si is more favorable. Obviously, $\gamma(\mu_{\mathrm{Si}})$ is simply a linear function of the chemical potential. Note that due to the missing inversion symmetry it is only possible to calculate an average of the (111) and the ($\bar{1}\bar{1}\bar{1}$) surface energy. The individual contributions are hard to isolate, a problem similar to the case of GaAs(111) [207].

The results are shown in Fig. 3.25. Clearly, the Si-dense surface terminations lead to the lowest surface energy average, even beyond the allowed interval for μ_{Si}. The lines cross deep in the Mn-rich growth regime. Consequently, the Si-dense surfaces are thermodynamically most stable. They are followed by the Si-sparse and Mn-sparse surfaces. The Mn-dense surfaces have the highest surface energy average.

All shown surface structures have a thickness of 21 layers. The results, especially the surface energies, are perfectly converged in this respect, as proven by a comparison with 17-layer structures (not shown here). During the calculations, the relevance of a dipole correction scheme has been assessed [208, 209]. Its effect has been found to be negligible, despite the inequivalence of the (111) and the ($\bar{1}\bar{1}\bar{1}$) surfaces.

Dieses Werk ist copyrightgeschützt und darf in keiner Form vervielfältigt werden noch an Dritte weitergegeben werden.
Es gilt nur für den persönlichen Gebrauch.

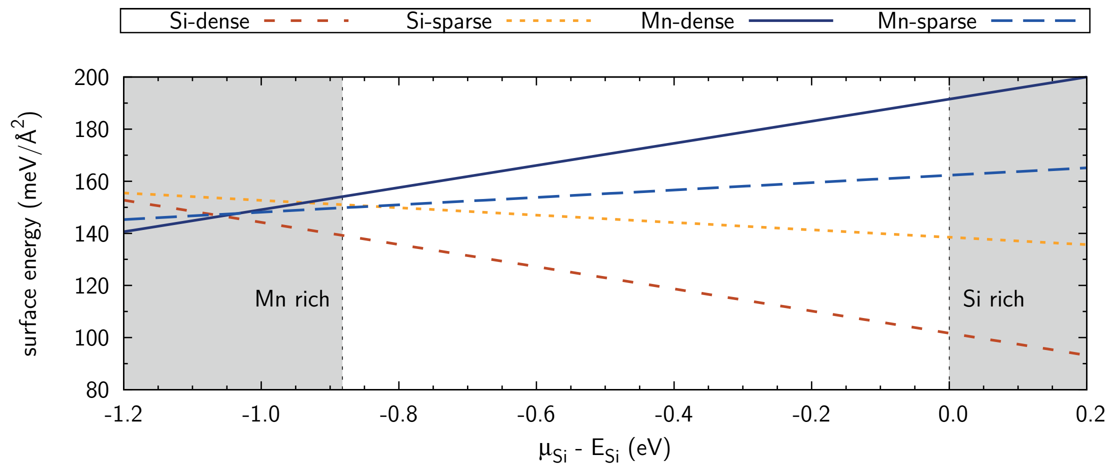

Figure 3.25 – Pairwise averaged surface energies $\gamma(\mu_{\text{Si}})$ of the different MnSi(111) and $(\bar{1}\bar{1}\bar{1})$ surfaces, classified according to their termination. The white region bounded by the vertical dashed lines marks the chemical potential range accessible in thermodynamic equilibrium, between Mn-rich and Si-rich growth conditions.

3.6.2 The MnSi/Si(111) and FeSi/Si(111) interfaces

The next important aspect that has to be discussed is the interface between an epitaxial film of a TM-Si compound in B20 structure and the Si(111) substrate. Si(111) provides two surfaces: the SDB and the TDB termination (cf. Fig. 3.4 on page 55). A TM monosilicide has four (111) and four $(\bar{1}\bar{1}\bar{1})$ surfaces.[21] This results in 16 possible interface combinations. In principle, one has to simulate all of them to determine the most stable interface.

The author circumvented this cumbersome procedure by taking into account the MnSi surface energies calculated above. At the interface to a Si substrate, the growth conditions will certainly be Si rich. It is therefore reasonable to choose a Si-dense termination for the silicide film. On the other hand, the Si(111)-SDB termination has a much lower surface energy than the TDB termination (see above). Moreover, MnSi(111)-(1×1) matches the Si(111)-$(\sqrt{3}\times\sqrt{3})$ surface unit cell, in which three Si(111) dangling bonds have to be compensated by the silicide. This happens to be the case for a Si-dense terminating layer, since it consists of three Si atoms per MnSi(111)-(1×1) surface unit cell.

The conclusion of this chain of thought is that the most stable interface is most certainly a single-dangling-bond–Si-dense interface. Figure 3.26(a) shows fully optimized, periodic Si(111)/MnSi(111)/Si(111) and Si(111)/FeSi(111)/Si(111) sandwich structures. The optimization includes the atomic positions as well as the supercell height in $[111]$ direction (c), the latter being equivalent to an optimization of the substrate-film spacing.

It is possible to verify the above reasoning by calculating the associated interface energies γ for the MnSi and the FeSi sandwich structure:

$$\gamma = \frac{1}{2A}\left\{E_{\text{slab}} - (N_{\text{Si}} - N_{\text{TM}})\mu_{\text{Si}} - N_{\text{TM}}E^{\text{strained}}_{\text{TM-Si}}\right\}\Big|_{\mu_{\text{Si}}=E_{\text{Si}}}.$$

The only difference to the MnSi surface situation discussed before is that here the TM monosilicide is laterally distorted. Thus, the author decided to use laterally distorted TM-Si

[21] In the following, the distinction between (111) and $(\bar{1}\bar{1}\bar{1})$ surfaces will be omitted for the sake of simplicity.

Dieses Werk ist copyrightgeschützt und darf in keiner Form vervielfältigt werden noch an Dritte weitergegeben werden.
Es gilt nur für den persönlichen Gebrauch.

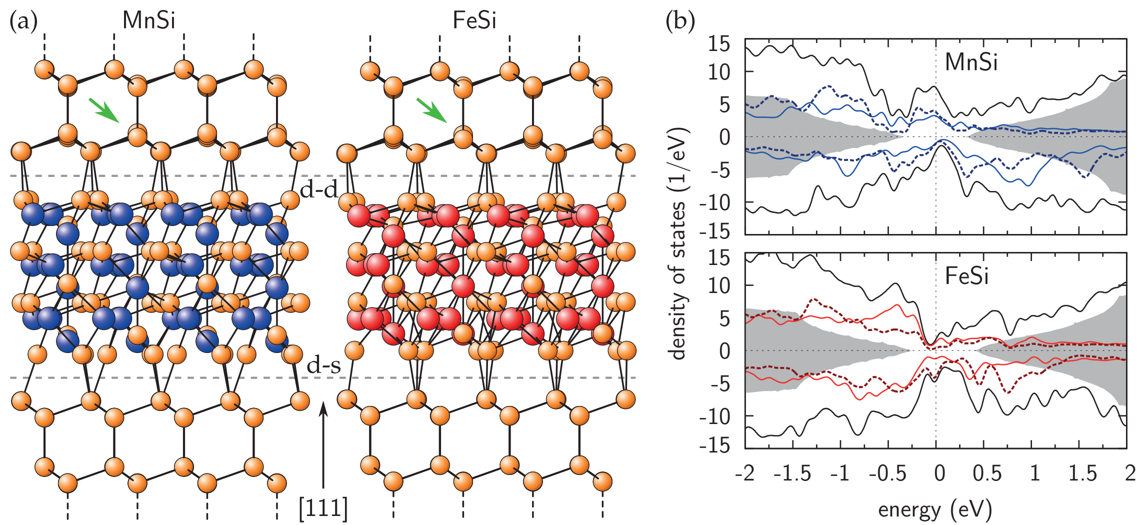

Figure 3.26 – Optimized interfaces of MnSi and FeSi with Si(111). (a) Atomic structure for MnSi (left) and FeSi (right). The two inequivalent interfaces are Si-dense–TM-sparse (d-s) and Si-dense–TM-dense (d-d). The green arrows indicate small distortions in the Si substrate on the d-d side. Orange (blue/red) spheres mark Si (Mn/Fe) atoms. (b) Spin-resolved electronic structure of the MnSi (top) and the FeSi (bottom) two-interface systems. The black lines indicate the (scaled) total DOS. The blue and red lines are sums of projections onto the 3*d* orbitals of the TM-sparse and TM-dense layers at the interfaces. The solid (dashed) lines belong to the d-s (d-d) interface. The gray shaded area indicates properly aligned Si bulk with its PBE band gap. The energy zero corresponds to the Fermi energy.

bulk as reservoir ($E^{\text{strained}}_{\text{TM-Si}}$). The chemical potential of Si, $\mu_{\text{Si}} = E_{\text{Si}}$, takes on the energy of Si bulk to model Si-rich growth conditions. The result for MnSi is $\gamma \approx 75$ meV/Å^2, a value that is significantly smaller than the surface energy of the relaxed bare Si(111)-SDB surface ($\gamma \approx 95$ meV/Å^2) or the mean of the MnSi(111)-Si-dense surface energies ($\gamma \approx 102$ meV/Å^2, cf. Fig. 3.25) under the same growth conditions. The result for FeSi is $\gamma \approx 70$ meV/Å^2 and thus very similar to the MnSi case. Again there are two inequivalent Si-dense terminated interfaces in the sandwich structures as a consequence of the missing inversion symmetry, and γ is an average over both of them (see above). They are termed “d-s” (Si-dense–TM-sparse) and “d-d” (Si-dense–TM-dense) in the following, according to the first two layers of the silicide at the interface.

The calculated lengths of the Si-Si bonds connecting the Si substrate and the TM monosilicide Si-dense layer are 2.37 Å (d-s) and 2.38 Å (d-d) for MnSi and 2.38 Å (d-s) and 2.39 Å (d-d) for FeSi. Although these values are quite similar, it is possible to state that the distances are slightly larger in the FeSi case than in the MnSi case. Moreover, they are also slightly larger than the bond length in bulk Si (2.37 Å). The Si substrate shows some distortions on the d-d side of the TM-Si layer [marked by the green arrows in Fig. 3.26(a)]. Hence, one can speculate that the d-d interface has a higher interface energy than the d-s interface.

Sandwich structures as those shown in Fig. 3.26(a) are not only a useful numerical setup to calculate interface energies. Since they include FM materials, they can also be interesting

Dieses Werk ist copyrightgeschützt und darf in keiner Form vervielfältigt werden noch an Dritte weitergegeben werden.
Es gilt nur für den persönlichen Gebrauch.

Table 3.7 – Interface TM magnetic moments (in μ_B) of the structures shown in Fig. 3.26. The strained-bulk values from Table 3.6 are also given for comparison. Note the antiparallel Fe-sparse moments in the FeSi case.

	MnSi		FeSi	
	Mn-sparse	Mn-dense	Fe-sparse	Fe-dense
d-s interface	3.93	0.71	−0.60	0.51
d-d interface	1.61	2.14	−0.46	1.60
strained bulk	1.22	1.85	0.57	1.30

in themselves in the context of spin filtering.[22] Figure 3.26(b) shows the electronic structure of both sandwich structures around the Fermi energy. In addition to the total DOS, PDOS curves provide some local information about the different interfaces. Although the MnSi and FeSi data looks clearly different, one can see that the Fermi energy is located in the middle of the Si band gap for both materials. The shown Si bulk DOS has been manually aligned such as to fit to PDOS curves of Si atoms sitting at some distance to the TM-Si compound. It is an interesting feature of these sandwich structures that for both materials the Fermi energy sits nearly in a "band gap" (DOS minimum) in one spin channel: For MnSi, the *minority* spin channel exhibits the minimum, while for FeSi it is the *majority* spin channel.[23] In any case, the spin polarization (difference of majority and minority DOS) at the Fermi level is quite high. For both MnSi and FeSi, it is higher close to the d-d interface than close to the d-s interface.

We have already seen that the proximity of a surface has a strong influcence on the magnetic moments. This is also the case for interfaces (cf. Table 3.7). However, while the magnetic structure of the MnSi d-s interface resembles that of the respective MnSi(111)-Si-dense surface (cf. Fig. 3.24), the d-d interface behaves differently, exhibiting larger magnetic moments as strained bulk. FeSi shows a very peculiar behavior: The magnetic moments localized at the Fe-sparse layers closest to one of both interfaces are oriented antiparallel to the rest of the Fe atoms in the silicide, in strong contrast to the MnSi case. This seems to be no artifact, since test calculations with initially constrained moments converged to the same solution after the relaxation of the constraints. Moreover, the calculations start with a parallel spin configuration, but converge nonetheless to the antiparallel solution. In conjunction with the presumably small Curie temperature of FM FeSi (see above), this behavior leads to the conclusion that MnSi is the more useful and reliable material in this context.

3.6.3 Coexisting $\sqrt{3} \times \sqrt{3}$ surfaces of MnSi/Si(111)

It is well established that deposition of some monolayers[24] (MLs) of Mn on a Si(111) substrate and subsequent careful annealing leads to film structures with a $\sqrt{3} \times \sqrt{3}$ surface pattern [192–195]. Recently, Hortamani *et al.* put forward a structural model for Mn monosilicide

[22] The structures shown in Fig. 3.26(a) can either be interpreted as TM-Si film between two Si electrodes, as suggested by the figure, or as Si film between two TM-Si electrodes due to the periodicity of the structure in [111] direction.

[23] Note that these DOS plots are smeared out to some degree due to a Gaussian broadening that is used. This visualization procedure has the disadvantage that it can close small gaps.

[24] One ML is defined as 7.8 atoms/nm^2, corresponding to one atom in a 1×1 unit cell of the Si(111) substrate.

Dieses Werk ist copyrightgeschützt und darf in keiner Form vervielfältigt werden noch an Dritte weitergegeben werden.
Es gilt nur für den persönlichen Gebrauch.

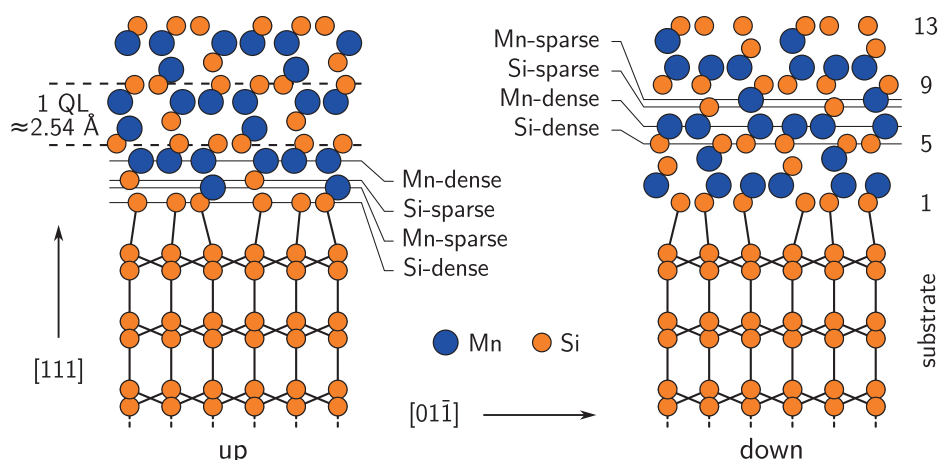

Figure 3.27 – Side views of the atomic structure of MnSi/Si(111) films, showing "up" (left) and "down" (right) stacking sequence, QL division, internal QL structure, and layer numbering. In the MnSi films, no bonds are displayed for better clarity. Note the different interfaces [cf. Fig. 3.26(a)]: d-s (left) and d-d (right).

growth on Si(111) [114]. The atomic structure of this model can be seen in Fig. 3.27 ("up"). Without further discussion or arguments, these authors use a d-s interface [cf. Fig. 3.26(a)] between MnSi(111) and Si(111). In this structural model, the $\sqrt{3} \times \sqrt{3}$ surface pattern actually does not belong to a real "reconstruction" in the strict sense of the word, but is simply the pattern observed for all MnSi(111) surfaces. Due to epitaxial growth, the material adopts the Si(111)-($\sqrt{3} \times \sqrt{3}$) surface lattice constant. Thus, the term "$\sqrt{3} \times \sqrt{3}$" frequently used in the literature (and also in this thesis) is related to the Si substrate and corresponds to the MnSi(111)-(1×1) surface unit cell. By using the surface energies presented above (cf. Fig. 3.25) one can now argue that the surface termination will always be made by a Si-dense layer, which is most stable, and hence growth can only take place in steps of single QLs. This QL-wise growth could actually be observed in experimental studies [193, 195].

However, the situation is more complex than this. First of all, MnSi films can possibly grow in two different stacking sequences on Si(111), which are referred to as "up" and "down" stackings in the following (cf. Fig. 3.27). This idea has been put forward for the first time by the author of this thesis [15]. The reasoning presented in the previous section justifies the choice made by Hortamani *et al.* [114] to use the d-s interface for the up stacking. Consequently, the d-d interface is used for the down stacking. Second, two possible structural chiralities exist in B20 TM monosilicides. Since the crystalline chirality determines the magnetic helicity, the two chiralities can be distinguished by using x-ray and polarized neutron small-angle diffraction [210, 211] or dark-field transmission electron microscopy imaging [108, 109]. However, since "left- and right-handed" structures can be interchanged by a mirror operation (involving a plane containing the [111] and [11$\bar{2}$] axes) which leaves the Si(111) substrate invariant, both chiralities are energetically degenerate, and it is possible to restrict oneself to up and down structures with one chosen handedness in theoretical studies. Actually, coexisting domains of left- and right-handed chirality have been found in MnSi films on Si(111) [108]. Last but not least, it has recently been observed for the first time that MnSi on Si(111) does *not* grow in QL steps, but also exhibits coexisting, differently corrugated surface terminations as "intermediate states" (cf. Refs. [15] and [206]). From a

Dieses Werk ist copyrightgeschützt und darf in keiner Form vervielfältigt werden noch an Dritte weitergegeben werden.
Es gilt nur für den persönlichen Gebrauch.

thermodynamic point of view, this coexistence is already interesting in itself. A much more striking implication was missed in Ref. [206]: It creates, for the first time, the possibility to draw conclusions about the internal layer stacking sequence in the MnSi films on the atomic scale.

Films formed by reactive epitaxy

Room-temperature deposition of 1.4 – 4.2 ML of Mn on a clean Si(111)-(7×7) substrate with subsequent annealing at 300 °C for 15 – 30 min leads to the formation of thin MnSi films with a clear $\sqrt{3}\times\sqrt{3}$ surface pattern [15,17]. This growth protocol is known as reactive epitaxy (or, more appropriately, as solid-phase epitaxy; the two terms are used synonymously in this thesis). Large-scale STM images of such MnSi films are shown in Fig. 3.28 for different Mn coverage. For 1.4 ML, the Si substrate is still visible through holes in the MnSi film. The MnSi surfaces exhibit a relatively high corrugation (HC, referring to the difference between maximum and minimum of the oscillations in the atomic-resolution STM images). The surface is still dominated by HC areas for 2.8 ML Mn coverage. However, with further increasing Mn coverage, areas exhibiting a low corrugation (LC) appear and start to expand. A similar observation has been made recently by Azatyan *et al.* [206].

The coexistence of HC and LC surface areas can be seen even more clearly in Fig. 3.29, in addition to the well-known QL terrace structure [193–195]. Line scans show that the LC regions always appear approximately 0.4 Å above the HC regions. From a quick comparison of such a height difference with the tentative structural model shown in Fig. 3.27 one can deduce that HC certainly belongs to a surface termination one layer below LC. By assuming that really a MnSi monosilicide structure has formed (the only alternative, Mn_5Si_3, is excluded later in this chapter; cf. Sec. 3.8 on page 112), one can try to determine the atomic structure of the film and the terminating surface layers. The guidelines for finding the best match are as follows: On the one hand, the resulting structural model has to explain the experimental STM observations for filled- and empty-state images. In particular, the goal is to find a *pair* of consecutive surface terminations that matches the HC and LC observations. On the other hand, the result has to be consistent with the calculated DFT surface energies and film formation energies. In addition to the possible terminations indicated in Fig. 3.27, several nonstoichiometric ones can arise, which have to be considered as well.

A possible starting point are the MnSi surface energies of cut bulk structures as discussed above (cf. Fig. 3.25 on page 89). It is, however, more appropriate to calculate similar quantities for real heterostructures containing the Si substrate and the epitaxially strained MnSi films, as shown in Fig. 3.27. The backside of the Si substrate has to be passivated by H atoms to mimic an infinitely extended bulk material. A familiar, but slightly different expression for the surface energies is

$$\Delta\gamma = \gamma(\mu_{\mathrm{Si}}) - \gamma_{\mathrm{sub}} = \frac{1}{A}\left\{E_{\mathrm{slab}} - E_{\mathrm{sub}} - (N_{\mathrm{Si}} - N_{\mathrm{Mn}})\mu_{\mathrm{Si}} - N_{\mathrm{Mn}} E_{\mathrm{MnSi}}^{\mathrm{strained}}\right\}, \qquad (3.11)$$

where $\gamma_{\mathrm{sub}} \approx 95$ meV/Å^2 is the surface energy of the relaxed bare Si(111) surface, chosen as reference, E_{slab}, E_{sub}, and $E_{\mathrm{MnSi}}^{\mathrm{strained}}$ are the DFT total energies of the H-passivated substrate with film, the H-passivated substrate without film, and laterally distorted bulk MnSi, respectively. N_i are the different numbers of atoms in the film, excluding the substrate. It is important to note here that a so defined "surface energy" γ is actually a combination of the real surface energy γ_{s} and the energy of the interface between the MnSi film and the

Dieses Werk ist copyrightgeschützt und darf in keiner Form vervielfältigt werden noch an Dritte weitergegeben werden.
Es gilt nur für den persönlichen Gebrauch.

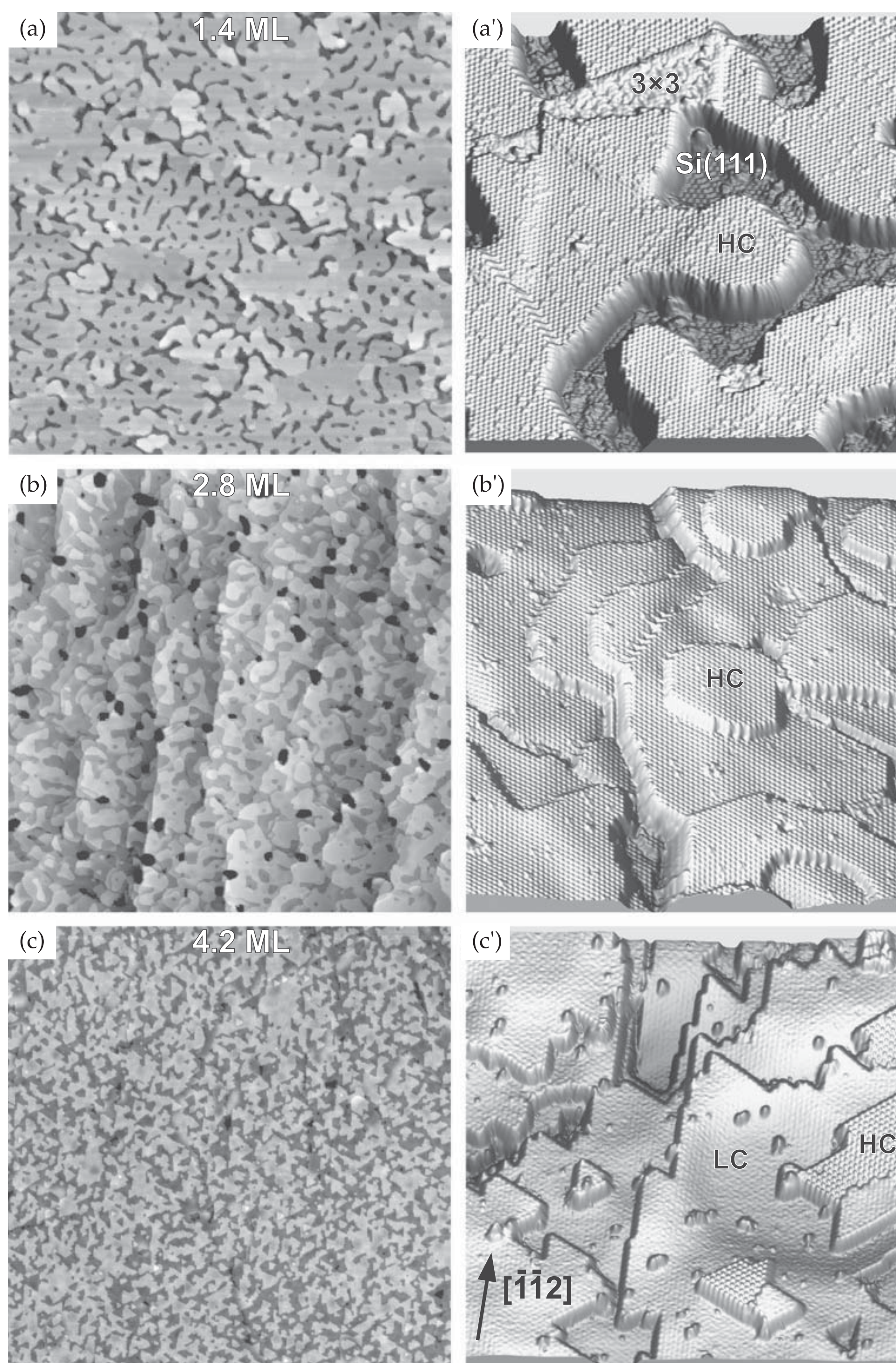

Figure 3.28 – STM images of MnSi thin films on Si(111) for higher Mn coverage between 1.4 and 4.2 ML. After Mn deposition at room temperature, the samples have been annealed at 300 °C for 15 – 30 min. The transition from a HC-dominated surface to a more LC surface with increasing amount of deposited Mn can clearly be seen. The image sizes are 500×500 nm^2 (left) and 50×50 nm^2 (right). Bias voltages range from −1.2 V to −1.8 V; the constant tunneling current is 0.2 nA. — STM images reproduced from Ref. [17]. © 2013 by Elsevier.

Dieses Werk ist copyrightgeschützt und darf in keiner Form vervielfältigt werden noch an Dritte weitergegeben werden.
Es gilt nur für den persönlichen Gebrauch.

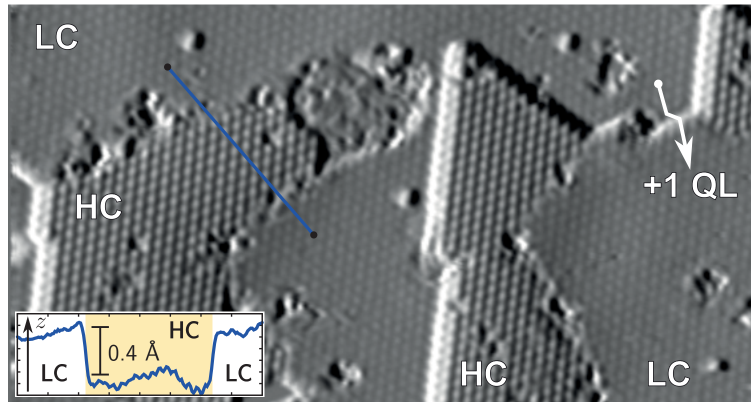

Figure 3.29 – Coexistence of HC and LC surface areas within one and the same QL for MnSi/Si(111) films. The experimental STM image has been recorded at a tunneling current of 0.2 nA and a bias voltage of −1.8 V. The MnSi film has been prepared by depositing 3.8 ML of Mn on a clean Si(111)-(7×7) surface at room temperature, followed by annealing at 300 °C for 30 min. The image size is 39×26 nm^2. The inset shows an averaged height profile of differently corrugated adjacent areas (belonging to one and the same QL), as schematically indicated by the blue line, to illustrate the height difference.

Si substrate γ_i, so that $\Delta\gamma = \gamma_\mathrm{s} + \gamma_\mathrm{i} - \gamma_\mathrm{sub}$. Advantageously, this definition removes the accumulating strain energy of the film, caused by epitaxial distortion of the material to the substrate lattice constant, from γ and makes terminations of films with different thickness comparable. From the energy difference of laterally (i.e, perpendicular to the [111] direction) distorted and undistorted bulk MnSi the strain energy can be deduced to be 115 meV per f.u. [cf. Fig. 3.17(a) on page 75], which translates into a contribution to γ of approximately 12 meV/Å^2 per QL. Again, the white region between the gray shaded areas in Fig. 3.30 indicates the range of μ_Si accessible in equilibrium.[25] Note that one could also choose μ_Mn to characterize the reservoir, since both chemical potentials are mathematically fully equivalent and can be interchanged via the equilibrium condition $\mu_\mathrm{Mn} = E_\mathrm{MnSi} - \mu_\mathrm{Si}$. In this work, the use of μ_Si reflects the mentality that the amount of Mn is fixed by deposition, but Si is available from the substrate reservoir and thus more variable. In addition, the more traditional film formation energies per area can be considered, as it has been done, for instance, in Refs. [112, 113, 212]:

$$E^\mathrm{form} - E^\mathrm{form}_\mathrm{sub} = \frac{1}{A}\left\{E_\mathrm{slab} - E_\mathrm{sub} - N_\mathrm{Mn}E_\mathrm{Mn} - N_\mathrm{Si}E_\mathrm{Si}\right\}. \tag{3.12}$$

These quantities are very similar to the surface energies derived from Eq. (3.2). The major difference is that no chemical potential is eliminated. Instead, both are set to the bulk reference values: $E_\mathrm{Mn/Si}$ are the diamond-Si and α-Mn bulk total energies. The film formation energies are shown in Fig. 3.30 for several film thicknesses. Again, the substrate formation energy $E^\mathrm{form}_\mathrm{sub} = \gamma_\mathrm{sub}$ is chosen as reference. The substrate is always considered to be in equilibrium with Si bulk, therefore γ_sub does not depend on a chemical potential variable. Since the formation of MnSi from elemental bulk sources is exothermic (see page 65), the curves in Fig. 3.30 have a downward slope on average.

[25] The validity of thermodynamic considerations should not be overestimated here, as discussed more deeply below, and thus the boundaries serve more as reference points than as absolute limits.

Dieses Werk ist copyrightgeschützt und darf in keiner Form vervielfältigt werden noch an Dritte weitergegeben werden.
Es gilt nur für den persönlichen Gebrauch.

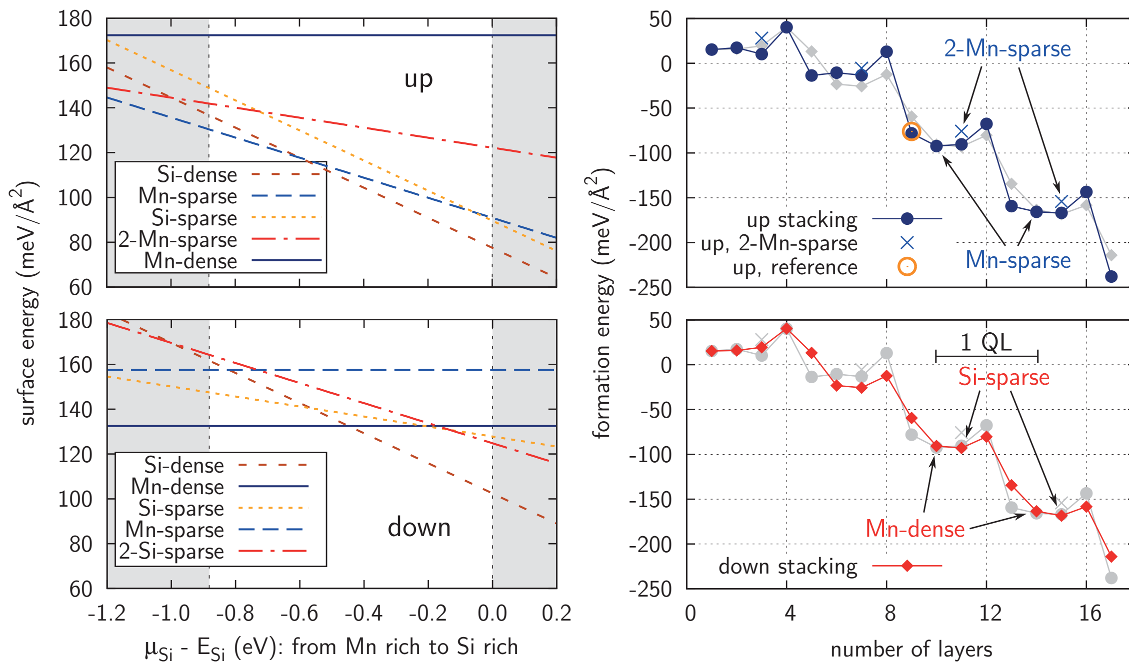

Figure 3.30 – Surface energies $\Delta\gamma = \gamma(\mu_{Si}) - \gamma_{sub}$ (left, starting with 13 layers, i.e., Si-dense) and film formation energies per area $E^{form} - E^{form}_{sub}$ (right) derived from simulated MnSi/Si(111) heterostructures of different thickness using Eqs. (3.11) and (3.12). The layer numbering is given in Fig. 3.27. Comparison with the "reference" value taken from Ref. [114] (all-electron LAPW) demonstrates the accuracy of the calculated energies. The formation energy curves clearly exhibit a QL periodicity. The marked classes of film terminations are the results of the matching procedure described in the text.

Let us now return to the discussion of the experimental STM images [15, 17]. Magnified sections of both HC and LC regions can be found in the leftmost column of Fig. 3.31. In the filled-state images, the HC areas display isolated, bright protrusions ordered on a hexagonal lattice with distances compatible with the Si(111)-($\sqrt{3} \times \sqrt{3}$) surface lattice constant. In addition, irregularly distributed triangular features are sometimes observed, which are probably caused by adatoms and neither shown nor discussed here.

For the structural analysis, these experimental STM images can be compared to theoretical ones derived from the DFT electronic structure. The author simulated STM images in the spirit of the Tersoff-Hamann approximation for all terminations of MnSi films up to 17 layers in thickness and for both the up and the down stacking. In the following, only the most convincing result of a lengthy combinatorial matching procedure is discussed.

The simulated STM images show a particularly high corrugation for the surface formed by a Mn-sparse layer on top of a Si-dense subsurface layer, being part of the up stacking sequence. We can see from Fig. 3.30 that this film termination has the lowest surface energy under Mn-rich conditions. The bright spots then represent single Mn atoms (cf. Fig. 3.31, up stacking column, top row). Line scans along the long diagonal of the surface unit cell show additional, distinct, smaller maxima at the midpoint between the bright features, which are also observed in the experimental line scans. These smaller maxima are caused by "rings" (marked green in Fig. 3.31, up stacking column, top right) formed by Si-dense and Mn-dense atoms in the subsurface layers, which are centered around the Mn-sparse atom one

Dieses Werk ist copyrightgeschützt und darf in keiner Form vervielfältigt werden noch an Dritte weitergegeben werden.
Es gilt nur für den persönlichen Gebrauch.

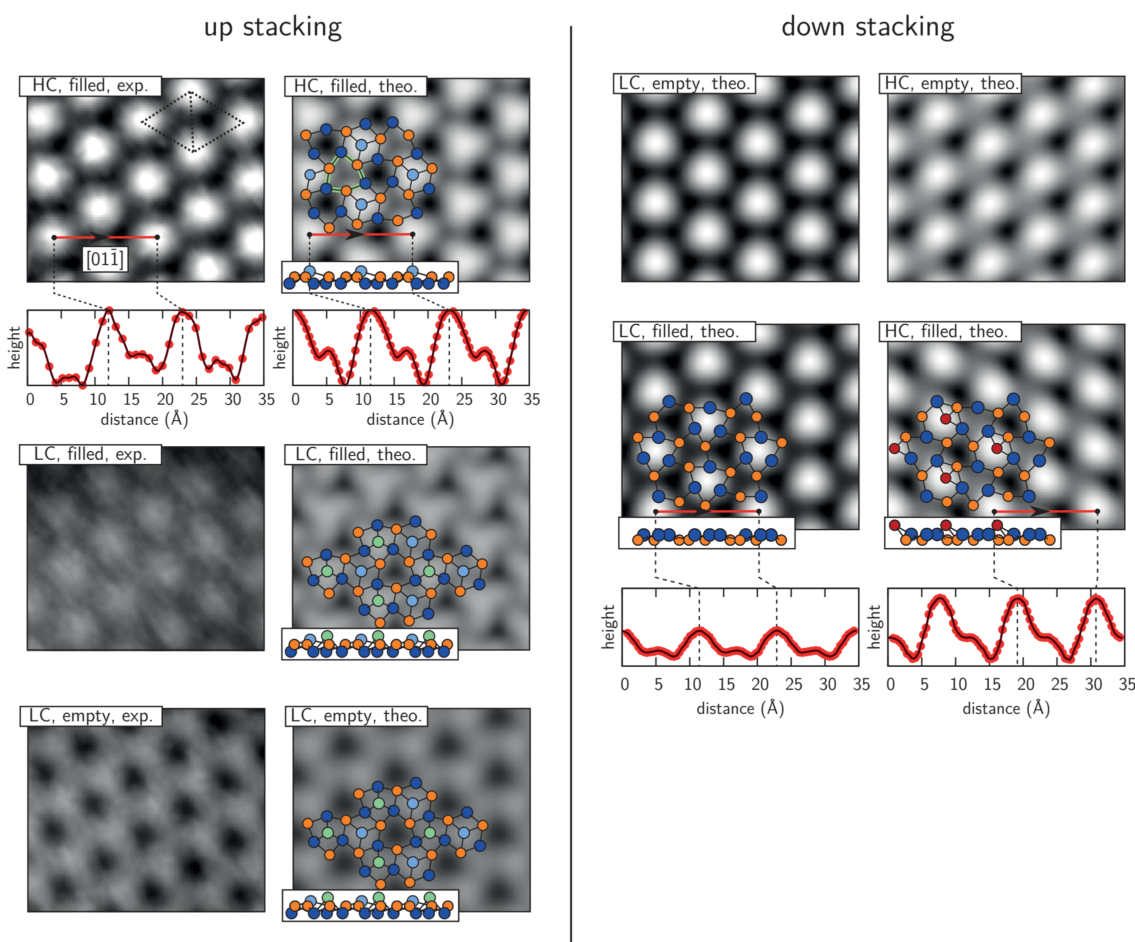

Figure 3.31 – Left column: Comparison of experimental atomic-resolution STM images and theoretical simulations for MnSi/Si(111) films that have been grown by reactive epitaxy. The simulated images correspond to the Mn-sparse and the 2-Mn-sparse terminations of a MnSi film in up stacking. HC and LC surface areas are shown as well as filled- and empty-state images. Experimental and theoretical line scans are compared for the filled-state image of a HC region. A part of the atomic structure is overlaid, in which smaller orange circles mark Si atoms, while bigger blue and green circles mark Mn atoms. The insets show side views of the film atomic structures (cf. Figs. 3.27 and 3.32). The dotted rhombus indicates the surface unit cell. Theoretical bias voltages are $V_{\mathrm{bias}} = -1.5$ V (upper row), $V_{\mathrm{bias}} = -1.4$ V (middle row), and $V_{\mathrm{bias}} = +1.2$ V (lower row); the critical density is always $\varrho_c = 10^{-5}$ / bohr^3. Right column: Simulated empty-state (upper row) and filled-state (middle row) STM images from the LC (left) and HC (right) MnSi film structures in down stacking ($V_{\mathrm{bias}} = \pm 1.2$ V, $\varrho_c = 10^{-6}$ / bohr^3). The lower row shows line scans of the simulated LC and HC filled-state images. In the overlaid atomic structures, smaller orange and red circles mark Si atoms, while bigger blue circles mark Mn atoms. The contrast of the LC images has been increased to provide better clarity.

Dieses Werk ist copyrightgeschützt und darf in keiner Form vervielfältigt werden noch an Dritte weitergegeben werden.
Es gilt nur für den persönlichen Gebrauch.

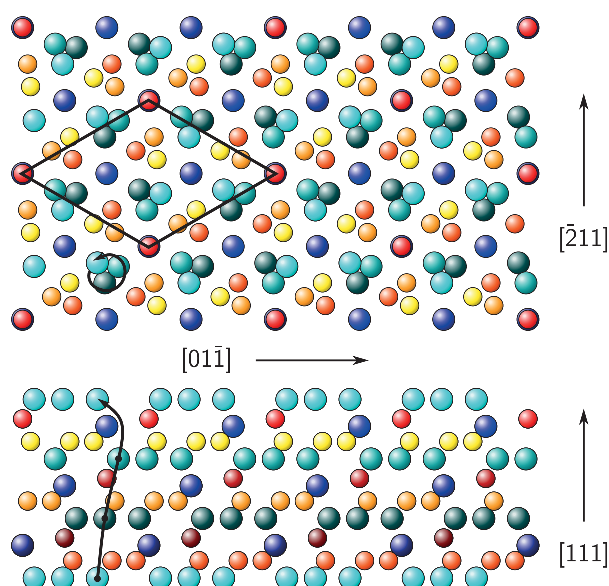

Figure 3.32 – Visualization of different dense and sparse layers of Mn and Si atoms within MnSi in B20 structure. 12 different colors are used to illustrate the 12 different layers in top and side view. Mn (Si) atoms are depicted by big, blue-green (small, red-orange) spheres. The black rhombus indicates the hexagonal unit cell in tow view. The arrows emphasize the chirality of the material, using a set of "rotating" Mn-dense atoms as example.

QL below. (The colorful atomic structure model shown in Fig. 3.32 can be helpful to verify this.)

For the LC areas, agreement with the experimental results is achieved by placing another Mn atom on the HC surface. This termination will be referred to as "2-Mn-sparse" termination in the following (cf. Fig. 3.31, up stacking column, middle row). It corresponds to a Si-sparse surface, which would follow Mn-sparse in the up stacking, but with the topmost Si atom *replaced* by a Mn atom. A peculiar feature of this termination is that the bright spots in the filled-state STM images are transformed into a connected, honeycomblike pattern in the empty-state images (cf. Fig. 3.31, up stacking column, bottom row), which agrees with the experimental observations. While the simulated STM images indicate LC for *all* dense surface terminations, this electronic feature is characteristic for the 2-Mn-sparse termination. It is a nonstoichiometric surface and higher in surface energy than Si-dense (cf. Fig. 3.30, top-left panel), but it may be realized under nonequilibrium conditions during growth. Finally, an important remark is that assigning the LC areas simply to a Si-sparse layer (that is, *without* replacement by Mn) would be inconsistent with its very strong corrugation in the STM simulations and with the experimentally observed fact that the LC regions expand as the Mn coverage is increased.

Films formed by codeposition of Mn and Si

It is now possible to utilize the same matching procedure to demonstrate that the film structure may be significantly different for other growth protocols used in the literature. For instance, MnSi films can also be grown by codeposition of Mn and Si on the Si(111) substrate (either simultaneously or by alternating atomic-layer deposition) followed by an annealing step [109,193,206,213]. With this growth protocol, only a moderate mobility of the deposited atoms is required to establish atomic order in the MnSi films, and one ends up with closed and rather smooth structures, possibly with single-layer or QL steps.

Recently, Azatyan *et al.* [206] also reported on the coexistence of smooth and corrugated regions, but for MnSi films grown by codeposition of Mn and Si and with considerable

Dieses Werk ist copyrightgeschützt und darf in keiner Form vervielfältigt werden noch an Dritte weitergegeben werden.
Es gilt nur für den persönlichen Gebrauch.

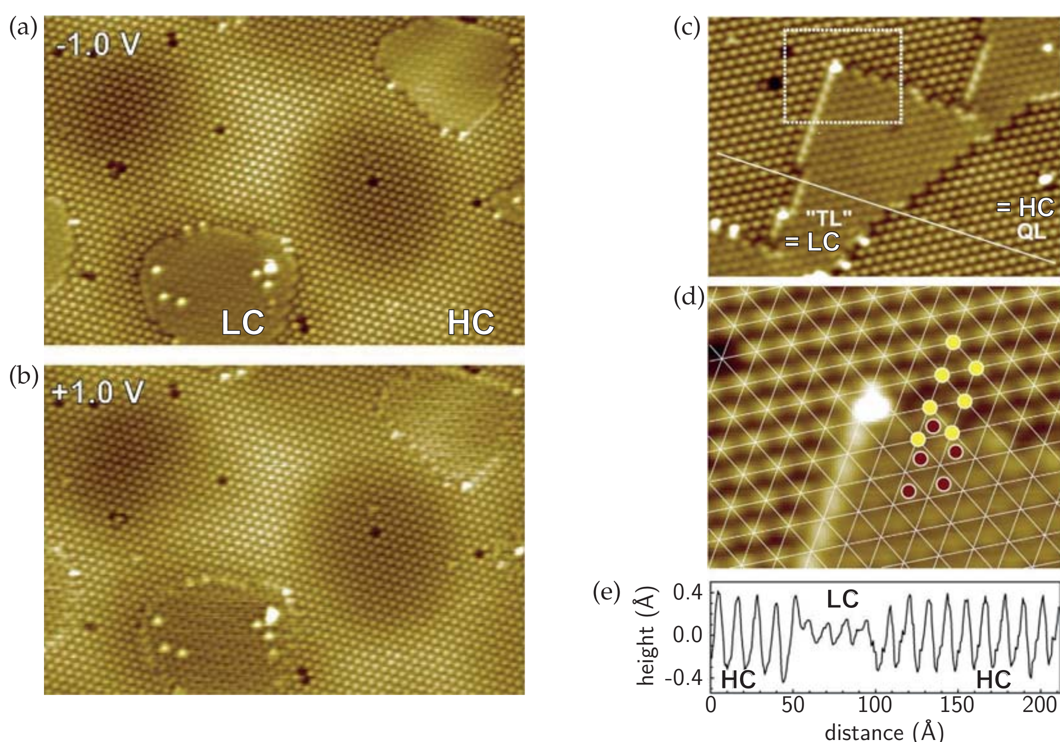

Figure 3.33 – STM images of MnSi thin films on Si(111) formed by codeposition of Mn and Si. Panels (a) and (b) show filled- and empty-state images, respectively (50×34 nm^2). Again, HC and LC surface areas coexist. This can also be seen in panel (c), which shows a second filled-state image (-1.0 V, 20×15 nm^2). (d) Magnification of the area in panel (c) that is marked by the dashed frame. The nodes of the superimposed hexagonal grid coincide with the protrusions of the HC region (yellow circles). Red circles mark the protrusions of the LC region. (e) Line scan along the white line in panel (c), crossing the LC region. — Reproduced with permission from Ref. [206]. © 2011 by Elsevier. Some labels have been added by the author of this thesis.

deviations from the observations that have been discussed above. First, their line scan shown in Fig. 3.33(e) severely differs from the experimental line scans shown above (cf. Fig. 3.31, up stacking column). Especially, the height order of HC and LC is reversed, and the HC valleys are even deeper than the LC valleys. Second, from their analysis of the two surface terminations, as shown in Fig. 3.33(d), one can deduce that HC is indeed *one* layer *above* LC, with the following argumentation: If one centers their superimposed hexagonal grid on the LC peaks (red circles), it becomes obvious that the HC peaks always appear in the center of those triangles that also contain the deepest minima of the LC region, which (as the author of this thesis knows from his simulations) correspond to the crystallographic adsorption sites of the next layer. Third, the "honeycomb transition" under bias voltage reversal is not seen at all in Figs. 3.33(a) and (b).

Without further proof, Azatyan *et al.* suggested in Ref. [206] the following tentative model on the basis of their observations: Starting from the up structure, as already Hortamani *et al.* did in Ref. [114], they assigned the HC areas to a Si-dense layer on top of a Mn-dense layer, the latter corresponding to the LC areas. However, exhaustive comparison with simulated STM images leads the author to question these structural assignments, namely for the following arguments: First, their HC areas cannot be assigned reasonably to the Si-dense

Dieses Werk ist copyrightgeschützt und darf in keiner Form vervielfältigt werden noch an Dritte weitergegeben werden.
Es gilt nur für den persönlichen Gebrauch.

termination of the up stacking due to the weak corrugation this surface exhibits according to the calculations. Moreover, simulated line scans along the long diagonal of the unit cell show clear secondary maxima between the main peaks for the Si-dense termination, which are absent in their experimental line scan [cf. Fig. 3.33(e)]. Second, the assignment of LC areas (observed *below* the HC areas by Azatyan *et al.*) to the Mn-dense termination appears unlikely because of its *extremely* high surface energy in the up stacking, even under Mn-rich growth conditions (cf. Fig. 3.30, top-left panel). A reconciliation of their STM images with the simulated results is only possible if one assumes the down stacking in their films. In this case, their HC STM images best match with simulated images of a Si-sparse layer on a Mn-dense subsurface layer, the latter corresponding to the LC regions. Following this interpretation, the bright spots in the HC (LC) images would arise due to the dangling bonds of single Si atoms (the Mn trimers being seen as one single spot). Simulated STM images of this assignment are shown in the down stacking column of Fig. 3.31. The absence of the honeycomb transition in the simulations strengthens the given interpretation: The LC peaks are distinct and invariant under bias voltage reversal. By comparing the absolute height of minima and maxima of the simulated HC and LC images, one finds that the HC maxima are above the LC maxima, while the HC minima are below the LC minima, in accordance with Azatyan's observations [cf. Fig. 3.31, down stacking column, lower row, and Fig. 3.33(e)]. The shoulders of the HC maxima are caused by Mn trimers in the underlying Mn-dense layer.

Adsorption stability of Mn and Si adatom layers

One can ask the question whether the adatom positions used in (i) the 2-Mn-sparse termination in the up stacking and (ii) the Si-sparse on Mn-dense termination in the down stacking are energetically preferable to other possible adsorption sites, and thus thermodynamically more stable. The answer can be given by calculating the adsorption energies, which can be defined as

$$\varepsilon = -\left(E_{\text{slab}} - E_{\text{sub}} - N_{\text{Mn}}E_{\text{Mn}}^{\text{atom}} - N_{\text{Si}}E_{\text{Si}}^{\text{atom}}\right), \tag{3.13}$$

where E_{slab}, E_{sub}, and $E_{\text{Mn/Si}}^{\text{atom}}$ are the total energies of the film structure with adsorbate, the reference film structure, and the isolated atomic elements, respectively. $N_{\text{Mn/Si}}$ are the numbers of adsorbed Mn and Si atoms. By this definition, ε is the adsorption energy per unit cell, which includes one or two adsorbed atoms in the following.

The up-Si-dense terminating layer has three principal adsorption sites which are referred to as A, B, and C in the following. The Si-Si distance in the surrounding Mn-Si rings increases from A to C (cf. Fig. 3.34, upper row). In the case of a Mn-sparse termination, site B is occupied by a Mn atom, continuing the crystal structure of MnSi(111). An additional Mn atom can now occupy site C (which would be the 2-Mn-sparse termination) or site A. Furthermore, a rearrangement of the Mn atoms to sites A *and* C is imaginable, leaving site B unoccupied. However, the adsorption energies (cf. Table 3.8) tell us that there is a clear preference of the 2-Mn-sparse configuration B+C.

Analogously, the down-Mn-dense terminating layer also has three principal adsorption sites A, B, and C (cf. Fig. 3.34, lower row). Again, site B corresponds to the Si adsorption site that continues the crystal structure. This site B exhibits a significantly higher adsorption energy than sites A and C, as one can see in Table 3.9. It is interesting to note that the center of site B proves to be unstable: The Si atom moves out of the center and approaches two of the three surrounding Mn atoms, thereby shifting charge from its p_z orbital (which is

Dieses Werk ist copyrightgeschützt und darf in keiner Form vervielfältigt werden noch an Dritte weitergegeben werden.
Es gilt nur für den persönlichen Gebrauch.

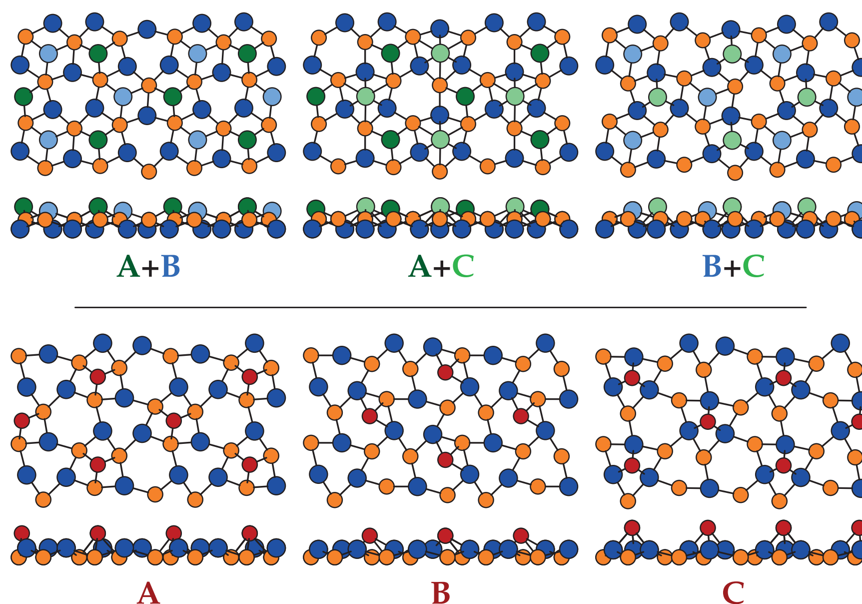

Figure 3.34 – Top and side views of structurally optimized Mn and Si adatom layers on different MnSi/Si(111) surface terminations. Upper row: Mn atoms on the up-Si-dense surface. The light blue circles depict adsorbed Mn atoms belonging to the subsequent Mn-sparse layer (site B), whereas dark green and light green circles represent Mn atoms sitting on the noncrystallographic adsorption positions (sites A and C, as in Fig. 3.31, up stacking column). Configuration B+C corresponds to the 2-Mn-sparse case discussed before. Lower row: Si atoms (red circles) on the down-Mn-dense surface. Site B corresponds to the Si-sparse termination.

Table 3.8 – Adsorption energies ε of two Mn layers on the up-Si-dense surface (cf. Fig. 3.34, upper row). ΔE is given relative to configuration B+C. Configurations A+B and B+C can alternatively be interpreted as single-Mn-adatom layer on the Mn-sparse surface termination.

	Adsorption energy (eV)		
Sites	1 Mn / Mn-sparse	2 Mn / Si-dense	ΔE (eV)
A+B	2.73	6.73	0.58
A+C	–	6.77	0.54
B+C	3.31	7.31	0.00

Table 3.9 – Adsorption energies ε of a single Si layer on the down-Mn-dense surface (cf. Fig. 3.34, lower row). ΔE is given relative to site B. The energy of a laterally fixed atom at the center of site B is also shown.

Site	Adsorption energy (eV)	ΔE (eV)
A	4.44	0.36
B (center)	4.70	0.10
B	4.80	0.00
C	4.51	0.29

Dieses Werk ist copyrightgeschützt und darf in keiner Form vervielfältigt werden noch an Dritte weitergegeben werden.
Es gilt nur für den persönlichen Gebrauch.

oriented perpendicular to the surface) into the lateral p_x and p_y orbitals and increasing its adsorption energy by 0.1 eV.

Summarizing, the calculated energies clearly show that other arrangements of the surface atoms than those discussed above as most probable surface terminations are energetically unfavorable and thus quite improbable.

In Ref. [206], additional Si was deposited on the HC area at room temperature without further annealing. As we have seen before, this HC region can be assigned to the Si-sparse surface in the down stacking. From calculated adsorption energies one can deduce that additional Si atoms on this surface will predominantly occupy site C, with an energy preference of about 0.2 eV over site A or a rearrangement of the Si atoms to sites A and C (not shown in the tables). Due to the tightness of the underlying Mn triangle, the Si adatom at this position sits 0.6 Å higher than the Si-sparse atom at site B (similar to Fig. 3.34, lower row, site C). If one simulates STM images for this structure (not shown), one finds discrete peaks at the Si adatom positions and no qualitative differences between filled- and empty-state images. Moreover, the STM height difference between the Si-sparse atom peak and the Si adatom peak is even 0.8 Å. This shows that there are no electronic effects which "hide" the adatom or lower the contrast, and that the adatom (or adatom layer) should be clearly visible in experimental STM images. This agrees with the observations reported in Ref. [206], and thus provides a further corroboration of the structural assignments which are put forward in this section.

Growth conditions and the validity of thermodynamic arguments

The analysis in the preceding part of the section has shown that MnSi films grown by codeposition of Mn and Si are clearly different from those grown by reactive epitaxy: The structures of Azatyan *et al.* [206] must be interpreted as down structures different from the up structures fabricated by the author's collaborators [15].

From the structural assignments made on the basis of experimental and theoretical STM images on the one hand and the calculated surface energies γ on the other hand, one can now draw conclusions about the prevailing growth conditions. In the case of reactive epitaxy, the films apparently grow under quite Mn-rich conditions, which corresponds to the left side of the surface energy plots in Fig. 3.30 on page 96. For such values of μ_{Si}, the Mn-sparse termination in up stacking is lowest in energy, consistent with its observation in the HC regions. The deposition of more Mn leads to the 2-Mn-sparse termination, which is only by about 10 meV/Å^2 higher in surface energy. The Si-dense termination, which lies energetically between them, is not observed. A possible explanation for this experimental fact is that the availability of Si is low: Without additional Si deposition, all Si atoms have to diffuse from the substrate into the island or film structures, which leads to deep holes or craters in the substrate [193]. Even if the films are not yet closed and Si atoms from the substrate can still diffuse more easily to the surface, this process is too slow to establish a Si-dense layer during the annealing period used in the film preparation. Thus, μ_{Si} should be interpreted as an effective, *local* chemical potential modeling the quasi-equilibrium in certain surface regions, not the equilibrium of the total structure with the Si substrate.

In contrast, codeposition of Mn and Si makes the diffusion of Si from the substrate mostly unnecessary. Films in down stacking will be terminated by Si-dense or Mn-dense layers

Dieses Werk ist copyrightgeschützt und darf in keiner Form vervielfältigt werden noch an Dritte weitergegeben werden.
Es gilt nur für den persönlichen Gebrauch.

in the first place, depending on the local value of the chemical potential.[26] The observed Mn-dense termination is favored for $\mu_{\text{Si}} - E_{\text{Si}} < -0.45$ eV, whereas a slightly more Si-rich surface may be realized by terminating the down stacking with a Si-sparse layer, which has the second-best surface energy under Mn-rich conditions (cf. Fig. 3.30).

Additional information about the film evolution during growth can be acquired from the formation energies E^{form} shown in Fig. 3.30. Superimposed on the overall downward slope, there are structures displaying the QL periodicity. The film growth can be kinetically blocked by the local maxima in E^{form} corresponding to the Mn-dense and Mn-sparse termination for the up and down stacking, respectively. This is consistent with (and a potential explanation for) the well-known QL terrace structure of MnSi films observed in previous studies [192, 193, 195]. On the other hand, the local minima of E^{form} are in line with the experimentally observed film terminations: For the down stacking, the Si-sparse and Mn-dense terminations locally have the lowest and second-lowest E^{form}. For the up stacking, the local minima of E^{form} occur for Mn-sparse and Si-sparse terminations. This is again in agreement with the observed structures if one takes into account that the (energetically only slightly higher) 2-Mn-sparse structure is formed instead of the Si-sparse structure simply due to lack of available Si atoms. Moreover, one can see from the formation energies in Fig. 3.30 why MnSi films consisting of only one QL are rarely observed in experiments [192, 193, 195]: Film formation from the bulk chemical elements is endothermic ($E^{\text{form}} - E^{\text{form}}_{\text{sub}} > 0$) for these very thin films.

Although the calculated surface and formation energies are consistent with the presented structural assignments, the author wants to emphasize that these concepts are strictly valid only for systems in thermodynamic equilibrium. Si, GaAs, or GaN, which are typically grown at temperatures between 550 and 750 °C, so that material, e.g. As, desorbs into the gas phase [214–216], are examples for which this type of description is close to reality. For the growth of epitaxially strained MnSi films on Si(111), the situation is different, although thermodynamic reasoning can still serve as a guideline: The thin films are metastable structures, since $\Delta\gamma = \gamma_{\text{s}} + \gamma_{\text{i}} - \gamma_{\text{sub}}$ is always positive, as one can see from Fig. 3.30. As a consequence, Volmer-Weber-like island formation is preferred over film growth (e.g., Frank-van-der-Merve growth occurs for $\Delta\gamma < 0$). This metastability restricts the growth temperatures to quite low values of about 300 °C in order to *prevent* MnSi from forming islands [114, 193, 195] instead of thin films. The DFT adsorption energies ε of Mn and Si atoms on (all) MnSi(111) surfaces calculated by the author are, however, in the range of 3 – 6 eV per atom. Thus, equilibrium between the film structure and the gas phase *cannot* be established. Since the low temperatures also reduce the atomic mobility on the surface, a *global* equilibrium of film and substrate is hard to achieve (as stated above), and the appearance of coexisting areas with different surface terminations of comparable energy becomes quite probable.

3.6.4 The 3 × 3 reconstruction of MnSi/Si(111)

In addition to surfaces with $\sqrt{3} \times \sqrt{3}$ periodicity, a 3×3 reconstruction has recently been observed for the first time [17]. It occurs at very early growth stages (for low Mn coverage) on small MnSi islands. This finding is quite interesting, since metals (unlike semiconductors)

[26]Note that here, for closed films, the surface termination will depend more strongly on the deposited Mn and Si coverages than in the case of reactive epitaxy.

Dieses Werk ist copyrightgeschützt und darf in keiner Form vervielfältigt werden noch an Dritte weitergegeben werden.
Es gilt nur für den persönlichen Gebrauch.

usually show no surface reconstruction (except for some famous counterexamples like Ir, Pt, and Au).

After the deposition of 0.1 ML of Mn on a clean Si(111)-(7×7) surface and subsequent annealing at 400 °C for 1 min, one observes small MnSi islands and Mn nanoclusters in STM images [cf. Fig. 3.35(a)]. The Mn nanoclusters form predominantly in the faulted halves of the Si(111)-(7×7) surface unit cells; the rate is approximately 95 % [151, 217, 218]. While recent DFT calculations studied only the faulted halves as a consequence [218], one can speculate that the energetic situation for Mn cluster formation will be less favorable in the unfaulted halves.

For a Mn coverage of approximately 0.8 ML, larger MnSi islands of different height form [cf. Fig. 3.35(b)]. Their surfaces are mostly HC with $\sqrt{3}\times\sqrt{3}$ periodicity. One can see how the topmost Si bilayer atoms in the vicinity of the islands are incorporated into the latter. The line scans [cf. Fig. 3.35(d)], compared to the Si(111)-(7×7) atomic structure (cf. Fig. 3.5, side view, on page 58), demonstrate that it is really one bilayer.[27] In addition to the HC regions, coexisting areas with a 3×3 pattern appear. They are found in an ordered and a disordered version [cf. Fig. 3.35(c)]. The ordered regions exhibit a hexagonal pattern of strong protrusions. The rhombi formed by those protrusions consist of two clearly different halves: One half contains a shallow minimum (like a saddle point), the other half a deep minimum. The line scans show that these areas appear approximately 0.5 Å below a HC $\sqrt{3}\times\sqrt{3}$ surface.

In the previous part of the section, the Mn-sparse surface termination of a MnSi film in up stacking has been assigned to the HC surfaces of islands or films grown by reactive epitaxy. It is thus reasonable to assume that the lower-lying (3×3)-reconstructed areas are terminated by a Si-dense layer (cf. Fig. 3.27 on page 92). However, such a termination would lead to a $\sqrt{3}\times\sqrt{3}$ surface pattern, as mentioned above, unless some reconstruction occurs. For instance, the Si-dense layer can be incomplete. This idea is used in the following as starting point for the determination of the atomic structure of the (3×3)-reconstructed areas.

The 3×3 surface unit cell contains up to 9 Si atoms (forming three trimers) in a Si-dense terminating layer on a Mn-dense subsurface layer. Their positions are determined by the B20 crystal structure [cf. Fig. 3.36(a)], and test calculations have shown that other positions are energetically unfavorable. One can now calculate total energies [and thus adsorption energies, similar to Eq. (3.13)] for a number of Si adatom configurations on these sites with different Si densities ranging from 3 – 9 adatoms per 3×3 surface unit cell.

The adsorption energies (cf. Table 3.10) show that three Si atoms prefer to adsorb as homogeneously distributed adatoms, instead of forming a complete and isolated trimer. On the other hand, six Si atoms prefer to adsorb as two trimers, instead of forming three incomplete trimers. This interaction effect can also be seen in the fact that the adsorption energy of two trimers is about 30 meV per Si atom higher than the energy arithmetic mean between one and three Si trimers.

The calculations show an interesting effect for the two-Si-trimer structure, which is displayed in Fig. 3.36(b). The two initially equally-sized trimers relax differently and become inequivalent: while one enlarges, the other shrinks in diameter. The final Si-Si distances are 3.25 Å and 2.66 Å, respectively. For comparison, the distances are 2.76 Å in an isolated trimer and 3.08 Å in the Si-dense case (three trimers). While the removal of every third Si

[27]Note that (i) a Si-Si bond has an experimental length of 2.35 Å, (ii) the topmost "reconstructed bilayer" of Si(111)-(7×7) is somewhat higher, and (iii) a single MnSi QL has a height of about 2.54 Å.

Dieses Werk ist copyrightgeschützt und darf in keiner Form vervielfältigt werden noch an Dritte weitergegeben werden.
Es gilt nur für den persönlichen Gebrauch.

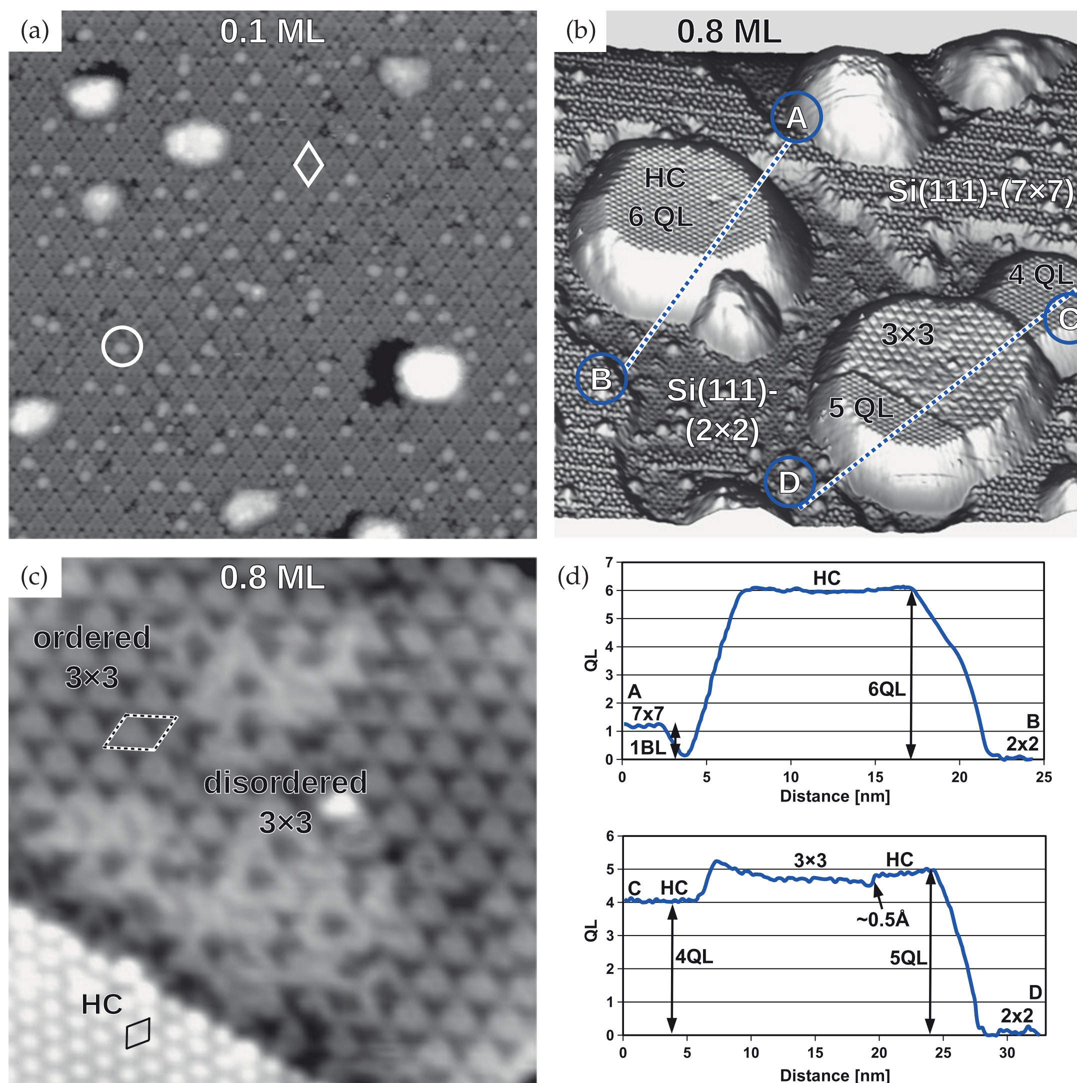

Figure 3.35 – STM images of Mn nanoclusters and MnSi islands forming on a clean Si(111)-(7 × 7) surface for low Mn coverage (0.1 and 0.8 ML). The circle in (a) marks one of the Mn nanoclusters [151, 217, 218] that form preferably (with a rate of approximately 95 % according to Ref. [151]) in the faulted halves of the Si(111)-(7 × 7) surface unit cells (white rhombus). (b) MnSi islands with coexisting $\sqrt{3} \times \sqrt{3}$ and 3 × 3 areas. (c) Magnification of the bottom-right MnSi island shown in (b). (d) Surface height profiles along the dashed lines in panel (b). The image sizes are 50 × 50 nm^2 in (a) and (b) and 12 × 12 nm^2 in (c). After Mn deposition at room temperature, both samples have been annealed at 400 °C for 1 min. Bias voltages range from −1.6 V to −1.8 V; the constant tunneling current is 0.2 nA. — Reproduced from Ref. [17]. © 2013 by Elsevier.

Dieses Werk ist copyrightgeschützt und darf in keiner Form vervielfältigt werden noch an Dritte weitergegeben werden.
Es gilt nur für den persönlichen Gebrauch.

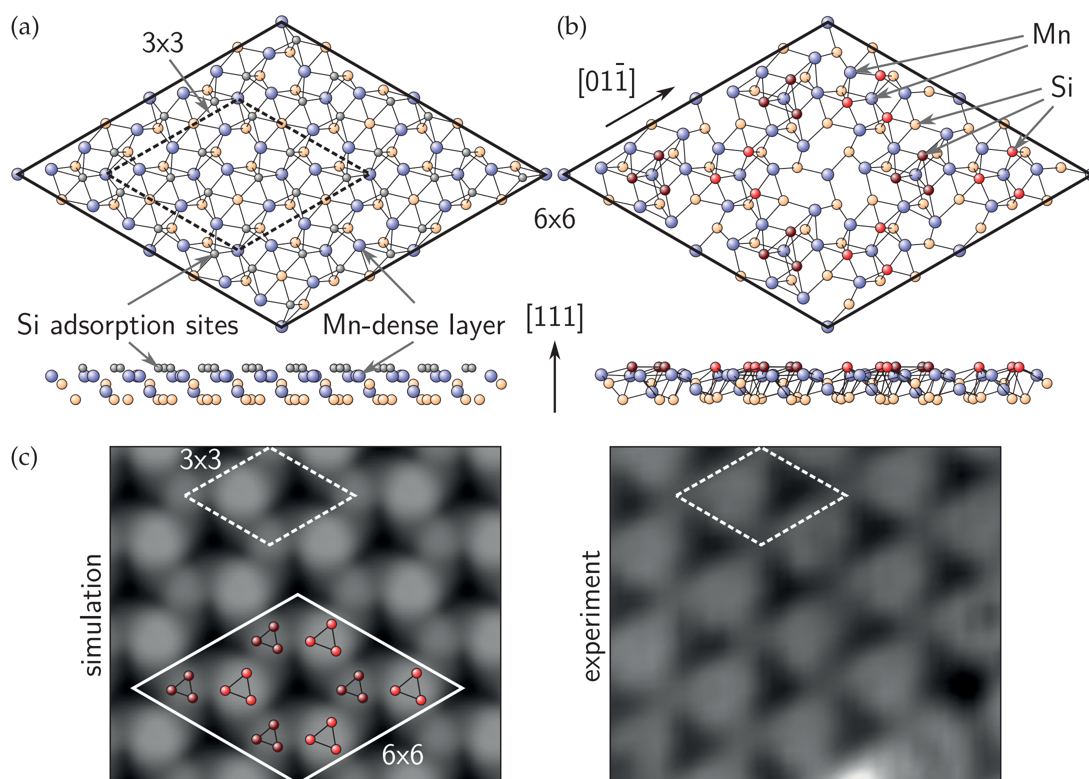

Figure 3.36 – (a) Top and side view showing the possible crystallographic Si adsorption sites (small gray spheres) on a Mn-dense subsurface layer in a 6×6 unit cell. A 3×3 unit cell containing 9 Si adsorption sites is marked by dashed lines. Blue and orange spheres depict Mn and Si atoms, respectively. (b) Atomic structure of the 3×3 two-Si-trimer model, shown in the same 6×6 unit cell for clarity. The smaller (larger) Si trimer is depicted by dark (bright) red spheres. (c) Comparison of a simulated STM image of the two-Si-trimer structure (left) and a detail of the experimental STM image from Fig. 3.35(c) (right). In analogy to (b), the 6×6 unit cell containing the topmost Si trimers is shown in white solid lines. The 3×3 unit cell (white dashed lines) is positioned as in (a). A bias voltage of -1.0 V (filled states) and 10^{-6} / bohr^3 critical density are used in the simulated STM images. — Reproduced from Ref. [17]. © 2013 by Elsevier.

Table 3.10 – Adsorption energies of different Si adatom configurations on the Mn-dense surface termination of a MnSi/Si(111) film in up stacking.

Si adatom configuration	Adsorption energy (eV)
3 Si, forming one trimer	5.643
3 Si, scattered on the surface	5.712
5 Si, one trimer, two atoms on different positions C1 – C5, see Ref. [17]	5.782 – 5.720
6 Si, three incomplete trimers	5.693
6 Si, two-Si-trimer structure	5.755
9 Si, three trimers, Si-dense	5.806

Dieses Werk ist copyrightgeschützt und darf in keiner Form vervielfältigt werden noch an Dritte weitergegeben werden.
Es gilt nur für den persönlichen Gebrauch.

trimer trivially increases the surface periodicity from $\sqrt{3} \times \sqrt{3}$ to 3×3, there is no *a priori* reason why the two remaining trimers should resize so significantly different. Actually, we can speak of a real reconstruction here, despite the metallic character of MnSi.

As a consequence of the different Si trimer size, simulated STM images clearly reproduce the three different height levels observed in experiment. The filled-state image in Fig. 3.36(c) shows that the dark part of each 3×3 surface unit cell corresponds to the missing Si trimer, while the brightest peak corresponds to the enlarged Si trimer (bright red spheres). The actual height (in the atomic structure) of both Si trimers is similar. Their different corrugation in the filled-state STM image is a consequence of the electronic structure: The smaller Si trimer is more strongly bound than the larger one, and thus the larger Si trimer has more states close to the Fermi energy. The empty-state STM image is not shown here, since it looks similar to the filled-state STM image.[28]

It is possible to find comparable adsorption energies to the six-atom case (two-Si-trimer structure) already for five Si atoms (cf. Table 3.10). By fixing one Si trimer and distributing the two remaining Si adatoms on the six unoccupied Si adsorption sites [cf. Fig. 3.36(a)], 15 different possibilities emerge, which reduce to five inequivalent cases due to the C_3 symmetry of the structure. The corresponding simulated STM images (not shown here; see Ref. [17]) still show a clear overall 3×3 surface periodicity.[29] The disordered 3×3 regions could thus correspond to random distributions of such adatom configurations. Probably, the system approaches the formation of a complete Si-dense layer in these areas.

Finally, it should be remarked that the presented model structure offers a kinetic, not a thermodynamic explanation for the formation of the 3×3 reconstruction. It would always be energetically more favorable to accumulate all Si adatoms on the surface in one region, forming a Si-dense termination there and leaving the residual areas terminated by the Mn-dense layer. On the other hand, the 3×3 reconstruction is not observed on large scales, but just on small islands where energy arguments alone can be misleading. Other ordering mechanisms related to confinement, island edge proximity, or surface tension might exist. It is thus acceptable to use the simulated STM images as primary guide for the structural assignment.

3.7 Magnetic properties of MnSi/Si(111) thin films

We have seen in the preceding sections that MnSi shows the most significant response to epitaxial strain, and we have learned about the atomic structure in which thin films of MnSi in B20 structure grow on Si(111) and how the stacking sequence can be influenced by the growth protocol. In this section, the magnetic properties of such heterostructures will be discussed, varying the film thickness and the magnetic configuration.

It has been argued in Sec. 3.4 that the behavior of thicker films can be described by the strained bulk material. Decreasing the film thickness increases the relevance of surface, interface, and confinement effects. Since the repetition period of the layer structure is quite

[28]For MnSi surfaces, the author found the general trend that filled-state STM images are more “reliable” for height arguments. Height differences derived from filled-state images follow the atomic lattice spacings far more closely than those derived from empty-state images, since the latter are more strongly influenced by electronic effects and can be misleading. Although this pitfall can be circumvented by DFT simulations, the author strongly recommends to use filled-state images for measurements of height differences.

[29]The free energy of such disordered adatom configurations can benefit from configurational entropy [139]. Here this effect has been found to be negligible in the relevant temperature range.

Dieses Werk ist copyrightgeschützt und darf in keiner Form vervielfältigt werden noch an Dritte weitergegeben werden.
Es gilt nur für den persönlichen Gebrauch.

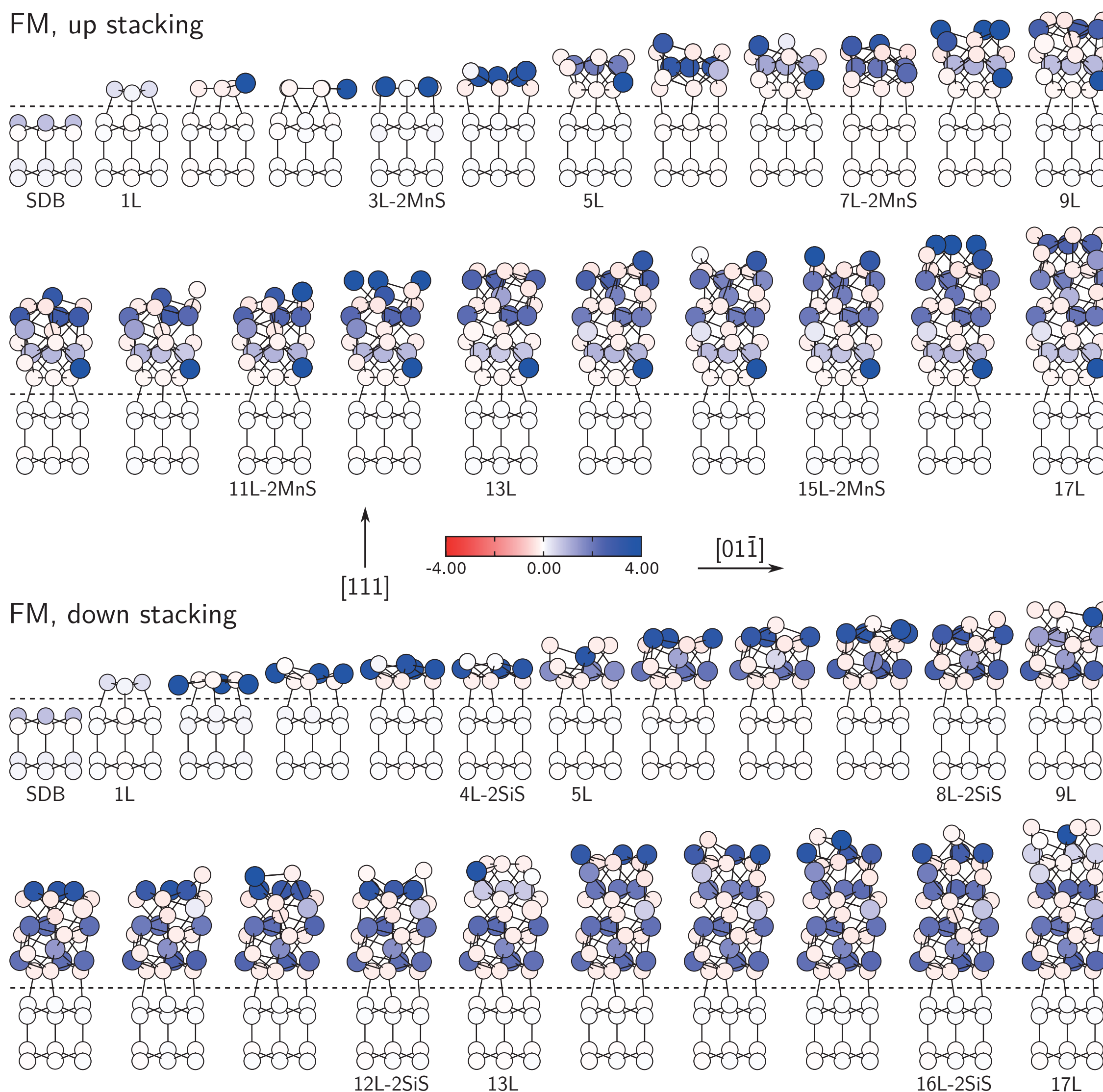

Figure 3.37 – Overview of the atomic and magnetic structure of MnSi films of successively increasing thickness in up and down stacking, shown together with two bilayers of the Si(111) substrate. Here the Mn spin alignment is always parallel (FM). Small, almost white (big) spheres depict Si (Mn) atoms. The color encoding shows the local magnetic moments (in μ_B). Note that also single atoms represent complete layers of similar atoms. The stacking sequences are Si-dense, Mn-sparse, Si-sparse, Mn-dense (up stacking) and Si-dense, Mn-dense, Si-sparse, Mn-sparse (down stacking). Both cases start from a relaxed Si(111)-SDB surface (3 μ_B per $\sqrt{3} \times \sqrt{3}$ cell). The nonstoichiometric surface terminations 2-Mn-sparse (2MnS, up stacking) and 2-Si-sparse (2SiS, down stacking) are also shown.

Dieses Werk ist copyrightgeschützt und darf in keiner Form vervielfältigt werden noch an Dritte weitergegeben werden.
Es gilt nur für den persönlichen Gebrauch.

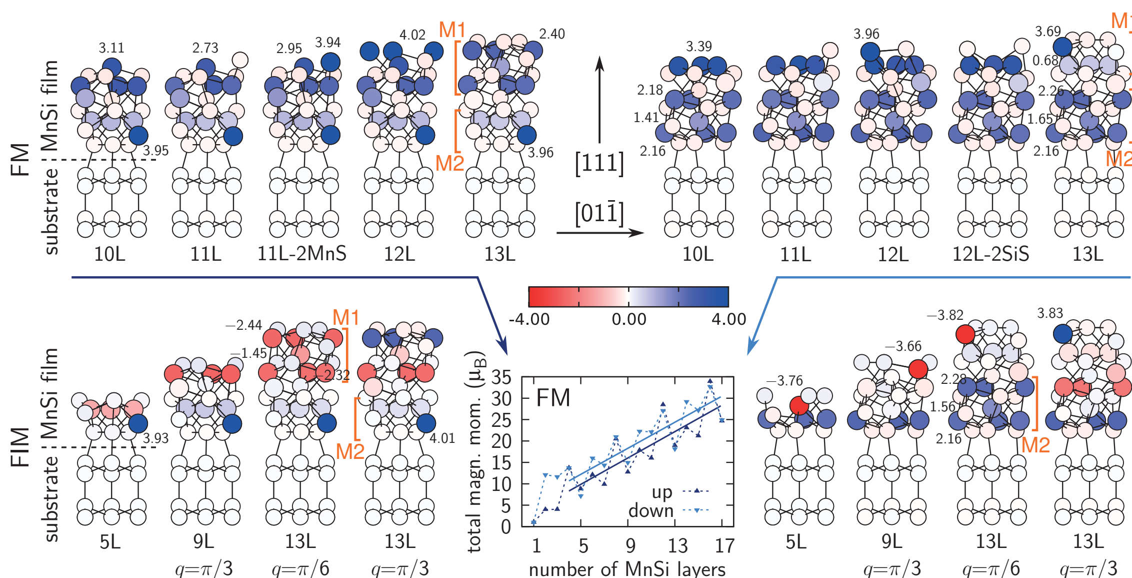

Figure 3.38 – Atomic structures and magnetic configurations of MnSi thin films of selected thickness together with two bilayers of the Si(111) substrate. The left (right) structures reflect the up (down) MnSi stacking. The upper (lower) row shows configurations of parallel (antiparallel) Mn spin alignments. Small, almost white (big) spheres depict Si (Mn) atoms. As in Fig. 3.37, the color encoding shows the local magnetic moments (in μ_B). For convenience, the value is explicitly written out for selected Mn atoms. M1 and M2 denote two spin motifs that arise frequently in the magnetic configurations. The inset shows the dependence of the total magnetic moment on the number of film layers n for FM alignment and two linear fits for up and down stacking.

large (12 layers, see above), these effects will not be restricted to ultrathin films, but may become noticeable even in films that are a few nanometers thick.

In this section, film structures with up to 17 layers of MnSi on Si(111) are discussed. Figure 3.37 provides an overview of the optimized atomic and magnetic structure in epitaxial MnSi films with FM (i.e., parallel) spin alignment. A significant interface difference exists between the up and the down stacking, where the lengths of the Si-Si bonds connecting the substrate and the thin film are 2.36 Å and 2.40 Å, respectively. On the other hand, their dependence on the film thickness is negligible (± 0.01 Å). The distances at the interfaces compare well with those found for the "sandwich structures" discussed on pages 89 ff., although the spread is slightly larger here. For comparison, the Si-Si bond length in PBE bulk Si is 2.37 Å. Additionally, some nonstoichiometric structures are shown: 2-Mn-sparse, following Si-sparse in up stacking, and 2-Si-sparse, following Mn-sparse in down stacking.

The dependence of the local magnetic moments on the film thickness can be seen in Fig. 3.38 for selected structures. Obviously, the Mn moments at both the interface and the surface deviate strongly from their values in strained bulk material (cf. Table 3.6 on page 77). This is especially striking for the Mn-sparse atom close to the interface in up stacking. One can also see the weak induced antiparallel Si moments in the MnSi films. The values of the interface Mn magnetic moments converge quickly with increasing interface-surface spacing. Any Si surface termination reduces the magnetic moment of the subsurface Mn layer, especially a Si-dense termination.[30] Figure 3.37 shows that the surface behavior of the magnetic

[30]This holds at least for films of more than 9 layers thickness.

Dieses Werk ist copyrightgeschützt und darf in keiner Form vervielfältigt werden noch an Dritte weitergegeben werden.
Es gilt nur für den persönlichen Gebrauch.

Table 3.11 – Energy differences (meV) per hexagonal $\sqrt{3} \times \sqrt{3}$ supercell of different FIM configurations (cf. Fig. 3.38, bottom row) with respect to FM configurations in MnSi thin films on Si(111). Positive values indicate a more stable FM configuration. The "bulk" values are expectations extrapolated from the strained-bulk results obtained in Sec. 3.4.

Stacking	5L	9L, $q = \pi/3$	13L, $q = \pi/6$	13L, $q = \pi/3$
Up	+215	−50	−45	−32
Down	+20	−136	−126	−76
Bulk	+139	+278	+416	

moments is repeated periodically. Moreover, one can see that the Mn-sparse surface termination in down stacking is unstable: The topmost Mn atom always lowers its vertical position below that of the Si-sparse atom.

The total magnetic moment of the considered film structures increases with each new layer of Mn and decreases again slightly as the successive Si layer is deposited, which can be seen from the inset in Fig. 3.38. Fitting the total magnetic moments as functions of the number of MnSi layers n to linear functions $f(n) = an + b$, separately for up and down stacking, provides the slopes $a = 1.54\ \mu_B$ ($1.52\ \mu_B$) and the offsets $b = 2.15\ \mu_B$ ($4.58\ \mu_B$) for up (down) stacking. The fitted slopes are already very close to the values obtained for bulk material under strain (cf. Table 3.6 on page 77). The different offsets are due to the different interface magnetic structure of up and down stacked films (cf. Fig. 3.38 and Table 3.7 on page 91). The higher offset b found for the down stacking is consistent with the higher magnetic moments at the d-d interface.

Similar to Sec. 3.4, one can now simulate different antiparallel (FIM) spin configurations within the collinear approximation. This has been done for film structures with 5, 9, and 13 layers of MnSi in up and down stacking, all being terminated by a Si-dense layer (Fig. 3.38, lower row). Since the 5-layer ultrathin films contain just two Mn layers, there are only two magnetic configurations: parallel or antiparallel. For the 9- and 13-layer structures, the author simulated cosine- and QL-shaped magnetic orderings starting from initial moments that follow Eq. (3.8), page 76, with $q = \pi/3$ and Eq. (3.9), page 78. In the 13-layer structures, $q = \pi/6$ has been used in addition, which results in a single smooth flip of the magnetic moment direction. In all cases, the QL AFM pattern was unstable and converged to the cosine pattern with $q = \pi/3$. This is in contrast to the bulk case, where the perfectly compensating QL AFM configuration is at least metastable, as discussed in Sec. 3.4.

The energy differences of these FIM configurations with respect to a FM alignment in structures of similar thickness can be seen in Table 3.11. The ultrathin 5-layer structures, especially the one in up stacking, prefer a parallel spin alignment. Quantum confinement effects in the film are very strong in this case. For thicker films, the situation is surprisingly different: The FIM configurations are *lower* in energy than the FM ones, independent of the stacking. Both up and down 9-layer structures benefit most from the magnetic moment flip; the energy difference is smaller for the 13-layer structures. Furthermore, in the 13-layer structures, a double flip with $q = \pi/3$ is less favorable than a single flip with $q = \pi/6$. For even thicker films, the energy benefit of a partially compensating magnetic order will presumably decrease further, finally turning into a preference of unidirectional alignment.

Dieses Werk ist copyrightgeschützt und darf in keiner Form vervielfältigt werden noch an Dritte weitergegeben werden.
Es gilt nur für den persönlichen Gebrauch.

It is interesting to compare these results to expected values that can be extrapolated from the strained-bulk results obtained in Sec. 3.4 by multiplication with the number of MnSi formula units contained in the film structures (cf. Table 3.11). For 5 layers in up stacking, the FM configuration is more stable than expected, while it is much weaker than expected for the down stacking. For 9 layers, the energy spacing FIM-FM is not only negative, but also smaller in absolute value than the expectation. This is even more pronounced for 13 layers.

The author confirmed the reliability and reproducibility of the presented results by performing a structural relaxation with FM spin orientation starting from FIM $q = \pi/6$ final coordinates for a 13-layer structure. The result agreed with the original FM calculation, which shows that indeed the magnetic structure is responsible for the energy differences.

In the different parallel and antiparallel magnetic configurations, certain recurring spin motifs can be identified, especially in the 13-layer structures (cf. Fig. 3.38). Of course, the motifs can appear in a spatial- and spin-inverted form. The magnetic pattern of the 13-layer down structure resembles strongly an upside-down version of its counterpart in up structure, although the inequivalent interface and surface are interchanged. Even the total magnetic moments are very similar. A major difference for both up and down stacked 13-layer films between $q = \pi/6$ and $q = \pi/3$ is the parallel and antiparallel spin orientation in the upper layers (motif M1). Thus, the FM order in motif M1 is presumably responsible for the lower energy of the $q = \pi/6$ configuration.

The conclusions from the aforementioned observations are twofold: First, the magnetic ordering temperature of most of the shown thin films will be lower than in strained bulk (thicker films). Second, for films below a certain thickness, the total magnetic moment will deviate significantly from a rough proportionality to the number of film layers. Note that all magnetic configurations studied here exhibit a sizable total magnetic moment that can be measured in the experiment, even those with an antiparallel spin configuration. These conclusions are in line with the experimental observations of Karhu *et al.* [108], whose measurements show a critical film thickness of about 6 nm, corresponding to approximately 95 layers, below which the ordering temperature T_C and the saturation magnetization M_{sat} drop below their respective bulk values. The 5-layer structures are beyond their experimental scope. Moreover, a significant deviation of the normalized remanent magnetization from the expected behavior in helical magnets,

$$M_r/M_{sat} \sim \sin(\zeta)/\zeta,$$

can be seen, where ζ is proportional to the film thickness n [108, 109]. Karhu *et al.* argued that defects could be responsible for their observations [108]. Here we see that the reasons are more systematic and lie within the electronic structure of MnSi, which is in a surprising way sensitive to quantum confinement and/or interface/surface effects.

Note that no claim is made here concerning the spatial direction of the magnetic moments, but just about their magnitude, relative orientation, and coupling. The magnetization will certainly lie in-plane, fixed by magnetic and shape anisotropy, and rotate helically around the [111] film normal. No remanent out-of-plane magnetization has been measured in the experiments of Karhu *et al.* [109].

Dieses Werk ist copyrightgeschützt und darf in keiner Form vervielfältigt werden noch an Dritte weitergegeben werden.
Es gilt nur für den persönlichen Gebrauch.

3.8 Interface and surface properties of Mn_5Si_3/Si(111)

It is not clear *a priori* that deposition of Mn on a Si(111) substrate with subsequent annealing necessarily leads to Mn monosilicide formation: Different intermetallic phases with different stoichiometry may be formed, since Si atoms can diffuse between film and substrate. Prior to finding a structural model based on a certain silicide it is therefore important to exclude the formation of other silicides with a different stoichiometry.

Experimentally, the film stoichiometry can be determined, for instance, by Rutherford backscattering spectrometry. On the one hand, this method is sensitive to different elements and their composition. On the other hand, it is selective for different depths within the probe (surface, interface, etc.). However, in the present case, the experimental film composition was unknown, and only STM information was available.

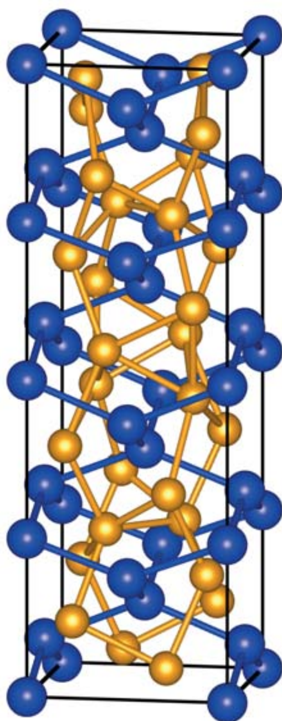

Figure 3.39 – Mn_4Si_7.

The basic experimental STM fact is the observation of a hexagonal $\sqrt{3} \times \sqrt{3}$ surface pattern for the Mn silicide films on Si(111). Thus, the most interesting Mn silicides are those that have (i) a cubic or hexagonal unit cell as bulk material and (ii) equilibrium lattice parameters that can be matched in some form with the Si(111)-$(\sqrt{3} \times \sqrt{3})$ substrate.

One can see from experimental phase diagrams of Mn-Si compounds (Fig. 3.23 on page 87) that only Mn_6Si (hexagonal), the itinerant AFM Heusler compound Mn_3Si (cubic) [219], Mn_5Si_3 (hexagonal), and MnSi (cubic) crystallize with an appropriate Bravais lattice. The experimental target Si(111)-$(\sqrt{3} \times \sqrt{3})$ surface lattice constant is roughly 6.65 Å. Mn_6Si has a lattice parameter $a = 8.96$ Å and is thus too large; moreover, it appears to be too Mn rich for thin film growth on a Si substrate. The cubic Mn_3Si can be transformed into a hexagonal unit cell like MnSi, which results in $a = 8.09$ Å. This value is also too large. The last compound is Mn_5Si_3, which is slightly more Mn rich than MnSi. Its hexagonal planar lattice parameter is $a = 6.91$ Å. This value is close to the substrate target value, and the competing formation of this compound cannot be excluded *a priori*. Hence, it will be discussed in the following.

On the Si-rich side of MnSi, one only finds the so-called "higher Mn silicides", which grow in the tetragonal crystal structure and are sometimes collected under the label $MnSi_{1.7}$. In fact, they all have a well-defined atomic structure and formula, like Mn_4Si_7, $Mn_{11}Si_{19}$, $Mn_{15}Si_{26}$, and $Mn_{27}Si_{47}$. All these compounds can be seen as Nowotny "chimney-ladder" phases, consisting of a Si (chimney) and a Mn (ladder) subsystem [220–223]. An overview of different crystal structures of the four mentioned $MnSi_{1.7}$ silicides can be found in Fig. 1 of Ref. [220]. Exemplarily, the calculated ground state atomic structure of Mn_4Si_7 is shown in Fig. 3.39, in which the bonds have been chosen such as to underline the chimney-ladder aspect.

The purpose of this section is the following: First, it demonstrates why one can be certain that indeed Mn monosilicide has been grown in the experimental samples discussed before. Second, although Mn_5Si_3 shows a magnetic behavior that is probably unsuitable for applica-

Dieses Werk ist copyrightgeschützt und darf in keiner Form vervielfältigt werden noch an Dritte weitergegeben werden.
Es gilt nur für den persönlichen Gebrauch.

tion in spintronics devices (see below), there is considerable interest in the similar material Mn_5Ge_3, which exhibits FM behavior with a Curie temperature around 300 K as bulk material and as epitaxial thin film on Ge(111) [224, 225]. Its epitaxial growth on Ge(111), which has been studied extensively very recently by experimentalists using ARPES, STM, reflection high-energy electron diffraction, and superconducting quantum interference device magnetometry [226–228], will certainly be similar to Mn_5Si_3/Si(111) growth. Thus, the structural results obtained in the following can be transferred to this case, which is more relevant at least from an applications point of view. A different interesting perspective is that Mn_5Si_3 films (grown, for instance, on a sapphire substrate) can be made FM by C doping [229, 230].

3.8.1 Bulk properties of Mn_5Si_3

At room temperature (that is, above the Néel point at 99 K), the intermetallic compound Mn_5Si_3 crystallizes in the $D8_8$ structure with a hexagonal unit cell (space group $P6_3/mcm$) and is paramagnetic [231].[31] Its unit cell contains two formula units (cf. Fig. 3.40). The Mn atoms form two inequivalent groups: Mn I and Mn II. The Wyckoff positions are:

$$\begin{aligned} \text{Mn I on the } 4d \text{ sites: } & \pm(1/3,2/3,0) \text{ and } \pm(2/3,1/3,1/2), \\ \text{Mn II on the } 6g \text{ sites: } & \pm(x,0,1/4), \pm(0,x,1/4), \text{ and } \pm(-x,-x,1/4), \\ \text{Si on the } 6g \text{ sites: } & \pm(y,0,1/4), \pm(0,y,1/4), \text{ and } \pm(-y,-y,1/4), \end{aligned}$$

with $x \approx 0.236$ and $y \approx 0.599$. The cell parameters are $a = 6.910$ Å and $c = 4.814$ Å [231]. Along the [001] direction, the stacking sequence is A-B-A-C-A-..., with pure Mn I layers (A) and mixed Mn II / Si layers (B and C; cf. Fig. 3.40). Since the material is invariant under the inversion operation, the mixed layers are equivalent. The actual magnetic ground state for very low temperatures is currently regarded to be AFM with a noncollinear spin orientation (AF1), which changes to a collinear AFM phase at around 66 K (AF2). The noncollinearity in the AF1 phase can be attributed to the topological frustration of the Mn sites. For both phases, the magnetic unit cell is orthorhombic and contains four formula units [231, 233].

The DFT-PBE calculations with a FM spin orientation carried out by the author led to $x = 0.245$, $y = 0.602$, $a = 6.90$ Å, and $c = 4.79$ Å, which is in good agreement with the mentioned experimental values. Both a and c results of the PBE calculation are slightly smaller than the experimental values. For comparison, the results of a NM calculation are $x = 0.238$, $y = 0.607$, $a = 6.72$ Å, and $c = 4.57$ Å. Thus, the complete absence of local moments leads to a much worse agreement between measured and calculated cell parameters. Moreover, the total energy in the NM case is by 319 meV/f.u. higher than for the FM spin alignment. According to the DFT calculations, the formation enthalpy in the FM state is $\Delta H = -2.658$ eV per f.u. (-2.082 eV per f.u. experimentally at room temperature [166]).

Handling the magnetic properties of Mn_5Si_3 correctly within DFT proved to be complicated. The author tried different collinear parallel and antiparallel spin alignments, but always found the FM state to be the most stable one. For instance, the orientation of the Mn moments can alternate from layer to layer along the [001] direction, so that Mn I and Mn II are antiparallel (283 meV/f.u. higher than FM state); or the moment direction can change after two layers, so that the Mn atoms of one pure and one mixed layer are parallel (228 meV/f.u. higher than FM state). A magnetic pattern similar to the AF2 model suggested

[31] Recently, the observation of Mn_5Si_3 nanowires with $D8_m$ structure has been claimed [232].

Dieses Werk ist copyrightgeschützt und darf in keiner Form vervielfältigt werden noch an Dritte weitergegeben werden.
Es gilt nur für den persönlichen Gebrauch.

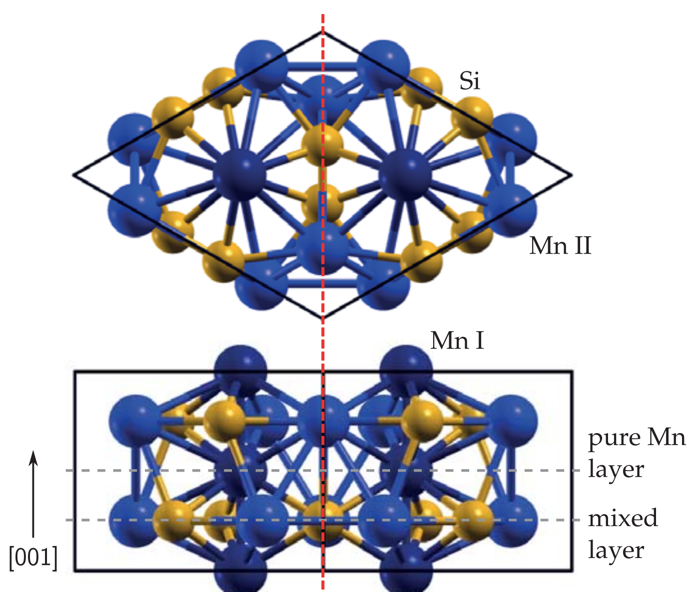

Figure 3.40 – Top (upper image) and side (lower image) view of the atomic structure of bulk Mn_5Si_3. The red dashed line indicates a mirror plane involving the short diagonal of the rhombus. Note that the long diagonal does *not* correspond to a mirror plane. The two different, inequivalent layers are marked in the side view.

in Ref. [231] for the temperature range between 66 and 99 K, which needs an orthorhombic unit cell containing four formula units, led to an energy value only 28 meV/f.u. higher than the FM result. It is conceivable that a noncollinear calculation will further lower the total energy. However, such noncollinear calculations are extremely time consuming for the large film structures that will be discussed in the next section. Moreover, the different atom coordination close to the interface and the surface will reduce the frustration and potentially change the magnetic order locally. Thus, the calculations are simply done with a FM magnetic moment alignment in the following. Since energy differences associated with magnetic orderings are usually small, surface and interface energy arguments are not affected by this issue.[32] It could have a small influence on simulated STM images, though. However, if the bias voltage is set to a not too small value, the surface topography will have a much higher effect on the STM images than the electronic structure.

3.8.2 Surfaces and Mn_5Si_3/Si(111) heterostructures

In contrast to MnSi in B20 structure, Mn_5Si_3 is invariant under the inversion operation. Thus, it is possible to create a slab structure with equivalent upper and lower surface. A consequence is that one can make nonaveraged statements about surface energies for this material, and also about the interface energies of $Mn_5Si_3/Si(111)$ heterostructures.

Surfaces of biaxially strained Mn_5Si_3

From Fig. 3.40 one can see that two (001) surface terminations are possible: a pure Mn layer consisting of Mn I atoms, and a mixed layer consisting of Mn II and Si atoms. The surface energies for these two surfaces, derived in the usual manner,

[32] Assuming an uncertainty of about 80 meV per unit cell due to a wrong magnetic ground state and an area of about 40 Å, interface and surface energies γ vary by 2 meV/Å^2, which is too small to be of relevance here, as we will see in the following.

Dieses Werk ist copyrightgeschützt und darf in keiner Form vervielfältigt werden noch an Dritte weitergegeben werden.
Es gilt nur für den persönlichen Gebrauch.

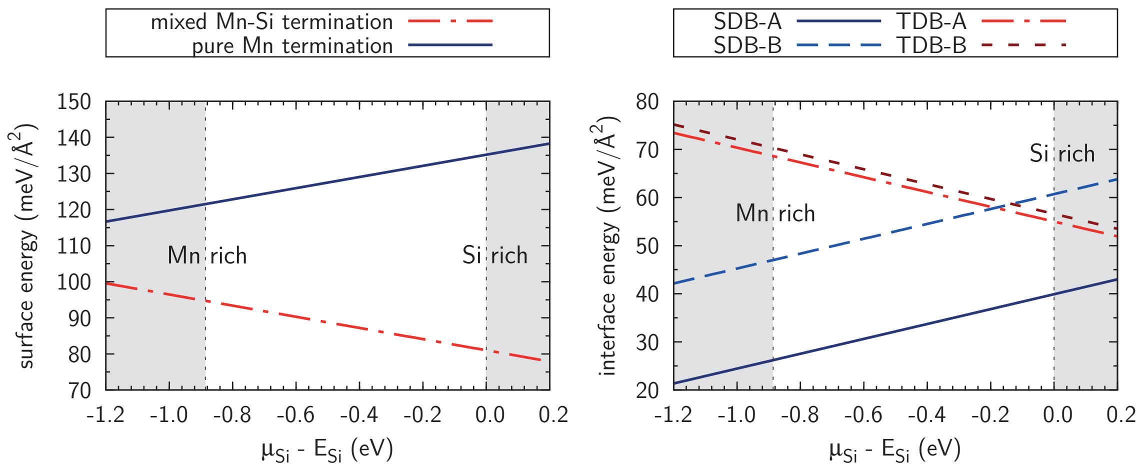

Figure 3.41 – Surface energies of the two different (001) surfaces of Mn_5Si_3 under biaxial strain as induced by a Si(111) substrate (left) and interface energies of different Mn_5Si_3/Si(111) interfaces (right).

$$\gamma(\mu_{\mathrm{Si}}) = \frac{1}{2A}\left\{E_{\mathrm{slab}} - \left(N_{\mathrm{Si}} - \frac{3}{5}N_{\mathrm{Mn}}\right)\mu_{\mathrm{Si}} - \frac{1}{5}N_{\mathrm{Mn}}E^{\mathrm{strained}}_{\mathrm{Mn_5Si_3}}\right\},$$

are shown in Fig. 3.41. The epitaxially strained material is of interest in the following; therefore, the surface energies have been calculated for biaxially strained Mn_5Si_3, with a cell parameter a that fits the Si(111)-$(\sqrt{3}\times\sqrt{3})$ surface lattice constant.

Since surfaces with different numbers of atoms are compared, it is again necessary to define reservoirs (and thus the chemical potentials that enter the surface energy expression). Here strained bulk Mn_5Si_3 ($E^{\mathrm{strained}}_{\mathrm{Mn_5Si_3}}$) has been chosen as reservoir in order to get rid of the strain energy that would otherwise accumulate with increasing slab thickness and complicate the comparison of structures with different thickness. The same strategy has been applied to the case of MnSi discussed above.

The allowed range for the chemical potential μ_{Si} is limited by the following considerations: If it is too high, Si will segregate from the silicide to the surface and form crystallites. Therefore, the condition $\mu_{\mathrm{Si}} \leq E_{\mathrm{Si}}$ must hold. On the other hand, a too low value will lead to the formation of bulk Mn islands on the surface. This imposes the constraint $\mu_{\mathrm{Si}} \geq E_{\mathrm{Si}} + \frac{1}{3}\Delta H = \frac{1}{3}(E_{\mathrm{Mn_5Si_3}} - 5E_{\mathrm{Mn}})$.[33]

It is evident that the mixed surface termination is much more stable (has a much lower surface energy) than the pure-Mn surface termination. This is consistent with the MnSi case discussed above, where Mn-rich surface terminations have been shown to be tendentially less stable than Si-rich terminations (cf. Fig. 3.25 on page 89).

The cell parameters of Mn_5Si_3 are slightly underestimated by the PBE functional, just as for MnSi discussed above. However, since here a is larger than the Si value, which was different for the B20 silicides, and since the Si lattice constant is overestimated by the PBE functional, the lattice mismatch is underestimated (experimental value −3.8 %, theoretical value −2.9 %). The deviation between the experimental and the theoretical lattice mismatch

[33] The condition $\mu_{\mathrm{Mn}} \leq E_{\mathrm{Mn}}$ translates into the given expression if inserted into the equilibrium condition.

Dieses Werk ist copyrightgeschützt und darf in keiner Form vervielfältigt werden noch an Dritte weitergegeben werden.
Es gilt nur für den persönlichen Gebrauch.

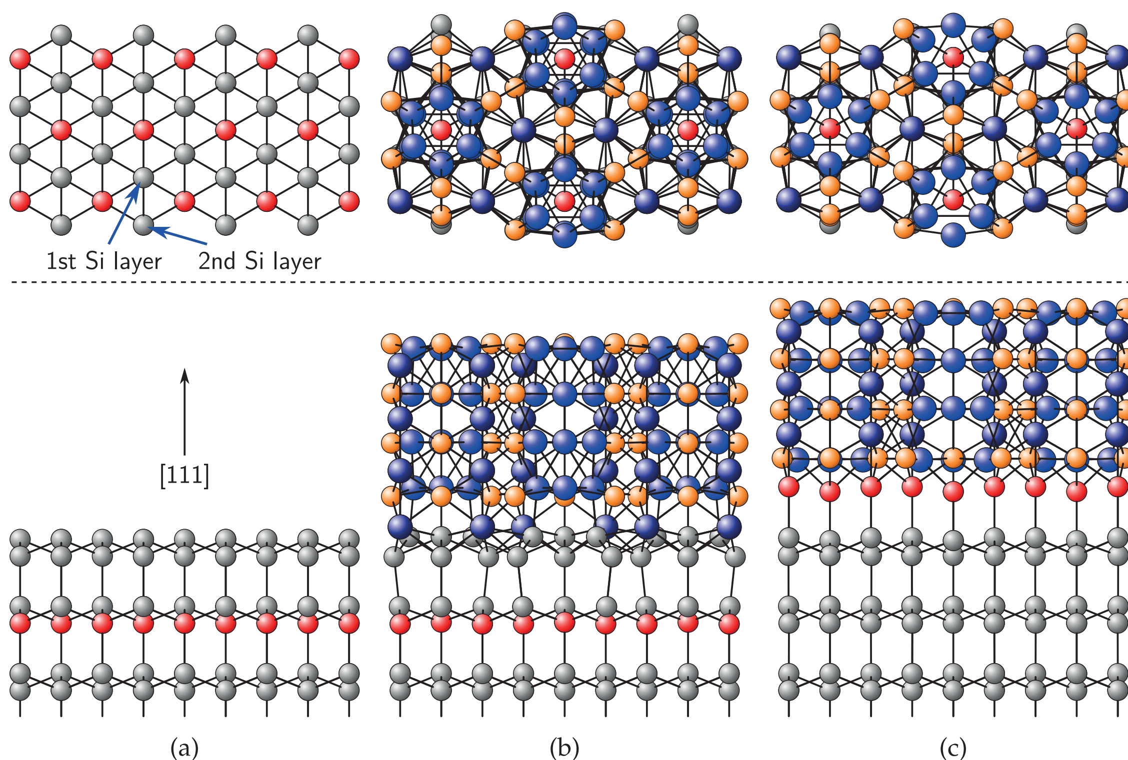

Figure 3.42 – Top and side views of different interface atomic structures of Mn_5Si_3/Si(111). (a) Si(111)-SDB surface for comparison. The fourth layer is marked in by red spheres. (b) The SDB interface. (c) The TDB interface. In this case, the red spheres mark the topmost Si layer of the substrate.

is smaller than for MnSi/Si(111), for which it has been shown above that such deviations do not affect the conclusions on the stability of surfaces and interfaces.

Interfaces of Mn_5Si_3/Si(111) heterostructures

The next question one has to address concerns the atomic structure of the Mn_5Si_3/Si(111) film-substrate interface. From the manifold of different possible interfaces the author considered two to be realistic: either a combination of a Si(111)-SDB terminated substrate and a pure Mn I interface layer of Mn_5Si_3 (referred to as "SDB" in the following), or a combination of a Si(111)-TDB terminated substrate and a mixed Mn II/Si interface layer of Mn_5Si_3 (referred to as "TDB" in the following). Both structures are displayed in Fig. 3.42. In both cases, film and substrate are aligned such that the different C_3 [001] symmetry axes of Mn_5Si_3, which pass through the Mn I atoms as well as through the center of the Mn II ring structures, coincide with those of the Si substrate (passing through the red marked Si atoms in Fig. 3.42).

The interface energies are given in Fig. 3.41 and show a clear preference of the SDB interface. The more Si-rich TDB interface is always less favorable, even near the Si-rich regime. Thus, the Mn_5Si_3/Si(111) interface will always be of the SDB type.

A further structural aspect is that the plane including the long diagonal of the hexagonal unit cell (cf. Fig. 3.40, top view) is neither a mirror plane of bulk Mn_5Si_3 nor of the properly

Dieses Werk ist copyrightgeschützt und darf in keiner Form vervielfältigt werden noch an Dritte weitergegeben werden.
Es gilt nur für den persönlichen Gebrauch.

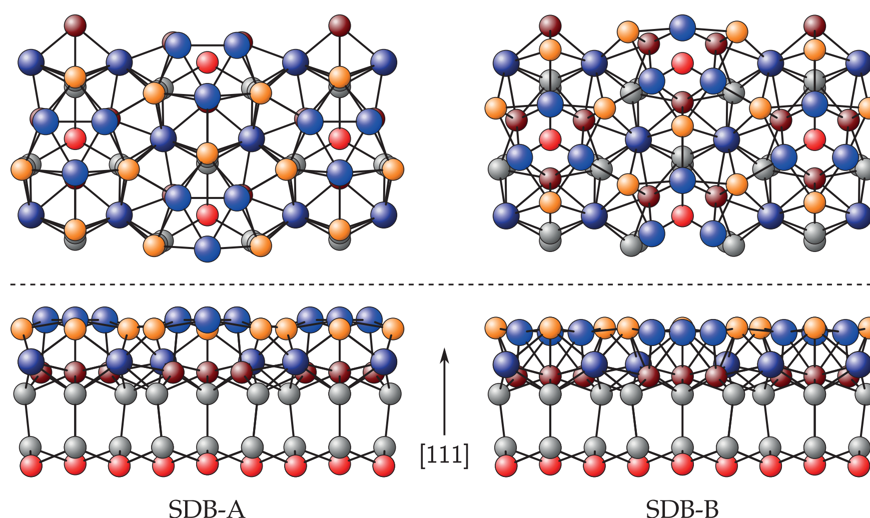

Figure 3.43 – Top and side views comparing the two different Mn_5Si_3/Si(111) SDB interfaces [cf. Figs. 3.41 and 3.42(b)]. The first, second, third, and fourth Si layer is marked in dark red, gray, gray, and bright red, respectively. Note the different orientation of the topmost mixed Mn II / Si layer with respect to the rest of the structure.

aligned Si(111) substrate (cf. Fig. 3.42). Thus, if one applies this mirror operation to the film material, but not to the substrate, one ends up with two inequivalent structures "A" and "B". This is displayed for the SDB interface in Fig. 3.43: In the A case, the film Mn II atoms are located over the first-layer Si atoms of the substrate, while the film Si atoms sit over the second-layer Si atoms of the substrate. In the B case, the film Si atoms are located close to the first-layer Si atoms of the substrate. The situation is similar for the case of the TDB interface (not shown). From Fig. 3.41 it becomes clear that the SDB-B interface is energetically much more unfavorable than the SDB-A interface. This also holds for the TDB interfaces; however, the energy difference is much smaller here, since the vertical spacing between the topmost substrate bilayer and the first mixed Mn II / Si layer in the film is larger due to the additional, in terms of symmetry "neutral" Si layer.

One can readily estimate from the surface energies γ_s and the interface energies γ_i shown in Fig. 3.41 that $\Delta\gamma = \gamma_s + \gamma_i - \gamma_{sub} > 0$ for all reasonable values of μ_{Si} if growth takes place on a Si(111) substrate, for which γ_{sub} ranges between 76 and 95 meV/Å^2, depending on the surface reconstruction (see above). Since $\gamma_s + \gamma_i$ becomes even larger for very thin Mn_5Si_3 films, one expects Volmer-Weber-like island formation in thermodynamic equilibrium, similar to the MnSi case discussed above. On the other hand, $\Delta\gamma$ is in any case much smaller here than for MnSi/Si(111). As a consequence of these aspects, the formation of epitaxial films requires careful growth and moderate annealing temperatures, but the growth process is more robust than in the MnSi case and less susceptible to island formation. Indeed, the related Mn_5Ge_3/Ge(111) films can typically be grown epitaxially at around 400 – 600 °C [224, 234, 235].

Dieses Werk ist copyrightgeschützt und darf in keiner Form vervielfältigt werden noch an Dritte weitergegeben werden.
Es gilt nur für den persönlichen Gebrauch.

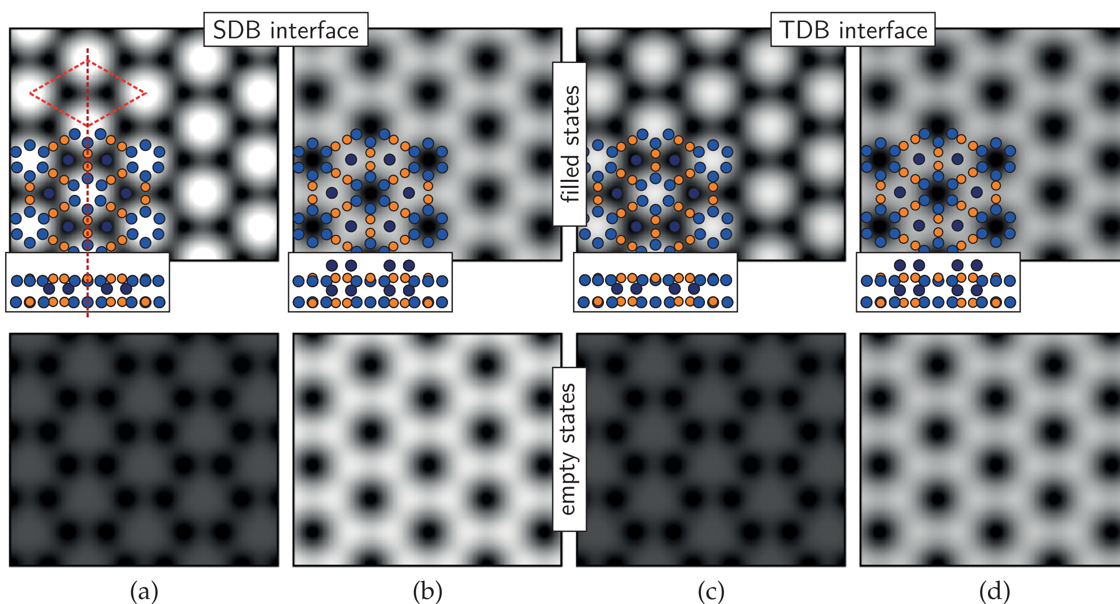

Figure 3.44 – Simulated STM images of Mn_5Si_3/Si(111). The upper row shows filled-state images, the lower row shows empty-state images. Images (a) and (b) belong to the SDB-A interface, (c) and (d) to the TDB-A interface. Images (a) and (c) show the mixed surface, (b) and (d) the pure Mn surface. A part of the atomic structure is overlaid: Smaller orange circles mark Si atoms, bigger blue circles Mn atoms. The dashed red rhombus marks the surface unit cell (cf. Fig. 3.40). The dashed red line indicates a mirror plane which is missing in the case of MnSi/Si(111). The bias voltage is ± 1.25 V, $\varrho_c = 10^{-6}$ / bohr^3, and the corrugation scale is 0.6 Å in all cases.

3.8.3 STM analysis of Mn_5Si_3/Si(111) surfaces

To exclude the growth of Mn_5Si_3 on Si(111) in the aforementioned experiments, it is sufficient to show that either the simulated STM images of different subsequent surfaces are not consistent with the experiment, or that the observed pattern and the behavior under bias voltage reversal do not agree.

Simulated STM images for the two different surface terminations and the two interfaces SDB-A and TDB-A are shown in Fig. 3.44. The corresponding film structures contain 7 – 9 layers of Mn_5Si_3 on a Si(111) substrate (cf. Fig. 3.42). The STM images of the mixed surface termination show peaks for filled and empty states in the center of the Mn II rings. The corrugation is smaller for empty states than for filled states. The pattern produced by the pure Mn surface termination looks clearly different. Instead of discrete peaks, both filled- and empty-state images show a honeycomb structure built up by the Mn I atoms. The corrugation is slightly larger for empty-state images than for filled-state images, in contrast to the mixed surface termination. The degree of corrugation is similar for both surface terminations; thus, speaking of LC and HC surface terminations is not reasonable here. The overall pattern of the simulated STM images is invariant under bias voltage reversal in all cases. No significant differences arise due to different interfaces, which shows that there is no influence of the interface on surface electronic properties over this distance (7 – 9 layers of Mn_5Si_3, ≈ 10 Å), probably due to metallic screening.

These observations and the surface energies shown above can be interpreted consistently: The far more stable mixed termination consists of many filled states and only few empty

Dieses Werk ist copyrightgeschützt und darf in keiner Form vervielfältigt werden noch an Dritte weitergegeben werden.
Es gilt nur für den persönlichen Gebrauch.

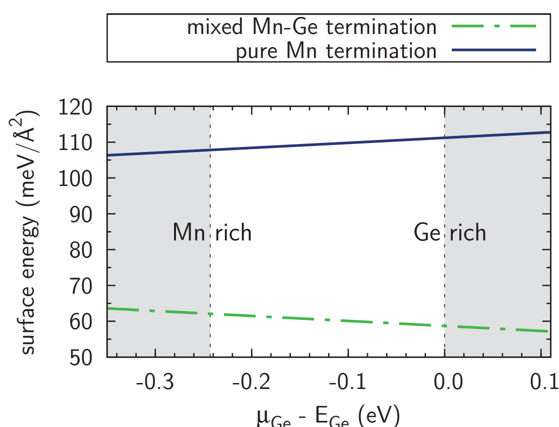

Figure 3.45 – Surface energies of the two different (001) surfaces of Mn_5Ge_3 under biaxial strain as induced by a Ge(111) substrate. Note the qualitative similarity to the Mn_5Si_3 case shown in Fig. 3.41.

states (which one would call "dangling bonds" in the case of a semiconductor surface), which is reflected by the corrugation difference. The unstable pure Mn termination induces much more empty states at the surface.

The simulated STM images clearly reflect the mirror symmetry of the $Mn_5Si_3(001)$ surface (involving the short diagonal of the surface unit cell): The two valleys between the peaks (mixed termination) or the two peaks making up the honeycomb pattern (pure Mn termination) are equivalent. However, this mirror symmetry is absent in the experimental STM images that have been discussed in Sec. 3.6.[34] This demonstrates that the experimentally grown films shown in Figs. 3.28, 3.29, and 3.31 cannot consist of Mn_5Si_3. Moreover, a honeycomb pattern has been observed only once in the experiment (for empty states, i.e., positive bias voltage), and the large surface energy difference of the two $Mn_5Si_3(001)$ surfaces precludes the coexistence of the pure-Mn and the mixed termination.

One can compare the simulated STM images for Mn_5Si_3 shown in Fig. 3.44 with those of Mn_5Ge_3 published in Ref. [235]. There is a close agreement for the pure Mn termination. The images for the mixed termination look slightly different at first sight; however, agreement is recovered for higher bias voltages (1.5 eV).

There seems to be some agreement in the literature that Mn_5Ge_3/Ge(111) films are terminated by a pure Mn layer, since one observes a honeycomb pattern in experimental STM images [226, 235]. This interpretation is in conflict with the calculated surface energies presented above, which clearly show the instability of the pure Mn surface termination not only for Mn_5Si_3 epitaxially strained to the Si(111)-($\sqrt{3}\times\sqrt{3}$) surface lattice constant (cf. Fig. 3.41), but also for Mn_5Ge_3 epitaxially strained to the Ge(111)-($\sqrt{3}\times\sqrt{3}$) surface lattice constant (cf. Fig. 3.45). The author is not aware of any publication discussing this obvious discrepancy. Although this issue is of no further importance here and beyond the scope of this work, one can speculate that a nonstoichiometric pure Si surface termination, in which the topmost Mn atoms have been replaced by Si atoms, might on the one hand lower the surface energy [similar to the MnSi/Si(111) case] while providing, on the other hand, potentially the experimentally observed honeycomb pattern. This is, however, subject of future investigations.

[34] At first sight, one might attribute a mirror plane involving the *long* diagonal of the surface unit cell to the STM images shown in Figs. 3.31 and 3.44, i.e., to both MnSi and Mn_5Si_3 on Si(111). This is, however, not correct, as a careful inspection reveals, and also not supported by the underlying atomic structure.

Dieses Werk ist copyrightgeschützt und darf in keiner Form vervielfältigt werden noch an Dritte weitergegeben werden.
Es gilt nur für den persönlichen Gebrauch.

Dieses Werk ist copyrightgeschützt und darf in keiner Form vervielfältigt werden noch an Dritte weitergegeben werden.
Es gilt nur für den persönlichen Gebrauch.

Chapter 4

Transition metal impurities in Si

Contents

4.1 Introduction and overview **122**
4.2 The H/Si(111) and H/GaAs(110) surfaces and surface states **123**
4.3 Transition metal impurities in bulk Si **127**
4.3.1 The semilocal GGA viewpoint 127
4.3.2 Effects of correlation and exact exchange 134
4.4 Wave function imaging of H/Si(111) subsurface impurities **137**
4.4.1 Bulklike impurity properties below passivated surfaces 139
4.4.2 Impurity-host interactions 140
4.4.3 Impurity-impurity interactions 146
4.4.4 Kinetic aspects of impurities near the H/Si(111) surface 148
4.5 Two-dimensional subsurface impurity layers and clusters **150**
4.5.1 Half-metallic impurity layers 150
4.5.2 Destabilization of the Si matrix by dense impurity layers 154
4.5.3 Impurity clusters 155
4.6 Subsurface doping with organic molecules **158**
4.6.1 Binding energies and exchange-correlation functionals 159
4.6.2 Adsorption of FePc on H/Si(111) 162
4.6.3 Subsurface doping 163

Dieses Werk ist copyrightgeschützt und darf in keiner Form vervielfältigt werden noch an Dritte weitergegeben werden.
Es gilt nur für den persönlichen Gebrauch.

4.1 Introduction and overview

After the discussion of FM 3*d* TM silicides as possible materials for future spintronics devices in the preceding chapter we now move to an alternative approach: the doping of semiconducting materials, e.g., Si, with "magnetic" 3*d* TM impurities like Cr, Mn, and Fe. Such a material can serve, for instance, as spin injector [236], since it reduces the conductivity mismatch problem [237].

This leads us to the highly and controversially debated field of dilute magnetic semiconductors (DMS). Exemplary in this context are a highly cited publication by Dietl *et al.* [238], which theoretically predicted high Curie temperatures in several Mn-doped zinc-blende semiconductors and caused intense, but mostly fruitless research with thousands of subsequent publications, and a recent critical "reply" to this work by Zunger *et al.* [239]. Another unanswered question concerns the magnetic interactions in Co-doped ZnO, where a large number of publications claim the existence of ferromagnetism, while an equally large number of publications deny it.[1] The currently most promising material, which has been dominating the field of DMS for some time now, is Mn-doped GaAs [248]. The trial-and-error approach that has been pursued so far for the identification of DMS materials systems has lead to slow progress of this field, since understanding the interactions in a DMS on a fundamental, atomic level is a prerequisite for rational materials design. This comprises both impurity-host and impurity-impurity interactions, which are responsible for the formation of local magnetic moments and the emergence of collective order between these moments, respectively.

In this chapter, a new idea is presented, founded on an *ab initio* theoretical basis, for the fundamental experimental study of *bulklike* impurity magnetism in semiconductors and insulators on the atomic scale using *surface* methods like (SP) STM. It relies on the preserved impurity electronic structure below passivated surfaces. While the proof of principle is given for the specific case of 3*d* TM impurities in Si, the method is generalizable to other cases, like, for instance, aforementioned Co-doped ZnO, and can lead to a considerably improved understanding of the magnetic behavior of these materials.

Since passivated surfaces play an important role in this strategy, the chapter begins with a discussion of the fully H-passivated Si(111) and GaAs(110) surfaces. Subsequently, different properties of 3*d* TM impurities in bulk Si are recapitulated. Special attention is paid to the reliability of semilocal exchange-correlation functionals in the DFT approach by comparing PBE, PBE+U, and hybrid functional (HSE06) results. This reliability is essential in the whole field of first-principles studies of TM-doped Si. Afterwards, the mentioned strategy to detect bulklike properties of impurities with surface experiments, which is the most important and fundamental aspect in this chapter, is demonstrated on the basis of large-scale first-principles computer simulations. This includes impurity-host interactions as well as impurity-impurity interactions. After kinetic considerations concerning the injection and migration of subsurface 3*d* TM impurities, the formation of two-dimensional subsurface impurity layers and clusters below the H/Si(111) surface is addressed. The chapter closes with a discussion of the experimentally motivated question whether or not it is possible to generate subsurface 3*d* TM impurities by deposition of organic molecules on the H/Si(111) surface.

[1] A small excerpt from the literature shall be given: Ferromagnetism is reported, for instance, by Refs. [240–243], while Refs. [244–247] report AFM or even paramagnetic behavior.

Dieses Werk ist copyrightgeschützt und darf in keiner Form vervielfältigt werden noch an Dritte weitergegeben werden.
Es gilt nur für den persönlichen Gebrauch.

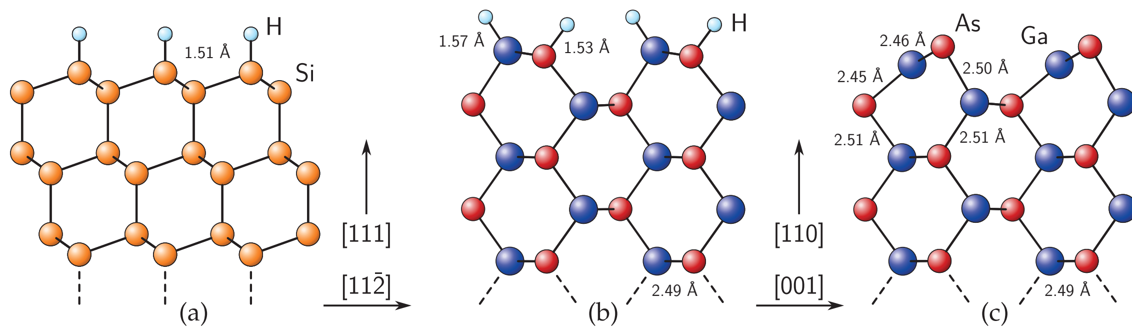

Figure 4.1 – (a) The relaxed H/Si(111) surface. (b) The relaxed H/GaAs(110) surface. (c) The (1×1)-"reconstructed" GaAs(110) surface. Selected bond lenghts are shown. All values have been derived from DFT-PBE-USPP calculations.

4.2 The H/Si(111) and H/GaAs(110) surfaces and surface states

In the previous chapter, properties of bulk Si and of different Si(111) surfaces have been discussed. The focus has been laid on structural and energetic aspects in the latter case, while the electronic properties have only been presented for the 7 × 7 reconstruction. In this section, the interdependence between surface structure and electronic properties will be discussed in a wider context. The GaAs(110) surface will also be mentioned due to its importance in recent STM experiments on Mn-doped GaAs (see below).

Technically, a passivating H layer can be applied to Si surfaces wet chemically by hydrofluoric acid etching [249–251]. This procedure provides highly homogeneous, perfectly saturated and unreconstructed surfaces. The atomic structure of unreconstructed, but relaxed Si(111) surfaces has been shown in Fig. 3.4 on page 55. In addition, Fig. 4.1(a) displays the relaxed atomic structure of the H-passivated Si(111) surface (DFT-PBE-USPP calculations). The H atoms sit exactly above the topmost Si atoms of the Si(111)-SDB surface, thus continuing the crystal structure. Due to the small size of the H atoms,[2] the H-Si bond length (1.51 Å) is much smaller than the Si-Si bond length in the TDB case (2.36 Å) or in bulk Si (2.37 Å). Since H provides one electron, the single dangling bond of Si can be saturated in a covalent way. Furthermore, one can see the influence of H passivation on the GaAs(110) surface in Figs. 4.1(b) and (c). Without the terminating H layer, the surface exhibits the well-known (1 × 1)-"reconstruction": The Ga atoms in the topmost Ga-As layer displace to positions below the exposed As atoms (an effect known as "buckling"). Application of a H layer reverses this effect and makes it less pronounced: The topmost Ga atoms move to slightly higher positions than their As partners in this case.

Figure 4.2 shows the surface band structure of the relaxed Si(111)-SDB and the buckled GaAs(110) surface. Due to the dangling bond, the bare Si(111)-SDB surface exhibits a magnetic moment of 1 μ_B per 1 × 1 surface unit cell. The corresponding surface state band lies in the band gap, close to the Fermi energy. In contrast, the GaAs(110) surface is not magnetic. Surface states in the vicinity of the band gap can be observed slightly above the topmost VB and below the lowest CB.[3]

In both cases, the application of a H layer shifts the surface states away from the Fermi energy. For Si(111), they can be observed at about −4.4 eV ($\bar{M}$ point) and −3.7 eV ($\bar{K}$ point).

[2]The covalent radii of H and Si are 0.32 Å and 1.11 Å, respectively [252].
[3]A detailed theoretical study of different III-V semiconductor (110) surfaces can be found in Ref. [253].

Dieses Werk ist copyrightgeschützt und darf in keiner Form vervielfältigt werden noch an Dritte weitergegeben werden.
Es gilt nur für den persönlichen Gebrauch.

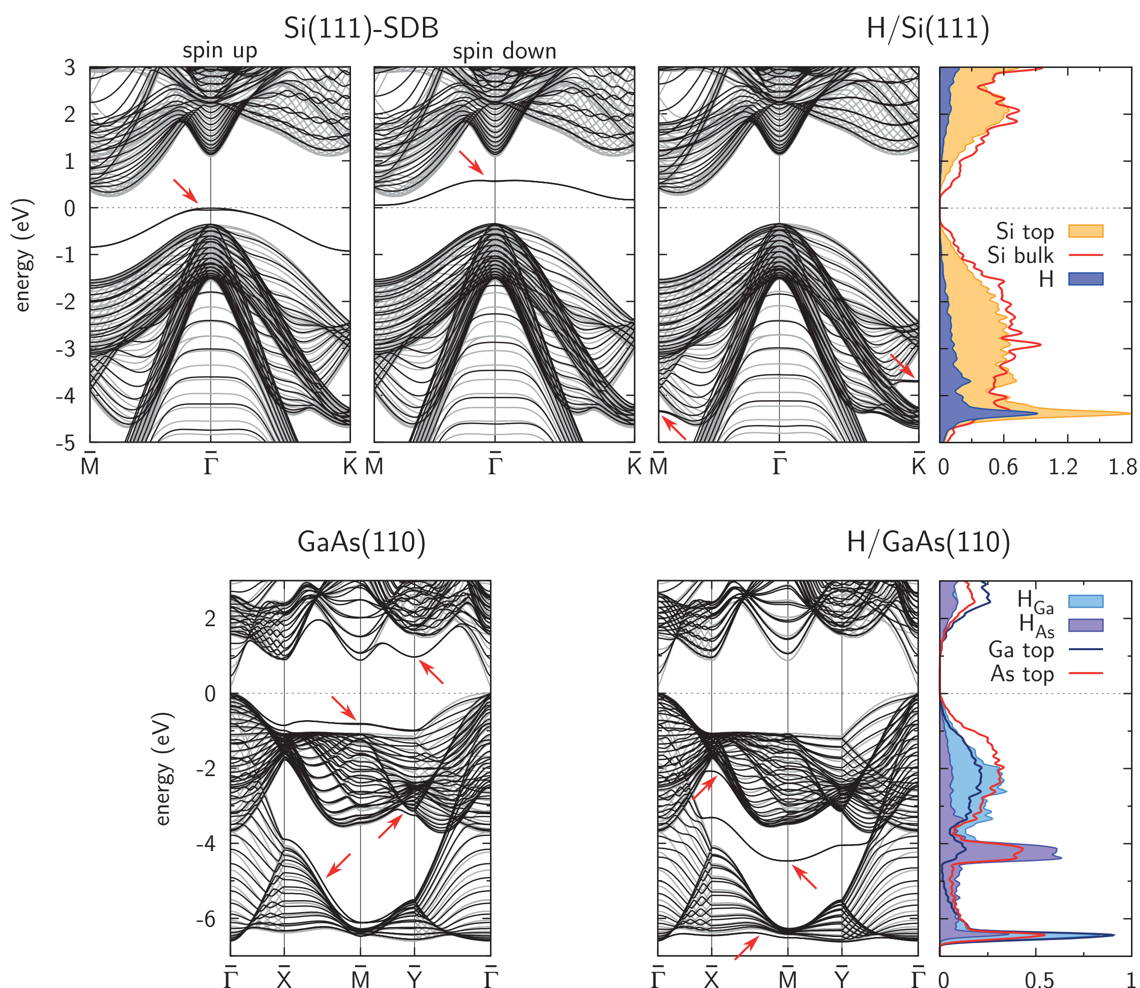

Figure 4.2 – Influence of H passivation on the surface band structure of the Si(111)-SDB (top row) and the GaAs(110) (bottom row) surface. The gray lines form the projected bulk band structure. For Si(111)-SDB, the spin-polarized surface states (red arrows) at the Fermi energy can clearly be seen. The application of a H layer saturates the dangling bonds and moves the surface states away from the band gap. The DOS plots correspond to the passivated structures [Figs. 4.1(a) and (b)] and show projections on the (sub-)surface H, Si, Ga, and As atoms. Note that all surface band structures have been derived from supercells containing two equivalent surfaces.

Dieses Werk ist copyrightgeschützt und darf in keiner Form vervielfältigt werden noch an Dritte weitergegeben werden.
Es gilt nur für den persönlichen Gebrauch.

The PDOS reveals their strong H-Si character. These findings are in qualitative agreement with recently published *ab initio* results by Li and Galli (LDA, Ref. [254]) and experimental photoemission values [255]; quantitative improvements can be achieved by using a quasiparticle self-energy approach within the *GW* approximation [254,255]. Comparison with Table I of Ref. [255] shows that the PBE Kohn-Sham energies of the surface states obtained in this thesis are already much closer to the experimental results than LDA energies. Another interesting observation is that there are almost no states with H character in an interval of about ± 1 eV around the Fermi energy. For GaAs(110), a surface state is shifted to about -4 eV (clearly visible between $\bar{X}$ and $\bar{Y}$ in Fig. 4.2) and has a strong H_{As} and As character (and only small H_{Ga} and Ga character).[4] Another surface state can be found around -6.4 eV. It shows almost no dispersion and contains contributions from all surface atoms, but predominantly from H_{Ga} and Ga.

Comparison of the surface band structure with the projected bulk band structure shows for both Si and GaAs that the band gap is slightly (artificially) enlarged due to confinement effects in a finite slab structure (cf. Fig. 4.2). For GaAs(110), this can be seen especially at the $\bar{\Gamma}$ point (CBM). Test calculations confirmed that the band gap width converges to the bulk value with increasing slab thickness.

In the case of a perfect H layer, the PBE binding energies per H atom are 3.39 eV and 2.34 eV for Si(111) and GaAs(110) substrates, respectively. This compares well with the LDA value of 3.5 eV for H on Si(111) reported in Ref. [256], where the authors used pseudopotentials in Kleinman-Bylander form.[5] The weaker binding of H atoms on the GaAs(110) surface is probably related to the absence of unsaturated surface bands already in the unpassivated case.

These values can be used to answer the question whether it is possible to passivate an existing Si(111) surface by application of H atoms from the gas phase. The experimental binding energy of a H_2 molecule is 4.52 eV [257], while PBE gives 4.45 eV. One can now compare the energies of two scenarios: On the one hand, the H_2 molecule can dissociate and adsorb on two dangling bonds (scenario A). On the other hand, the molecule can remain intact and refuse to adsorb on the surface (scenario B). In the latter case, the unpassivated surface is assumed to be either ideally SDB terminated or (2×1)-reconstructed with Pandey chains. The second assumption is realistic for room-temperature cleavage of a grown sample. The energy difference between these two scenarios A and B is:

$$\Delta E^{2\times 1} = E_{\mathrm{A}} - E_{\mathrm{B}} = -2E_{\mathrm{bind}}^{\mathrm{H/Si(111)}} + E_{\mathrm{bind}}^{\mathrm{H_2}} + \varepsilon, \qquad \varepsilon = 2E_{\mathrm{SDB}}^{1\times 1} - E_{\mathrm{Pandey}}^{2\times 1},$$

where $\varepsilon \geq 0$ accounts for possible reconstructions. According to Ref. [126], this energy gain is $\varepsilon \approx 0.472$ eV in LDA. By using $E_{\mathrm{bind}}^{\mathrm{H_2}} = 4.45$ eV one arrives at $\Delta E^{2\times 1} \approx -2.33$ eV for the ideal SDB termination and $\Delta E^{2\times 1} \approx -1.86$ eV for (2×1)-reconstructed Pandey chains.[6] In both cases, scenario A is energetically preferable. A similar result has been obtained in Ref. [126]. One should keep in mind, however, that the energy barrier between scenarios A and B is potentially quite large. Thus, the formation of H_2 molecules should be avoided. Moreover, the application of the passivating H layer has to be done carefully in order not to remove the already adsorbed H atoms.

[4] In this context, "H_{Ga}" shall denote the H atoms that sit close to the surface Ga atoms.

[5] The reader will note once more the LDA (PBE) overbinding (underbinding) here.

[6] Mixing LDA and PBE results is inconsistent. However, (i) only energy *differences* are mixed, and (ii) the correction ε will be smaller in PBE than in LDA, which even corroborates the conclusion.

Dieses Werk ist copyrightgeschützt und darf in keiner Form vervielfältigt werden noch an Dritte weitergegeben werden.
Es gilt nur für den persönlichen Gebrauch.

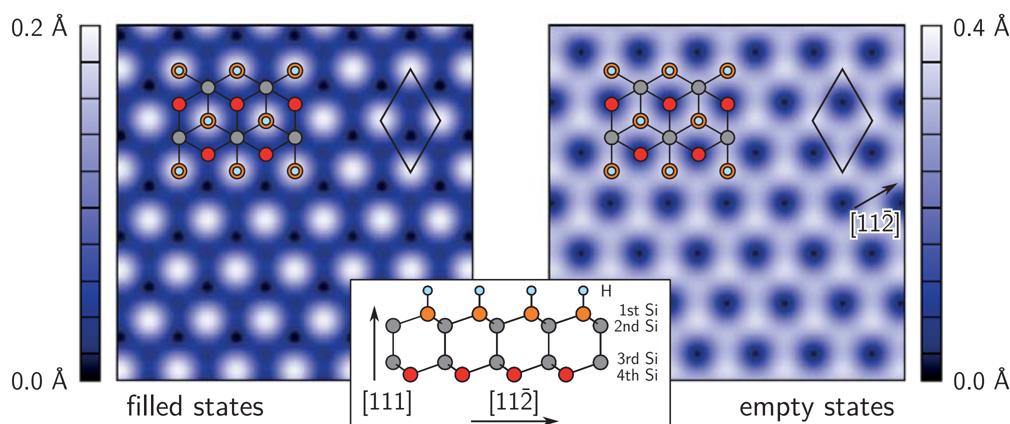

Figure 4.3 – Simulated constant current ($\varrho_c = 10^{-7}$ / bohr^3) STM images of H/Si(111). The panel on the left shows filled states (from E_F to -1.0 eV below the VBM), while the panel on the right shows empty states (from E_F to $+0.6$ eV above the CBM). Note that the color scales are different: The corrugation of the empty-state image is twice as large (0.4 Å) as in the filled-state case (0.2 Å). The different colors used in the overlaid atomic structure depict different Si layers. The black rhombi indicate the same 1×1 surface unit cell in both images.

Figure 4.3 shows filled- and empty-state STM images of H/Si(111), simulated from the DFT-PBE electronic structure. The filled-state image shows a hexagonal grid of isolated, round protrusions and agrees well with a similar theoretical image reported earlier [LDA, Ref. [254], Fig. 3(b)]. The protrusions are located at the H sites, i.e., above the atoms of the first Si layer. The minima are located above the atoms of the second (and third) Si layer; however, the difference to the sites above the atoms of the fourth Si layer is very small. Reversing the bias voltage leads to a clearly different result: The empty-state image shows a honeycomb pattern. Still, the H sites are most strongly pronounced, but the difference to the sites above the atoms of the second Si layer is small (and depends to some extent on the chosen bias voltage). The minima are now clearly located above the atoms of the fourth Si layer. All these aspects can be seen easily by comparing the two black rhombi in Fig. 4.3; their corners coincide with the H sites.

A possible explanation for this peak-to-honeycomb transition lies in the different nature of bonding and antibonding states. The filled-state images map occupied, bonding states of the VB which are localized at the center of the Si-Si bonds (cf. Fig. 3.1 on page 49). In contrast, the empty-state images map unoccupied, antibonding states of the CB. These are located "behind" the Si atoms on the opposite side of the Si-Si bonds. In particular, they can be found on top of the second-layer Si atoms, which is why these sites light up in the empty-state images.

The corrugation values of the simulated images agree with very recent STM measurements of the H/Si(111) surface by Gruyters *et al.* [251] for *n*-type, P-doped samples. Especially, their empty-state images exhibit a larger corrugation than the filled-state images (for bias voltages of similar magnitude). Moreover, the transition from isolated peaks to a honeycomblike pattern is also observed. The minima are always detected at the same positions, irrespective of the bias voltage sign,[7] but, since the difference between the two local minima (above the atoms of the second and fourth Si layer) is small in the present simulations, other effects can

[7]Gruyters *et al.* [251] *assign* these positions to the fourth Si layer (red circles in Fig. 4.3).

Dieses Werk ist copyrightgeschützt und darf in keiner Form vervielfältigt werden noch an Dritte weitergegeben werden.
Es gilt nur für den persönlichen Gebrauch.

easily lead to this experimental observation, e.g., the finite size or imperfections of the STM tip.

In any case, the *sites* where the H atoms can be found are most strongly pronounced. Consequently, Ref. [254] attributes the origin of the corresponding protrusions to the H atoms. The good agreement of PBE, *GW*, and experimental electronic structures mentioned above provides confidence in the STM simulations. It is, however, not entirely clear if the protrusions really stem from the H atoms. First, the atomic H-Si distance is much larger (1.51 Å) than, for instance, the corrugation in the filled-state image (0.2 Å). On the other hand, Si atoms are larger than H atoms, which could lead to a reduction of the corrugation. Second, as already mentioned above, there are nearly no states with H character around the Fermi energy, but many Si states (cf. Fig. 4.2). Hence, the statement that the H atoms are responsible for the protrusions seen in the STM images can be questioned; but this detail is just a side remark and of no further importance in this thesis.

Another interesting aspect is the following: Due to finite temperatures one could imagine that the light H atoms tend to vibrate and blur the spots in the experiment. The measured frequency (energy) of the H-Si bending mode on Si(111) is around 637 cm^{-1} (79 meV), and the value for the H-Si stretching mode is 2080 cm^{-1} (258 meV) [258]. The former is certainly excited to some extent at room temperature, but it will freeze out for low temperatures. The latter is negligible. Note that high-resolution STM experiments which study individual atoms or impurities can be carried out at low temperatures [251].

4.3 Transition metal impurities in bulk Si

Since the early DFT studies of the 1980s [259–261], interest in TM impurities in a Si host matrix has not ceased. The reason is that Si-based spintronics devices [5] would be highly valuable, since Si and TMs are cheap and can be found in abundance. Moreover, our semiconductor industry and technology is optimized for Si processing. Consequently, there is still a remarkable activity in this field. For instance, formation energies and magnetic properties of isolated TM impurities and impurity pairs have been studied recently [161], and the dependence of magnetism on the doping concentration has been investigated [68, 262]. Another interesting subject are Mn δ doping layers embedded in a Si matrix [263–265].

4.3.1 The semilocal GGA viewpoint

The 3*d* TM impurities are known to be interstitial diffusers in Si, while substitutional impurities are rare and supposed to form only by recombination with a Si vacancy [266]. This behavior can be understood from DFT calculations. Figure 4.4 shows the formation energies of isolated Cr, Mn, and Fe interstitial and substitutional T_d impurities[8] in a Si host matrix as functions of the impurity magnetic moment μ:

$$E^{\text{form}}(\mu) = E_{\text{tot}}^{\text{TM in Si host}}(\mu) - E_{\text{tot}}^{\text{pure Si host}} - E_{\text{bulk}}^{\text{TM}} + \Delta N_{\text{Si}} E_{\text{bulk}}^{\text{Si}}, \tag{4.1}$$

a quantity similar to Eq. (3.6) on page 65. For interstitial (substitutional) impurities, a value of $\Delta N_{\text{Si}} = 0$ ($\Delta N_{\text{Si}} = 1$) has to be used. The bulk reservoirs $E_{\text{bulk}}^{\text{TM}}$ are the same as those used in the context of Eq. (3.6). No further charge-dependent corrections are included, since only

[8] In this section, “interstitial” means “tetrahedral interstitial” with T_d symmetry. The case of hexagonal interstitial impurities with D_{3d} symmetry is not discussed here (cf. Ref. [161]).

Dieses Werk ist copyrightgeschützt und darf in keiner Form vervielfältigt werden noch an Dritte weitergegeben werden.
Es gilt nur für den persönlichen Gebrauch.

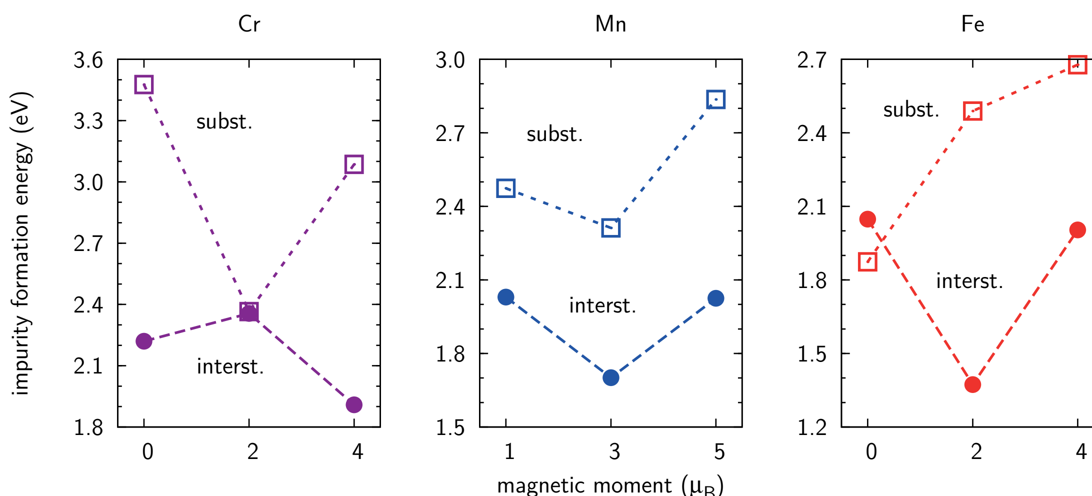

Figure 4.4 – Formation energies as functions of the magnetic moment for different isolated interstitial (filled circles) and substitutional (open squares) Cr, Mn, and Fe impurities in bulk Si. In each case, the lowest formation energy marks the ground state.

neutral impurities (cells) are discussed in the following. The atomic structure of interstitial and substitutional impurities in Si is illustrated in Fig. 4.5(a).

It becomes obvious from Fig. 4.4 that the magnetic ground state of an interstitial impurity is always more stable than the magnetic ground state of the corresponding substitutional impurity. The different magnetic ground states agree with the available electron paramagnetic resonance (EPR) measurements [267] and earlier DFT studies [161,261,262]. All formation energies are positive, which means that the segregation into bulk phases (or even the formation of TM-Si compounds, cf. Sec. 3.3.3) is preferred. On the other hand, kinetic barriers obstruct impurity migration up to room temperature; this aspect will be discussed in Sec. 4.4.4. The binding energies are positive (that is, stable) in all cases.

In addition to these well-known results, Fig. 4.4 shows the energy differences to excited magnetic states, which have been derived from two consecutive calculations in each case: First, a constrained total moment calculation generated an effective potential V_{KS} [cf. Eq. (2.11)] for a certain magnetic moment. In a second step, the constraint was relaxed, but the SCF cycle started from the previously generated effective potential. In all cases, the excited states were found to be metastable, which means that the SCF cycle did not relax into a state with a different magnetic moment. However, care has to be taken *without* such a sophisticated procedure. The common belief is that DFT will converge to the ground state. This is *not* the case here. Only for Fe impurities does the SCF cycle converge to the correct ground state. For Mn and Cr, erroneous results can easily be produced.[9]

Another aspect that can lead to erroneous results is an artificial impurity-impurity interaction caused by the periodic boundary conditions. If the Si supercell, in which the impurity is embedded, is chosen too small, the impurity will interact with its periodic images. This causes a small, artificial dispersion of the impurity bands and can lead to a situation where the impurity states are unequally occupied in the Brillouin zone, especially if the Fermi energy is located within a group of states that lie energetically close together. This effect can be

[9]For instance, Ref. [68] reports a magnetic moment of 1 μ_B for isolated substitutional and interstitial Mn impurities in a 216-atom Si cell.

Dieses Werk ist copyrightgeschützt und darf in keiner Form vervielfältigt werden noch an Dritte weitergegeben werden.
Es gilt nur für den persönlichen Gebrauch.

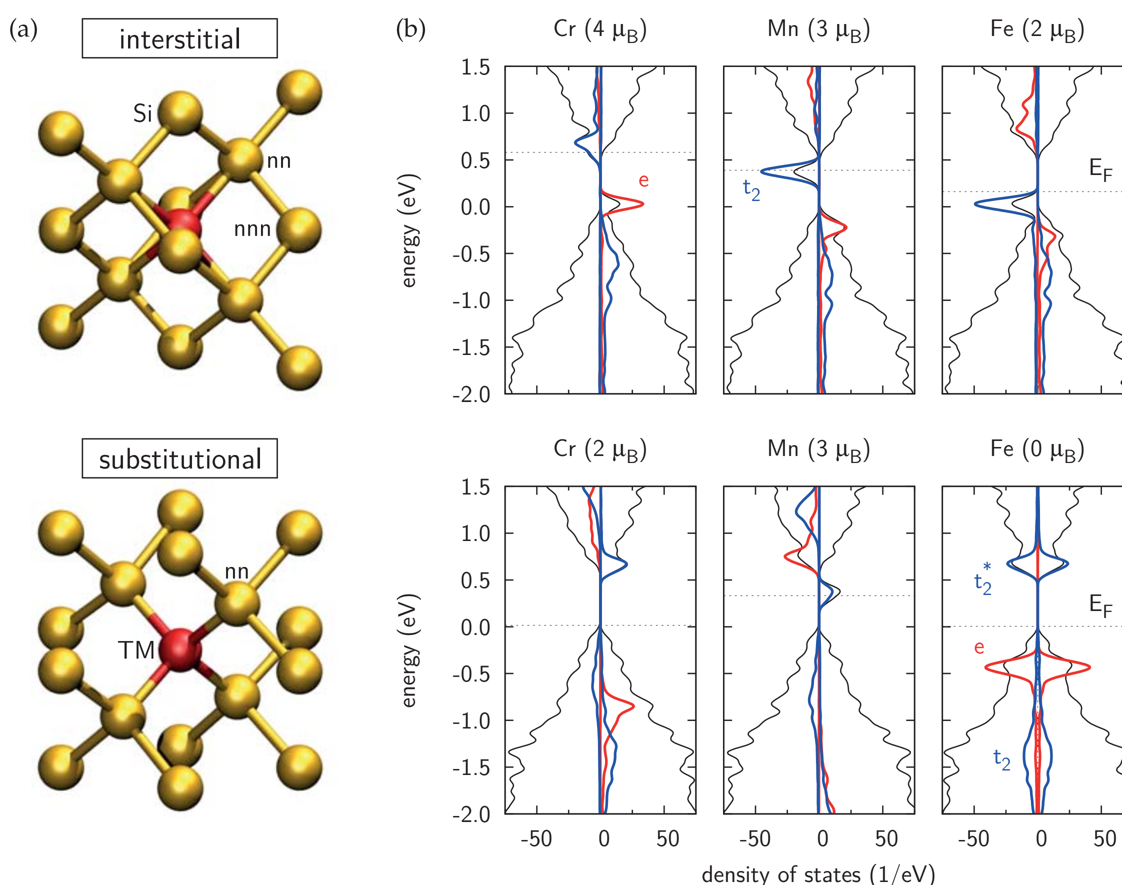

Figure 4.5 – Atomic (a) and electronic (b) structure of different isolated interstitial (top row) and substitutional (bottom row) TM impurities in bulk Si in their magnetic ground state, calculated with the PBE exchange-correlation functional. Nearest-neighbor (nn) and next-nearest-neighbor (nnn) Si atoms are indicated in (a). The blue lines in (b) depict projections of the total DOS (black lines) onto TM 3*d* orbitals which belong to the t_2 representation, while the red lines correspond to the *e* representation. The projections are scaled by a factor of 6 for clarity, and all states are broadened by a Gaussian function. The energy zero coincides with the VBM of the Si host material, while the horizontal dashed line marks the position of the Fermi energy.

Dieses Werk ist copyrightgeschützt und darf in keiner Form vervielfältigt werden noch an Dritte weitergegeben werden.
Es gilt nur für den persönlichen Gebrauch.

self-energizing. In order to check for the occurrence of such a phenomenon, the author performed calculations for Mn and Cr in which a *fixed* number of states was occupied at every $\vec{k}$ point. This is in contrast to usual smearing methods where a different number of states can be occupied at different $\vec{k}$ points. The test results obtained by using fixed occupations were found to agree with the conventionally calculated results where a smearing method was employed.

Usually, the model of Ludwig and Woodbury for interstitial and substitutional $3d$ TM impurities in Si [268] is used to get a qualitative understanding of the magnetic moments and the electronic structure. It makes basically three statements: First, the $4s$ electrons of the isolated TM atom will be promoted to orbitals with high $3d$ character after implantation of the TM atom into the Si host. Thus, the impurity configuration will be d^n in the interstitial case if the isolated TM atom has n valence electrons. For a substitutional impurity, four electrons have to “compensate” for the missing Si atom, and consequently the configuration will be d^{n-4}. Second, the crystal field will split the TM $3d$ states into two groups of orbitals with either t_2 or e symmetry.[10] For interstitial impurities, the t_2 orbitals are energetically lower than the e orbitals, and vice versa for substitutional impurities. Third, it is assumed that the states are filled according to Hund’s rule. The deviation of (semilocal) DFT results for early $3d$ interstitial and late $3d$ substitutional impurities (e.g., Fe) from the last assumption has already been found several years ago [260].

The TM impurity states caused in the fundamental band gap of Si are usually considered to be “deep”, i.e., not very close to the CB or the VB [260, 261, 266]. The DFT-PBE electronic structure of isolated Cr, Mn, and Fe interstitial and substitutional T_d impurities in Si can be seen in Fig. 4.5(b). One can observe a clear filling scheme for interstitial impurities: The majority spin t_2 and e states are already completely filled in all three cases. From Cr to Fe, the minority spin t_2-like states are successively filled with electrons and move from the CBM to the VBM. More generally, a relative shift of *all* $3d$ states towards lower energies with respect to the Si states can clearly be seen as one moves through the TM series. For Fe, the minority spin t_2 states above the VBM are completely filled, which underlines that the t_2 peak consists of three states. Two unoccupied e states can be seen in the CB, which will certainly be filled for Co and Ni [260]. In a NM calculation, an interstitial Fe impurity leads to t_2 states piling up at the VBM and a sharp, half occupied e peak at the Fermi energy (not shown). It is not surprising that this NM configuration is highly unstable. Therefore, the magnetic symmetry is broken and the system ends up in a spin-polarized state.

There is a similar filling scheme for substitutional impurities, but the situation is slightly more complex in this case. It is therefore beneficial for the understanding to start with a more precise analysis of the electronic structure (beyond the Ludwig-Woodbury model). Exemplarily, Fig. 4.6 shows hybridization diagrams for interstitial and substitutional Fe impurities. In the substitutional case, the five Fe $3d$ orbitals on the left are split into three t_2 and two e orbitals due to the tetrahedral crystal field. On the right, the four dangling sp^3 orbitals (caused by the missing Si atom) of the Si host rehybridize and then form three bonding t_2 and three antibonding t_2^* orbitals with the corresponding Fe $3d$ states (sp-d hybridization). The state named a_1 has no equivalent on the TM side and cannot hybridize. It can be observed in a PDOS plot as a small peak with Si $3s$ character (not shown here). Analogously, the two Fe e orbitals have no matching states on the Si side and consequently show no signs

[10] The five TM $3d$ states are split into three t_2 and two e states, according to their transformation behavior (irreducible representations of the T_d symmetry group).

Dieses Werk ist copyrightgeschützt und darf in keiner Form vervielfältigt werden noch an Dritte weitergegeben werden.
Es gilt nur für den persönlichen Gebrauch.

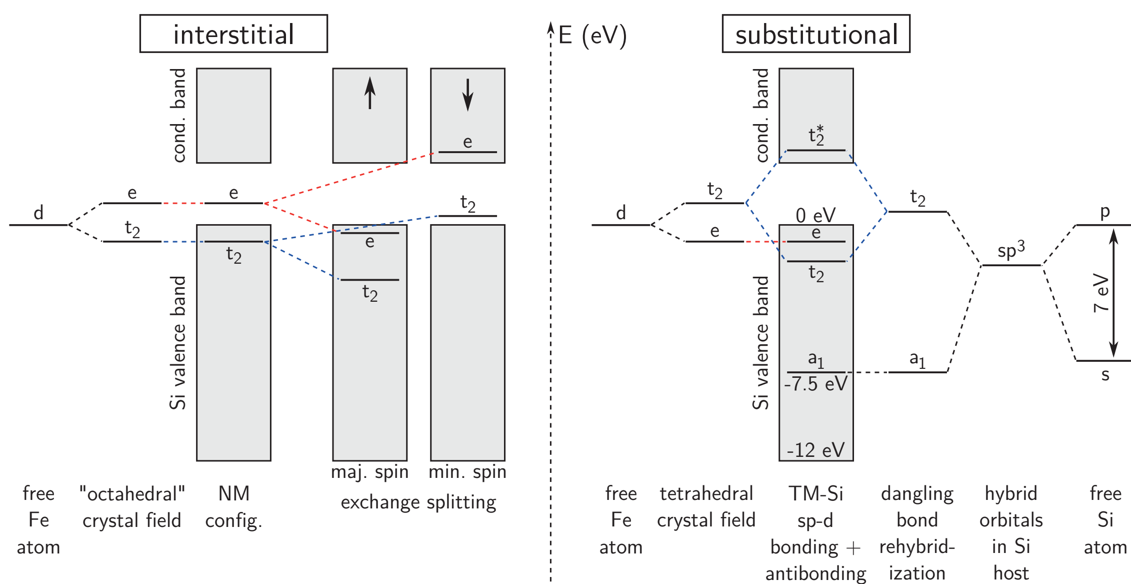

Figure 4.6 – Schematic hybridization diagram for interstitial (left, 2 μ_B) and substitutional (right, 0 μ_B) Fe impurities in Si. The energy values have been taken from the PBE calculations.

of hybridization or dispersion in Fig. 4.5(b). Since Fe and the Si dangling bonds provide $8+4=12$ valence electrons and each state can be doubly occupied, all states up to the anti-bonding t_2^* states are filled. For Mn and Cr, the situation is similar, although the occupation is different. The t_2-e-t_2^* energy level ordering remains. Due to the exchange splitting, the minority spin e state is depleted (Cr) and, instead, a majority spin t_2^* state is occupied by one electron (Mn).

It is important to note here that the substitutional Fe impurity deviates from the expected Ludwig-Woodbury high-spin behavior [260]. It is still an open question whether its experimental magnetic moment really vanishes. We will come back to this issue later.

In the interstitial case, the five Fe 3d orbitals are also split into three t_2 and two e orbitals due to the crystal field, but the energy ordering is reversed when compared with the substitutional case. One should note here that the crystal field generated by the four nearest-neighbor Si atoms (2.40 Å) is still tetrahedral. However, it is superimposed by an octahedral field generated by six next-nearest-neighbor Si atoms (2.73 Å), as one can see in Fig. 4.5(a). More importantly, the interactions with the host material are significantly different: Since all Si bonds remain saturated, the TM impurity cannot form strongly hybridized orbitals with its surrounding. This is reflected, for instance, by the sharp minority spin Fe t_2 peak close to the VBM [cf. Fig. 4.5(b)], which has (i) strong Fe, but only weak Si character, and (ii) more contributions from the next-nearest-neighbor Si atoms than from the nearest-neighbor Si atoms (not shown). Even though the 3d projections are scaled up in Fig. 4.5(b), comparison of 3d projection and total DOS for the interstitial and substitutional cases reveals the stronger hybridization in the substitutional case. For Mn, which can be used as an example, the localized states in the gap exhibit much more Si character for a substitutional than for an interstitial impurity.

Although the impurity-host interaction is stronger in the substitutional case, the formation of interstitial impurities is more favorable (cf. Fig. 4.4). This is not related to the different

Dieses Werk ist copyrightgeschützt und darf in keiner Form vervielfältigt werden noch an Dritte weitergegeben werden.
Es gilt nur für den persönlichen Gebrauch.

Table 4.1 – Optimized TM-Si nearest-neighbor bond lengths (Å) for isolated interstitial (I) and substitutional (S) impurities in bulk Si. Variants of the GGA(+U) have been used in all cases. For comparison, the ideal Si-Si bond length is 2.37 Å here. — The agreement with previous work is very good. Without U, all substitutional bonds are smaller than the respective interstitial bonds. It is remarkable that substitutional Fe deviates significantly from the otherwise quite similar values. This can be traced to the vanishing magnetic moment: If the relaxation is performed with a constrained total moment of 4 μ_B, the bond enlarges to 2.36 Å, and inclusion of correlation effects via PBE+U with $U = 3$ eV leads to 2.39 Å. The latter value would fit nicely into the Cr-Mn-Fe sequence.

	Cr		Mn		Fe	
	I	S	I	S	I	S
this work, USPP, PBE	2.47	2.41	2.43	2.40	2.40	2.25
this work, $+U = 3$ eV	2.50	2.49	2.45	2.47	2.41	2.39
Ref. [262], USPP, PBE	–	–	2.43	2.40	2.40	2.25
Ref. [161], PAW, PW91	2.46	2.40	2.43	2.38	2.41	2.26

lattice distortions, as Shaughnessy *et al.* pointed out recently [262], but is rather an electronic effect. The impurity formation energy difference is independent of the TM reservoir,

$$E_{\text{subs}}^{\text{form}} - E_{\text{inter}}^{\text{form}} > 0 \quad \Longrightarrow \quad E_{\text{tot}}^{\text{TM subs in Si}} + E_{\text{bulk}}^{\text{Si}} > E_{\text{tot}}^{\text{TM inter in Si}},$$

and shows that even the large (negative) binding energy of Si (which lowers the value of the substitutional side of the equation) cannot compensate for the repulsive response of the Si host electronic structure to the presence of a substitutional impurity.

In order to provide a visual impression of the *spatial* influence of a TM impurity on the electronic structure of the surrounding Si host, Fig. 4.7 shows exemplarily the effect of a single interstitial or substitutional Fe impurity. The density plots show ILDOS differences (with respect to unperturbed Si) for different energy integration intervals [cf. Eq. (3.7) on page 67]. If the integration interval comprises the whole VB, the ILDOS is equal to the valence charge density. The two other plots correspond to the upper part of the VB and the lower part of the CB [cf. Fig. 4.5(b)].[11] From the PDOS for interstitial Fe one can deduce that the VB plots contain Fe t_2 and e states, while the CB plot shows e states. The plot of the entire VB for substitutional Fe shows t_2 and e states, while the plot for the upper part of the VB contains e states only. The CB plot provides an impression of the antibonding t_2^* states. At the Fe site, the section through the e states resembles strongly a d_{z^2} orbital, which is in fact part of the e representation. All images show a strong increase (blue) of the ILDOS around the Fe site, which is simply due to the additional Fe states. In the case of substitutional Fe, the striking depletion areas (red) at its nearest Si neighbors are a relaxation effect, since the Fe-Si distance is much smaller than the Si-Si distance (cf. Table 4.1). Thus, the Si charge density moves with the Si atom towards the Fe site.

It becomes obvious from Fig. 4.7 that the impurity wave functions (meaning here, in a more general and practical sense, the changes induced in the host electronic structure by

[11] The energy integration intervals are given with respect to the *unperturbed* bulk Si band structure. For instance, "upper part of the VB" means integration from −1.0 eV below the VBM to the Fermi energy, which lies in the band gap for both sites. Analogously, "lower part of the CB" means integration from the Fermi energy to +0.6 eV above the CBM.

Dieses Werk ist copyrightgeschützt und darf in keiner Form vervielfältigt werden noch an Dritte weitergegeben werden.
Es gilt nur für den persönlichen Gebrauch.

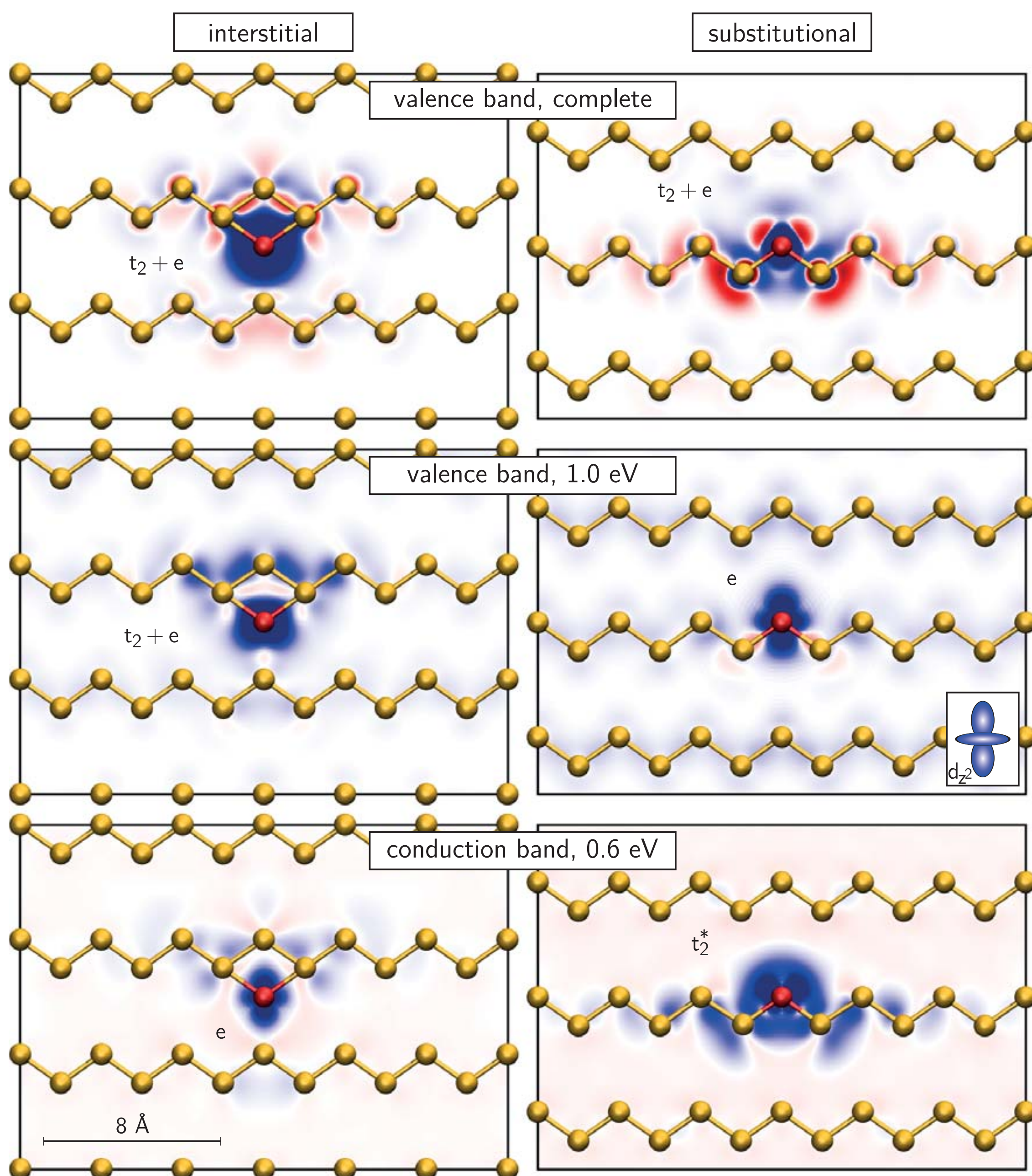

Figure 4.7 – Influence of an isolated Fe (red atom) interstitial (left column) or substitutional (right column) impurity on different ILDOS in bulk Si. Differences with respect to pure Si are shown (red means negative, blue means positive). The integration comprises the complete VB (i.e., the valence charge density), the upper part (1.0 eV) of the VB, and the lower part (0.6 eV) of the CB (from top to bottom). The (110) sections are formed by $[1\bar{1}0]$ and [001] axes. The density plot range is always $\pm 0.01/\,\mathrm{bohr}^3$. The small "background noise" in the middle and bottom row images is simply due to slightly different ILDOS integration intervals for the perturbed and the unperturbed system.

Dieses Werk ist copyrightgeschützt und darf in keiner Form vervielfältigt werden noch an Dritte weitergegeben werden.
Es gilt nur für den persönlichen Gebrauch.

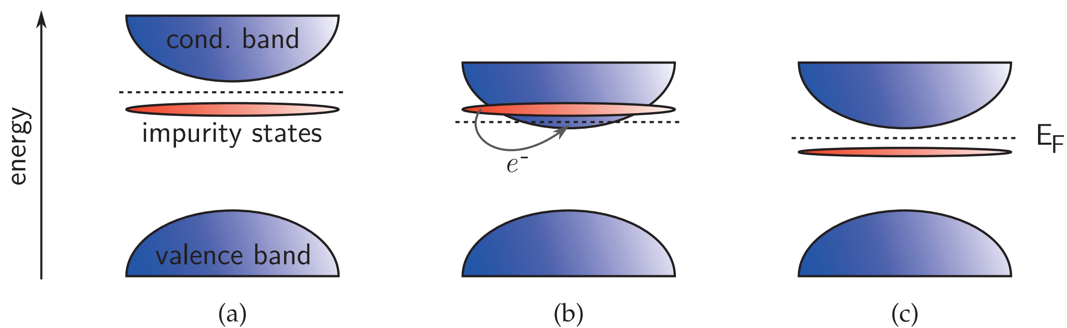

Figure 4.8 – Illustration of a possible DFT error in the description of impurities in semiconductors due to the band gap problem. The horizontal dashed line indicates the position of the Fermi energy. (a) Experimental situation with completely filled impurity states. (b) Qualitatively wrong DFT description with too small a band gap but rigid impurity state positioning, which leads to an erroneous occupation of the CB states. (c) Qualitatively correct DFT description with too small a band gap and repositioned impurity states.

the presence of the impurity) extend along the Si-Si bonds of the host material, which lie in the chosen (110) plane. Their magnitude decays rapidly with increasing distance from the center. The diameter of the impurity wave functions can be estimated from the ILDOS differences ($> 10^{-4}$/bohr^3) to be at least $d = 20$ Å here.[12] In order to get a finite magnetic exchange coupling between two TM impurities, the wave functions need to overlap. Hence, assuming the TM-TM distance d in [110] direction on average, the necessary concentration of TM atoms in a Si matrix can be estimated to be $x \approx 0.7\%$. This value is in the range of recent theoretical work, where concentrations between $x \approx 12.5\%$ and 0.5% have been studied [68, 161, 262]. For comparison, two examples for experimental work are given: Reference [269] reports FM behavior of Mn-doped Si at room temperature ($x \approx 0.1\%$ via ion implantation). Reference [270] reports a uniform distribution of Fe impurities in Fe_xSi_{1-x} DMS films grown by molecular beam epitaxy on Si(100) for $x \approx 4\%$; it is speculated that ferromagnetism occurs below 26 K. It should be mentioned here that the magnetic TM-TM interaction (and thus the ordering temperature) will not only decrease rapidly with increasing TM-TM distance, but also oscillate between FM and AFM coupling (similar to the Ruderman-Kittel-Kasuya-Yosida interaction). This aspect will be revisited later in this chapter.

4.3.2 Effects of correlation and exact exchange

Two further aspects are interesting and shall be touched upon here. First, one can ask how the inclusion of on-site correlation affects the results presented above. An increased electron-electron correlation can modify the energy of the impurity 3d states and thus the impurity-host interaction. Moreover, if adjacent impurities start to interact, they will form an impurity band of small band width. This corresponds to the situation with a large U/t ratio in a Hubbard model, and consequently a DFT study of impurity-impurity interactions could possibly benefit from additional on-site correlation contributions. Second, the issue of the too small Si band gap has to be solved. This deficiency of the PBE exchange-correlation functional has the following consequences: In any case, one cannot expect a *quantitatively*

[12] This shows that even large cubic 216/217-atom supercells with 16.4 Å edge length (23.2 Å in [110] direction) barely lead to *really* isolated TM impurities.

Dieses Werk ist copyrightgeschützt und darf in keiner Form vervielfältigt werden noch an Dritte weitergegeben werden.
Es gilt nur für den persönlichen Gebrauch.

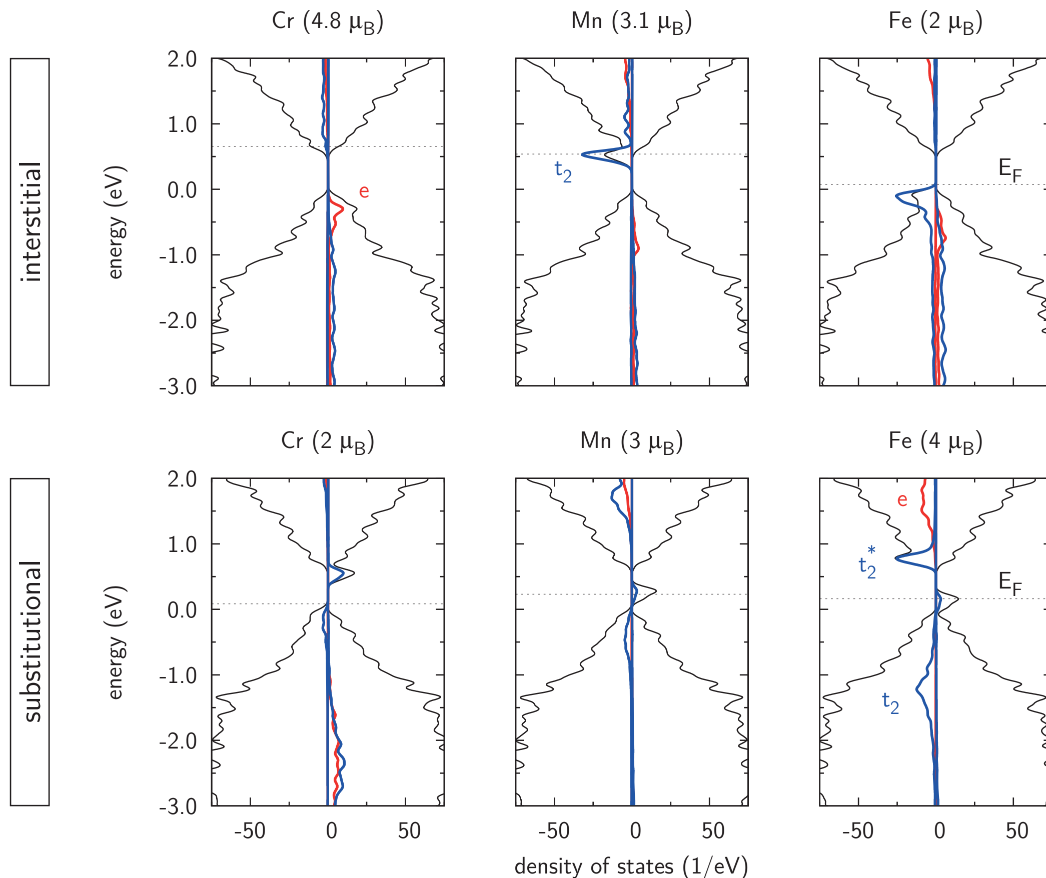

Figure 4.9 – Electronic structure of different isolated interstitial (top row) and substitutional (bottom row) TM impurities in bulk Si in their magnetic ground state, calculated with the PBE+U approach ($U = 3$ eV). As in Fig. 4.5, the blue lines depict projections of the total DOS (black lines) onto TM 3d orbitals which belong to the t_2 representation, while the red lines correspond to the e representation. The projections are scaled by a factor of 6 for clarity, and all states are broadened by a Gaussian function. The energy zero coincides with the VBM of the Si host material, while the horizontal dashed line marks the position of the Fermi energy.

correct positioning of the impurity states in the vicinity of the band gap. This is not highly problematic since the Kohn-Sham eigenvalues are only auxiliary quantities, as discussed before. If the positioning is *qualitatively* correct, the band gap problem can be overcome by a more or less simple rescaling of the energy eigenvalues, and consequently PBE ground state results are proven to be useful [cf. Fig. 4.8(c)]. This is not only important in the context of this thesis, but also for almost all recent theoretical work in this field, like Refs. [68, 161, 262–265, 271], which all rely on the qualitative validity of results obtained with the PBE exchange-correlation functional.

Figure 4.9 shows results of electronic structure calculations within the PBE+U framework for $U = 3$ eV. Such a rather small U value is motivated by a recent publication by Küwen *et al.* [68], who studied correlation effects in highly Mn- and Fe-doped bulk Si. The increased splitting between occupied and unoccupied 3d states leads to some qualitative changes. The first observation is that the dispersion of impurity states within the VB and the CB increases. More important are the impurity 3d states around the band gap. For interstitial

Dieses Werk ist copyrightgeschützt und darf in keiner Form vervielfältigt werden noch an Dritte weitergegeben werden.
Es gilt nur für den persönlichen Gebrauch.

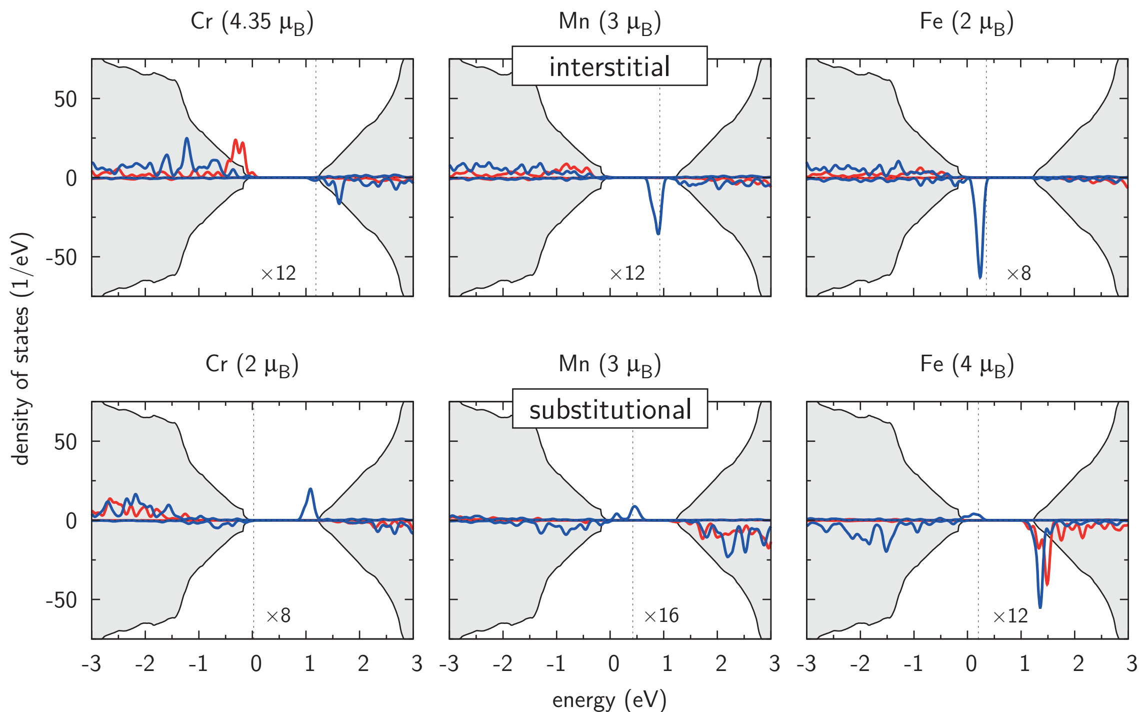

Figure 4.10 – Electronic structure of different isolated interstitial (top row) and substitutional (bottom row) TM impurities in bulk Si in their magnetic ground state, calculated with the HSE06 hybrid functional and the PAW method. As in Fig. 4.5, the blue lines depict projections of the total DOS onto TM 3*d* orbitals which belong to the t_2 representation, while the red lines correspond to the *e* representation. The projections are scaled by different (printed) factors to improve clarity, and all states are broadened by a Gaussian function. The energy zero coincides with the VBM of the Si host material, while the vertical dashed line marks the position of the Fermi energy. The gray shaded areas indicate the properly aligned total DOS of unperturbed bulk Si.

Cr, the *e* states (t_2 states) are pushed into the VB (CB), which leads to a filling of the lowest part of the CB. A similar effect occurs for interstitial Mn, where the t_2 states touch the CBM. For interstitial Fe, the fully occupied t_2 states are partially pushed into the VB. The t_2^* states seem to be lowered for substitutional Cr and Mn. Most interestingly, the magnetic ground states have been (in principle) identical to the PBE results so far. However, the magnetic ground state of substitutional Fe is now predicted to be 4 μ_B, and the substitutional impurities follow a simple level filling scheme (successive occupation of the majority spin t_2^* states). The energy differences of the (now) excited magnetic states with 0 μ_B and 2 μ_B with respect to 4 μ_B are 137 and 678 meV in the presence of U, respectively.

Some of these results might be interesting from the point of view that magnetism can be mediated by partially filled bands. However, since the band gap is still too small, it is questionable whether these PBE+U results are indeed closer to reality.

An additional, much more notable viewpoint can be provided by a different exchange-correlation functional. Hybrid functionals like HSE06, which include a certain percentage of exact nonlocal Fock exchange (cf. Sec. 2.2.3), lead to a larger spacing of VB and CB in bulk Si (cf. Table 3.2 on page 52). The drawback of these functionals is that they are computationally *extremely* demanding. Consequently, the HSE06 results for isolated interstitial and substitutional impurities in Si shown in Fig. 4.10 are based on the PBE Si lattice constant and the

Dieses Werk ist copyrightgeschützt und darf in keiner Form vervielfältigt werden noch an Dritte weitergegeben werden.
Es gilt nur für den persönlichen Gebrauch.

PBE-relaxed atomic structure.[13] This is not problematic, since the HSE06 Si band gap is not strongly affected by using the PBE lattice constant instead of the HSE06 value [cf. Table 3.2 and Fig 3.2(d)]. Moreover, not as many $\vec{k}$ points as in the PBE(+U) calculations can be used. While the $\vec{k}$-point grid still ensures a good convergence quality of the results, the PDOS plots in Fig. 4.10 are not as precise as their PBE(+U) counterparts (Figs. 4.5 and 4.9). Thus, in order to improve the clarity of the figure, the (properly aligned) Si DOS in the background has been taken from a HSE06 bulk Si calculation.

As for PBE+U, one can observe an increased dispersion of the impurity states within the VB and the CB. For interstitial Cr, the Fermi energy only touches the CBM (in contrast to the PBE+U result). There is a (barely visible) t_2 state which is not entirely pushed into the CB, and an e state near the VBM. This is similar to the PBE result. The t_2 peak is lowered in energy for interstitial Mn and Fe. For interstitial Fe, it is completely filled and located roughly 0.2 eV above the VBM. The behavior of the t_2^* states for substitutional Cr and Mn is similar to PBE+U. HSE06 splits the partly occupied t_2^* peak more strongly. For substitutional Fe, the electronic structure resembles the PBE+U results. Again, a magnetic moment of 4 μ_B is predicted.

The overall impression is that the PBE and HSE06 exchange-correlation functionals both lead to very similar results, which means that for 3d TM impurities in Si we have the situation displayed in Fig. 4.8(c). This corroborates the reliability of PBE calculations. Such a statement must not be underestimated, since it is of fundamental importance in the whole field of *ab initio* calculations for Si spintronics.

The hybrid functional HSE06 leads to the same magnetic ground states as PBE+U, which have been discussed above. Especially, it also predicts a high-spin state with a magnetic moment of 4 μ_B for the substitutional Fe impurity. Such a result would fit into the framework of the Ludwig-Woodbury model, but the high-spin state could also be erroneously favored: While hybrid functionals are known to be superior to semilocal GGA functionals like PBE for Kohn-Sham band gaps and cohesive energies in semiconductors and molecules, it is *not* clear that they work reasonably for magnetic systems. In order to solve this open question, an experimental procedure is required that can discriminate between interstitial and substitutional impurities and measure the magnetic moment locally. Such a procedure is outlined and theoretically demonstrated in the following section.

4.4 Wave function imaging of H/Si(111) subsurface impurities

We have seen in the last section how different interstitial and substitutional TM impurities interact with the Si host matrix. Moreover, the extension of the impurity wave functions has been estimated. It has been shown that this pure *ab initio* viewpoint is certainly reliable, since (i) the results agree with existing EPR measurements, and (ii) the more advanced hybrid exchange-correlation functional HSE06 provides a qualitatively similar picture as semilocal GGA functionals like PBE do. However, a difference between PBE and PBE+U/HSE06 results has been found for the substitutional Fe impurity. The question arises whether or not it is possible to visualize and measure experimentally (i) the extension of impurity wave

[13] The supercells consisted of at least 216 atoms. Only a small $\vec{k}$-point grid and no structural relaxation beyond the PBE coordinates (in the presence of an impurity) were possible, since the convergence of a *single* SCF step took more than one month on 64 CPU cores.

Dieses Werk ist copyrightgeschützt und darf in keiner Form vervielfältigt werden noch an Dritte weitergegeben werden.
Es gilt nur für den persönlichen Gebrauch.

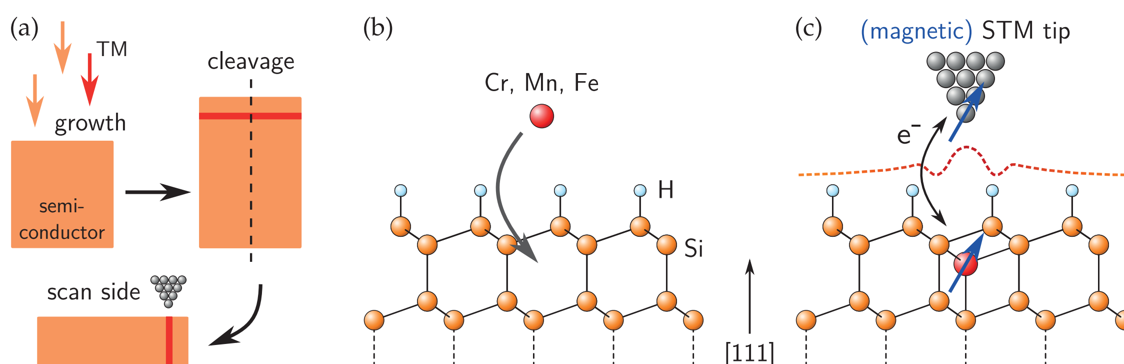

Figure 4.11 – (a) Principle of cross-sectional STM, as it is used nowadays to measure subsurface impurities in semiconductors. (b) Subsurface TM impurity injection after application of a passivating H layer. (c) Local information about the subsurface TM impurity can be obtained with (SP) STM.

functions, (ii) the local magnetic moment of an impurity, and (iii) the magnetic interaction strength between adjacent impurities.

Naturally and eventually we are interested in the properties of *bulk* impurities, since an envisaged spintronics device will contain the impurities in this form. Bulk measurements of impurity magnetic moments can be done with EPR or with x-ray absorption techniques like x-ray magnetic circular dichroism (XMCD [246,247]). The drawback of these methods is that they do not provide *local* information on the atomic scale, as desired, but *average* over a large area. Moreover, a substitutional Fe impurity with (potentially) vanishing magnetic moment would be invisible to EPR, and its XMCD signal would be hard or impossible to distinguish from that of interstitial Fe impurities or Fe precipitates. While EPR is sensitive also to small impurity concentrations that are typical for semiconductor doping, the amount of impurities has to be much higher for XMCD measurements,[14] which is problematic especially in the case of the substitutional Fe impurity.[15]

Such local information can be provided by state-of-the-art STM. For instance, there exists a large amount of recent literature on subsurface Mn impurities in GaAs [272–278]. The impurities are inserted into the semiconductor host during growth [cf. Fig. 4.11(a)]. Subsequently, the sample is cleaved *in situ*, and the side facet is scanned by STM. This procedure is known as *cross-sectional* STM. Moreover, SP STM is used nowadays to explore the magnetic properties of TM atoms at (semiconductor) surfaces [94, 279, 280]. However, there is also a drawback to this approach: Since STM is a surface analysis technique, it can only map information about (sub-)surface impurities. The behavior of the impurities is known to be biased by the presence of the surface: There can be hybridization between the impurity states and surface states or dangling bond states [281], and also charge transfer phenomena can occur. While these effects are interesting in themselves (one could think, for instance, of magnetism mediated by surface states), all these processes can strongly modify the impurity-host and impurity-impurity interactions, as we will see below, and we aim here at a technique that is able to locally image the *bulk* behavior of impurities. The approach demonstrated below paves a new route to the fundamental understanding of magnetic interactions in DMS.

[14] For instance, a ZnO sample with a Co concentration of almost 11 % has been used in Ref. [246].

[15] Statistical considerations using the impurity formation energies given in Fig. 4.4 on page 128 show that less than one substitutional Fe impurity will exist among 10^8 interstitial Fe impurities at room temperature in (perfect, hypothetical) thermodynamic equilibrium.

Dieses Werk ist copyrightgeschützt und darf in keiner Form vervielfältigt werden noch an Dritte weitergegeben werden.
Es gilt nur für den persönlichen Gebrauch.

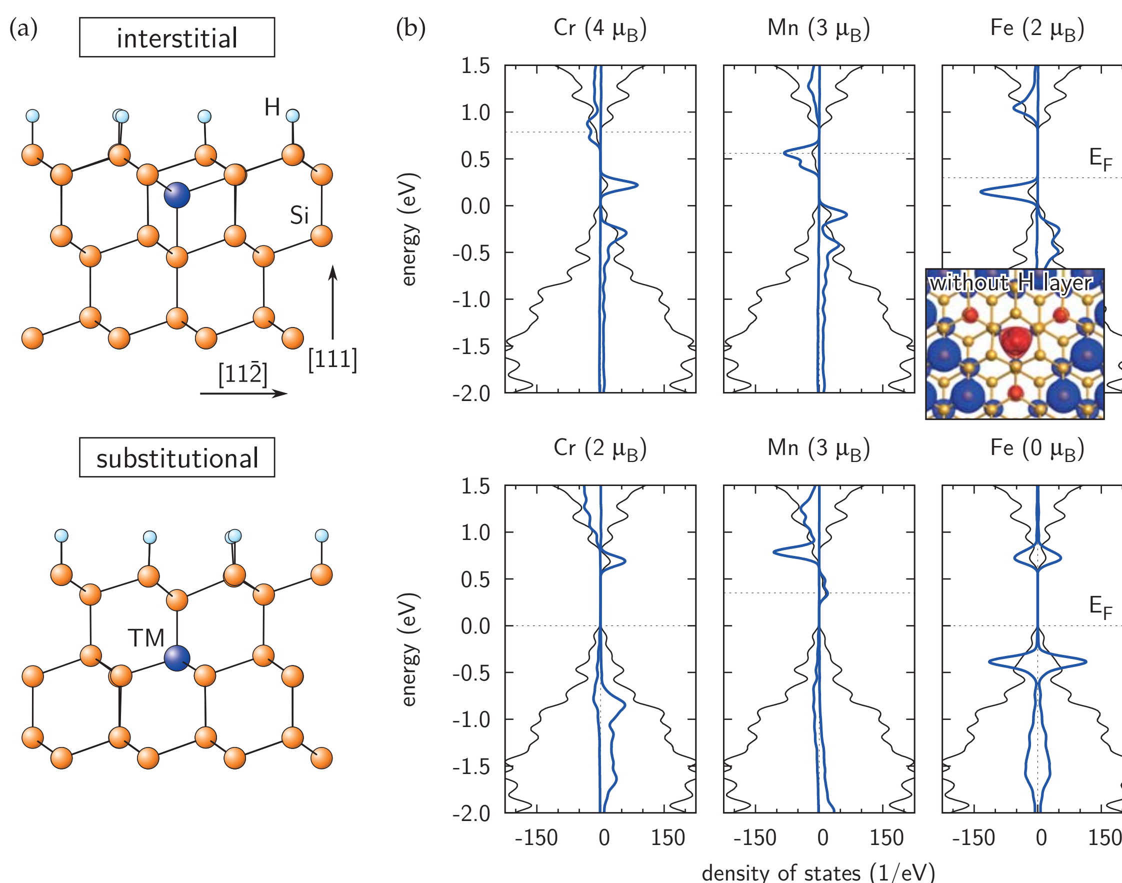

Figure 4.12 – Atomic (a) and electronic (b) structure of different isolated interstitial (top row) and substitutional (bottom row) TM impurities close to the H/Si(111) surface in their magnetic ground state (PBE). The blue lines in (b) depict projections of the total DOS (black lines) onto TM 3*d* orbitals. The projections are scaled by a factor of 12 for clarity, and all states are broadened by a Gaussian function. The energy zero coincides with the VBM of the Si host material, while the horizontal dashed line marks the position of the Fermi energy. The small inset shows a top view of spin density isosurfaces (blue/red meaning positive/negative) for a subsurface interstitial Fe impurity (located in the center of the inset) *without* H passivation.

4.4.1 Bulklike impurity properties below passivated surfaces

The idea is to study TM impurities below *passivated* surfaces like the H/Si(111) surface, as illustrated in Figs. 4.11(b) and (c). Such a H layer can be applied by wet chemistry [249] *a priori* with subsequent impurity injection, or *a posteriori* after growth of a doped sample and cleavage. As already discussed above in Sec. 4.2, one can also try to deposit dissociated H_2 molecules instead of etching. After the preparation of the sample, it can be studied by STM or even SP STM, which is used nowadays to explore the magnetic properties of TM atoms at (semiconductor) surfaces [94,279,280]. In the following, the theoretical proof is given that this comparatively simple approach is indeed capable of providing *bulklike* results.

The first step is to realize that the "bulk" electronic structure of a TM impurity remains intact in the vicinity of the H/Si(111) surface. Figures 4.12(a) and (b) show the atomic and electronic structure of isolated interstitial and substitutional Cr, Mn, and Fe impurities close to the H/Si(111) surface. Note that the Si band gap is slightly larger in the finite

Dieses Werk ist copyrightgeschützt und darf in keiner Form vervielfältigt werden noch an Dritte weitergegeben werden.
Es gilt nur für den persönlichen Gebrauch.

surface slab geometry used here than in the bulk case due to confinement effects, as it has already been discussed in Sec. 4.2. In addition, the reduced symmetry provides more freedom for the impurity states to split up slightly. The t_2 and e representation labeling is invalid now. Keeping these two aspects in mind, comparison with Fig. 4.5 reveals a very close agreement between impurities in bulk Si and H/Si(111) subsurface impurities. Especially, the magnetic ground state is preserved. Moreover, the impurities are very close to the surface here, and it is reasonable to expect a rapid convergence towards perfect bulk behavior with increasing impurity-surface distance. The rate of convergence will certainly depend on the actual extension of the wave function.

The situation is *very* different if the H surface passivation is not applied. In this case, the aforementioned surface phenomena occur, which bias the electronic structure of the impurity. The small inset in Fig. 4.12(b) shows a spin density isosurface for an interstitial Fe impurity close to the unpassivated Si(111)-SDB surface. We neglect possible surface reconstructions for the moment. Strong structural relaxations occur around the Fe impurity. Beyond some radius around the impurity one can see the spin polarization of the surface Si atoms (due to the dangling bonds). In contrast, the local magnetic moment at the Fe site is almost halved with respect to its bulk value. In the vicinity of the impurity almost no spin polarization can be observed at the surface Si atoms. It is needless to say that this situation reflects nothing of the bulk impurity behavior, which underlines the importance of the surface passivation.

4.4.2 Impurity-host interactions

After realizing that the electronic structure of the TM impurity is preserved below the passivated surface, let us now proceed as illustrated in Fig. 4.11(c). Figure 4.13 shows simulated empty- and filled-state STM images of isolated interstitial Cr, Mn, and Fe impurities below the H/Si(111) surface. They have been derived from the PBE electronic structure. A side view of the corresponding atomic structure can be seen in Fig. 4.12(a). Since the wave functions (and thus the STM images) are very sensitive quantities that show strong interference effects with the periodic images (due to periodic boundary conditions) even if the total energy of the system is already well converged, very large surface unit cells have to be used [Si(111)-(9×9)]. All filled-state images have a quite similar, triangular appearance and show a depression above the TM impurity as well as pronounced H atoms in the $[11\bar{2}]$, $[\bar{2}11]$, and $[1\bar{2}1]$ directions. There is not much element specificity visible. More interesting are the empty-state images. Although the absolute value of the applied bias voltage (energy integration interval) is lower than in the filled-state case, the corrugation is twice as large. The features induced by the subsurface impurities are clearly different from those in the filled-state case. Their diameter is roughly $d = 20$ Å and agrees with the considerations made above in the context of Fig. 4.7. Hence, the extension of the impurity wave functions, which depends on the impurity-host interactions, can be measured with this approach. Moreover, the different chemical elements lead to differences in the STM images. The Cr feature has a ringlike shape with additional protrusions at the H atoms in the $[11\bar{2}]$, $[\bar{2}11]$, and $[1\bar{2}1]$ directions. In contrast, the Fe feature consists of a central region resembling a caltrop, which is sharply separated from the protrusions at the H atoms in the $[11\bar{2}]$, $[\bar{2}11]$, and $[1\bar{2}1]$ directions. Mn appears visually as a mixture of the Cr and the Fe feature. These differences are caused by the different amount of t_2- and e-like states from the minority spin channel

Dieses Werk ist copyrightgeschützt und darf in keiner Form vervielfältigt werden noch an Dritte weitergegeben werden.
Es gilt nur für den persönlichen Gebrauch.

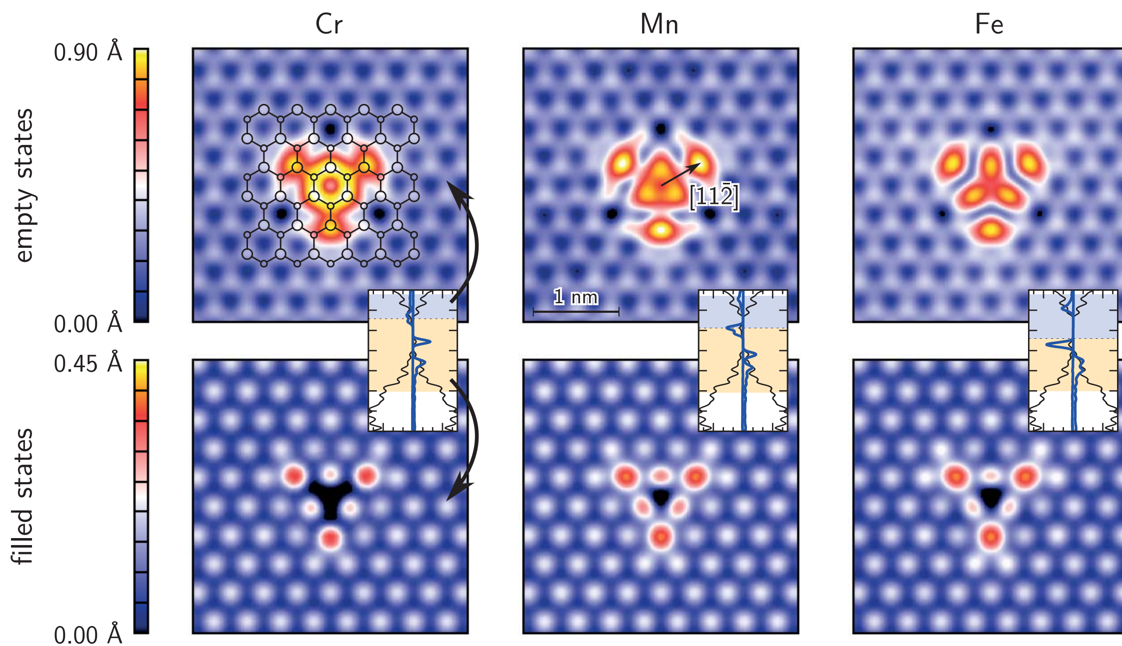

Figure 4.13 – Simulated empty- and filled-state constant current ($\varrho_c = 10^{-7}$ / bohr^3) STM images of interstitial Cr, Mn, and Fe impurities (located in the center of each image) below the H/Si(111) surface. In analogy to Figs. 4.3 and 4.7, the empty-state images include the states from E_F to +0.6 eV above the H/Si(111) host CBM, while the filled-state images include the states from E_F to −1.0 eV below the host VBM, as indicated by the blue and orange shaded areas in the small PDOS plots [cf. Fig. 4.12(b)]. Bigger circles mark the H/Si layers, smaller circles the second Si layer. A side view of the atomic structure can be seen in Fig. 4.12(a).

included in the STM image [cf. Fig. 4.12(b) and the small PDOS plots in Fig. 4.13] and the different degree of hybridization between these states and the CB states of Si.

More information about the impurity can be obtained with SP STM, which is sensitive to its magnetic state. If the direction of the local impurity magnetic moment is fixed due to an external magnetic field (which is required anyway in order to properly align the magnetic moments of the sample relative to the STM tip), the SP STM will provide a contrast between the two spin channels that is related in its magnitude to the value of the magnetic moment.[16] This is demonstrated in Fig. 4.14, again for interstitial Cr, Mn, and Fe impurities as well as for empty and filled states, in analogy to Fig. 4.13. The magnetic-contrast images are significantly different for the three chemical elements, regardless of the bias voltage sign. The empty-state images show a large contrast for Cr (4 μ_B) and a smaller contrast for Fe (2 μ_B). Moreover, the shape of the features is different, especially in the central region. One can see clearly from Fig. 4.14 that the spin polarization induced in the host electronic structure is anisotropic. For the empty states, for instance, it extends along the [11$\bar{2}$], [$\bar{2}$11], and [1$\bar{2}$1] directions (cf. Fig. 4.13). The magnetic-contrast images show the *maximal* contrast, i.e., the case of an ideal, half-metallic STM tip (cf. Sec. 2.3.3). In reality, the contrast will be lower due to spin fluctuations and the missing half-metallicity, but only downscaled and still visible under appropriate conditions (low temperatures, high magnetic fields, etc.).

[16]Note that the local impurity magnetic moment will follow the external magnetic field, while the SP STM tip can preserve its magnetic orientation [282].

Dieses Werk ist copyrightgeschützt und darf in keiner Form vervielfältigt werden noch an Dritte weitergegeben werden.
Es gilt nur für den persönlichen Gebrauch.

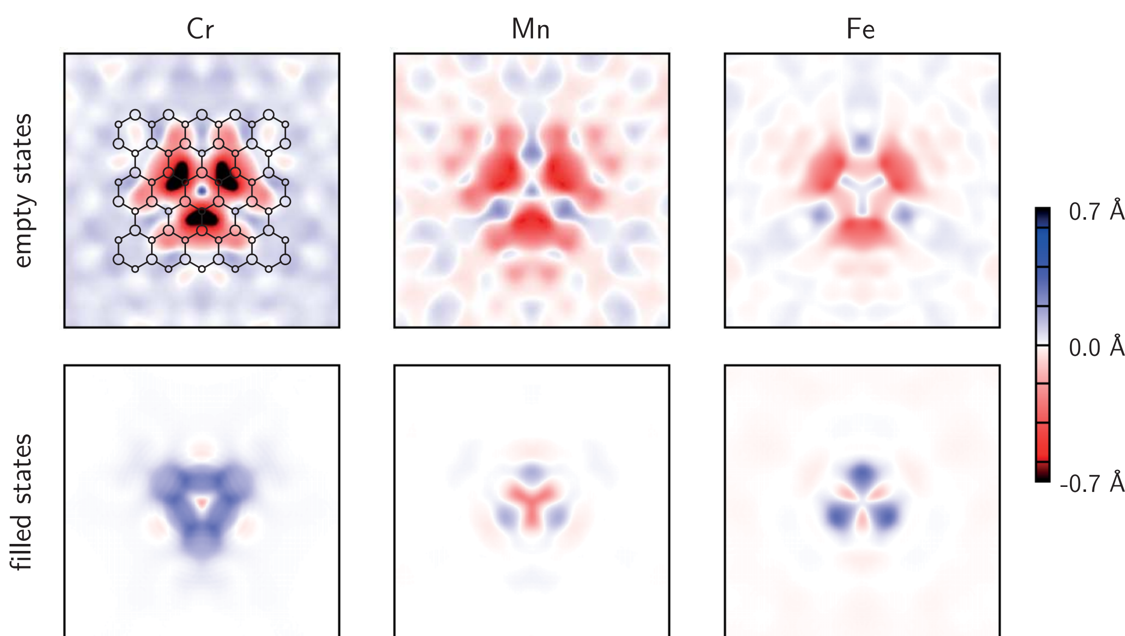

Figure 4.14 – Simulated SP STM magnetic-contrast images for interstitial Cr, Mn, and Fe impurities below the H/Si(111) surface, in analogy to Fig. 4.13. Blue (red) areas correspond to a stronger influence of the majority (minority) spin channel. Bigger circles mark the H/Si layers, smaller circles the second Si layer. The energy integration intervals have been chosen analogously to Fig. 4.13.

The substitutional Fe impurity

An interesting application of this approach is the substitutional Fe impurity in Si. As discussed above, the DFT results strongly depend on the methodology in this case. Figure 4.15 shows simulated (SP) STM images for PBE (0 μ_B) and PBE+U (4 μ_B). The PBE+U result is shown since it provides a roughly similar electronic structure as hybrid functionals do; hence, the STM image should also look similar.[17] As for the interstitial impurities, the corrugation is much higher in the empty-state case. The PBE images show a strong depression (filled states) or a compact feature that is formed by the three H/Si sites that lie closest to the impurity. In-plane, the feature is obviously smaller for substitutional impurities than for interstitial impurities. The depression in the filled-state image is partially caused by an inwards relaxation of the Si atom above the Fe impurity (vertical distance to the Si plane: -0.22 Å). The empty-state image shows no sign of this effect. In contrast, the images simulated from the PBE+U electronic structure show three distinct protrusions at the H/Si sites, irrespective of the bias voltage sign. Instead of an inwards relaxation, the Si atom is pushed away from the Fe impurity (vertical distance to the Si plane: $+0.12$ Å). This is related to the different Fe-Si bond lengths with and without U (cf. Table 4.1 on page 132). The local magnetic moment at the Fe site, if it exists, can clearly be seen in the SP STM magnetic-contrast images, irrespective of the applied bias voltage sign.

Recently, the STM observation of a substitutional Fe impurity below a H/Si(111) surface has been claimed by Gruyters *et al.* [251]. Their images show the mentioned depression for filled states, and the corrugation of their empty-state feature is similar to that of the sim-

[17] Treating a surface slab of the size used in this study [Si(111)-(9 × 9)] with hybrid functionals is not worthwhile, if possible at all.

Dieses Werk ist copyrightgeschützt und darf in keiner Form vervielfältigt werden noch an Dritte weitergegeben werden.
Es gilt nur für den persönlichen Gebrauch.

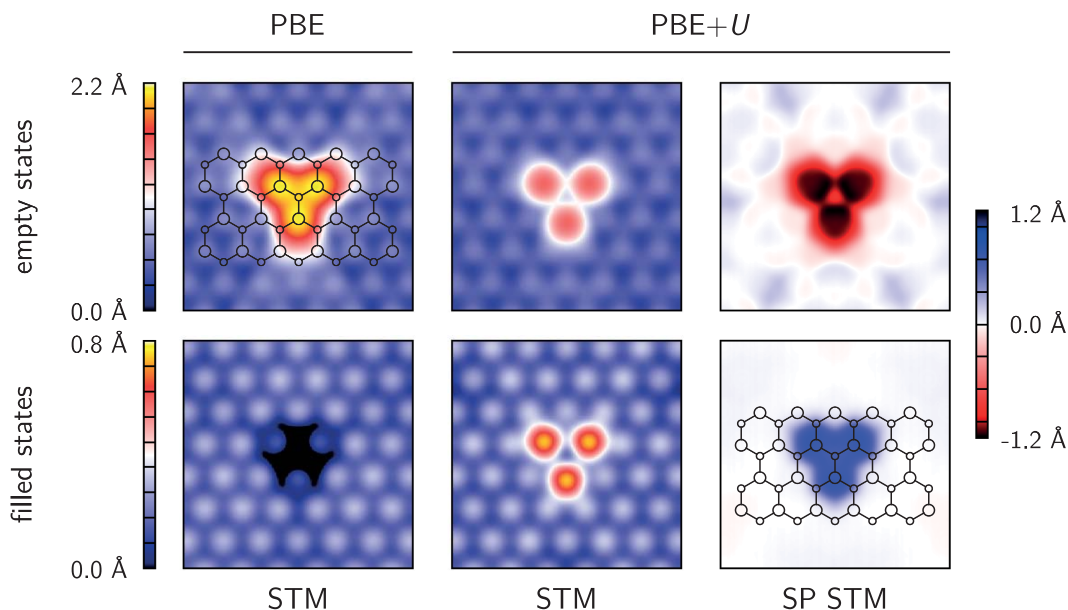

Figure 4.15 – STM and SP STM magnetic-contrast images of a substitutional Fe impurity below the H/Si(111) surface [cf. Fig. 4.12(a)] located in the center of each image, simulated from the PBE (left column) and the PBE+U (middle and right column, $U = 3$ eV) electronic structure. Bigger circles mark the H/Si layers, smaller circles the second Si layer. The magnetic moment of 4 μ_B can clearly be seen in the SP STM images. The energy integration intervals have been chosen analogously to Fig. 4.13.

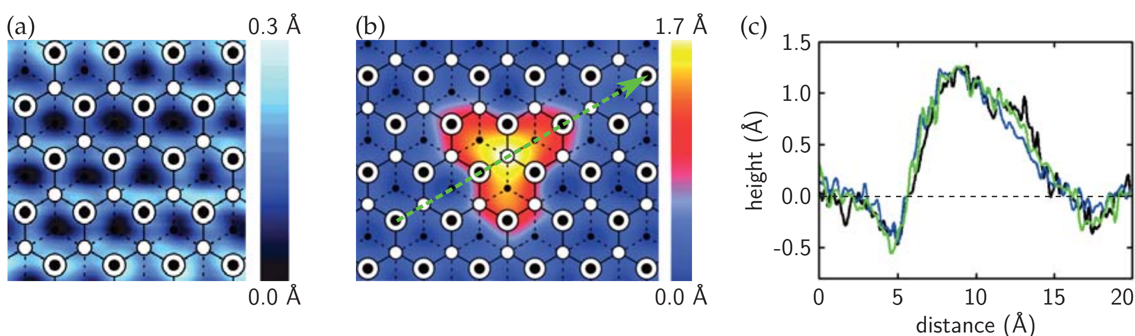

Figure 4.16 – Experimental empty-state STM images showing (a) the unperturbed H/Si(111) surface and (b) the feature potentially induced by a substitutional Fe impurity below the H/Si(111) surface. The bias voltage and constant current are +2.0 V and 50 pA, respectively. (c) Line scans along the green arrow (and its equivalents rotated by 120° about the [111] axis) in panel (b). The structural model used by Gruyters *et al.* [251] is indicated as follows: first Si layer and H atoms: large white circles with central black circles; second Si layer atoms: white circles; fourth Si layer atoms: small black circles; first-to-second-layer bonds: solid black lines; third-to-fourth-layer bonds: dashed black lines. — Printed with permission from M. Gruyters.

Dieses Werk ist copyrightgeschützt und darf in keiner Form vervielfältigt werden noch an Dritte weitergegeben werden.
Es gilt nur für den persönlichen Gebrauch.

ulated result [around 1.7 Å, cf. Figs. 4.16(b) and (c)]. Note that interstitial impurities lead to only half this corrugation according to Fig. 4.13. Moreover, position and extension of their empty-state feature agree with Fig. 4.15. From this (and from their scanning tunneling spectroscopy results, which are not shown here) one could conclude that they indeed observed a substitutional Fe impurity without magnetic moment. However, the orientation of the whole feature with respect to the surrounding H/Si(111) pattern does *not* agree with the simulated results. Tentatively, one could speculate that the structural assignment made for the pure H/Si(111) pattern in Sec. 4.2 and Fig. 4.3 on page 126, but also by Gruyters *et al.*, cf. Fig. 4.16(a), is incorrect. Modifying this "interpretation" of the unperturbed H/Si(111) areas, e.g., by interchanging the assignment of second and fourth Si layer, does not lead to an improvement of the situation, since in this case the impurity would sit on an *interstitial* site. Moreover, according to the simulated results shown in Figs. 4.13 and 4.15, the three H/Si sites around the impurity are pronounced in both the interstitial and the substitutional case, which implies that the small black dots in Fig. 4.16(b), which also mark the clear minima in the unperturbed H/Si(111) area, have to correspond to the H/Si positions (first Si layer). Consequently, this attempt to reconcile experiment and theory requires an interchange of first and fourth layer in their structural assignment of the H/Si(111) surface, which seems highly improbable to the author of this thesis.

Even though it appears for the moment that the STM images of Gruyters *et al.* [251] do not support the theoretical modeling (we will briefly revisit this point later in this chapter), it is possible to devise a strategy for solving the puzzle concerning the magnetic ground state of the substitutional Fe impurity:

1. Determine the orientation of the H/Si(111) substrate (i.e., the positions of the second and the fourth Si layer) by STM imaging of the CB (empty states). Optimal: Record data for the VB (filled states) *simultaneously* by constantly reversing the bias voltage.

2. Find an Fe impurity centered at the position of the *second* layer. The images shown in Fig. 4.15 can serve as guidance.

3. Record the magnetic contrast with SP STM at this location.

As Fig. 4.15 shows, the difference in the local electronic structure due to the different magnetic moments can already be observed with conventional STM. However, SP STM is able to provide additional evidence. If no magnetic contrast is visible, the substitutional Fe impurity bears no magnetic moment, and consequently the semilocal DFT result is correct, while hybrid functionals and DFT+U erroneously overestimate the energy gain associated with magnetic moment formation. If, on the contrary, a magnetic contrast is visible (which is calculated to be strong, ± 1.2 Å), hybrid functional predictions are correct, and the deviations from the Ludwig-Woodbury model reported by Beeler *et al.* [260] are only an artifact of semilocal DFT. Thus, SP STM in the proposed setup, which allows for detection of the impurity site and the magnetic moment *at the same time*, offers the unique opportunity to decide about the issue of the substitutional Fe high-spin state. Since answering this question is of fundamental importance, carefully performed experiments realizing the aforementioned strategy would be highly valuable. They could become a benchmark for the applicability of hybrid functionals in the field of DMS.

Dieses Werk ist copyrightgeschützt und darf in keiner Form vervielfältigt werden noch an Dritte weitergegeben werden.
Es gilt nur für den persönlichen Gebrauch.

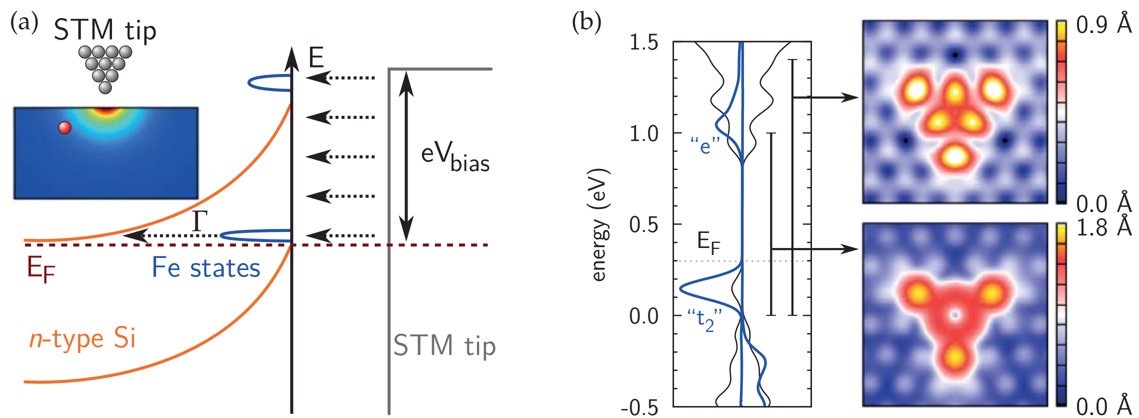

Figure 4.17 – Possible effect of tip-induced band bending. (a) TIBB scheme for a subsurface interstitial Fe impurity in *n*-type Si, together with an illustration of a tip-induced local electrostatic potential. (b) Modified STM images of an interstitial Fe impurity, showing t_2-like states (lower image) or a mixture of t_2- and e-like states (upper image) together with parts of the H/Si(111) CB.

Tip-induced band bending

The local electrostatic potential of the STM tip can influence subsurface impurities. This has been demonstrated recently by experimentalists in the group of P. M. Koenraad [283, 284] for Si impurities close to the GaAs(110) cleavage surface: The Si impurities ionize due to the presence of the STM tip, i.e., they change their charge state as a consequence of tip-induced band bending (TIBB) near the surface. The experiments have been carried out at low temperatures (around 5 K) with *n*-type GaAs, and the TIBB necessary for the ionization was estimated to be 150 – 180 $\pm$ 50 meV.

If we assume *n*-type Si, a subsurface interstitial Fe impurity will still be neutral, since its states are either completely filled (around the VBM) or completely empty (above the CBM; cf. Fig. 4.12). The application of a strong positive bias voltage at low tip-surface distances can now lead to the situation shown in Fig. 4.17(a): The Si bands are bent upwards, and the minority spin t_2 states can be depleted. As a consequence, the empty-state STM maps the formerly filled impurity t_2-like states instead of the empty e-like states, in conjunction with parts of the H/Si(111) CB, or a mixture of t_2- and e-like states, depending on the bias voltage. Figure 4.17(b) visualizes in a first approximation how this could affect the recorded STM image. The exclusion of the e-like states in the CB leads to a more ringlike, connected feature. In contrast, only including the t_2-like states in addition to the conventional STM image (cf. Fig. 4.13) does not produce a significantly different result. Note that the electronic structure used for the simulation of these images is still that of a neutral impurity, and only different integration intervals have been used (that do *not* start from or end at the Fermi energy). Moreover, the tunneling rate between the tip and the impurity has to be lower than the tunneling rate Γ between the t_2-like impurity states and the Si CB. Otherwise, Coulomb blockade phenomena in the TM impurity can add to the complexity.

The TIBB depends strongly on the tip shape, the tip-surface distance, and the applied bias voltage [283]. Thus, such tip-induced modifications of the subsurface impurity can be minimized or avoided by choosing adequate experimental conditions.

Dieses Werk ist copyrightgeschützt und darf in keiner Form vervielfältigt werden noch an Dritte weitergegeben werden.
Es gilt nur für den persönlichen Gebrauch.

The Kondo effect

The Kondo effect arises due to the interaction of the electrons of a magnetic impurity with the conduction electrons of a surrounding NM host. This leads to a screening of the impurity spin and to an electronic resonance at the Fermi energy. One can observe the Kondo effect in single TM atoms on metal surfaces using scanning tunneling spectroscopy, for instance, in Co atoms on the (111) and (100) surfaces of Cu, Ag, and Au [285–287]. Around zero bias, the tunneling conductance shows a characteristic dip (due to the Kondo resonance) and has a Fano line shape.

The question arises whether the Kondo effect plays a role for isolated TM impurities in Si or not. High densities of carriers are necessary which can scatter at the impurity (like in metals). Typical metal carrier densities are around 10^{22} cm^{-3} (Cu, Ag, and Au), while usual values for n-type Si range from 10^{15} to 10^{19} cm^{-3}, depending on the doping. Thus, the Kondo effect will certainly be of minor importance for isolated TM impurities in semiconductors.

4.4.3 Impurity-impurity interactions

The method described so far is useful not only to study the interactions of isolated impurities with the surrounding host material. Another interesting aspect is the magnetic exchange interaction of neighboring impurities, which can exhibit a quite complicated behavior. Due to their spatial separation, impurity pairs and small clusters will keep their local properties. However, the energy difference between parallel and antiparallel orientation of the local magnetic moments will depend on their distance and on the relative spatial orientation of the impurities in the host lattice.[18] In the following it will be shown, exemplarily for interacting interstitial Fe impurities, that the interaction properties are even *quantitatively* preserved in the vicinity of the H/Si(111) surface, which proves that the interaction properties of impurities in the *bulk* material can be obtained from *surface* experiments.

It is demonstrated in Fig. 4.18 how the magnetic exchange interaction between adjacent TM impurities can be measured with SP STM. Both magnetic states (FM/AFM, meaning parallel/antiparallel orientation of the two local magnetic moments) lead to a very similar STM image, which is essentially a superposition of two individual images. Thus, no magnetic information can be obtained here. However, the SP STM is able to resolve the antiparallel ordering in the AFM case. In the shown example, the AFM state is 8 meV per Fe atom lower in energy than the FM state (cf. Table 4.2) and would therefore be observed in experiments. The calculated SP STM contrast of ± 0.5 Å is large enough to distinguish the FM from the AFM alignment. If the local properties of the interacting impurities were, for some reason, not retained, this would be visible in (SP) STM images and revealed by comparison with images of isolated impurities. (Note the similarity between Figs. 4.13, 4.14, and 4.18).

Given a grown sample with a random distribution of many impurities one can select isolated pairs and measure the sign of their interaction energy (FM/AFM) as a function of their distance vector. The results can be compared with the calculated values given in Table 4.2, which show that there is a strong dependence of the magnetic exchange interaction on the distance vector of the impurity pair. This behavior directly reflects the anisotropy in the impurity-induced spin polarization of the host electronic structure (cf. Fig. 4.14). Moreover, an externally applied and gradually increased magnetic field can be used to measure

[18] For a fixed host material one can say that sign and magnitude of the magnetic exchange interaction depend on the *distance vector* of an impurity pair.

Dieses Werk ist copyrightgeschützt und darf in keiner Form vervielfältigt werden noch an Dritte weitergegeben werden.
Es gilt nur für den persönlichen Gebrauch.

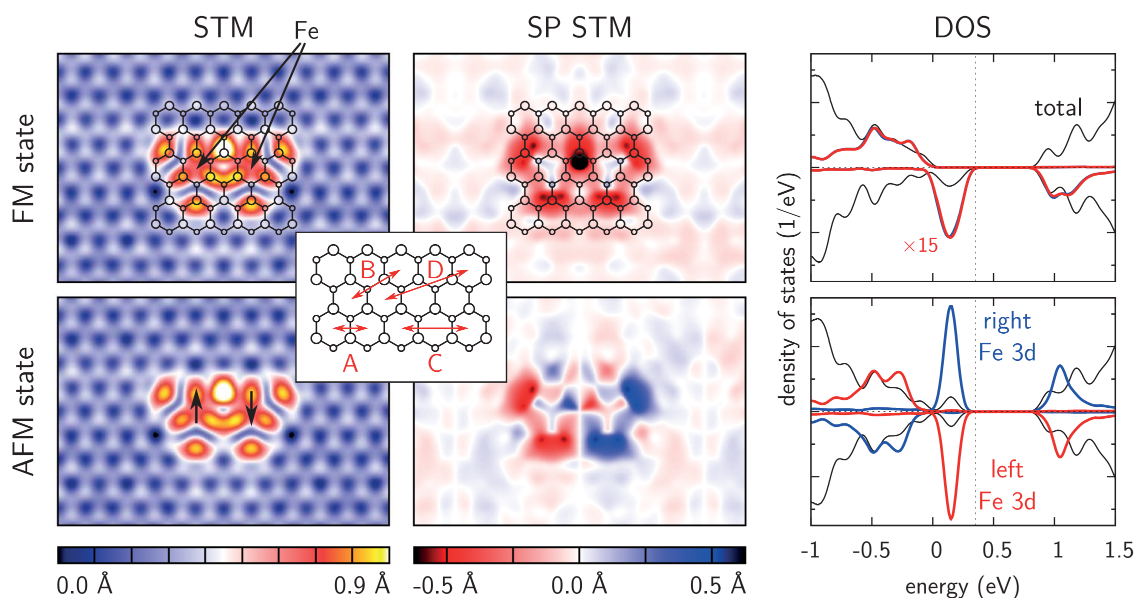

Figure 4.18 – Simulated STM and SP STM magnetic-contrast images of two interacting subsurface interstitial Fe impurities. The applied empty-state bias voltage (energy integration interval) is equivalent to that used in Figs. 4.13 and 4.14, which show results for the *isolated* Fe impurity. The central inset defines the different impurity pair configurations A, B, C (shown here), and D (cf. Table 4.2). Bigger circles mark the H/Si layers, smaller circles the second Si layer. The right column shows the corresponding total DOS and projections on the Fe $3d$ orbitals. The energy zero coincides with the VBM of the Si host material, while the vertical dashed line marks the position of the Fermi energy.

the magnitude of the magnetic exchange interaction by determining the Zeeman energy at which the moments align parallel (switching), given that the ground state is AFM and that the interaction is not too strong to be overcome by the magnetic field (e.g., configuration D in Table 4.2). Thus, the two impurities should not be located too close together for this part of the experiment. Additionally, care has to be taken not to influence the impurity magnetism with the SP STM tip stray field [94].

The interaction energies given in Table 4.2 show that there is indeed a quantitative agreement between the Fe-Fe interactions in bulk Si and those close to the H/Si(111) surface, even though the impurities are *maximally* close to the surface here. One can speculate that, in general, the degree of agreement will depend on the extension of the impurity wave functions. It is certainly an appropriate picture that the interaction between two impurities in a Si host is mediated along the Si-Si bonds, since this is where the individual impurity wave functions overlap. The total interaction can be understood as a sum of partial, differently intense interactions arising from all possible paths connecting the two impurities through the crystal, similar to a path integral. In general, the partial interactions will show a rapid decay towards zero with increasing length of the corresponding path, simply due to the decay of the wave function. The more the impurity wave functions are extended, the more paths will contribute significantly, and the presence of a surface removes some of these paths and modifies the total interaction strength. Interestingly, this does not pose any conceptual difficulties for the suggested procedure of extracting interaction strengths from (SP) STM observations: If the extension of the impurity wave functions is large, one can still detect

Dieses Werk ist copyrightgeschützt und darf in keiner Form vervielfältigt werden noch an Dritte weitergegeben werden.
Es gilt nur für den persönlichen Gebrauch.

Table 4.2 – Energy differences $\Delta E = E_{AFM} - E_{FM}$ (±0.5 meV) per Fe atom and distances of two interacting interstitial Fe impurities in the H/Si(111) subsurface layer [cf. Fig. 4.12(a) and the inset in Fig. 4.18] and in bulk Si. $\Delta E > 0$ indicates a more stable FM configuration. Configuration D, whose $|\Delta E|$ is already below the numerical accuracy, is included to indicate the finite interaction range.

Configuration	A	B	C	D
Fe-Fe distance (Å)	3.90	6.70	7.75	10.22
ΔE, H/Si(111) (meV)	+47	+3	−8	−0.2
ΔE, bulk Si (meV)	+44	+2	−7	−0.2

impurities that are buried deeper within the host material. Thus, one can use these in the experiment instead of impurities located very close to the surface. Consequently, the number of possible interaction paths is increased again, and the interaction strength converges towards the bulk value. Simulated STM images (not shown) for interstitial Cr, Mn, and Fe impurities with different impurity-surface distance (for instance, one Si-Si distance further away from the surface) demonstrate that their properties are still detectable at the surface.

Scope of the method: Co-doped ZnO

The presented technique is not restricted to TM impurities in Si. Basically any impurity in any host material can be studied, given that a surface exists that can be passivated. As mentioned in the introduction, a quite intensely studied and controversially disputed system is Co-doped ZnO. Up to now, the existence or absence of FM order is an open question [243, 246]. The approach outlined throughout this chapter can lead to valuable experimental answers in this field. It has been shown recently that low-temperature (200 K) exposition of the ZnO($10\bar{1}0$) surface to H atoms yields a fully passivated surface [288]. Hence, the impurity-host interactions (i.e., local magnetic moments) of isolated Co impurities below this surface and the distance-dependent magnetic exchange interactions of different subsurface Co impurities can be studied by STM and SP STM, which would enable an assessment of their contribution to the magnetic properties of doped bulk ZnO.

4.4.4 Kinetic aspects of impurities near the H/Si(111) surface

One could expect that a passivated surface like H/Si(111) is chemically absolutely inert. It has been shown recently that this is not the case, since even the coinage metal Cu adsorbs on H-passivated Si surfaces [289]. In this section we will take a look at the kinetic barriers that are involved in a direct injection process and subsurface migration of 3*d* TM impurities below the H/Si(111) surface.

Figure 4.19 shows the impurity formation energies for Cr, Mn, and Fe atoms that enter the H/Si(111) slab from the vacuum along a [111] path towards the first subsurface interstitial site. For each data point, the whole structure has been optimized (i.e., relaxed), while the TM coordinates have been kept fixed. The first observation is that the surface is attractive, i.e., the TM atom adsorbs from the gas phase and gets incorporated in the structure. While traversing the H layer does not pose any difficulties, the two topmost Si layers (the first Si bilayer) induce two kinetic barriers. For Cr, the two barriers are merged. The barrier height

Dieses Werk ist copyrightgeschützt und darf in keiner Form vervielfältigt werden noch an Dritte weitergegeben werden.
Es gilt nur für den persönlichen Gebrauch.

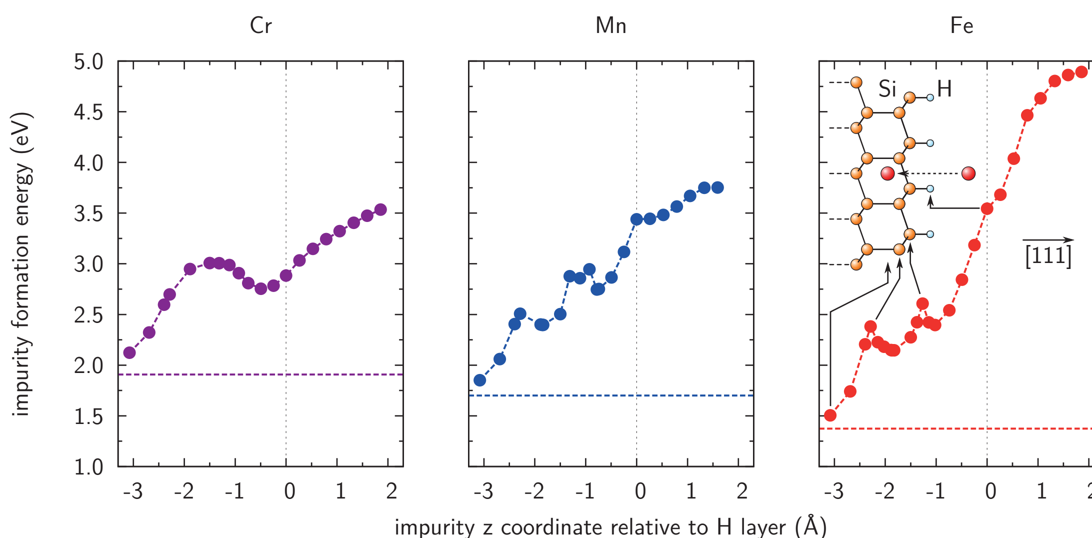

Figure 4.19 – Impurity formation energies for Cr, Mn, and Fe atoms along a [111] path towards the first subsurface interstitial site traversing the H layer. The horizontal dashed line marks the impurity formation energy in bulk Si, while the vertical dashed line marks the position of the H layer.

(entering the Si structure) is 252, 200, and 235 meV for Cr, Mn, and Fe, respectively. While these barriers can be easily overcome with the kinetic energy from the gas phase, it should be kept in mind that in the real TM injection process a part of the energy will be dissipated into the phonon system.

The formation energies are always positive, which means that formation of bulk TM material is preferred. It is thus reasonable to assume that an exposition of the surface to a dense TM vapor will lead to TM clustering on the surface instead of subsurface injection. Since the subsurface kinetic barriers are quite high for a TM impurity that intends to leave the Si matrix, the doped structure, once obtained, is thermally stable.

The horizontal dashed lines in Fig. 4.19, which mark the impurity formation energies in bulk Si, indicate that the impurity can further lower its energy slightly by diffusing away from the subsurface interstitial position deeper into the Si host. Figure 4.20 shows the kinetic migration barrier between two different subsurface interstitial sites for isolated Cr, Mn, and Fe impurities. A similar barrier has to be overcome for further diffusion leading away from the surface. The Si bilayer which is traversed poses a barrier of 725, 658, and 740 meV for Cr, Mn, and Fe, respectively, and thus obstructs further migration deeper into the Si host below room temperature.[19] The barriers have a shape similar to those shown in Fig. 4.19. The Cr barrier is merged and resembles a Gaussian function, whereas the Mn and Fe barriers have two peaks and a local minimum in between. Note that the final interstitial site (which is located below a H atom) has a higher formation energy than the initial site (corresponding to the target location in Fig. 4.19), which makes the former less favorable than the latter. The total magnetic moment of the supercell is found to remain unchanged during the transition.

[19] Reference [266] reports an activation energy (i.e., barrier height) of 680 meV for interstitial Fe in *bulk* Si, which has been obtained by fitting experimental data to an exponential function.

Dieses Werk ist copyrightgeschützt und darf in keiner Form vervielfältigt werden noch an Dritte weitergegeben werden.
Es gilt nur für den persönlichen Gebrauch.

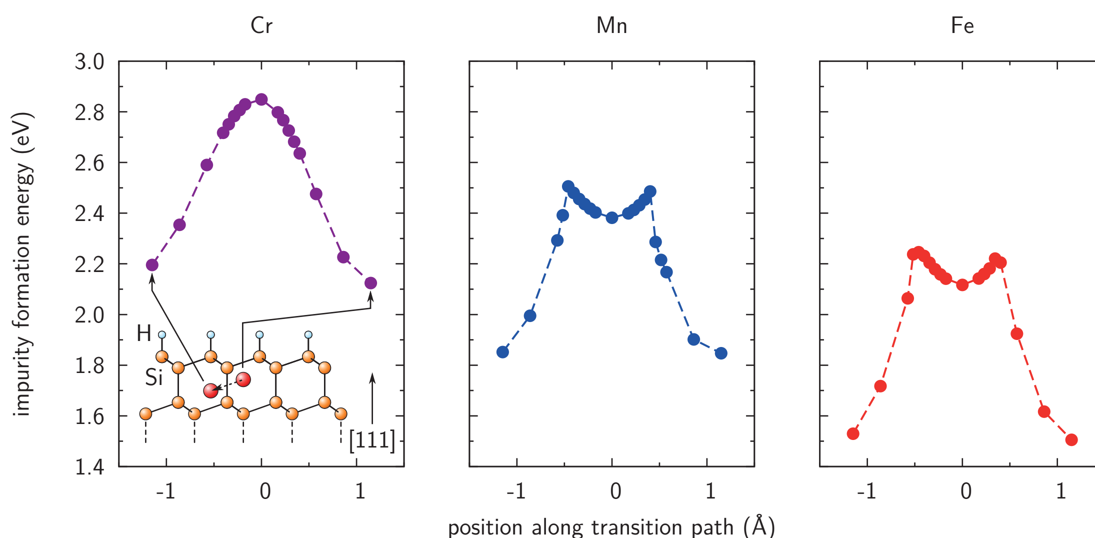

Figure 4.20 – Kinetic migration barrier between two different subsurface interstitial sites for isolated Cr, Mn, and Fe impurities. The center of the transition path corresponds to the midpoint between the two Si bilayers that are traversed.

4.5 Two-dimensional subsurface impurity layers and clusters

4.5.1 Half-metallic impurity layers

An interesting idea frequently found in the literature on TMs in Si is the so-called δ doping: Thin layers of interstitial or substitutional impurities are inserted into the semiconducting material during growth. If the concentration is chosen correctly, the two-dimensional magnetic interaction potentially establishes a desired form of ferro- or antiferromagnetism and can even lead to half-metallicity, where one spin channel is metallic while the other one is semiconducting [263–265].

Such δ layers, consisting of a hexagonal arrangement of interstitial Cr, Mn, and Fe impurities in a (111) plane of Si, are studied in this section. Since the central idea of this chapter is that bulklike information about the magnetic state can be detected by using surface experiments, the δ layers are prepared close to the H/Si(111) surface [cf. Fig. 4.12(a)] and thus form a continuation of the preceding sections.

Formation energies of different subsurface TM δ layers as functions of the TM-TM distance, and thus of the impurity density in the δ layer, are shown in Fig. 4.21. The two curves in each panel correspond to FM and row-wise AFM magnetic ordering, the latter being indicated in Fig. 4.22(a). The distances are given in units of the Si(111)-(1×1) surface lattice constant (3.866 Å here) and thus correspond to (half) the lateral supercell size for FM (AFM) TM-TM interaction, respectively.

The first aspect one can observe here is that the formation energies converge towards their respective value for isolated subsurface impurities with increasing TM-TM distance (for comparison, see Figs. 4.19 and 4.20), which is, of course, expected and shows that the DFT calculations work correctly. A qualitative difference between Cr and Mn, on the one hand, and Fe, on the other hand, is that this convergence occurs from below in the former case, while in the latter case the formation energy is a decreasing function with increasing

Dieses Werk ist copyrightgeschützt und darf in keiner Form vervielfältigt werden noch an Dritte weitergegeben werden.
Es gilt nur für den persönlichen Gebrauch.

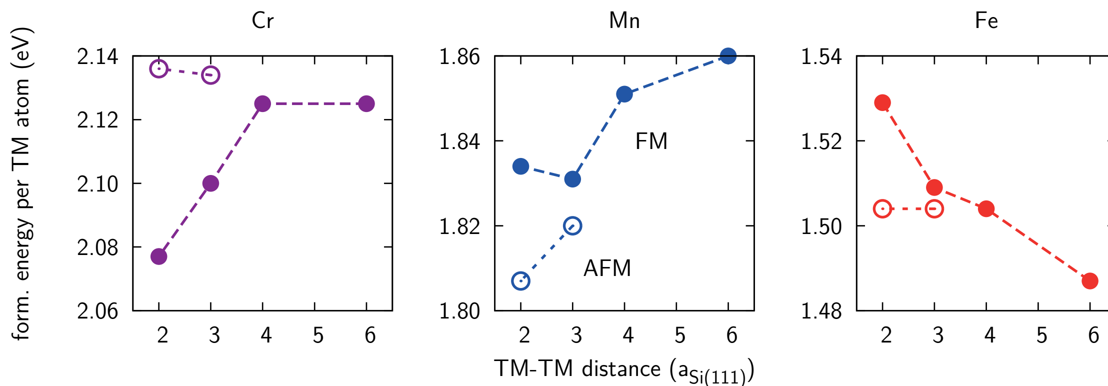

Figure 4.21 – Formation energies of two-dimensional δ layers of interstitial Cr, Mn, and Fe impurities directly below the H/Si(111) surface [cf. Fig. 4.12(a)] as functions of the TM-TM distance [in units of the Si(111)-(1 × 1) surface lattice constant] and thus of the impurity density in the δ layer. Compared are the FM (filled circles) and the row-wise AFM (open circles) configurations.

TM-TM distance. In short, Fig. 4.21 shows that the TM-TM interaction in a (111) δ layer is repulsive and AFM for Fe, attractive and AFM for Mn, and attractive and FM for Cr. The energy difference between the FM and the row-wise AFM configuration is about 60 meV/Cr in the latter case. It is interesting that the Cr layer shows these strong FM trends in Si, since usually Cr is a material with AFM coupling, both in bulk and as single ML on Ag(111) [290] or Pd(001) [291]. This is most certainly related to the 1/3 occupation of the minority spin t_2 peak [cf. Fig. 4.5(b) on page 129].

In addition to the attractive FM coupling between different Cr sites, there is a very high degree of spin polarization at the Fermi energy in the 1/4 layer,[20] which is hence nearly half-metallic (cf. Fig. 4.22). In the 1/9 layer, there are no majority spin states near the Fermi energy, so this layer is indeed perfectly half-metallic. Consequently, one can expect a highly spin-polarized metallic transport in two dimensions. Alternatively, a spin-filtering effect can arise if the current flow is perpendicular to the impurity layer. The AFM Fe layers are semiconducting, since the filled minority spin t_2 peak is only slightly broadened. This broadening increases with decreasing Fe-Fe distance and is probably responsible for the repulsive behavior.

Due to the C_3 symmetry of the H/Si(111) surface, the row-wise AFM pattern shown in Fig. 4.22(a) can be rotated by 120° about the [111] axis normal to the surface without changes in the total energy. Moreover, it can also be rotated equivalently by 60°, which is caused by the additional reflection symmetries. Hence, the interaction of a certain TM atom with the six TM atoms in its neighborhood does *not* depend on the direction. Since the geometry is hexagonal in all cases, the row-wise AFM configuration is probably not the real magnetic ground state for Mn and Fe. One can expect an additional (minor) lowering of the energy in the case of noncollinear magnetism, as it occurs for a single Cr ML on Ag(111) [290]. There, the energy is lowered by additional 14% of the FM–row-wise-AFM difference by going to the noncollinear Néel state.

It is actually possible to determine the magnetic ground state of each δ layer by using surface experiments. As an example, simulated STM and SP STM images for an Fe δ layer with

[20] The densities are called "1/4" and "1/9" in the following, which refers to the fraction of interstitial sites in the δ layer that are occupied by a TM atom.

Dieses Werk ist copyrightgeschützt und darf in keiner Form vervielfältigt werden noch an Dritte weitergegeben werden.
Es gilt nur für den persönlichen Gebrauch.

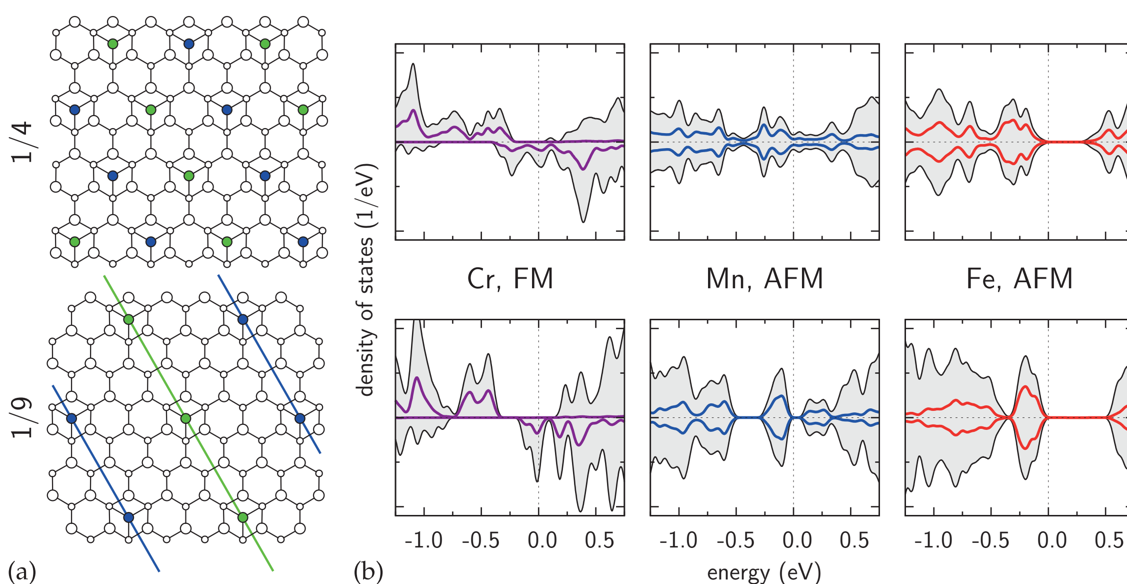

Figure 4.22 – (a) Atomic structure and (b) total DOS (black lines, shaded areas) with projections onto TM 3*d* orbitals (colored lines) of a two-dimensional δ layer of interstitial Cr, Mn, and Fe impurities directly below the H/Si(111) surface [cf. Fig. 4.12(a)]. The chosen magnetic states are those with minimal formation energies according to Fig. 4.21. The PDOS is *not* rescaled this time, and the Fermi energy has been chosen as reference. The atomic structures (a) show the distribution, density, and magnetic ordering (in the case of row-wise AFM ordering) of the TM impurities (colored circles) in the Si host. Bigger white circles mark the H/Si layers, smaller white circles the second Si layer.

1/9 density are shown in Fig. 4.23. All panels resemble superpositions of the features caused by isolated impurities (cf. Figs. 4.13 and 4.14). Similar to the case of two interacting interstitial impurities, conventional STM can hardly distinguish between the different magnetic states. In contrast, the different rows of alternating local magnetic moment orientation can clearly be seen in the SP STM magnetic-contrast images. The SP STM image for the row-wise AFM configuration will change slightly if the magnetic ground state is a noncollinear Néel state. In this case, at most three different TM site intensities will be observable, depending on the relative orientation of tip and sample magnetization.[21]

The Mermin-Wagner theorem

In the context of δ layer magnetism one should be aware of the Mermin-Wagner theorem [292], which states that there cannot be perfect, spontaneous FM or AFM order (second-order phase transition) in a one- or two-dimensional, *isotropic* Heisenberg system for finite temperatures $T > 0$. This theorem can be proven mathematically by using a Bogoliubov inequality. The physical reason behind it is that the excitation of spin waves is extremely easy (infinitesimal excitation energies) in such systems. However, real magnetic systems are rarely isotropic, and the implications of the Mermin-Wagner theorem should not be overestimated. In the present case, each TM site is subject to an uniaxial easy-axis or -plane mag-

[21] If the tip magnetization is aligned (anti-)parallel to one of the TM atom magnetizations, only two different TM site intensities will be observable. If the tip magnetization is aligned orthogonal to one of the TM atom magnetizations, three different TM site intensities will be observable.

Dieses Werk ist copyrightgeschützt und darf in keiner Form vervielfältigt werden noch an Dritte weitergegeben werden.
Es gilt nur für den persönlichen Gebrauch.

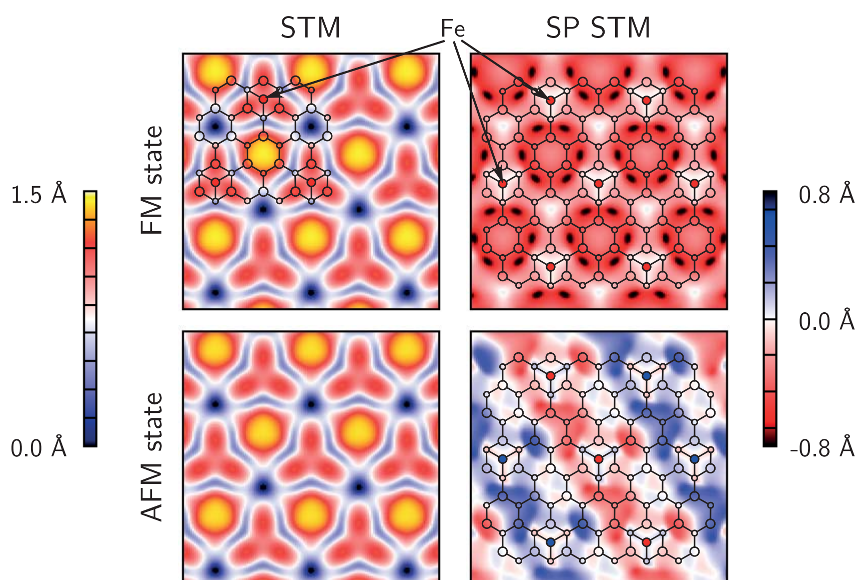

Figure 4.23 – Simulated STM and SP STM magnetic-contrast images of a δ layer of subsurface interstitial Fe impurities (marked by red/blue circles for a local spin magnetic moment that points up/down) with 1/9 density. Results are shown for two different magnetic states: FM and row-wise AFM (cf. Fig. 4.22). Bigger circles mark the H/Si layers, smaller circles the second Si layer. The images have been derived from empty states and can be compared with Figs. 4.13 and 4.14, which show analogously obtained results for an *isolated* Fe impurity.

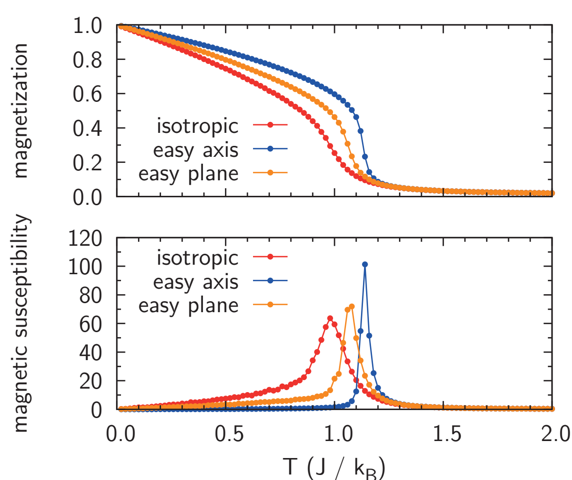

Figure 4.24 – Magnetization and magnetic susceptibility curves as functions of the temperature T resulting from Monte Carlo simulations of the two-dimensional, hexagonal, classical Heisenberg model. Compared are the isotropic ($\Delta = 0$) and anisotropic ($\Delta = \pm 0.1 J$) case. Note the finite-size effects and the large fluctuations even for low temperatures. The latter are suppressed in the case of an easy-axis anisotropy.

Dieses Werk ist copyrightgeschützt und darf in keiner Form vervielfältigt werden noch an Dritte weitergegeben werden.
Es gilt nur für den persönlichen Gebrauch.

netic anisotropy (arising from spin-orbit coupling or dipolar interaction). These anisotropies can be described by an additional term $-\Delta \sum_i S_i^z \cdot S_i^z$ in the Heisenberg model and can stabilize the magnetic order [293], even though Δ is probably small due to the weak spin-orbit coupling in Si [265]. A similar effect can be achieved by slight deviations from the strictly two-dimensional case. If the system possesses an easy plane instead of an easy axis, the model approaches the XY model with increasing anisotropy $|\Delta|$. The latter shows a Kosterlitz-Thouless transition towards a quasi-ordered phase [294]. Figure 4.24 displays magnetization and magnetic susceptibility curves resulting from Monte Carlo simulations of the two-dimensional, hexagonal, classical Heisenberg model, Eq. (3.4), with different uniaxial anisotropies Δ.[22] The pseudo-transition observable for the isotropic system near $T = 1.0\ J/k_B$ is a finite-size effect.[23] Indicative for the instability of the ordered phase are the strong spin fluctuations (magnetic susceptibility) persisting down to zero temperature. Similar arguments apply for the easy-plane anisotropy ($\Delta < 0$). In contrast, the stabilizing effect of an easy-axis anisotropy ($\Delta > 0$) can clearly be seen: The magnetic susceptibility shows a sharp singularity at the transition temperature, below which the spin fluctuations are strongly suppressed.

4.5.2 Destabilization of the Si matrix by dense impurity layers

Theoretical simulations in the field of δ doping are usually done by using bulk supercells which contain a reasonably large fraction of the semiconductor matrix and one layer of TM impurities. These supercells induce "fixed" boundary conditions in all three spatial directions, which means that although local atomic relaxations are possible, more considerable rearrangements of the semiconductor matrix are unintentionally inhibited.

During the research on H/Si(111) subsurface impurities, their clustering, and two-dimensional layer formation the author made an interesting observation: For dense layers of interstitial Cr, Mn, and Fe impurities, the surface structure, which usually looks like cut bulk due to the H passivation, collapses and locally forms a structure similar to a highly coordinated TM silicide. Unfortunately, the final structure turns out to be completely NM. For this reason, the dense δ layer has been left out in the previous section (cf. Fig. 4.21). On the other hand, this rearrangement was found to occur only for quite dense impurity layers. For the less dense δ layers discussed above, the integrity of the Si matrix is preserved.

In order to investigate this issue in more detail, and to exclude that the proximity of the surface plays a decisive role in the rearrangement, the author performed a more flexible form of the aforementioned bulk supercell calculations. The problem in conventional treatments arises due to the supercell periodicity in the direction perpendicular to the impurity δ layer. Let $z \parallel [111]$ be this direction in the following. In order to circumvent this problem, the δ layers of interstitial Cr, Mn, and Fe impurities have been placed in the center of a thick Si slab with two H-passivated (111) surfaces far away from the impurities. Consequently, one ends up with a system that has open boundary conditions with respect to the z coordinate: Although the slab is still periodic in the xy plane, as desired, it possesses the necessary flexibility for major structural rearrangements. Especially, the half of the slab *above* the impurity δ layer can move freely in the xy plane (and also in z direction, if necessary) without being hindered by the periodic image of the half *below* the impurity δ layer.

[22] The system size was $N = 100 \times 100$ lattice sites. The author used 6.4×10^6 Monte Carlo steps for equilibration and measurements. Each Monte Carlo step consisted of N spin updates. The temperature T was gradually decreased.
[23] A. Hucht, Universität Duisburg-Essen, Duisburg. Private communication.

Dieses Werk ist copyrightgeschützt und darf in keiner Form vervielfältigt werden noch an Dritte weitergegeben werden.
Es gilt nur für den persönlichen Gebrauch.

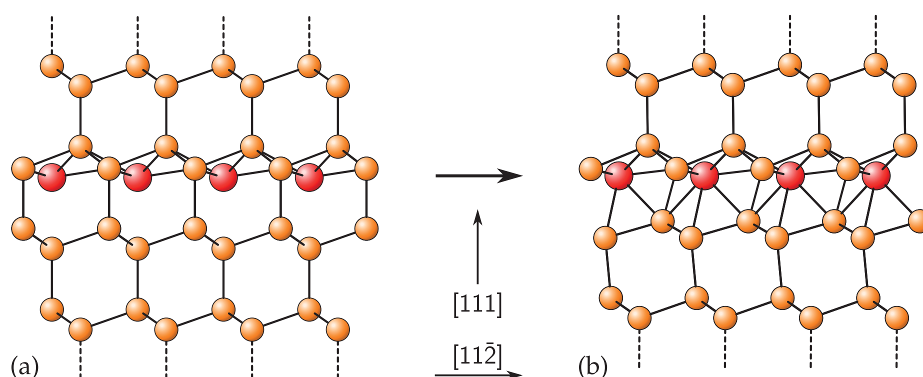

Figure 4.25 – Destabilization of the Si matrix by a dense δ layer of interstitial TM impurities. (a) Optimized atomic structure of an interstitial Fe δ layer without destabilization of the Si matrix due to periodic boundary conditions in all spatial directions. The Fe atoms have already left their ideal interstitial position. (b) If the periodicity perpendicular to the δ layer is lifted, the Si matrix rearranges and forms a NM silicide layer of high coordination.

A representative result can be seen in Fig. 4.25(b), which shows the structural rearrangements induced by a closed (1/1 density) δ layer of interstitial Fe impurities. This demonstrates that the same rearrangement that arises in the vicinity of the H/Si(111) surface also occurs in bulk Si. In line with the situation close to the passivated surface, the final structure obtained here is NM for Cr, Mn, and Fe, which means that any local spin polarization vanishes. This result has been obtained and verified by comparison of FM, AFM, and NM calculations. On the other hand, the highly coordinated structure has been found to be only favorable for dense impurity layers, which means that sparse impurity layers (as discussed above) can indeed be realized without structural rearrangements. The conclusion is that *ab initio* results on TM impurity layers have to be handled with care if the structural properties were not studied appropriately.

4.5.3 Impurity clusters

It has been shown above that a closed (111) layer of interstitial TM impurities in Si leads to a destabilization of the semiconductor and to vanishing magnetic moments. One way to circumvent this problem is to use less dense δ layers, which have already been discussed above. A second possibility is offered by small two-dimensional impurity clusters, which can also be seen as discontinuous δ layers. In this case one can benefit from the stronger impurity-impurity interaction, which increases the ordering temperature, while preserving at the same time the integrity of the semiconductor. Another interesting aspect one could think of is SP STM imaging of more complex TM-TM interactions within the clusters. The procedure will be similar to the study of the Fe-Fe interaction discussed above (cf. Fig. 4.18 on page 147).

In the following, we will focus on two-dimensional clusters consisting of interstitial Fe impurities below the H/Si(111) surface. Figure 4.26 shows several atomic and magnetic structures of subsurface Fe clusters. In addition to the single and double impurities discussed above we can see clusters containing three, four, and six Fe atoms. The first row represents the respective magnetic ground state, which is FM in all cases. This is already a major qualitative difference with respect to the more sparse δ layers: Instead of AFM interaction,

Dieses Werk ist copyrightgeschützt und darf in keiner Form vervielfältigt werden noch an Dritte weitergegeben werden.
Es gilt nur für den persönlichen Gebrauch.

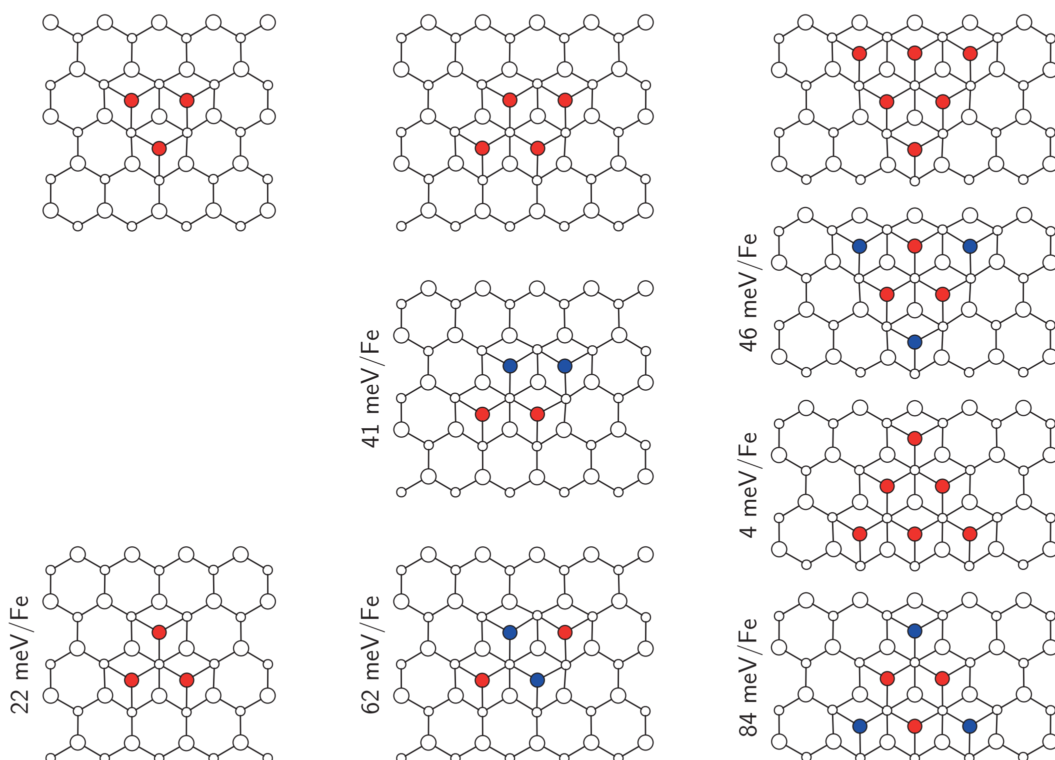

Figure 4.26 – Atomic and magnetic structure of several subsurface interstitial-Fe clusters. The Fe atoms are marked by red/blue circles for a local spin magnetic moment that points up/down. Bigger white circles mark the H/Si layers, smaller white circles the second Si layer. The printed energies are differences per Fe atom with respect to the topmost cluster in each column, which has the lowest energy.

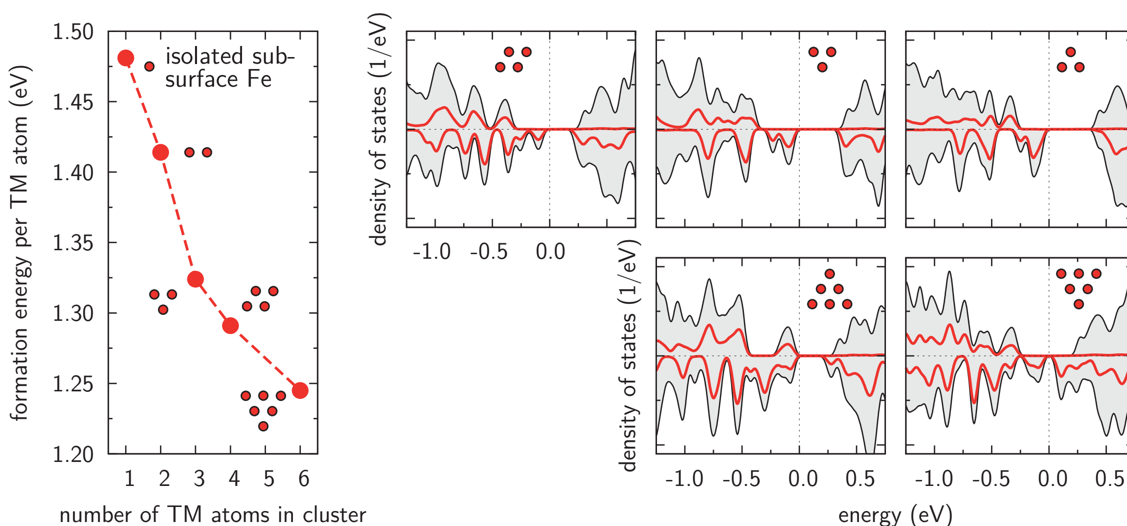

Figure 4.27 – Cluster formation energies per Fe atom, total DOS (black lines, shaded areas) and summed-up projections onto the Fe 3d orbitals (red lines) for different subsurface interstitial-Fe clusters in their ground state FM configuration. The small cluster symbols directly refer to Fig. 4.26. The PDOS for the isolated subsurface Fe atom (two interacting Fe atoms) can be found in Fig. 4.12 (Fig. 4.18), while those of different Fe δ layers are shown in Fig. 4.22.

Dieses Werk ist copyrightgeschützt und darf in keiner Form vervielfältigt werden noch an Dritte weitergegeben werden.
Es gilt nur für den persönlichen Gebrauch.

all studied Fe clusters show FM coupling due to the small Fe-Fe distance. Moreover, the energies required for different magnetic excitations in the clusters indicate a stronger Fe-Fe interaction than in the δ layers (cf. Fig. 4.21, Fe panel, FM-AFM difference), which reduces internal spin fluctuations.[24] Finally, one can see that the spatial orientation of the cluster with respect to the surrounding Si matrix has an influence on the formation energy and also on the magnetic excitation energy. Calculations prove that the total magnetic moment of a FM cluster is always the number of atoms in the cluster times the magnetic moment of an isolated interstitial impurity (2 μ_B for Fe).

The cluster formation energies are compared in Fig. 4.27. Each shown value corresponds to the cluster with the lowest formation energy in the respective class (atom number). Two things can be observed here: First, the formation of clusters is advantageous, since the formation energy decreases with increasing cluster size. This is contrary to the repulsive behavior of the Fe impurities in the δ layers. Second, the formation energies of all clusters are smaller than those of the δ layers (cf. Fig. 4.21, Fe panel). This increasing stability of Fe clusters leads to the picture that each cluster acts as individual object, not just as an array of impurities. Different clusters can "communicate" via the weak dipolar interaction or, if their separation is small, the stronger exchange interaction. The results shown in Fig. 4.27 stem from Si(111)-(6×6) supercells, which lead to some exchange interaction between the clusters and their periodic images, especially for the larger clusters.

Similar to the AFM Fe δ layers, the whole structure remains semiconducting even in the presence of FM Fe clusters. This can be seen from the DOS plots in Fig. 4.27. The reason is the completely filled minority spin t_2 peak which defines the VBM. The band gap is almost closed for the more stable six-atom cluster, but only in the minority spin channel. Thus, a FM arrangement of such clusters shows almost half-metallic properties.

One can deduce from Fig. 4.27 that a FM semiconductor can be created if the total magnetic moments of neighboring clusters align parallel. Even though the details of two-cluster interactions are an additional chapter and beyond the scope of this thesis, some considerations shall be given. In addition to the exchange interaction of adjacent clusters, which usually dominates the interaction energy and can be determined from DFT calculations with large supercells comprising many (at least two) clusters, the magnetic dipole-dipole interaction can play a role:

$$E_{\text{d-d}} = \frac{\mu_0}{4\pi}\frac{1}{r^3}\left\{\vec{\mu}_1\vec{\mu}_2 - \frac{3}{r^2}(\vec{\mu}_1\vec{r})(\vec{\mu}_2\vec{r})\right\}\ , \tag{4.2}$$

where $\vec{\mu}_i$ are the magnetic moments of the individual clusters and $\vec{r}$ is the distance vector of the two clusters.

Let us consider the example of two six-atom Fe clusters ($\mu_i = 12\ \mu_B$) with distance $r = 6a_{\text{Si(111)}} \approx 23.2$ Å that lie in the same subsurface plane. If the magnetization points out of plane, the latter term in Eq. (4.2) vanishes. In this case, antiparallel orientation of the magnetic moments is preferred and $E_{\text{d-d}} \approx -0.62\ \mu$eV. If, on the other hand, the clusters are magnetized in plane, the latter term dominates and $E_{\text{d-d}} \approx -1.24\ \mu$eV for parallel alignment. Thus, in this geometry, in-plane ferromagnetism leads to the lowest potential energy.

One can see from the smallness of these energies that the magnetic dipole-dipole interaction is indeed very weak when compared to the exchange interaction. The order of magnitude is similar to values the author would expect for magnetocrystalline anisotropy energies

[24] Note that the comments on noncollinear magnetism made for the δ layers above also apply to the clusters, but cause no difficulties in the argumentation. Their magnetic ground state is FM.

Dieses Werk ist copyrightgeschützt und darf in keiner Form vervielfältigt werden noch an Dritte weitergegeben werden.
Es gilt nur für den persönlichen Gebrauch.

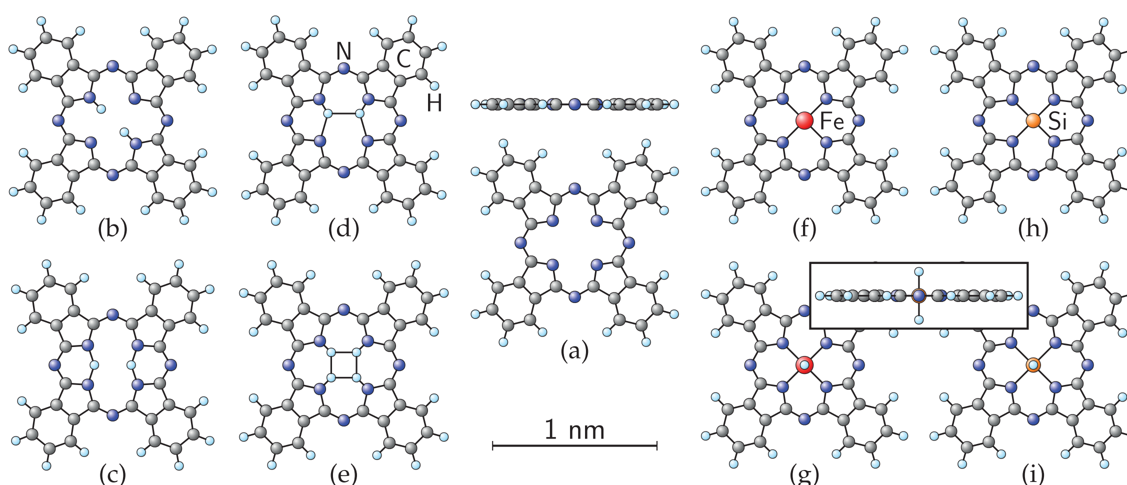

Figure 4.28 – Atomic structure of Pc rings with different centers. The empty ring (a) can bind two H atoms in different configurations (b) – (d) [where configuration (b) has the highest binding energy], four H atoms (e), a single Fe atom (f), or a single Si atom (h). Moreover, the latter two can bind two additional H atoms above and below the molecular plane (g), (i).

caused by the spin-orbit interaction. The precise determination of the latter is a delicate issue in DFT, which is also a consequence of their smallness for the relatively light elements involved here. In summary, the answer to the question how different clusters align their magnetic moments with respect to each other depends on a sensitive balance of magnetocrystalline anisotropy and dipole-dipole interaction for large cluster-cluster distances and on the exchange interaction for small distances.

4.6 Subsurface doping with organic molecules

So far we have discussed different properties of isolated and interacting 3*d* TM impurities in bulk Si and below the H/Si(111) surface in this chapter, and it has been shown how these properties can be detected. Another important aspect is how the subsurface impurities can be generated. It is, of course, possible to grow a doped sample, as indicated in Fig. 4.11(a) on page 138, followed by the application of the H layer and subsequent search for suitable impurities. The *targeted* implantation of subsurface impurities *a posteriori*, i.e., after the passivation, needs a more careful handling, since simply exposing the H/Si(111) surface to a dense TM vapor will presumably lead to TM clustering *on top of* the surface and not to subsurface doping (cf. Sec. 4.4.4). It has been *claimed* recently by Gruyters *et al.* that the generation of subsurface impurities can be achieved by room-temperature deposition of organic molecules with 3*d* TM centers on the H/Si(111) surface [251]. This aspect will be assessed in this section.

Several organic molecules can bind TM atoms. Interesting examples that play an important role in nowadays science (medicine and biology as well as physics) are the porphyrins and the slightly larger phthalocyanines (Pc). In both cases, a single TM atom can occupy the center of the molecule by substituting two H atoms. This changes, for instance, the spectral properties and thus the color of the molecule.

Dieses Werk ist copyrightgeschützt und darf in keiner Form vervielfältigt werden noch an Dritte weitergegeben werden.
Es gilt nur für den persönlichen Gebrauch.

Some examples shall underline the relevance of these molecule classes: Hemoglobin, an important constituent of red blood cells (erythrocytes) and relevant for the O transport in our blood, contains porphyrins with Fe centers. Chlorophyll molecules, essential for photosynthesis, are based on porphyrins with a Mg ion in the center, which shows that not only TM atoms, but also other elements can be bound in the center of such molecules. Another interesting aspect is that phthalocyanines, porphyrins, and their derivatives like naphthalocyanines, with certain side chains, are used nowadays in photodynamic cancer treatment [295]. For this application they usually contain a Zn center, but appear also with Al, Si, or Ge centers. The idea is based on the phototoxicity of these molecules: They absorb photons from the visible part of the electromagnetic spectrum, which excite the molecules and thus induce a subsequent chemical reaction, for example, with O. The molecules are injected intravenously into the blood and accumulate in the tumor, or are applied externally in the case of skin tumors. Subsequently, the tumor is irradiated with laser light (endoscopically, if necessary). Phthalocyanines are of special interest here, since they absorb light in a convenient part of the visible spectrum where the penetration depth of the photons is high enough (about 15 mm; light transmission through tissue is wavelength dependent). The advantage of such a therapy is the reduction (or absence) of side effects connected to classical treatments like chemo- or radiation therapy.

In physics, the study of organic molecules is a large field of ongoing intense research. Among many other things one is interested in the adsorption of molecules on different surfaces (metallic [296], semiconducting [67, 297], or insulating [298]), magnetic properties of molecules that include TM atoms and their interactions with different substrates (FM and NM [299,300]), and magnetic switching phenomena [301], which aim at spin-dependent molecular electronics [302]. If deposited on metal surfaces, the Kondo effect can be observed in magnetic molecules [303, 304].

In this section, we will discuss energetic aspects of different Pc molecules, the influence of different (semilocal and hybrid) exchange-correlation functionals with special focus on iron phthalocyanine (FePc), its adsorption on H/Si(111), and finally the possibility to inject its central Fe atom into the H/Si(111) substrate.

4.6.1 Binding energies and exchange-correlation functionals

A reasonable starting point for numerical investigations are isolated molecules in the gas phase.[25] Figure 4.28 shows optimized atomic structures of different (partially hypothetical) Pc molecules. The corresponding binding energies of different central atoms in an empty Pc ring are given in Table 4.3. They are defined as

$$\varepsilon = -\Big(E_{\text{molecule}} - E_{\text{empty Pc ring}} - \sum_i \Delta N_i\, E_i^{\text{atom}}\Big), \qquad (4.3)$$

where the first two terms are the total energies of the molecule and the empty Pc ring as reference, ΔN_i is the difference of atoms of species i between molecule and reference, and E_i^{atom} denotes the total energy of an isolated atom of species i. Already two H atoms are strongly bound in the Pc ring, with a binding energy twice as large as that of a H_2 molecule (PBE: 4.45 eV). On the other hand, four bound H atoms are less favorable than two bound H

[25] Note that the DFT treatment of MnPc and FePc is a tricky issue due to their numerical instability [305]. Moreover, the actual ground state of FePc, for instance, is still under debate, even experimentally (see Ref. [297] and references therein). DFT+U is *not* used here in order to obtain unbiased binding energies.

Dieses Werk ist copyrightgeschützt und darf in keiner Form vervielfältigt werden noch an Dritte weitergegeben werden.
Es gilt nur für den persönlichen Gebrauch.

Table 4.3 – Binding energies [Eq. (4.3)] and magnetic moments of different central atoms in an empty Pc molecule, calculated with the PBE exchange-correlation functional and the USPP method. Fe + 2H and Si + 2H correspond to (g) and (i) in Fig. 4.28.

	Fe	Fe + 2H	Si	Si + 2H	2H	4H
E_{bind} (eV)	9.59	12.27	8.51	14.57	9.22	12.58
m (μ_B)	2	0	2	0	0	2

	Ti	Cr	Mn	Co	Cu
E_{bind} (eV)	10.87	9.52	9.11	9.96	7.69
m (μ_B)	2	4	3	1	1

Table 4.4 – Binding energies (eV) of a central Fe atom or two H atoms in FePc and Pc, respectively, calculated with different exchange-correlation functionals and Hartree-Fock (HF). The results have been obtained from an USPP and an all-electron approach.

	USPP	All-electron calculations					
	PBE	PBE	LDA	B3LYP	PBE0	HSE06	HF
Fe in FePc	9.59	9.57	11.74	8.23	8.69	8.72	5.81
2H in Pc	9.22	9.24	10.59	9.15	9.24	9.27	6.27

atoms plus an isolated H_2 molecule. Fe is even more strongly bound than two H atoms, as are most of the other studied TM atoms, especially Ti. It is also possible to bind a Si atom in a Pc ring, even though the binding energy of two H atoms is slightly larger. The Si atom is more strongly bound in a Pc ring than in Si bulk (cf. Table 3.1 on page 50). Both FePc and SiPc can bind two additional H atoms above and below the molecular plane. While in the former case of FePc the formation of an isolated H_2 molecule is energetically more favorable, the latter case of SiPc with two adsorbed H atoms is stable against decomposition with an energy gain of 1.61 eV.

In addition to the binding energies, Table 4.3 also lists the spin magnetic moments of different molecules. The values for the more common molecules (like MnPc, FePc, CoPc, CuPc, or just Pc) are well known [303, 306]. Moreover, also TiPc and CrPc bear (high) magnetic moments. Most peculiarly, SiPc has a magnetic moment of 2 μ_B; we will come back to this aspect later.

The extremely high binding energies of the TM atoms in a Pc ring are surprising. In order to obtain more viewpoints on this topic, FePc and a Pc ring with two H atoms have been treated, in addition, with different exchange-correlation functionals (cf. Table 4.4) in an all-electron approach (FHI-aims code [83]). Of particular interest are hybrid functionals like B3LYP, PBE0, and HSE06, since they are frequently used for organic molecules (see, for instance, Ref. [307]). The results of Hartree-Fock calculations are also given for completeness. The first thing to note is that the PBE results obtained with the USPP and the all-electron approach agree very well. As expected, LDA gives even higher binding energies than PBE for both molecules (overbinding). For FePc, the binding energies provided by the hybrid

Dieses Werk ist copyrightgeschützt und darf in keiner Form vervielfältigt werden noch an Dritte weitergegeben werden.
Es gilt nur für den persönlichen Gebrauch.

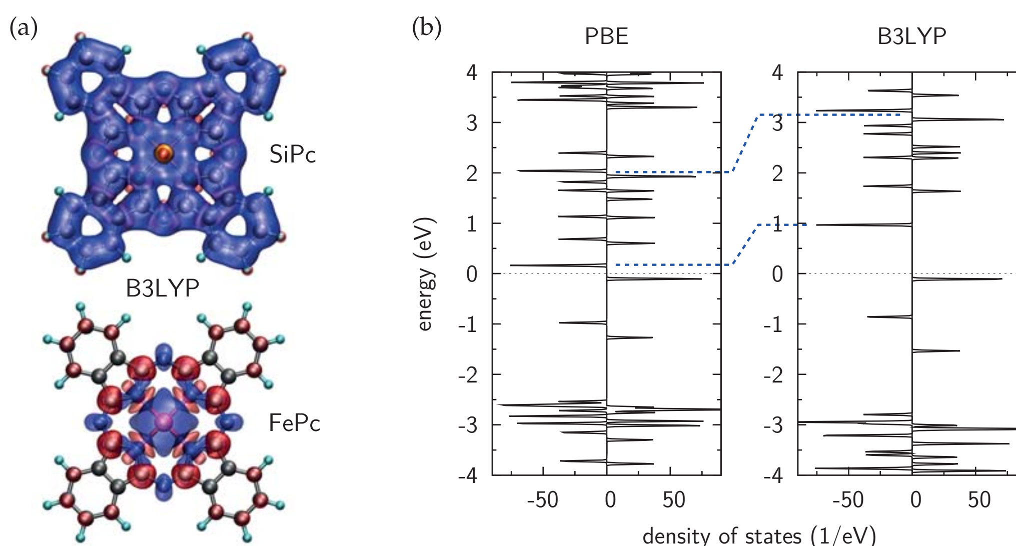

Figure 4.29 – Silicon phthalocyanine. (a) Atomic structure (cf. Fig. 4.28) and spin density isosurfaces for SiPc (top) and FePc for comparison (bottom) as derived from all-electron hybrid functional (B3LYP) calculations (blue/red meaning positive/negative). The isosurface density is $10^{-3}/\text{Å}^3$ for both molecules. (b) Spin-resolved electronic structure of SiPc as calculated with the PBE and B3LYP exchange-correlation functionals. The horizontal dashed line marks the Fermi energy, and the blue dashed lines connect two equivalent positions in the electronic spectra and serve as guide to the eye.

functionals are roughly 1 eV smaller than the PBE binding energies, but still very high. For the Pc ring with two H atoms, hybrid functionals give binding energies similar to the PBE value. The Hartree-Fock calculations lead to significantly smaller binding energies in both cases; however, this is certainly not the most appropriate technique for larger organic molecules, since it ignores all correlation effects. The magnetic moment of FePc is 2 μ_B in all cases. While in LDA and GGA (PBE) the Fe atom is more strongly bound than two H atoms, the reversed prediction is made by hybrid functionals and Hartree-Fock. HSE06 and PBE0 provide very similar results, which shows that the screening of the Coulomb interaction is irrelevant on the present length scale. From these additional results one can conclude that the binding energies provided by PBE are indeed reasonable.

Excursion: Silicon phthalocyanine and d_0 magnetism in molecules

As we have seen above, Si atoms can be bound in Pc rings (cf. Table 4.3). It is interesting to note that the resulting SiPc molecules bear a magnetic moment of 2 μ_B.[26] Thus, one has a situation like d_0 magnetism [308, 309], but with molecules instead of doped oxides. From Fig. 4.29(a) one can deduce another interesting aspect: In contrast to FePc, where the spin density is quite localized at the Fe atom in the center, the spin density is highly delocalized over the whole π system in SiPc. In order to demonstrate that this delocalization (and also the existence of the magnetic moment) is not an artifact of PBE, the shown results have been taken from a B3LYP hybrid functional all-electron calculation. Moreover, Fig. 4.29(b)

[26] This magnetic moment has been found to be stable: Constrained total magnetic moment calculations for a value of 0 μ_B have lead to a 0.1 eV higher total energy.

Dieses Werk ist copyrightgeschützt und darf in keiner Form vervielfältigt werden noch an Dritte weitergegeben werden.
Es gilt nur für den persönlichen Gebrauch.

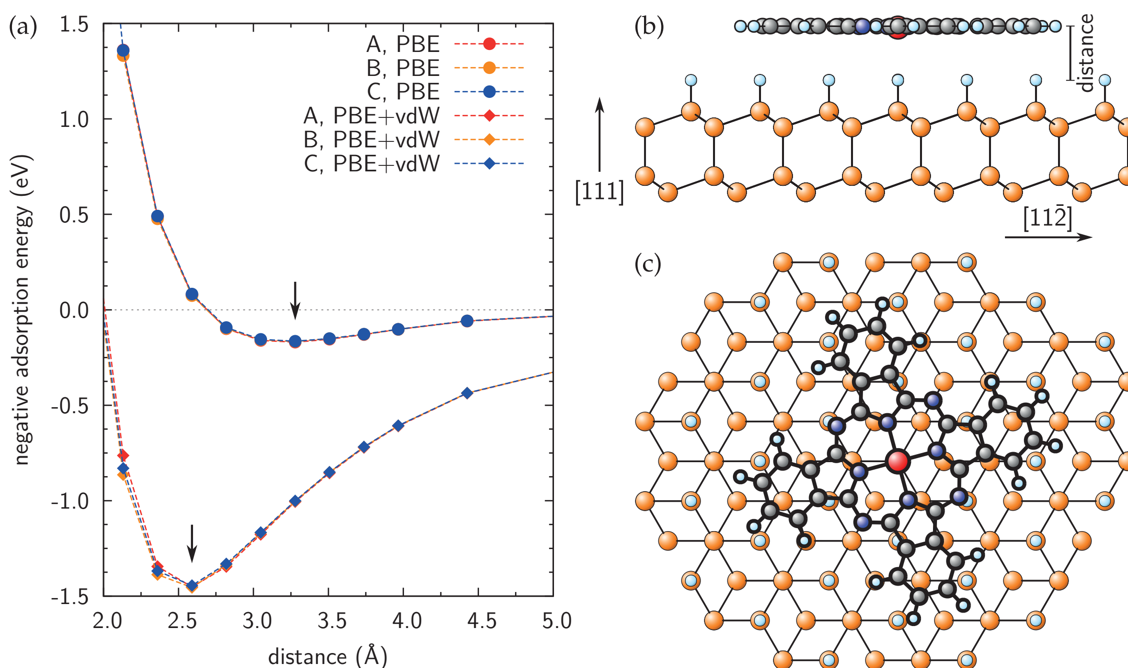

Figure 4.30 – Adsorption of a single FePc molecule on the H/Si(111) surface. (a) Adsorption energies (negative) as functions of the molecule-surface distance, comparing PBE (circles) and PBE+vdW (diamonds) results. The black arrows mark the respective minima. Three different adsorption sites are compared (see text). (b) Side and (c) top view of an FePc molecule adsorbed on a H/Si(111) A site. The atom colors refer to Fig. 4.28.

compares the electronic structure of SiPc as calculated with the two exchange-correlation functionals. One can see that the splitting of the energy levels is larger for B3LYP, but qualitatively similar to the PBE result. Especially, the description of HOMO and LUMO orbitals agrees. The delocalized spin density can facilitate the magnetic interaction with a substrate, or with neighboring molecules through a substrate. One is, for instance, currently interested in Pc molecules on graphene [310, 311].

4.6.2 Adsorption of FePc on H/Si(111)

After the discussion of the gas phase properties of different Pc molecules, we will now move to the adsorption of an FePc molecule on the H/Si(111) surface. Figure 4.30(a) shows the (negative) adsorption energies of FePc on the H/Si(111) surface as functions of the molecule-surface distance. Three different adsorption sites (lateral positions of the central Fe atom) are compared: first Si layer positions, i.e., above a H atom (A), second Si layer positions (B), and fourth Si layer positions (C). The curves have been obtained from rigid atomic structures (no relaxation beyond the individual equilibrium geometries). Successive calculations including atomic relaxation have shown that site A is always the most stable. The energy differences with respect to sites B and C are small (below ≈ 5 and 16 meV for PBE and PBE+vdW, respectively). The PBE+vdW calculations have been carried out in a completely consistent manner, i.e., an appropriate Si lattice constant has been used (cf. Table 3.1 on page 50) in the H/Si(111) slab, as well as an adjusted H-Si distance.

Dieses Werk ist copyrightgeschützt und darf in keiner Form vervielfältigt werden noch an Dritte weitergegeben werden.
Es gilt nur für den persönlichen Gebrauch.

The results shown in Fig. 4.30(a) are similar to those obtained for other hybrid inorganic-organic systems like PTCDA[27] on Ag(111) by using the PBE exchange-correlation functional with and without the vdW correction [296]. It is, however, interesting that already pure PBE shows an adsorption minimum for a strongly vdW-dominated (physisorbed) system like FePc on H/Si(111). The adsorption energy provided by PBE is certainly far too low, while the equilibrium molecule-surface distance will be overestimated. PBE+vdW strongly reduces the molecule-surface distance to ≈ 2.6 Å and predicts a much higher adsorption energy of 1.46 eV. For PTCDA on Ag(111), the same vdW correction that is used here [123] severely overestimates the adsorption energy by ≈ 1 eV (40%), while providing an almost correct molecule-surface distance at the same time [296]. It appears reasonable to assume that the performance of PBE+vdW will be somewhat better here due to the higher importance of the vdW interaction in the present system. The adsorbed molecule retains its gas phase magnetic moment of 2 μ_B in both the PBE and the PBE+vdW calculations.

The inclusion of vdW interactions is not only important to obtain *quantitatively* better results. Several additional test calculations have shown that they are of fundamental, *qualitative* importance for modeling the chemisorption of an FePc molecule at a surface defect, i.e, a missing H atom in the H/Si(111) surface layer. The repulsive forces between the molecule and the surface are so strong in semilocal DFT that chemisorption at such defects hardly ever occurs. If, on the other hand, a vdW correction is included, the repulsive forces and the molecule-surface distance are reduced and the defect orbitals can interact with the molecular orbitals. This can lead to a stronger bonding and to changes in the magnetic properties of the molecule. Since there is currently a strong interest in the field of vdW corrections in electronic structure theory [312–314], different approaches can be tested on such a system.

4.6.3 Subsurface doping

As we have seen in Fig. 4.4 on page 128, the formation energy of isolated interstitial and substitutional Cr, Mn, and Fe impurities in Si is positive, which means that the formation of TM bulk material is favored. Thus, implantation of impurities *a posteriori* has to be done carefully to prevent TM cluster formation on top of the surface.

It has been put forward recently by Gruyters *et al.* that subsurface doping could be possible by deposition of FePc molecules on the H/Si(111) surface at room temperature [251]. In this experiment, FePc molecules were evaporated from a crucible of an electron beam evaporation source onto the H/Si(111) surface. Subsequent STM analysis of molecule-free areas showed several induced features that were attributed to subsurface substitutional Fe impurities (cf. Fig. 4.16 on page 143). However, the binding energies discussed above (cf. Table 4.4) show that the Fe atom is very strongly bound to the organic part of the FePc molecule and thus quite difficult to extract. From an energetic point of view this raises the question whether the doping strategy suggested by Gruyters *et al.* [251] is realistic.

For a first step in addressing this question, DFT total energy differences $\Delta E = E_{\text{final}} - E_{\text{initial}}$ of several different scenarios for the injection of isolated interstitial or substitutional Fe impurities into the H/Si(111) subsurface layers can be considered under the constraint that the number of atoms of each species has to be conserved. These differences are shown in Table 4.5. For instance, the Fe atom could leave the FePc molecule and replace a Si atom in the host (substitutional Fe); subsequently, the Si atom is incorporated in the rest of the

[27]PTCDA is the common abbreviation of "3,4,9,10-perylene tetracarboxylic dianhydride".

Dieses Werk ist copyrightgeschützt und darf in keiner Form vervielfältigt werden noch an Dritte weitergegeben werden.
Es gilt nur für den persönlichen Gebrauch.

Table 4.5 – Different scenarios for the injection of isolated interstitial or substitutional Fe impurities into the H/Si(111) subsurface layers [cf. Fig. 4.31] from organic FePc and FePc-2H molecules. ΔE is the DFT total energy difference between the initial and the final configuration. A negative value indicates that the final configuration is preferred.

Scenario	ΔE (eV)
FePc + pure H/Si(111) $\rightarrow$	
Fe substitutional + SiPc	+2.79
Fe substitutional + SiPc-2H + 2× H-Si bond broken	+3.51
Fe substitutional interacting with Si self-interstitial + empty Pc ring	+8.60
Fe substitutional + Si self-interstitial + empty Pc ring	+10.73
Fe interstitial + empty Pc ring	+6.15
Fe interstitial + Pc + 2× H-Si bond broken	+3.70
FePc-2H + pure H/Si(111) $\rightarrow$	
Fe substitutional + SiPc-2H	−0.60
Fe substitutional interacting with Si self-interstitial + Pc	+2.05
Fe interstitial + Pc	−0.40

molecule, forming SiPc (where the Si atom is more strongly bound than in bulk Si, which lowers ΔE for this scenario; cf. Sec. 4.6.1). Moreover, two H atoms could leave the passivating H layer and adsorb on the SiPc molecule [cf. Fig. 4.28(i)]. The defect energy associated with a missing H atom can be approximated by the H-Si binding energy (PBE: 3.39 eV, cf. Sec. 4.2). A third possibility is the formation of a Si self-interstitial impurity, which can either interact with the substitutional Fe impurity or be isolated from it. One can see from Table 4.5 that all scenarios in which one tries to remove the Fe atom from the center of an FePc molecule with subsequent implantation into the H/Si(111) matrix are energetically highly unfavorable, also when compared to typical room-temperature energies (25 meV) and irrespective of the final site (interstitial or substitutional). Note that only the total energies of different initial and final states are considered here; in addition, different kinetic barriers caused by intermediate states will inhibit Fe exchange processes.

The situation remains unchanged even if one takes into account the lower binding energies for FePc as provided by the hybrid functionals (cf. Table 4.4). Although one has to calculate everything (different molecules and impurities in Si) consistently with the same exchange-correlation functional for a reliable final statement, one can estimate by subtracting 1 – 2 eV that ΔE would still be positive, even if hybrid functionals were used.

The reason for the highly positive values of ΔE lies in the stability of the initial state, but also in the suboptimal final states. Let us now assume that, by chance, two H atoms adsorb on the pure FePc molecule in its gas phase [cf. Fig. 4.28(g) and Fig. 4.31(a)]. If the Fe atom sits on a substitutional site after the reaction [cf. Fig. 4.31(c)], the removed Si atom can be incorporated in the Pc ring, which results in SiPc with two additional H atoms above and below the molecular plane (SiPc-2H). This scenario optimizes both E_{initial} (missing H_2 dissociation) and E_{final} (high binding energy of SiPc-2H) and indeed leads to a negative total energy difference ΔE. If the Fe atom is not incorporated on a substitutional site, but on an

Dieses Werk ist copyrightgeschützt und darf in keiner Form vervielfältigt werden noch an Dritte weitergegeben werden.
Es gilt nur für den persönlichen Gebrauch.

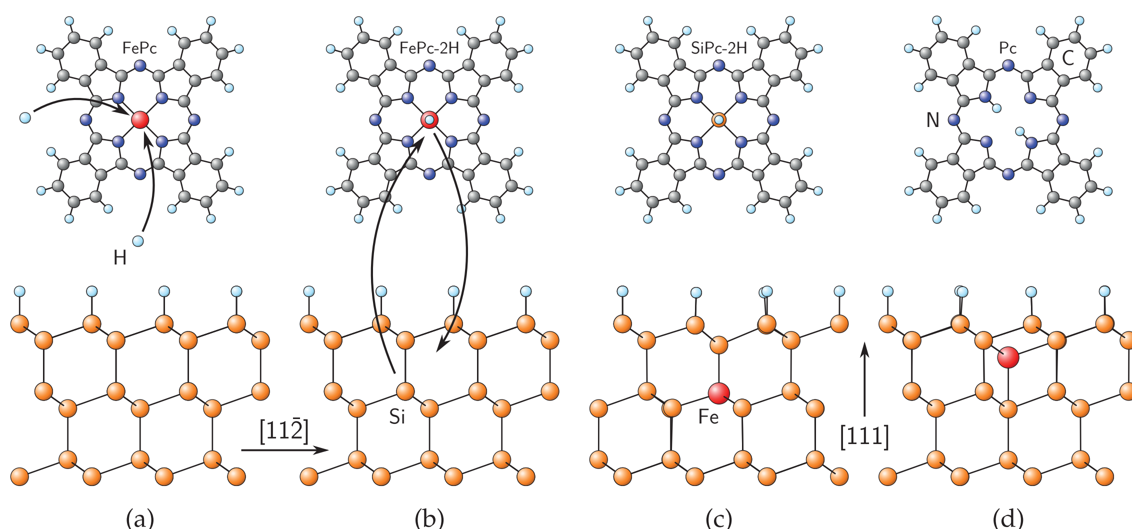

Figure 4.31 – Illustration (not to scale) of different scenarios with negative ΔE for the injection of interstitial or substitutional Fe impurities into the H/Si(111) subsurface layers from the organic molecule FePc. Adsorption of two excess H atoms on FePc (a) leads to FePc-2H (b). Subsequently, the Fe atom can interchange with a Si atom (c) or move to an interstitial site (d), while the two H atoms stabilize the molecule.

interstitial site [cf. Fig. 4.31(d)], not SiPc-2H, but a simple Pc molecule (with two H atoms in its central region) remains after the reaction; this scenario also leads to a negative ΔE.

Neglecting kinetic barriers for the moment, this means that the latter two scenarios could be statistically relevant. The crucial point, however, is the adsorption of two H atoms on the pure FePc molecule prior to the reaction at the H/Si(111) surface. This could be realistic if, in addition to the FePc molecules, free H atoms are evaporated from the crucible in the experiment, or if unbound H atoms exist in the vicinity of the passivated surface. (Remember that the molecule deposition was carried out at room temperature in the experiments [251].) The spontaneous dissociation of H_2 molecules is improbable due to their high binding energy.

One can conclude from the theoretical viewpoint that, at least in principle, it is *possible* to experimentally implant Fe impurities below the H/Si(111) surface by room-temperature deposition of FePc molecules. However, the necessary steps in the reaction are quite improbable, which is mainly related to the high binding energy of the central Fe atom in FePc. This high binding energy is consistently predicted by different exchange-correlation functionals (cf. Table 4.4), even by state-of-the-art hybrid functionals which are known to provide quite accurate binding energies for (organic) molecules [52,54]. Moreover, it cannot be entirely excluded that *no* Fe impurities are implanted in the experiment (see also the discussion above in Sec. 4.4.2). The observed features in the experimental STM images [251] could also be caused by surface defects like H vacancies. The H atoms could subsequently adsorb on the FePc molecules and alter their electronic properties (and thus cause their different appearance observed in the STM images [251]). Consequently, it is suggested here that more detailed experimental (and also theoretical) investigations should be done in this field.

Dieses Werk ist copyrightgeschützt und darf in keiner Form vervielfältigt werden noch an Dritte weitergegeben werden.
Es gilt nur für den persönlichen Gebrauch.

Dieses Werk ist copyrightgeschützt und darf in keiner Form vervielfältigt werden noch an Dritte weitergegeben werden.
Es gilt nur für den persönlichen Gebrauch.

Chapter 5

Magnetic tunnel junctions with Heusler electrodes

Contents

5.1 Introduction and overview . . . 168
5.2 Properties of Co_2MnSi and MgO . . . 169
5.2.1 The Heusler alloy Co_2MnSi . . . 169
5.2.2 The insulator MgO . . . 173
5.3 Phonon influence on the half-metallic gap . . . 174
5.3.1 Phonon dispersion relations . . . 174
5.3.2 Random frozen phonons . . . 175
5.4 Magnetic tunnel junctions . . . 177
5.4.1 Atomic and electronic structure of the interface . . . 178
5.4.2 Parallel electrode magnetization: Transport and spincalorics . . . 180
5.4.3 Antiparallel electrode magnetization: Interface magnons . . . 189

Dieses Werk ist copyrightgeschützt und darf in keiner Form vervielfältigt werden noch an Dritte weitergegeben werden.
Es gilt nur für den persönlichen Gebrauch.

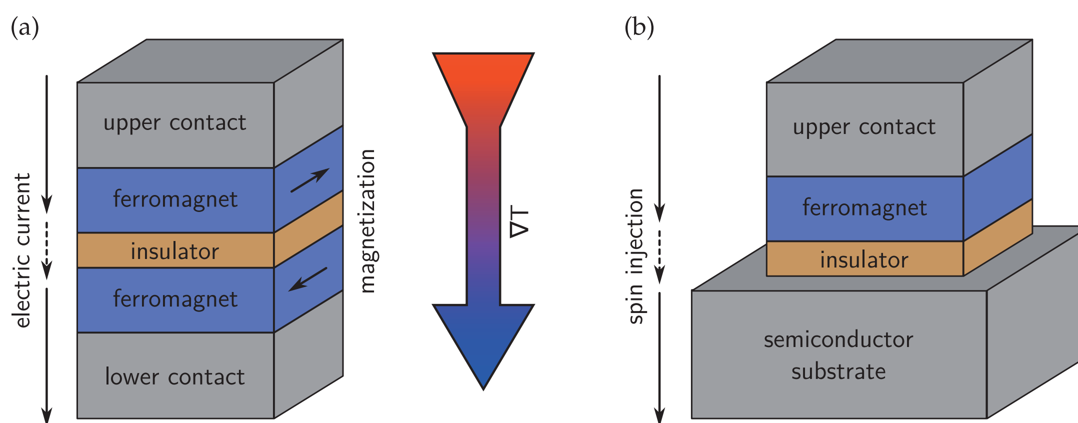

Figure 5.1 – Magnetic tunnel junction (a) and spin injection device with a semiconductor substrate (b). Either an electric field or a thermal gradient can be applied to both structures.

5.1 Introduction and overview

Transition metals appear in conjunction with Si not only as silicides or DMS. It is also possible to form a magnetic TM-Si alloy in which the TMs are dominant. An example is the FM ternary Heusler compound Co_2MnSi. Its peculiar magnetoelectronic properties (for instance, its half-metallicity [315] and high Curie temperature) make it very interesting in the fields of spintronics and spincalorics, especially as material for magnetic tunnel junctions (MTJs).

Such a MTJ is schematically shown in Fig. 5.1(a). The magnetic orientation of one of the two FM layers is usually fixed, while that of the second layer can be reversed, for instance, by an external magnetic field or by exploiting the spin torque induced by a "misaligned" spin-polarized current of high density (current-induced magnetization switching [316]).

The electronic transport through the MTJ depends on the relative magnetization direction of the two magnetic layers. This tunnel magnetoresistance (TMR) effect should be very large for Co_2MnSi electrodes as a consequence of their half-metallicity. The interplay of relative magnetic orientation and conductance in MTJs can be used for data storage. MTJs can form building blocks in magnetoresistive random access memory (MRAM) modules, which combines nonvolatility of the stored information, unlimited endurance, and fast (≈ 5 ns) random access [6, 7]. In principle, only a *significant*, *detectable* difference between the two magnetic states (parallel and antiparallel electrode magnetization) is necessary for this type of application. There is no need for an *infinite* resistance in the antiparallel case (which one would expect for the half-metallic Co_2MnSi electrodes). However, one can imagine that maximizing the resistance contrast between parallel and antiparallel electrode magnetization makes the devices faster, more efficient, and less prone to perturbations.

It has been found in previous research that the performance of half-metallic ferromagnets in this context is not as good as expected. While the TMR ratio is indeed large for low temperatures, it decreases rapidly with increasing temperature. For instance, Ishikawa *et al.* recently reported a TMR ratio of 705 % at 4.2 K and 182 % at room temperature [317], while Liu *et al.* achieved almost 2000 % at 4.2 K and up to 350 % at room temperature (with an additional CoFe buffer layer as substrate for the lower electrode [318]).[1] Several possible reasons exist for this behavior, including magnons, phonons, interface states [320, 321], the interface

[1]For a more extensive collection of experimental results the reader is referred to Table 6.1 in Ref. [319].

Dieses Werk ist copyrightgeschützt und darf in keiner Form vervielfältigt werden noch an Dritte weitergegeben werden.
Es gilt nur für den persönlichen Gebrauch.

composition [321, 322], and thermal variations of the hybridization of those states that form the half-metallic gap [323]. In this chapter, it is shown on the basis of DFT calculations (i) that the effect of phonons is negligible at room temperature and (ii) that inelastic tunneling involving thermally activated interface magnons is among the most probable explanations for the observed behavior.

Interestingly, the information stored in a MTJ can also be read out by application of a thermal gradient instead of an electric field. The Seebeck voltage, which arises in a MTJ due to a thermal gradient between the two electrodes, can be used to detect the state of the electrode magnetization [324]. This magneto-Seebeck effect can be expected to be very large in the case of half-metallic electrodes. Note that no charge current flows in the readout process, which is different in conventional MRAM modules [6]. In this chapter, electronic transport and spincaloric properties of epitaxial Co_2MnSi/MgO(001)/Co_2MnSi MTJs and their dependence on the interface structure will be shown. In addition to the approximate method by Sivan and Imry [325], which is conventionally used to obtain thermoelectric quantities like the Seebeck coefficient, a different, more general approach is presented, from which the former follows in the limit of small thermal gradients.

The results shown in this chapter can also be seen from another point of view. A ferromagnet/insulator/semiconductor setup can be used as spin injector [cf. Fig. 5.1(b)]. Using Co_2MnSi as ferromagnet should lead to a very high spin polarization of the injected carriers. The insulating layer serves again as tunneling barrier and avoids the conductivity (impedance) mismatch problems [5, 237]. The current can be driven by an external electric field (applied voltage) or by an external temperature gradient [326]. Recent experimental work has shown that epitaxial growth of MgO(001) on Si(001) is possible [327,328]. Furthermore, Co_2MnSi/MgO/Ge(001) structures have been grown [329]. This demonstrates that the outlined concept can be realized. A similar approach that suggests Al/Co_2TiSi/Al and Al/Co_2TiGe/Al heterostructures for spin injection into Si has been published recently [18].

5.2 Properties of Co_2MnSi and MgO

5.2.1 The Heusler alloy Co_2MnSi

The atomic structure of the FM ternary Heusler alloy Co_2MnSi is quite simple (when compared to the MnSi compounds, for instance). It is a *full* Heusler alloy since it possesses two Co atoms per f.u. These Co atoms form cages in which eightfold coordinated Mn and Si atoms are enclosed [cf. Fig. 5.2(a)]. This so-called $L2_1$ structure of full Heusler alloys can be described by a fcc Bravais lattice with an atomic basis consisting of two Co atoms at $(0,0,0)a_0$ and $(\frac{1}{2},\frac{1}{2},\frac{1}{2})a_0$, a Mn atom at $(\frac{1}{4},\frac{1}{4},\frac{1}{4})a_0$, and a Si atom at $(\frac{3}{4},\frac{3}{4},\frac{3}{4})a_0$. The space group is $Fm\bar{3}m$, which includes the inversion operation.[2] The experimental lattice constant is $a_0 = 5.654$ Å [330]. Table 5.1 provides a comparison of theoretical values, calculated with the USPP and the all-electron LAPW techniques. Agreement with experiment is even better than for bulk Si (cf. Table 3.1 on page 50) or the TM silicides (cf. Table 3.3 on page 63), and the agreement between USPP and all-electron results is very good. The all-electron results displayed in Fig. 5.2(b) as red diamonds together with the USPP band structure demonstrate the high quality of the pseudopotentials used here.

[2]If the given atomic basis coordinates are used, a fractional translation is necessary for the inversion operation. It is also possible to center the structure around either a Mn or a Si atom, which makes the inversion symmetry obvious.

Dieses Werk ist copyrightgeschützt und darf in keiner Form vervielfältigt werden noch an Dritte weitergegeben werden.
Es gilt nur für den persönlichen Gebrauch.

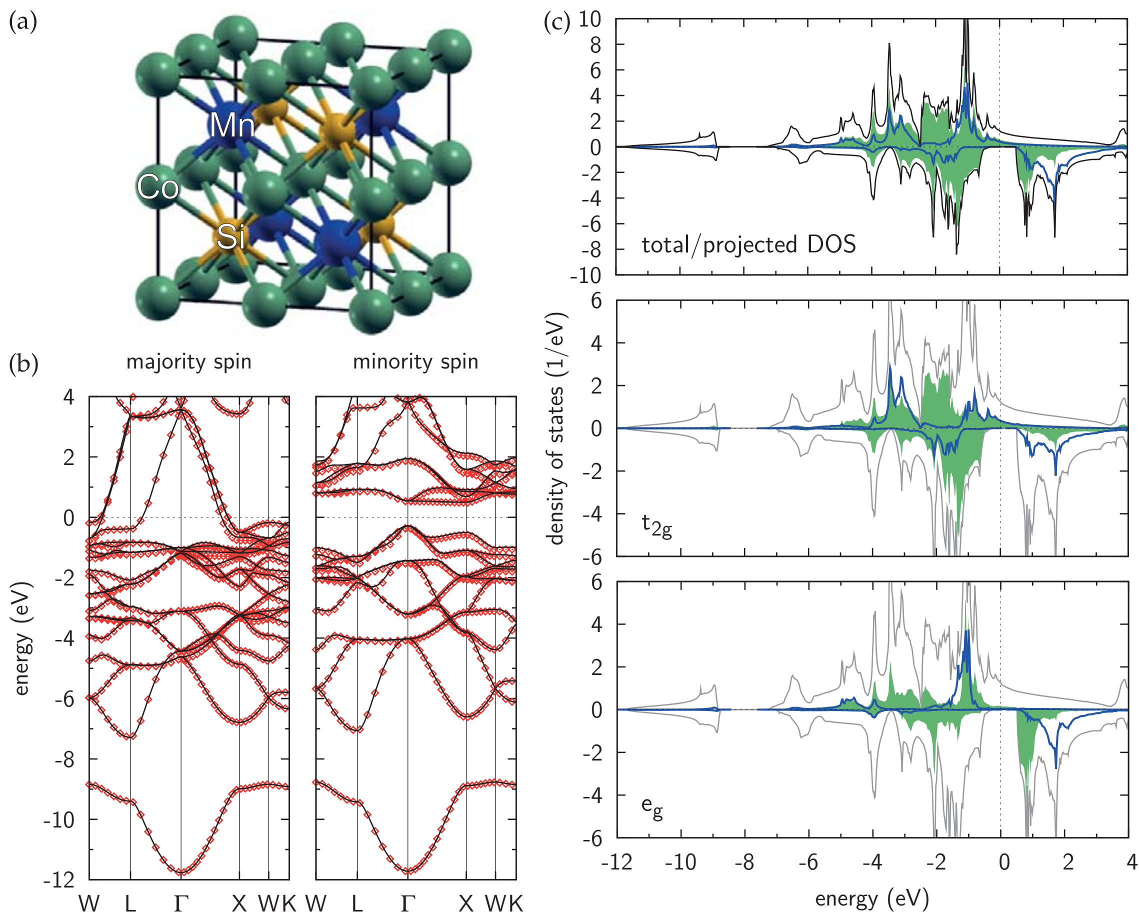

Figure 5.2 – Structural and electronic properties of bulk Co_2MnSi from USPP-PBE calculations. (a) Atomic structure in a simple cubic cell. (b) Band structure for the two different spin channels. The band gap in the minority spin channel at the Fermi energy (zero energy) is clearly visible. The red diamonds are all-electron results for comparison. (c) Total DOS (black and gray lines) and projections onto the 3*d* t_{2g} and e_g orbitals of Co (green) and Mn (blue).

It follows from the crystal structure that the Co-Co distance is larger ($a_0/2$) than the Co-(Mn/Si) distance ($a_0\sqrt{3}/4 \approx a_0/2.3$). Nevertheless, the generally accepted hybridization scheme by Galanakis *et al.* states that Co-Co hybridization is the first step, which is followed by a hybridization of the resulting orbitals with the atomic orbitals of the Mn and Si atoms [331]. It is presumed that this special hybridization leads to the most striking property of Co_2MnSi: It has a wide (indirect, $\Gamma - X$) band gap ($\varepsilon_G \approx 0.81$ eV) in the minority spin channel, which can clearly be seen in the band structure and DOS plots in Fig. 5.2. This special situation where one spin channel is metallic, while the other one is semiconducting or insulating, is referred to as “half-metallicity” [315]. The energy difference between the highest occupied state in the minority spin channel and the Fermi energy is $\varepsilon_S \approx 0.29$ eV. One can see from Fig. 5.2(c) (and also from Fig. 5.3) that the band gap in the minority spin channel is delimited by Co 3*d* states. The VBM is formed by t_{2g} states, while the CBM is

Dieses Werk ist copyrightgeschützt und darf in keiner Form vervielfältigt werden noch an Dritte weitergegeben werden.
Es gilt nur für den persönlichen Gebrauch.

Table 5.1 – Structural, electronic, and magnetic properties of bulk Co_2MnSi. USPP and all-electron results are compared. The exchange-correlation functional is always PBE. M_{tot} is the total magnetic moment per unit cell. Note that the definitions of the local magnetic moments m differ: While the USPP results correspond to Löwdin charges, the spin density has been integrated inside muffin-tin spheres for the LAPW results.

	this work USPP	Ref. [319] LAPW	Ref. [198] LAPW
a_0 (Å)	5.633	5.629	5.636
B_0 (GPa)	217	–	226
ε_G (eV)	0.81	0.84	0.81
ε_S (eV)	0.29	0.35	0.33
m_{Co} (μ_B)	0.97	1.07	1.06
m_{Mn} (μ_B)	3.17	2.91	2.92
m_{Si} (μ_B)	−0.09	−0.04	−0.04
M_{tot} (μ_B)	5.00	5.00	5.00

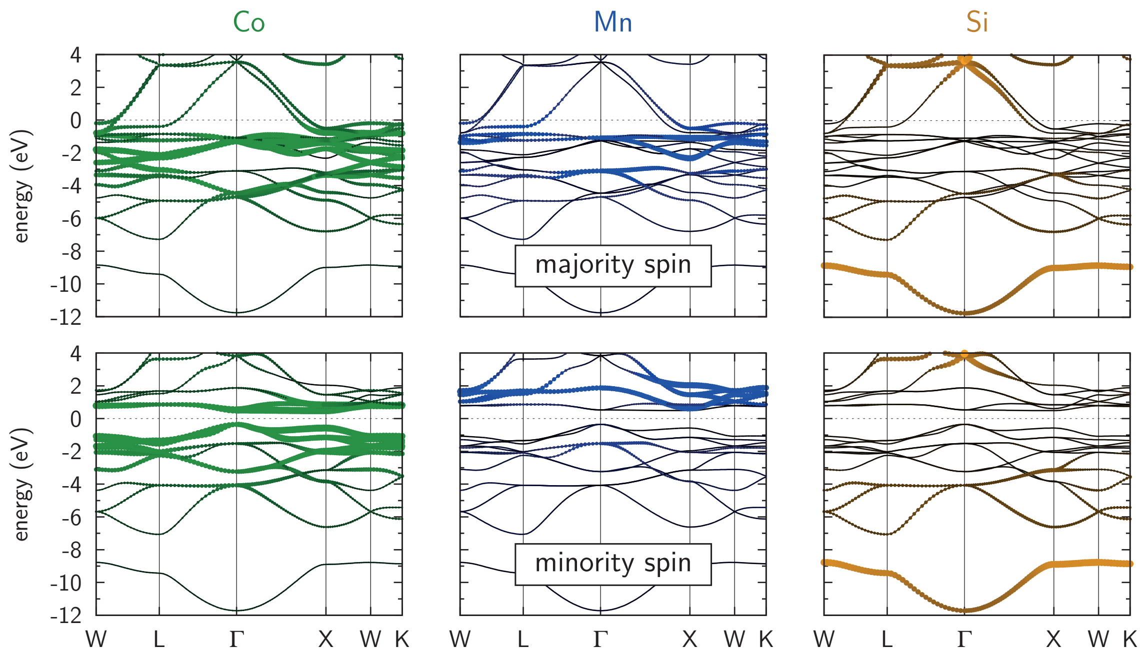

Figure 5.3 – All-electron (LAPW) band structure plots of bulk Co_2MnSi with superimposed band character (the band thickness and color brightness being proportional to the contribution of the corresponding element). The upper row shows the majority spin channel, while the lower row shows the minority spin channel. Again, one can clearly see that Co states delimit the band gap. The band character scaling is different for Co/Mn and Si. The numerical parameters are similar to those used in Ref. [319].

Dieses Werk ist copyrightgeschützt und darf in keiner Form vervielfältigt werden noch an Dritte weitergegeben werden.
Es gilt nur für den persönlichen Gebrauch.

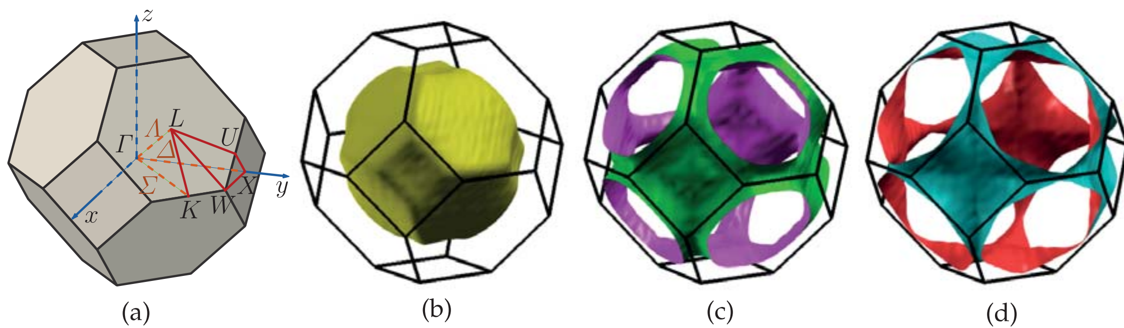

Figure 5.4 – Calculated Fermi surface sheets of bulk Co_2MnSi derived from the PBE electronic structure. (a) Nomenclature in the first Brillouin zone of the fcc lattice. (b) – (d) Majority spin Fermi surface sheets for the three different bands that cross the Fermi energy [cf. Fig. 5.2(b)].

formed by e_g states.[3] The region around the Fermi energy is free of Si states (cf. Fig. 5.3, Si panels).

A necessary consequence of the band gap in the minority spin channel is an integer total spin magnetic moment, which, in turn, is *not* a sufficient condition for half-metallicity. The DFT calculations give a total spin magnetic moment of 5.00 μ_B per f.u., which can also be found experimentally (e.g., 5.07 μ_B in Ref. [330]). This total magnetic moment is formed by the Co (≈ 1 μ_B) and Mn atoms (≈ 3 μ_B, cf. Table 5.1). One can also observe an induced antiparallel moment at the Si sites [198]. Spin-orbit interaction is of no importance here [319]. The Curie temperature of Co_2MnSi, $T_C = 985$ K [330], is very high, but lower than the corresponding value for Co_2FeSi [19]. This is not too surprising, since Mn and different Mn compounds often show AFM tendencies, whereas Fe is a strongly FM metal. Like many Heusler alloys, Co_2MnSi follows a Slater-Pauling-like rule: Galanakis *et al.* pointed out that the total magnetic moment of many full Heusler alloys can be connected to the number of valence electrons via $M_{tot} = N_{val} - 24$ [332].

Recent DFT calculations employing the many-body quasiparticle *GW* approximation have corroborated the view of Co_2MnSi being a half-metallic ferromagnet, even though the Fermi energy is shifted from the center of the band gap towards the VBM [333].[4] While there is a broad consensus in the theoretical literature that Co_2MnSi is half-metallic, one gets a more ambivalent impression from reading the experimental literature. The half-metallicity of Co_2MnSi can be investigated experimentally by using techniques like XMCD, neutron diffraction, point contact Andreev reflection (PCAR), spin-resolved photoemission spectroscopy, or tunneling spectroscopy.[5] While measurements of the saturation magnetization usually agree with the integer DFT result, most PCAR and spectroscopy experiments only show spin polarizations between 50 – 80 %, even at very low temperatures. This is usually attributed to deficiencies like structural disorder in the Heusler material and chemical reactions at the interfaces in MTJs. Theoretical investigations, especially on the influence of structural disorder, have been carried out recently [319]. Since these deficiencies are of technical nature and neither related to finite temperatures nor relevant in the following, they will not be discussed here in more detail. A very recent publication claims a large spin polariza-

[3] Galanakis *et al.* actually proposed that the band gap is delimited by t_{1u} and e_u states [331]. As in their work, the projections shown here cannot distinguish t_{2g} from t_{1u} states and e_g from e_u states.
[4] Moreover, these calculations suggest that Co_2FeSi should also be half-metallic, which it is not in DFT-PBE.
[5] For a collection of experimental data the reader is referred to Ref. [319].

Dieses Werk ist copyrightgeschützt und darf in keiner Form vervielfältigt werden noch an Dritte weitergegeben werden.
Es gilt nur für den persönlichen Gebrauch.

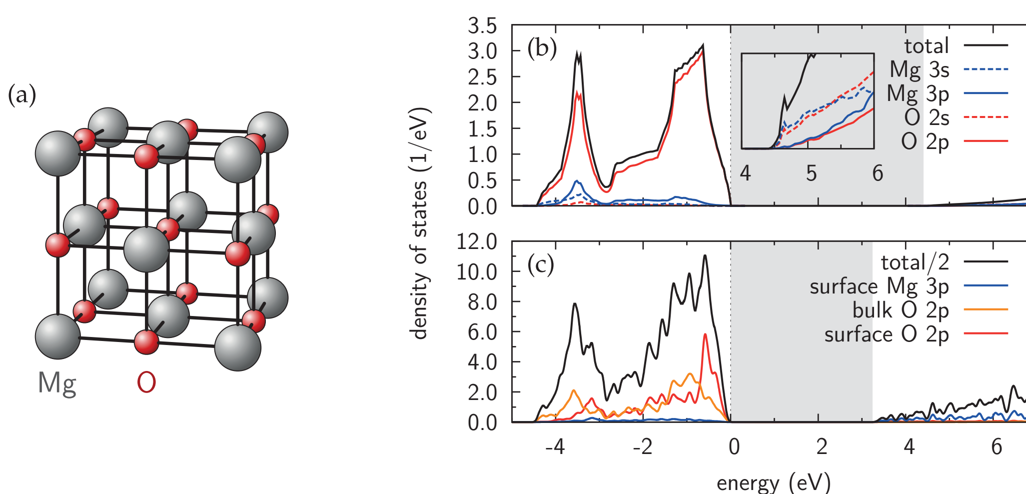

Figure 5.5 – (a) Rock-salt structure of the insulator MgO. (b) Total DOS (black lines) and projections (colored lines) of bulk MgO as calculated with the PBE exchange-correlation functional. The inset shows a magnification of the CB. The vertical dashed line marks the Fermi energy, and the direct band gap is highlighted by the gray shaded area. (c) Total DOS (black lines) and projections (colored lines) of a MgO(001) surface slab.

tion of around 93% in 70 nm Co_2MnSi films grown epitaxially on MgO(001) and a 30 nm Co_2MnGa buffer layer on the basis of ultraviolet and x-ray photoemission spectroscopy experiments [334].

For the analysis of transport properties in the following it is helpful to know the Fermi surface of bulk Co_2MnSi. According to Fig. 5.2(b), the Fermi energy is crossed by three different bands. The corresponding Fermi surface sheets are shown in Fig. 5.4. All three bands cross the Fermi energy along $\Gamma - X$ (Δ symmetry line), as one can also see from the band structure plots in Figs. 5.2(b) and 5.3. However, while one band crosses the Fermi energy also along $\Gamma - L$ (Λ symmetry line), which leads to a closed Fermi surface sheet, the other two bands cross the Fermi energy along $W - L$, which leads to Fermi surface sheets with "necks" along the different [111] directions. The former has a mixed Co-Mn character, while the latter have predominantly Co character.

5.2.2 The insulator MgO

The insulator MgO grows in the rock-salt crystal structure [cf. Fig. 5.5(a)], which can be modeled by a fcc Bravais lattice with a two-atomic basis. Its experimental lattice constant is 4.212 Å [335], but the values show some spread in the literature (see Ref. [336] for an overview). Reference [336] reports theoretical results derived with different methodologies which range from 4.091 to 4.218 Å. The USPP-PBE result used in this thesis is 4.265 Å, which agrees well with the LAPW-PBE value of 4.261 Å reported in Ref. [40]. The bulk modulus is 146 GPa and thus considerably lower than the experimental results, which lie between 160 and 180 GPa [336]. Both the lattice constant and the bulk modulus reflect (once more) the typical PBE underbinding behavior.

Figure 5.5(b) shows the total and projected DOS of bulk MgO. The VB has almost exclusively O 2p character, while the CB is dominated by Mg 3s states (and Mg 3p states at higher energies). Both bands are separated by a large gap. This behavior is expected for a highly

Dieses Werk ist copyrightgeschützt und darf in keiner Form vervielfältigt werden noch an Dritte weitergegeben werden.
Es gilt nur für den persönlichen Gebrauch.

ionic system like MgO, since all O 2p states are filled up with the Mg 3s electrons. However, the VB has also some Mg 3p (and slight Mg 3s) character, whereas the CB shows some O 2s character in addition. The PBE band gap (4.4 eV) is direct and much smaller than the experimental one (7.9 eV [49]).

If the crystal is rotated by 45° about the [001] axis, MgO can be matched epitaxially to full Heusler alloys like Co_2MnSi. The calculated (experimental) lattice mismatch with Co_2MnSi is -6.6% (-5.1%), which means that the epitaxial MgO layer is subject to in-plane compressive strain. Consequently, the material will distort tetragonally and expand in [001] direction. The optimized cell height is 4.503 Å, which is 5.6% larger than the MgO lattice constant. The band gap increases to 5.0 eV. These results are similar to the LAPW results reported in Ref. [319].

According to PBE calculations, the MgO(001) surface is almost planar with a small outward relaxation (0.02 Å) of the O atoms. Figure 5.5(c) shows the total and projected DOS of a MgO slab (without biaxial strain) with two equivalent (001) surfaces. Despite the broken bonds, the interface remains insulating. The band gap is smaller for the (001) surface (3.4 eV here, 3 eV in LDA [337]) than for bulk MgO. This narrowing is mainly caused by energetically lowered CB 3p states of surface Mg atoms. Moreover, one can observe an accumulation of surface O 2p states close to the VBM when compared with the PDOS of bulk O atoms.

5.3 Phonon influence on the half-metallic gap

The question that shall be addressed in this section is in how far the electronic structure of bulk Co_2MnSi, and especially the half-metallic band gap, is affected by (thermally excited) lattice vibrations, i.e., phonons (electron-phonon coupling). First, the phonon dispersion relations, obtained by using DFPT, are discussed. Subsequently, a statistical approach is presented which provides information about the response of the electronic structure to distortions of the atomic structure.

5.3.1 Phonon dispersion relations

Figure 5.6 shows calculated phonon dispersion relations of bulk Co_2MnSi that have been obtained by using DFPT (cf. Sec. 3.4.2 on page 80). Similar to the phonon spectrum of MnSi (cf. Fig. 3.20 on page 82), the Si modes are those with the highest energy, since Si atoms are lighter than Co and Mn atoms. The Co modes are concentrated in the energy interval between 25 and 35 meV, whereas the Mn atoms vibrate most intensely around certain $(\nu, \vec{q})$ points like those close to the W point at 24 meV, or along the $\Gamma - L$ (Λ) symmetry line around 36 meV.

Such a phonon dispersion relation does not provide information about the changes induced in the electronic spectrum. Moreover, it does not include information beyond the harmonic approximation. In conjunction with the eigenvectors (displacement patterns) and the Bose distribution function it can be used to generate thermalized ensembles of explicit atom displacements. However, a more direct route will be used in the following.

Dieses Werk ist copyrightgeschützt und darf in keiner Form vervielfältigt werden noch an Dritte weitergegeben werden.
Es gilt nur für den persönlichen Gebrauch.

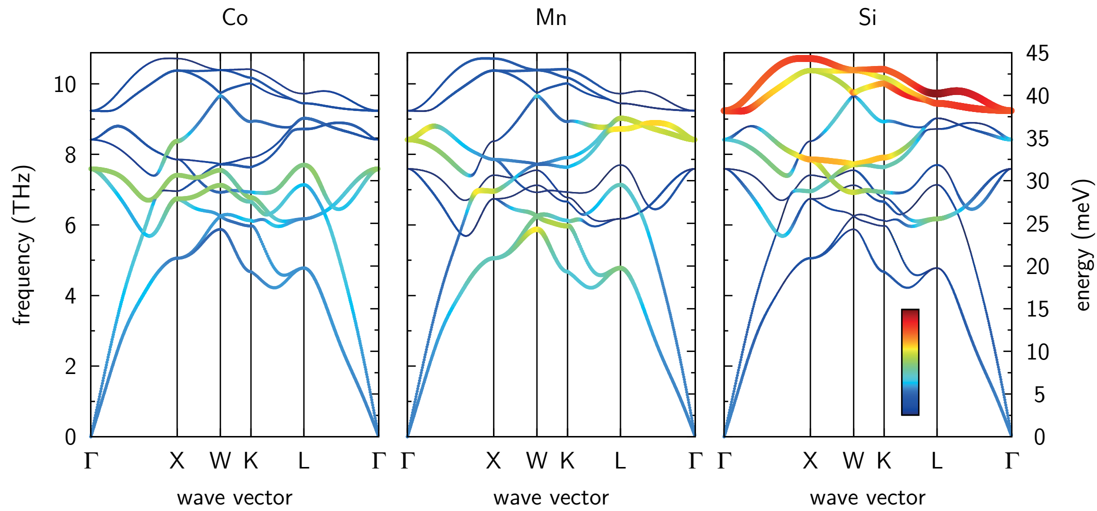

Figure 5.6 – Calculated phonon dispersion relations of bulk Co_2MnSi. The coloring and width of the bands indicate the single-atom band character $\chi_s(\nu, \vec{q})$ [thin blue (thick red) bands depict the minimum (maximum)]; the different panels correspond to the different chemical elements.

5.3.2 Random frozen phonons

The approach that is used here to estimate the electronic response of bulk Co_2MnSi to lattice vibrations resembles the frozen phonon approach, but with completely random atom displacements instead of well-chosen configurations. Although providing only a "static" picture it is a reasonable method, since the electronic system accommodates rapidly to any ionic configuration. Anharmonic effects are included, together with changes in the hybridization due to "structural fluctuations".[6]

Starting from a 32-atom fcc supercell for bulk Co_2MnSi with ideal structure, each atom in the supercell is randomly displaced within a sphere with radius δr around its ideal position. Consequently, it can also occur that an atom is not displaced at all. Thus, the radial probability density $P(r)$ and average distance $\bar{r}$ from the ideal position are in each case

$$P(r) = \frac{3r^2}{(\delta r)^3}\Theta(\delta r - r), \qquad \bar{r} = \int_0^\infty \mathrm{d}r\, r\, P(r) = \frac{3}{4}\delta r,$$

where $\Theta(r)$ is the Heaviside step function. Subsequently, a DFT calculation provides the total energy difference with respect to the ideal structure E_i and the electronic DOS $D_i^\sigma(E)$. For a given δr, several ($\tilde{N} = 250$) randomly distorted structures have been generated and evaluated to get a statistically significant result.[7] Afterwards, the average response of the electronic system to random distortions can be calculated:

$$\tilde{D}^\sigma(E) = \frac{1}{\tilde{N}}\sum_{i=1}^{\tilde{N}} D_i^\sigma(E).$$

[6] This effect is similar to the variation of the hybridization due to *spin* fluctuations [323].
[7] This means that for each δr value $\tilde{N}$ DFT calculations of different Co_2MnSi supercells have been performed (convergence of the density plus subsequent post processing for DOS).

Dieses Werk ist copyrightgeschützt und darf in keiner Form vervielfältigt werden noch an Dritte weitergegeben werden.
Es gilt nur für den persönlichen Gebrauch.

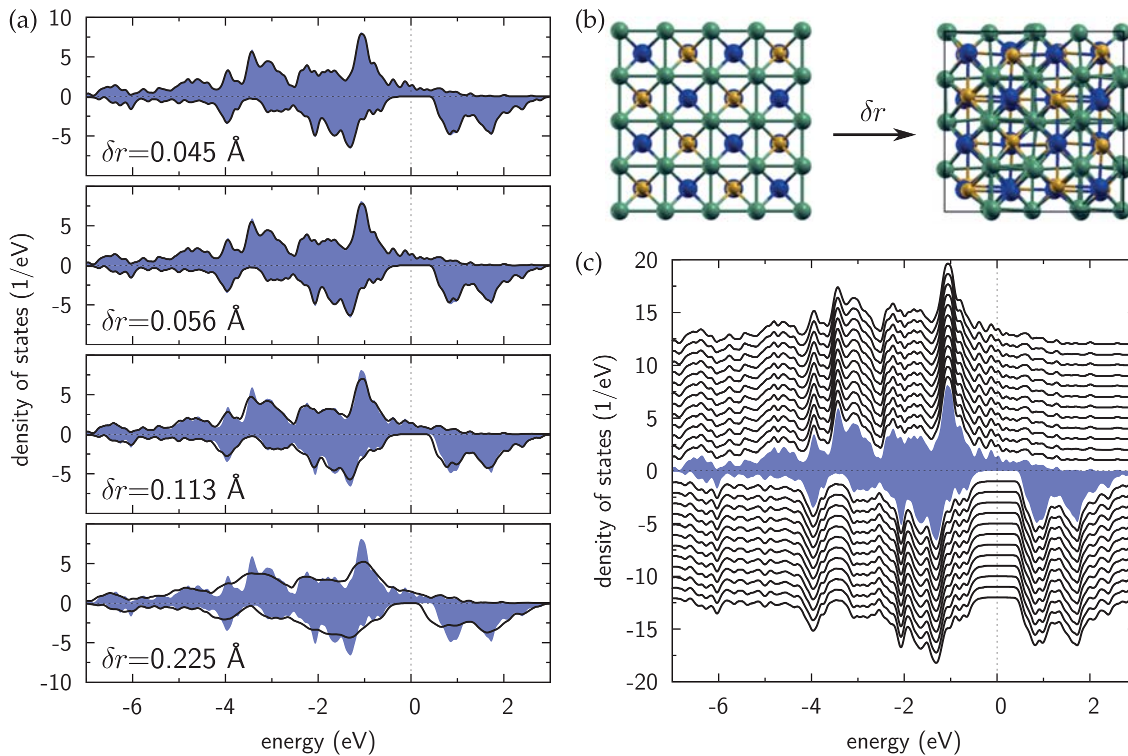

Figure 5.7 – (a) Average response of the spin-resolved electronic structure of bulk Co_2MnSi, $\tilde{D}^{\sigma}(E)$, to differently intense structural distortions as exemplarily illustrated in (b). The blue shaded area corresponds to the total DOS of the ideal structure per f.u. (c) Thermal evolution of this response, $D^{\sigma}(E,T)$, for temperatures ranging from 200 (innermost curves) to 2400 K (outermost curves), which is already far beyond the Curie temperature (985 K). The Fermi energy of the ideal structure has been used as reference.

The results are shown in Fig. 5.7(a) for different values of δr. While small variations of the structure leave the DOS almost unchanged, significant differences can be observed for $\delta r \gtrsim 0.1$ Å, which corresponds to values larger than 1.8 % of the Co_2MnSi lattice constant. The broadening that arises for the larger peaks is not surprising. More interesting is the fact that the half-metallic band gap starts to narrow from the CB. Similar observations have been made for bulk Co_2MnSi considering nonquasiparticle states [338] and spin wave excitations [339], but also for other Heusler compounds like NiMnSb [340]. However, the half-metallic character of the material remains intact here.

So far, all results are characterized only by their maximal displacement δr. It is possible to introduce a temperature T by using the total energies E_i (per f.u.) to generate a canonical ensemble. Four different sets of 250 structures each have been included in the ensemble, each set belonging to a certain sphere radius $\delta r \in \{0.045, 0.056, 0.113, 0.225\}$ Å. The temperature-dependent DOS is the ensemble average:

$$D^{\sigma}(E,T) = \sum_{i=1}^{N} \frac{\exp(-\frac{E_i}{k_B T})}{Z(T)} D_i^{\sigma}(E), \qquad Z(T) = \sum_{i=1}^{N} \exp\left(-\frac{E_i}{k_B T}\right),$$

where $N = 4\tilde{N} = 1000$ is the total number of evaluated random structures. Note that the total set comprises relatively excited structures as well as almost ideal structures with total

Dieses Werk ist copyrightgeschützt und darf in keiner Form vervielfältigt werden noch an Dritte weitergegeben werden.
Es gilt nur für den persönlichen Gebrauch.

energies close to the ground state. Moreover, it does include the ideal (i.e., the ground state) structure.

The DOS curves for different temperatures T are shown in Fig. 5.7(c) and make clear that thermally induced lattice vibrations have no significant influence on the half-metallic band gap for all reasonable temperatures (i.e., below the Curie temperature) and even beyond. Overall, the deviations from the ideal DOS are very small. This is related to the high energies required to displace the atoms beyond $\delta r \approx 0.1$ Å. Consequently, thermally excited bulk phonons cannot account for the strong decrease of the TMR ratio of Co_2MnSi/MgO MTJs. Even if one assumes that interface phonons are more easy to excite due to the broken crystal periodicity, it appears unlikely that they will lead to a drastically different picture. A detailed investigation of lattice vibrations at the interfaces is subject of future work. Moreover, the influence of structural distortions on the magnetic coupling (excitation energies) is an aspect that should be explored.

Outlook: Electron-phonon coupling from unfolded supercell band structures

The electron-phonon coupling leads to a temperature-dependent broadening of the band structure [i.e., the spectral function $A(\vec{k},E)$]. It is possible to treat the thermal atom displacements within the coherent potential approximation [341]. This method is more commonly employed for the investigation of random substitutional alloys, which can also be studied by using a supercell approach [342]. The supercell approach should be accompanied by a band unfolding scheme in order to obtain a more instructive band structure in the Brillouin zone of the primitive cell, since the latter is larger than the Brillouin zone of the supercell. The procedure presented above can be seen as analogue to the supercell approach for alloys, but for electron-phonon coupling. The author intends to apply a band unfolding scheme for plane waves [342, 343] to the randomly distorted structures in future work. Subsequently, the ensemble average of all the unfolded bands will provide the spectral function with temperature-dependent broadening:

$$A^{\sigma}(\vec{k},E;T) = \sum_{i=1}^{N} \frac{\exp(-\frac{E_i}{k_B T})}{Z(T)} A_i^{\sigma}(\vec{k},E), \qquad A_i^{\sigma}(\vec{k},E) = \sum_{n,m} |\langle \vec{K},m,i,\sigma|\vec{k},n,\sigma\rangle|^2 \, \delta(\varepsilon^{\sigma}_{\vec{K},m,i} - E),$$

where $\vec{K}$, belonging to the supercell Brillouin zone, unfolds into $\vec{k}$, which belongs to the Brillouin zone of the primitive cell. The band indices n and m label the Kohn-Sham states of the primitive cell and of the supercell, respectively. This spectral function will lead to the same conclusions as the DOS curves shown in Fig. 5.7, but it will provide a different, more detailed viewpoint.

5.4 Magnetic tunnel junctions

This section is about epitaxial $Co_2MnSi/MgO(001)/Co_2MnSi$ MTJs. After a recapitulation of the atomic and electronic structure of different possible interfaces between the Heusler electrodes and the insulator, the two important states of the electrode magnetization are considered separately: In the parallel case, electronic transport, spincaloric properties, and their dependence on the interface structure are analyzed. A more general approach to spincaloric properties is presented. In the antiparallel case, the influence of interface magnons on the TMR ratio at finite temperatures is qualitatively discussed.

Dieses Werk ist copyrightgeschützt und darf in keiner Form vervielfältigt werden noch an Dritte weitergegeben werden.
Es gilt nur für den persönlichen Gebrauch.

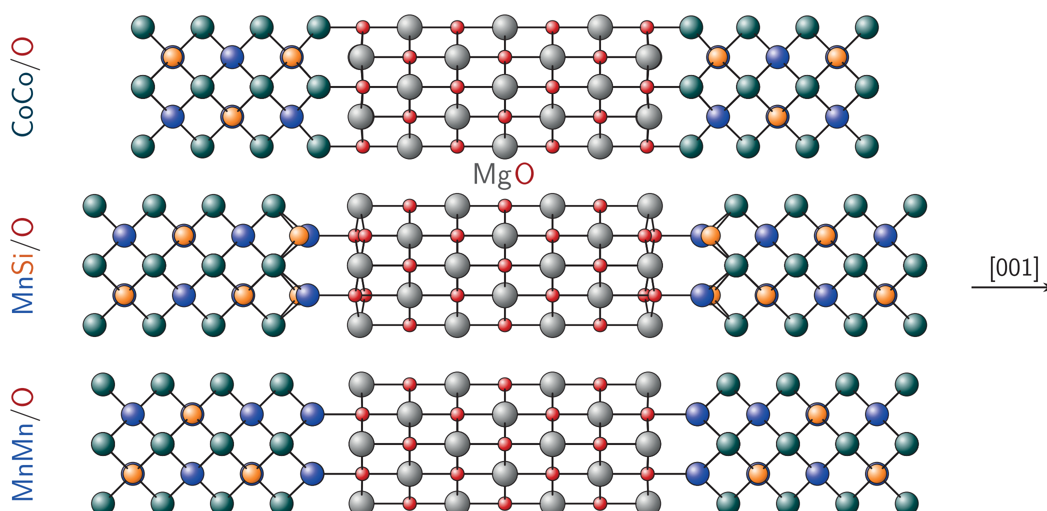

Figure 5.8 – Optimized atomic structure of epitaxial $Co_2MnSi/MgO(001)/Co_2MnSi$ MTJs with the three different interface terminations considered here: CoCo/O top, MnSi/O top, and MnMn/O top.

5.4.1 Atomic and electronic structure of the interface

The full Heusler alloy $Co_2MnSi(001)$ can be matched epitaxially to MgO(001) if either of them is rotated by 45° about the [001] axis. In Fig. 5.8 we can see the atomic structure of the epitaxial $Co_2MnSi/MgO(001)$ interface for the three different terminations considered here: CoCo/O top, where both Co atoms sit on top of the O atoms of the insulator; MnSi/O top, where the Mn and Si atoms sit on top of the O atoms; and analogously MnMn/O top, which is a nonstoichiometric interface with Mn_{Si} substitutions. The selection of these three interfaces (out of many more different interface structures) is motivated by recent studies of the thermodynamic properties of different $Co_2MnSi(001)$ surfaces [344] and different epitaxial $Co_2MnSi/MgO(001)$ interfaces [321]. It has been found that the CoCo/O and MnSi/O interfaces are the most stable ones, while the MnMn/O interface can be grown under nonequilibrium conditions and exhibits interesting properties (see below).

The laterally smallest supercell that can be used to model these MTJs is tetragonal, with an in-plane lattice constant of $a_{Co_2MnSi}/\sqrt{2}$. Thus, it contains Co_2MnSi in its rotated form. Ideally (that is, prior to any relaxations), each plane in the Heusler regions contains two atoms: Co-Co, Mn-Si, Co-Co, Si-Mn, and so forth, while in the barrier region each plane contains four atoms: Mg-Mg-O-O or O-O-Mg-Mg. Structural optimization comprises (i) the length of the tetragonal cell (and thus the Co_2MnSi-MgO spacing) and (ii) the atomic positions.

The results of the optimization procedure are shown in Fig. 5.8. Both the CoCo/O and the MnMn/O interface are planar. The Co-O bond length is the shortest with 2.10 Å (2.09 Å according to Ref. [321]), while the Mn-O bond length is 2.35 Å (2.40 Å). In contrast, the MnSi/O interface is corrugated: There seems to be some repulsion between Si and O atoms.[8] Consequently, the Si atoms move towards the next CoCo layer in the Heusler electrode, while the Mn atoms form bonds with the O atoms. The Si-O distance is 3.13 Å (3.17 Å [345]), and the Mn-O distance is 2.20 Å (2.27 Å [321], 2.25 Å [345]) now. A similar effect occurs in the

[8]It is also possible that the under-coordinated interface Mn atoms simply prefer a different bonding angle with their Si neighbors due to rehybridization.

Dieses Werk ist copyrightgeschützt und darf in keiner Form vervielfältigt werden noch an Dritte weitergegeben werden.
Es gilt nur für den persönlichen Gebrauch.

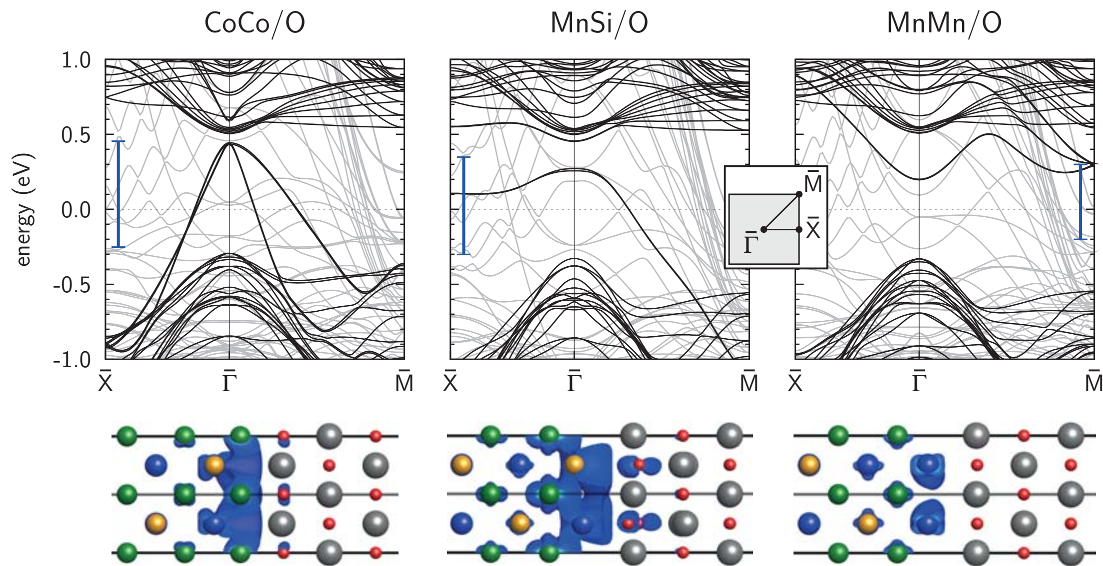

Figure 5.9 – Interface band structure of the $Co_2MnSi/MgO(001)$ interface for the three different terminations (cf. Fig. 5.8). The minority (majority) spin channel is displayed by black (light gray) lines. The Fermi energy is chosen as reference. The labeling refers to the 2D-BZ of the MTJ cell, which is rotated by 45° about the [001] axis with respect to the bulk unit cell of Co_2MnSi. The lower row shows visualizations of the minority spin interface states, i.e., ILDOS isosurfaces (blue) according to Eq. (3.7). The same critical density is used in all three images. The atom colors follow Fig. 5.8. The blue bars in the band structure plots depict the corresponding integration intervals.

first MgO layer at the interface. Obviously, there is a good agreement of the present results with those obtained by Hülsen *et al.* (LAPW, Ref. [321]) and Miura *et al.* (USPP, Ref. [345]). Small differences with respect to the literature arise mostly due to the different MgO barrier sizes used in the calculations (3 layers in Ref. [321], 7 layers here), as the author verified by performing calculations with different MgO thickness. The influence of the all-electron approach is negligible. The electrode-electrode distance across the insulating spacer layer is largest for MnSi/O and smallest for CoCo/O (cf. Fig. 5.8).

While the structurally optimized CoCo/O and MnSi/O interfaces induce interface states at the Fermi energy, the MnMn/O interface remains half-metallic (cf. Fig. 5.9), in agreement with the results of Hülsen *et al.* [321]. The latter observation has also been made for the purely Mn-terminated $Co_2MnSi(001)$ surface and has been attributed to its strong surface-subsurface coupling [344]. Further analysis of these interface states shows that they are predominantly formed by Co and Mn out-of-plane orbitals (d_{z^2}, d_{xz}, d_{yz}) in the vicinity of the interface [321].[9]

The ILDOS isosurfaces in Fig. 5.9 show the spatial nature of the interface states in the band gap. They are indeed localized at the interface. In the CoCo/O case the interface states extend over the first three Heusler layers and the first MgO layer at the interface. For MnSi/O even four Heusler layers participate considerably, and it becomes obvious that predominantly the O atoms contribute to the interface states in the MgO layer. The MnMn/O interface shows no contributions from MgO, but from the first three Heusler layers. For

[9] The z axis has been chosen to be parallel to the [001] direction and thus perpendicular to the layer plane.

Dieses Werk ist copyrightgeschützt und darf in keiner Form vervielfältigt werden noch an Dritte weitergegeben werden.
Es gilt nur für den persönlichen Gebrauch.

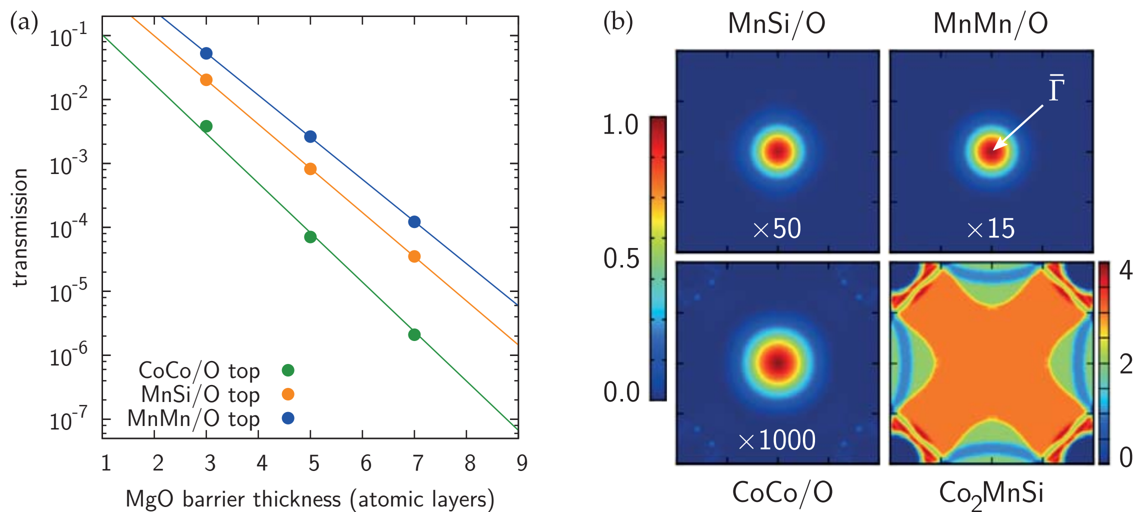

Figure 5.10 – (a) Dependence of the majority spin transmission $T_\uparrow(E)$ through the discussed $Co_2MnSi/MgO(001)/Co_2MnSi$ MTJs for $E = E_F$ on the MgO barrier thickness and on the interface termination. The exponential suppression of the transmission with increasing tunneling barrier thickness can be seen. (b) Contour plots of the majority spin transmission $T_\uparrow(E, \vec{k}_\perp)$ in the 2D-BZ for $E = E_F$, 5 layers of MgO, and different interface terminations. It can be seen that the latter strongly affect the transmission. Note the different scaling factors. The $\vec{k}_\perp$-resolved transmission through a tetragonal unit cell of bulk Co_2MnSi is also shown. The 2D-BZ corresponds to the inset in Fig. 5.9.

CoCo/O and MnSi/O the interface states are delocalized in the interface plane, while for MnMn/O they are more confined to the interface atoms.

A characteristic quantity for MTJs is the TMR ratio, which relates the electrical conductance G (or, equivalently, the resistance R) in the cases of parallel and antiparallel electrode magnetization. The TMR ratio can be defined as

$$\text{TMR ratio} = \frac{R_{\text{AP}} - R_{\text{P}}}{R_{\text{P}}} = \frac{G_{\text{P}} - G_{\text{AP}}}{G_{\text{AP}}},$$

since $R_i = G_i^{-1}$. Hence, a TMR ratio of 100% means that $R_{\text{AP}} = 2R_{\text{P}}$ and, equivalently, that $G_{\text{P}} = 2G_{\text{AP}}$. An approximation of the TMR ratio in the limit of small voltages (linear response) is given by Jullière's diffusive transport model [346]:

$$\text{TMR ratio} = \frac{2P_{\text{L}}P_{\text{R}}}{1 - P_{\text{L}}P_{\text{R}}}, \qquad P = \frac{D^\uparrow(E_{\text{F}}) - D^\downarrow(E_{\text{F}})}{D^\uparrow(E_{\text{F}}) + D^\downarrow(E_{\text{F}})},$$

where $P_{\text{L/R}}$ is the polarization in the left/right electrode at the Fermi energy and can be derived from the DOS $D^\sigma(E)$. This definition of the TMR ratio lacks, however, any contribution from quantum-mechanical matrix elements. Since the electrodes are equivalent and half-metallic in this case, G_{AP} and $D^\downarrow(E_{\text{F}})$ vanish. Consequently, $P = 1$, and therefore the TMR ratio is, at least in principle, infinite, regardless of G_{P} or $D^\uparrow(E_{\text{F}})$.

5.4.2 Parallel electrode magnetization: Transport and spincalorics

In the case of parallel magnetization of the half-metallic electrodes, a conventional tunneling current can flow at least in the majority spin channel. In Fig. 5.10(a) we can see how the

Dieses Werk ist copyrightgeschützt und darf in keiner Form vervielfältigt werden noch an Dritte weitergegeben werden.
Es gilt nur für den persönlichen Gebrauch.

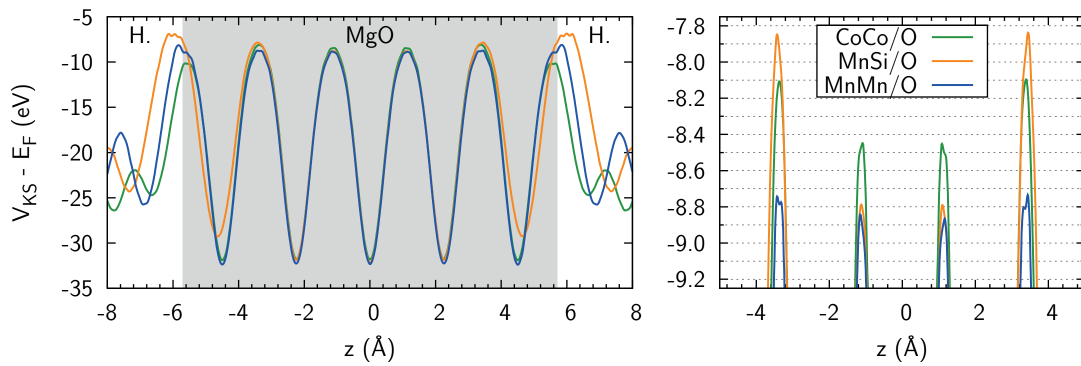

Figure 5.11 – Majority spin Kohn-Sham potentials $V^{\uparrow}_{KS}(\vec{r})$ of MTJs with 5 layers of MgO (gray shaded region) between Co_2MnSi electrodes (H.), for which the scattering problem is solved. The potentials have been aligned with the Fermi energies of the corresponding systems ($V_{KS} = 0$ eV here) and averaged in the xy plane. The right panel is a magnification of the left panel.

majority spin transmission at the Fermi energy $T_{\uparrow}(E_F)$ depends on the MgO barrier thickness and on the interface termination. The transmission has been obtained from the DFT effective potentials by using the scattering method described in Sec. 2.4. For all three interfaces one observes an exponential decay of the transmission with the barrier thickness a,

$$T(E_F) \sim e^{-2\kappa a + \xi}, \qquad \kappa \sim \sqrt{E_C},$$

which is characteristic for tunneling through a potential barrier. The transmission is smallest for the CoCo/O interface and largest for the MnMn/O interface. The contour plots of the majority spin transmission $T_{\uparrow}(E_F, \vec{k}_{\perp})$, which are displayed in Fig. 5.10(b) in the 2D-BZ, show that the contributing channels are mostly concentrated around the $\bar{\Gamma}$ point (normal incidence). However, there are also small satellite peaks in the vicinity of the $\bar{M}$ point in the case of the CoCo/O interface. For comparison, the majority spin transmission through a tetragonal unit cell of bulk Co_2MnSi at the Fermi energy is also shown in Fig. 5.10(b). It represents the available incoming or receiving transmission channels and is equivalent to the projected Fermi surface (cf. Fig. 5.4 on page 172).

The slopes 2κ in Fig. 5.10(a), which are a result of fitting the data points, are not equal, but largest for CoCo/O and smallest for MnMn/O (cf. Table 5.2). This can be understood largely on the basis of tunneling through potential barriers of different height. Figure 5.11 shows the xy-plane-averaged Kohn-Sham potentials $V^{\uparrow}_{KS}(\vec{r})$. While the position of the Fermi energy is

Table 5.2 – Energy differences E_V and E_C, which are defined in the image on the right, and results 2κ of the transmission data fitting [cf. Fig. 5.10(a)]. The unit of 2κ refers to the layer spacing of strained bulk MgO.

Interface	E_V (eV)	E_C (eV)	2κ (0.444 Å^{-1})
CoCo/O	2.72	2.28	1.780
MnSi/O	3.08	1.92	1.590
MnMn/O	3.18	1.82	1.516

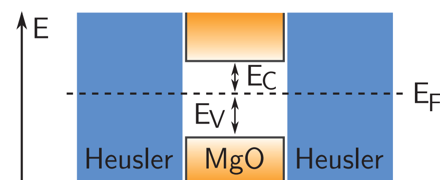

Dieses Werk ist copyrightgeschützt und darf in keiner Form vervielfältigt werden noch an Dritte weitergegeben werden.
Es gilt nur für den persönlichen Gebrauch.

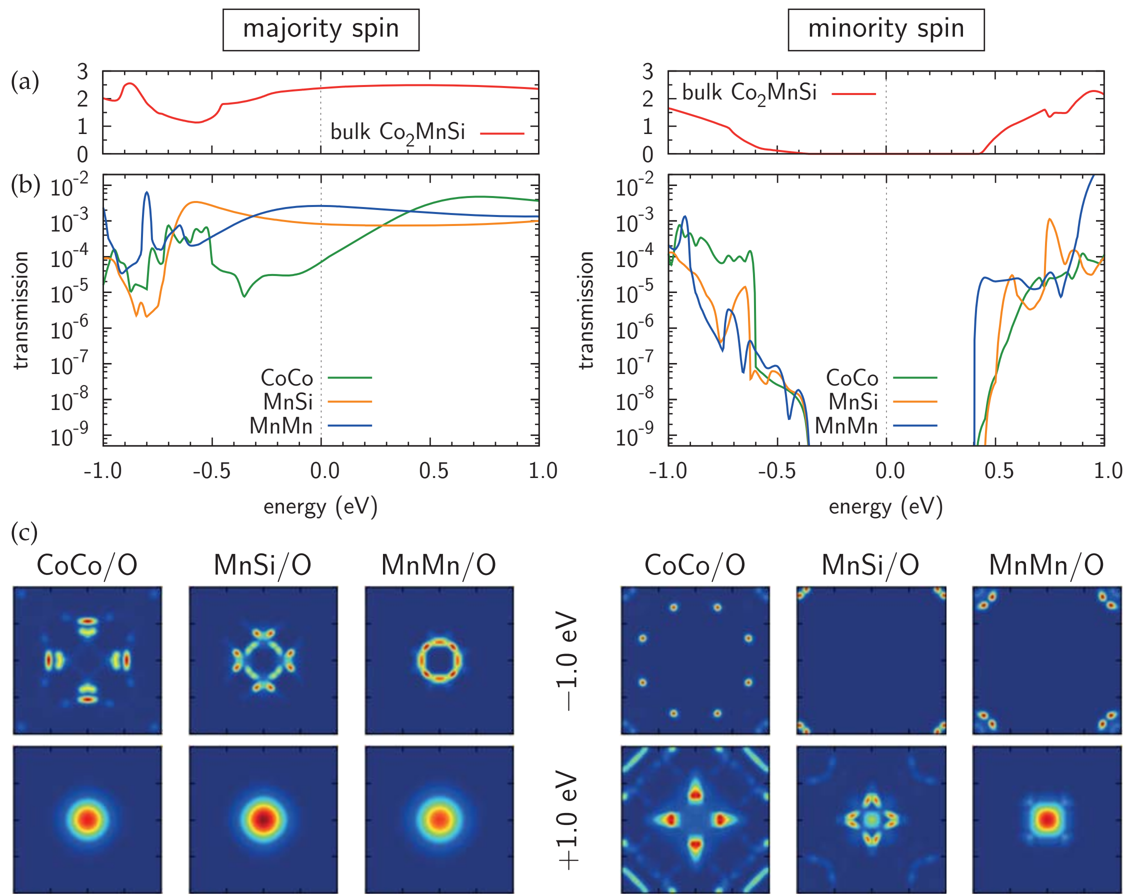

Figure 5.12 – Majority (left) and minority (right) spin transmission $T_\sigma(E - E_F)$ through (a) bulk Co_2MnSi and (b) MTJs with 5 layers of MgO. (c) Contour plots of $T_\sigma(E, \vec{k}_\perp)$ [similar to Fig. 5.10(b)] for two selected energies relative to E_F. Note that all contour plots show tunneling transport and have different color scales (but fixed zero) to emphasize the *qualitative* differences.

fixed by the semi-infinite Heusler electrodes (at $V_{KS} = 0$ eV here), the MgO potential barrier height shows a dependence on the interface termination. This can be seen from the minima and maxima of the potential around the center of the barrier region. Moreover, one can see significant differences between the three potentials at the interfaces, which are related to the different involved atomic species as well as to the different electrode-barrier spacings.[10] Consistent with the transmission sequence, the electrons have to tunnel through the highest barrier for the CoCo/O system, while the MnMn/O barrier is lowest.

This aspect can also be studied more quantitatively. Relevant in the sense of a potential barrier is the energy difference E_C between the Fermi energy $E = E_F$ of the MTJ and the CBM of epitaxial MgO, which is given in Table 5.2, together with the energy difference E_V between the Fermi energy and the VBM of epitaxial MgO. Of course, $E_V + E_C = 5.0$ eV is the band gap of epitaxial MgO, as mentioned above. E_V and E_C have been obtained from matching the averaged Kohn-Sham potential of tetragonally distorted bulk MgO to the averaged potential of the MTJ cells in the center of the MgO barrier. Obviously, the Fermi energy is indeed

[10] The electrode-barrier spacing is largest for MnSi/O and smallest for CoCo/O, which is directly reflected by the averaged potentials.

Dieses Werk ist copyrightgeschützt und darf in keiner Form vervielfältigt werden noch an Dritte weitergegeben werden.
Es gilt nur für den persönlichen Gebrauch.

located *within* the band gap of epitaxial MgO, so that the insulator forms a tunneling barrier. The ratios κ'/κ (between all three interfaces: 1.12, 1.05, and 1.17) can now be compared to $\sqrt{E'_C/E_C}$ (1.09, 1.03, and 1.12). The good agreement shows that the tunneling barrier model for the thickness dependence of the transmission is appropriate at the Fermi energy.

The transmission $T_\sigma(E)$ can be calculated from the DFT effective potentials for any energy argument, not only at E_F. Since for each energy the whole 2D-BZ has to be sampled, this procedure is very time consuming. The results in an energy interval of ± 1.0 eV around E_F are shown in Fig. 5.12, together with the energy-resolved transmission through a tetragonal unit cell of bulk Co_2MnSi, which can serve as reference.[11] Note that the whole energy range is within the MgO band gap (cf. Table 5.2). For the majority spin channel the transmission exhibits a smooth behavior for energies above $E_F - 0.3$ eV regardless of the interface termination. The appearance of several features below this energy coincides with the more structured majority spin DOS of bulk Co_2MnSi 0.5 eV below its Fermi energy (cf. Fig. 5.2 on page 170). Moreover, Fig. 5.12 clearly shows that the transmission curves cannot be matched by scaling the curves (i.e., exponentiation) or shifting the Fermi energies. Since electrodes and barriers are equal in all systems, the *qualitative* differences in the transmission properties can only stem from the interface termination. This proves that the interface has a strong influence on transport properties beyond simply modifying the MgO potential barrier height (which we have seen above).[12] Moreover, we can see here that atomistic first-principles simulations are a prerequisite for a more detailed understanding of quantum transport beyond theoretical modeling.

The minority spin transmission vanishes around the Fermi energy due to the half-metallic band gap of the Heusler electrodes. Beyond this gap, the minority spin transmission is mostly much smaller than the majority spin transmission. Like the curves of the latter, those of the former exhibit a highly individual behavior, which points again to the influence of the interface.

Although all transmission through the barrier is due to tunneling, it is in general not concentrated around normal incidence ($\bar{\Gamma}$). The contour plots shown in Fig. 5.12(c) demonstrate that the structure of $T_\sigma(E, \vec{k}_\perp)$ within the 2D-BZ can be quite complex. Hence, it is *not* sufficient to restrict the 2D-BZ sampling to the area around the $\bar{\Gamma}$ point (or to use just the $\bar{\Gamma}$ point). Consequently, the results of Miura *et al.* [345] for the energy-resolved transmission $T_\sigma(E)$ are even qualitatively different.[13]

Calculation of the Seebeck coefficients

The Seebeck coefficients can be obtained by using the approach of Sivan and Imry [325] starting from the central quantity $T_\sigma(E)$ (cf. Sec. 2.4 on page 42) and the Fermi distribution function $f = f_{\mu=E_F,\,T}(E)$, where E_F denotes the Fermi energy of the MTJ cell.[14] Within Mott's two-current model, the spin-projected and temperature-dependent conductance is expressed as

[11] The transmission has been obtained by considering an artificial system in which both the electrodes and the scattering region consist simply of bulk Co_2MnSi. It is an upper limit for the transmission through the MTJ cell. The same has been done to obtain the bulk transmission panel shown in Fig. 5.10(b).

[12] This statement does *not* refer (directly) to the interface states, since they do *not* contribute to the transmission in this context.

[13] The results of Miura *et al.* [345] for $T_\sigma(E, \vec{k}_\perp = \bar{\Gamma})$ agree with those obtained by the author for testing purposes (not shown here).

[14] The reader will certainly not confuse the transmission $T(E)$ with the temperature T.

Dieses Werk ist copyrightgeschützt und darf in keiner Form vervielfältigt werden noch an Dritte weitergegeben werden.
Es gilt nur für den persönlichen Gebrauch.

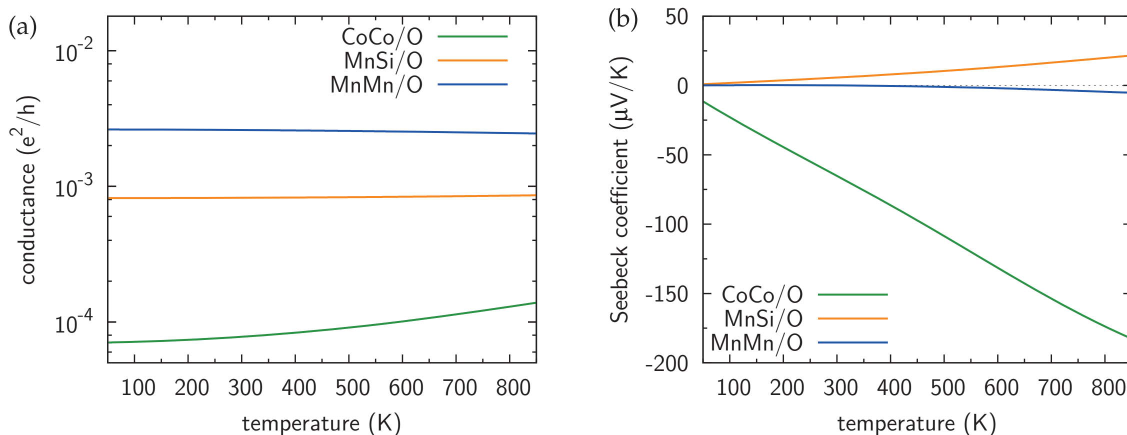

Figure 5.13 – Conductance $G_\uparrow(T) \approx G(T)$ (a) and Seebeck coefficient $S_{\text{eff}}(T) \approx S_\uparrow(T) \approx S_{\text{spin}}(T)$ (b) for $Co_2MnSi/MgO(001)/Co_2MnSi$ MTJs with 5 layers of MgO.

$$G_\sigma(T) = -\frac{e^2}{h} \int \mathrm{d}E \, \frac{\partial f}{\partial E} \, T_\sigma(E). \tag{5.1}$$

Note the equivalence of $G_\sigma(T)$ to the expression given in Sec. 2.4 for zero temperature, since $-\partial f/\partial E \to \delta(E - E_{\text{F}})$ for $T \to 0$. The spin-projected Seebeck coefficients then take on the form

$$S_\sigma(T) = -\frac{1}{eT} \frac{\int \mathrm{d}E \, \frac{\partial f}{\partial E} \, (E - E_{\text{F}}) \, T_\sigma(E)}{\int \mathrm{d}E \, \frac{\partial f}{\partial E} \, T_\sigma(E)}. \tag{5.2}$$

They are not additive ($S_\uparrow + S_\downarrow \neq S$) due to the different denominators and do not have a strict physical meaning. However, with these quantities the effective ("charge") and the spin-dependent Seebeck coefficient can be expressed as

$$S_{\text{eff}} = \frac{G_\uparrow S_\uparrow + G_\downarrow S_\downarrow}{G_\uparrow + G_\downarrow} \quad \text{and} \quad S_{\text{spin}} = \frac{G_\uparrow S_\uparrow - G_\downarrow S_\downarrow}{G_\uparrow + G_\downarrow}. \tag{5.3}$$

Thus, the two spin channels are treated as parallel connected resistors here. The spin-dependent Seebeck coefficient is a measure for the thermally induced spin accumulation. The precise meaning of the temperature T used in these equations will become transparent later, since actually there should be *two* temperatures, T_{L} and T_{R}, corresponding to the left and the right lead, respectively.

Results for the epitaxial $Co_2MnSi/MgO(001)/Co_2MnSi$ MTJs are shown in Fig. 5.13. For the temperature range considered here there are no relevant contributions to G from the minority spin channel ($G_\downarrow/G_\uparrow < 2.5 \cdot 10^{-4}$) due to the half-metallic band gap in the electrodes. Thus, $S_{\text{eff}} \approx S_\uparrow \approx S_{\text{spin}}$, which means that the entire voltage generated under a temperature gradient is converted into a spin accumulation. The conductance is largest for the MnMn/O interface and smallest for the CoCo/O interface, as one could have expected from Figs. 5.10 and 5.12(b). In contrast, the CoCo/O interface leads to the largest Seebeck coefficient (in absolute value), while it is smallest for the MnMn/O interface.

These results, especially the latter one, can be anticipated from the transmission curves shown in Fig. 5.12(b). Equation (5.2) makes it clear that the Seebeck coefficient strongly

Dieses Werk ist copyrightgeschützt und darf in keiner Form vervielfältigt werden noch an Dritte weitergegeben werden.
Es gilt nur für den persönlichen Gebrauch.

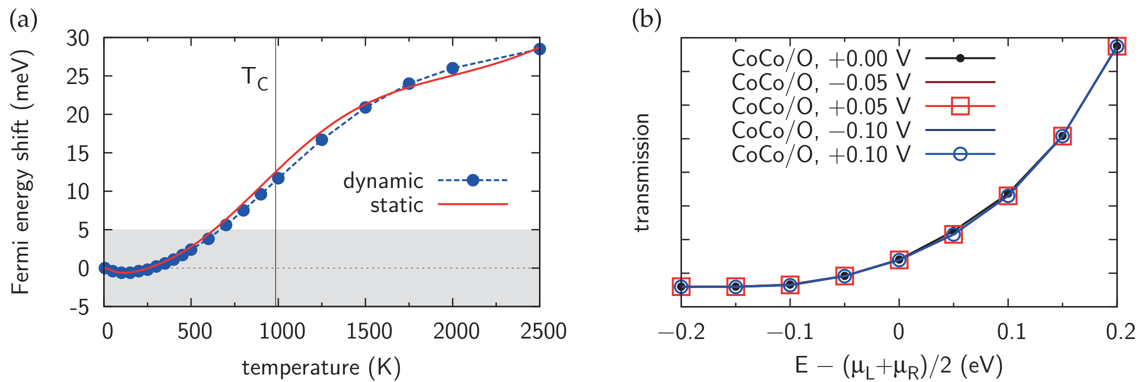

Figure 5.14 – (a) Variation of the chemical potential (Fermi energy) with the temperature in bulk Co_2MnSi. It can be calculated from the $T = 0$ rigid band structure ("static") or with different Fermi-Dirac smearing during the SCF runs ("dynamic"). (b) Finite-bias influence of small voltages V on the transmission $T(E,V)$ through a $Co_2MnSi/MgO(001)/Co_2MnSi$ MTJ with CoCo/O interfaces and 5 layers of MgO. One can see that effects of finite bias voltages are negligible here.

depends on the asymmetry of the transmission $T_\sigma(E)$ around the Fermi energy E_F. If, for instance, the Fermi energy lies in a band gap, the Seebeck coefficient can be tailored by shifting the Fermi energy towards one of the band edges. This can be done by doping or adequate selection of the electrode materials. Another (equivalent) route is a shifting of the entire band gap (VBM and CBM) around the Fermi energy, which can be done, for instance, by using different Heusler spacer layers between a fixed electrode material, or by exploiting the band structure modifications induced by the epitaxial strain [18, 19].

The disadvantage of the Seebeck coefficient is that it is a very sensitive quantity. One issue is the temperature dependence of the chemical potentials in the leads, which is shown in Fig. 5.14(a) for bulk Co_2MnSi. It can be calculated either from a fixed zero-temperature band structure, or by using a Fermi-Dirac smearing with different temperatures during the SCF runs. Both methods lead to quite similar results for Co_2MnSi, which means that the response of the electronic system to the temperature-increased smearing is small. For the temperatures of interest here, the shift of the chemical potential is smaller than ± 5 meV. Thus, one can neglect the influence of temperature-dependent Fermi energies. It should be noted that, in general, crossing the boundary of ± 5 meV, although it appears to be small, can already lead to significantly distorted results. We will come back to the aspect of temperature-dependent Fermi energies below in the context of a more flexible theory than the Sivan-Imry approach.

An alternative route to spincaloric properties

The approach used so far is currently the standard route to calculating thermoelectric properties of systems on the atomic scale. It has been used recently by the author to investigate $Al/Co_2TiSi/Al$ and $Al/Co_2TiGe/Al$ heterostructures [18]. However, Eq. (5.2) is only approximatively valid and works best for *small* thermal gradients between the two contacts. It is, though, possible to arrive at thermoelectric properties by using a more exact way and *without* calculating a Seebeck coefficient at all. This is presented in the following.

In the end one is interested in a current I or a voltage $V = (\mu_L - \mu_R)/e$ arising as a response of the MTJ to an applied thermal gradient or, more precisely, to the two applied temperatures $T_{L/R}$ in the left and the right electrode. If the circuit is closed, a thermally driven

Dieses Werk ist copyrightgeschützt und darf in keiner Form vervielfältigt werden noch an Dritte weitergegeben werden.
Es gilt nur für den persönlichen Gebrauch.

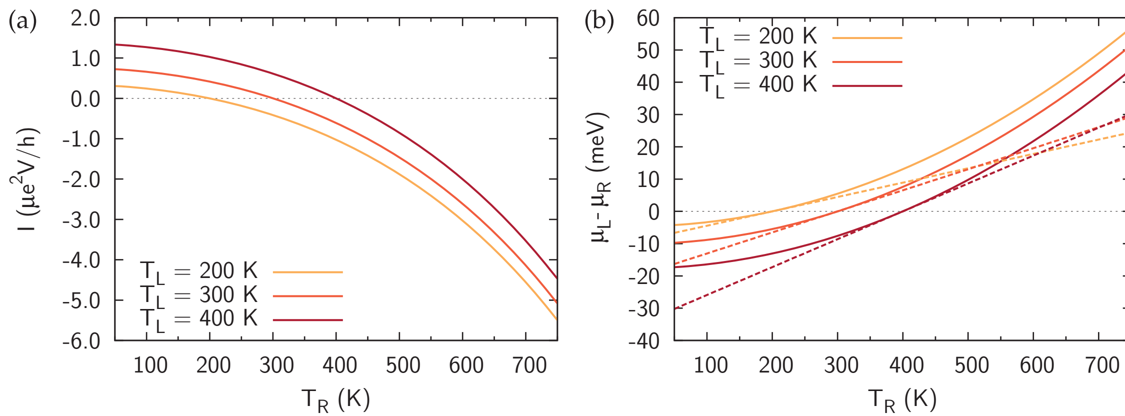

Figure 5.15 – (a) Thermally driven current $I(T_\mathrm{L}, T_\mathrm{R})$ as calculated from Eq. (5.4) for $Co_2MnSi/MgO(001)/Co_2MnSi$ MTJs with CoCo/O interfaces and 5 layers of MgO. (b) Comparison of $\mu_\mathrm{L} - \mu_\mathrm{R} = eV(T_\mathrm{L}, T_\mathrm{R})$ (solid lines) as determined from solving Eq. (5.5) and corresponding voltages calculated from $S_\mathrm{eff}(T_\mathrm{L})$ (dashed lines) for the same system as used in (a).

current I will flow, which can be calculated directly from the Landauer-Büttiker formula, Eq. (2.20):

$$I(T_\mathrm{L}, T_\mathrm{R}) = \frac{e}{h} \int \mathrm{d}E \, [f_{T_\mathrm{L}}(E) - f_{T_\mathrm{R}}(E)] \, T(E). \tag{5.4}$$

Since no counteracting electric field can build up ($V = 0$), it follows that $\mu_\mathrm{L} = \mu_\mathrm{R} = E_\mathrm{F}$; thus, the chemical potentials have been omitted in the formula. As an example, the current calculated for our Co_2MnSi-based MTJs with CoCo/O interfaces and 5 layers of MgO can be seen in Fig. 5.15(a).

If we consider, on the other hand, an open circuit without a current, $I = 0$, the charge flow induced by the thermal gradient has to be compensated by an electric field which is proportional to V. By using the Landauer-Büttiker formula once more, we can now write:

$$0 \stackrel{!}{=} \frac{e}{h} \int \mathrm{d}E \, \left[f_{\mu_\mathrm{L}, T_\mathrm{L}}(E) - f_{\mu_\mathrm{R}, T_\mathrm{R}}(E)\right] T(E). \tag{5.5}$$

The goal is to find a pair $(\mu_\mathrm{L}, \mu_\mathrm{R})$ that solves this integral equation, which parametrically depends on the temperatures T_L and T_R. Since the voltage drop across the device will be symmetric, the following assumption is reasonable:

$$(\mu_\mathrm{L} + \mu_\mathrm{R})/2 = E_\mathrm{F},$$

which can be used to eliminate one of the variable chemical potentials. The transmission $T(E)$ in Eq. (5.5) is not recalculated for appropriately shifted bands here (finite-bias effects). Therefore, even this approach is an approximation which works best for small voltages V. Luckily, thermally induced voltages are usually small enough, especially in the present temperature range. It is shown explicitly in Fig. 5.14(b) that finite-bias effects are indeed negligible here.[15] An improved version of Eq. (5.5) would read:

$$0 \stackrel{!}{=} \frac{e}{h} \int \mathrm{d}E \, \left[f_{\mu_\mathrm{L}, T_\mathrm{L}}(E) - f_{\mu_\mathrm{R}, T_\mathrm{R}}(E)\right] T(E, \frac{\mu_\mathrm{L} - \mu_\mathrm{R}}{e}),$$

[15] The shown transmissions $T(E, V)$ have been calculated for several bias voltages V from symmetrically shifted bands in the leads around the common Fermi energy for $V = 0$. Due to the symmetric setup of the MTJ cell, the sign of the bias voltage has no influence.

Dieses Werk ist copyrightgeschützt und darf in keiner Form vervielfältigt werden noch an Dritte weitergegeben werden.
Es gilt nur für den persönlichen Gebrauch.

but is computationally even more demanding than the aforementioned approach, since $T(E,V)$ has to be calculated for several bias voltages V.[16] Especially in conjunction with thermally induced transport, which requires larger energy integration intervals than field-driven transport, this can be tedious.

If the differences between $T(E)$ and $T(E,V)$ are not negligible, finite-bias effects can be included in the present approach by calculating $T(E,V)$ for some discrete values of V [as shown in Fig. 5.14(b)] and using an interpolation in between. Moreover, the thermal variation of the chemical potentials in the leads can be readily included [cf. Fig. 5.14(a)]. Both aspects are, however, of minor importance for the system under consideration here (as mentioned above) and therefore postponed to future work.

The solutions of Eq. (5.5) can be found, for instance, by using numerical integration and the bisection method starting from $\mu_L = \mu_R = E_F$. This provides the voltage response $V(T_L, T_R)$ of the MTJ as shown exemplarily in Fig. 5.15(b). On the other hand, the Sivan-Imry Seebeck coefficient $S_{\text{eff}}(T)$ defined in Eq. (5.3) can be understood as first-order Taylor expansion coefficient of this voltage,

$$eV(T_L, T_R) = S_{\text{eff}}(T_L) \cdot (T_L - T_R) + \mathcal{O}(T_R^2).$$

This becomes obvious from Fig. 5.15(b), where the dashed lines approximate the "real" voltage curves around $T_R = T_L$. One can see that the Sivan-Imry approach provides quite good results for small thermal gradients. Nevertheless, any deviation of the voltage from a linear dependence is beyond the reach of the Sivan-Imry approach.

Both current I and voltage V are given in Fig. 5.16 for several possible combinations of T_L and T_R. Due to the symmetric setup of the MTJ cell, all panels are antisymmetric with respect to the dashed diagonal line ($T_L = T_R$). The thermally induced voltages do not exceed 80 mV, which justifies the approach [Eq. (5.5)] *a posteriori*. There is no simple linear dependence between I and V, although one could get this impression from Fig. 5.16. The sign of I and V is reversed for MnSi/O with respect to CoCo/O and MnMn/O, which is consistent with the conventionally determined Seebeck coefficients shown in Fig. 5.13(b), as is the sign flip that can be observed in current and voltage for the MnMn/O interface.

Thermally operated MRAM modules

Let us close with a practical example: If the two electrodes are operated around room temperature at 290 and 310 K, respectively, the voltages generated by a single MTJ will be 1.30 mV, -0.11 mV, and -1.48 μV for CoCo/O, MnSi/O, and MnMn/O interfaces, respectively. Consequently, the magnitude and the sign of the thermally induced voltage can be tailored by exploiting the fact that the MTJ interface formation can be controlled by adjusting the growth conditions [321]. Since especially the CoCo/O voltage can be measured without problems, $Co_2MnSi/MgO(001)/Co_2MnSi$ MTJs, grown under Co-rich conditions, can be used in future "thermo-MRAM" modules (cf. Fig. 5.17), where the stored information is read out without a flowing charge current. This is different in conventional MRAM modules [6]. The application of a thermal gradient is only necessary for the readout process; the stored information is not lost if $T_L = T_R$. Moreover, it can be exploited that the current (and thus the possible power) scales with the area of the MTJ, whereas the voltage can be increased by a serial arrangement of MTJs.

[16] In Ref. [347], for instance, which addresses *field-driven* transport through Fe/MgO/Fe MTJs, $T(E,V)$ was calculated for several bias voltages V from symmetrically shifted bands.

Dieses Werk ist copyrightgeschützt und darf in keiner Form vervielfältigt werden noch an Dritte weitergegeben werden.
Es gilt nur für den persönlichen Gebrauch.

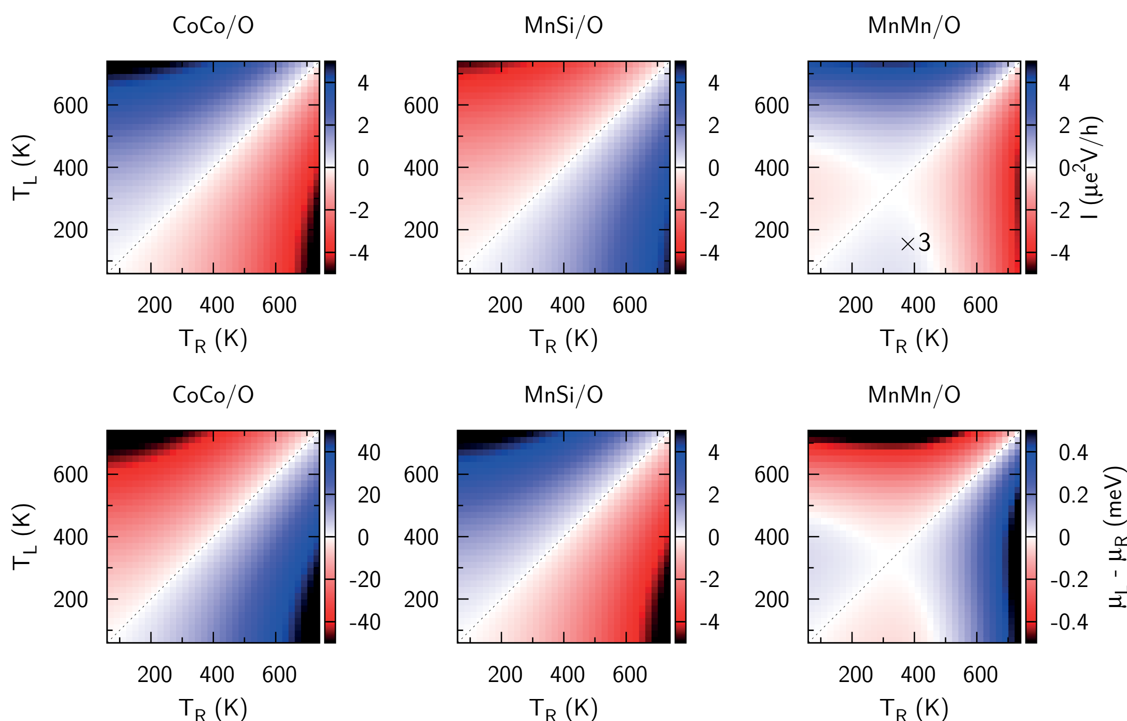

Figure 5.16 – Thermally driven closed-circuit current $I(T_L, T_R)$ as calculated from Eq. (5.4) (upper row) and open-circuit voltages $\mu_L - \mu_R = eV(T_L, T_R)$ as determined from solving Eq. (5.5) (lower row) for $Co_2MnSi/MgO(001)/Co_2MnSi$ MTJs with different interfaces and 5 layers of MgO.

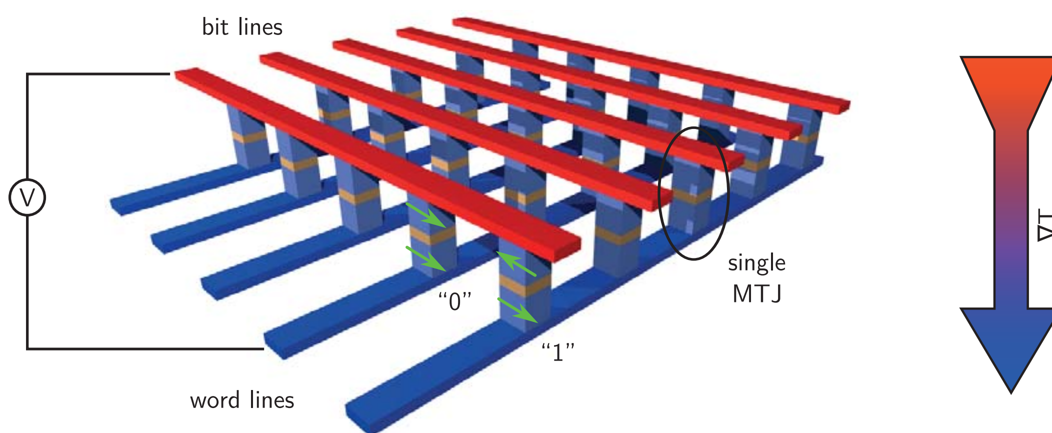

Figure 5.17 – Schematic illustration of a suggested thermo-MRAM module in the cross-point architecture based on the magneto-Seebeck effect. The thermal gradient between the bit lines and the word lines generates a voltage between them that can be used to detect the state (parallel/antiparallel electrode magnetization) of a selected MTJ and thus the information stored in it. Writing units and transistors are not shown here.

Dieses Werk ist copyrightgeschützt und darf in keiner Form vervielfältigt werden noch an Dritte weitergegeben werden.
Es gilt nur für den persönlichen Gebrauch.

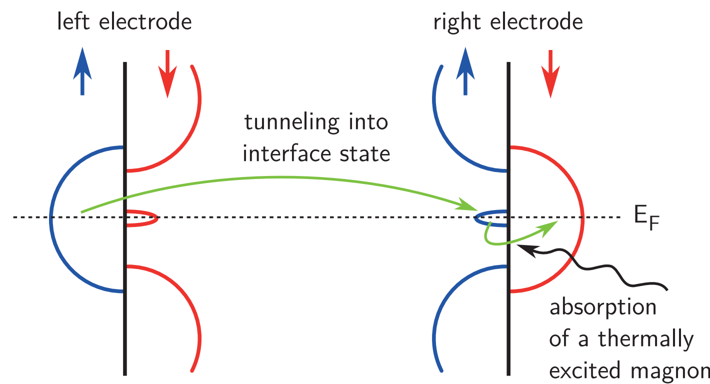

Figure 5.18 – Schematic illustration of magnon-assisted tunneling through a MTJ.

5.4.3 Antiparallel electrode magnetization: Interface magnons

One of the central motivations to use half-metallic Co_2MnSi Heusler electrodes for MTJs lies in the idea that they should completely block any current in the case of antiparallel electrode magnetization and thus lead to an infinite TMR ratio. As already mentioned in the introduction, one can indeed achieve high TMR ratios in low-temperature experiments, but not at room temperature. This means that a tunneling current flows even if the electrodes are magnetized antiparallel, and the underlying process has to be thermally activated.

A possible explanation for this parasitic current is based on inelastic tunneling processes involving interface states [320] and magnons as illustrated in Fig. 5.18. An electron can tunnel (without spin flip) from the majority spin reservoir of the left electrode to a minority spin interface state in the antiparallel-magnetized right electrode. Usually, this state would be blocked afterwards: Due to the missing bulk states in the right electrode, the electron cannot leave the interface state in this direction. Hence, no further current can flow. If, however, the electron flips its spin due to absorption of a (e.g., thermally excited) magnon, it can leave the interface region. Energy and momentum of the magnon are transferred to the electron, which makes the process inelastic. Subsequently, the interface state is unoccupied again, and another electron can tunnel into it from the left lead.

One can now argue against this model for the parasitic current that the Curie temperature of Co_2MnSi is far above room temperature, which means that only very few bulk magnons are thermally excited at room temperature. If, on the other hand, the exchange coupling is weaker near the interface to MgO, the excitation of interface magnons becomes easier and thus more probable.

In order to analyze the influence of the interface on magnetic excitations, the energies ΔE required to reverse the local spin moments ($\approx 3\,\mu_B$) of different sets of Mn atoms in a single (001) plane have been calculated in bulk Co_2MnSi and close to the Co_2MnSi/MgO(001) interface (cf. Fig. 5.19). Supercells with a large extension in [001] direction have been used to decouple the Mn planes that contain reversed moments; Fig. 5.19 shows only small parts of these cells. While the basic magnetic ordering in the whole supercell has been FM, the initial spin density within a selected (001) plane has been chosen according to different magnetization patterns in the Mn sublattice,

$$m_{\mathrm{Mn}}(\vec{r}) = m^0_{\mathrm{Mn}}\, \mathrm{sgn}\Big\{\cos(\vec{q}\,\vec{r})\Big\}, \tag{5.6}$$

Dieses Werk ist copyrightgeschützt und darf in keiner Form vervielfältigt werden noch an Dritte weitergegeben werden.
Es gilt nur für den persönlichen Gebrauch.

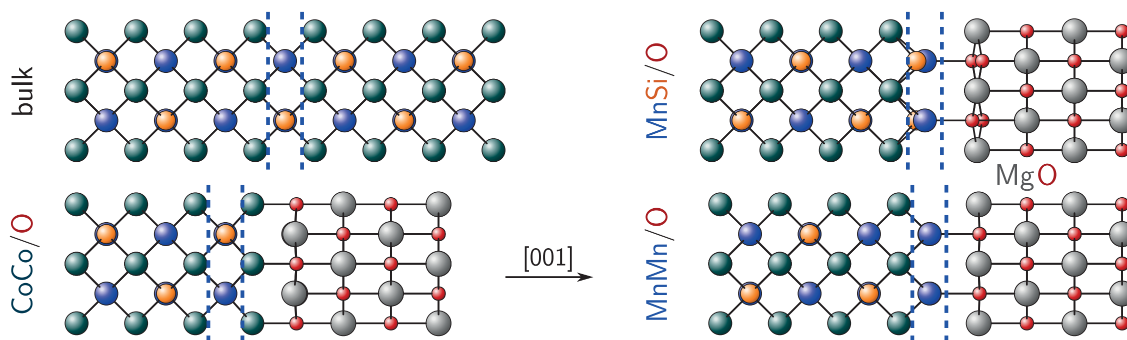

Figure 5.19 – Illustration of the Mn (001) sublattices in bulk Co_2MnSi and close to differently terminated epitaxial $Co_2MnSi/MgO(001)$ interfaces which have been used to study the effect of reversed local spin moments. For each case, different subsets of Mn moments have been reversed within the (001) layer enclosed by the vertical dashed blue lines.

where the position vector $\vec{r}$ points to different Mn sites and the wave vector $\vec{q}$ has been chosen to point either in [100] ($\bar{X}$) or in [110] ($\bar{M}$) direction. Subsequently, the DFT calculation has been converged to the metastable state that is compatible with the initial condition. The excitation energies are compared in Table 5.3, together with two figures indicating different magnetization patterns of the (001) Mn sublattice. Different magnitudes of $\vec{q}$ have been realized numerically by using supercells of different lateral extension and are given in Table 5.3 with respect to q_0, the largest possible wave vector magnitude (shortest wavelength) in the studied direction. Since this magnetic moment reversal is meant to provide insight into possible spin fluctuations that arise on a much shorter time scale than structural changes, further atomic relaxation beyond the aforementioned optimized interface structures has been suppressed.[17]

It becomes obvious from Table 5.3 that the presence of the interface strongly lowers the magnetic excitation energies by more than a factor of 2. In the case of the MnSi/O (or MnMn/O) interface this appears to be easily understandable, since the Co "cage" around the Mn atoms is halved and thus the stabilizing Mn-Co interaction is reduced. Calculations of the exchange coupling constants J_{ij} with the DFT-KKR technique and Liechtenstein's formalism [348,349] show that the Mn-Co coupling is dominant and of FM nature in Co_2MnSi [19]. On the other hand, a quantitatively similar reduction is observed even if the Mn atoms *are* still surrounded by Co atoms (CoCo/O interface). Unfortunately, the SCF cycles of many configurations did not converge here (marked by a dash), but the available two values provide a clear picture. In the case of the nonstoichiometric MnMn/O interface the magnetic excitation energies are even smaller than for the CoCo/O or the MnSi/O interface. Moreover, a local spin moment modulation with an even shorter wavelength can be realized for this interface termination. Reversing one of the two Mn local spin moments at the interface leads to an increase of the total energy by only 49 meV/Mn (crystallographically "correct" Mn reversed) or 53 meV/Mn (substituted Mn_{Si} reversed).

[17]Note that a spin fluctuation in the FM phase is usually only a small variation of the local moments or their direction, not an entire reversal of local moments. Nevertheless, the author makes the reasonable assumption that the following conclusions will also hold for small variations. This is based on the idea of an idealized $\Delta E \sim \alpha\{1-\cos(\vartheta)\}$ behavior, where ϑ is the angle of a certain local moment with respect to the sample magnetization and 2α is the energy associated with a fully reversed local moment.

Dieses Werk ist copyrightgeschützt und darf in keiner Form vervielfältigt werden noch an Dritte weitergegeben werden.
Es gilt nur für den persönlichen Gebrauch.

Table 5.3 – Comparison of magnetic excitation (local spin moment reversal) energies ΔE (meV) in a two-dimensional Mn sublattice of a bulk $Co_2MnSi(001)$ plane and close to differently terminated epitaxial $Co_2MnSi/MgO(001)$ interfaces (cf. Fig. 5.19 for side views of the different structures). The energies are given per Mn atom in the sublattice. The two directions of $\vec{q}$ refer to fcc bulk Co_2MnSi, as indicated in the figures. Note that a direct comparison of the MnMn/O interface results with the bulk MnSi layer results is strictly not valid; nevertheless, the values are given for completeness.

q/q_0	Bulk	CoCo/O	MnSi/O	MnMn/O
$\vec{q} \sim \bar{M}$				
1/4	467	–	179	–
1/2	473	–	190	–
1/1	464	223	213	149
$\vec{q} \sim \bar{X}$				
1/2	482	–	205	188
1/1	496	209	242	171

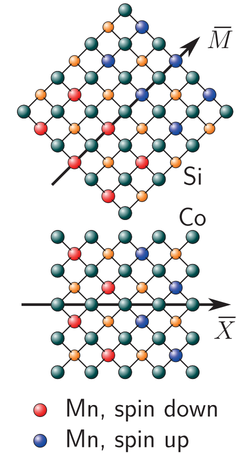

If the energy required for a local spin moment reversal is halved, as it has been found in the present calculations, the excitation probability for corresponding magnons increases drastically. This is especially the case for the mentioned short-wavelength magnons near a half-metallic MnMn/O interface. As a consequence, the thermal excitation of *interface* magnons is much more probable than the thermal excitation of *bulk* magnons. The latter can be considered to be rare at room temperature due to the high Curie temperature of Co_2MnSi. Thus, the process outlined above, in which the interface states are rapidly depleted due to magnon-induced spin-flip processes, is reasonable and among the most probable explanations for the experimentally observed temperature-dependent reduction of the TMR ratio of epitaxial $Co_2MnSi/MgO(001)/Co_2MnSi$ MTJs.

The preceding discussion, although being mostly qualitative so far, already contains the most important fundamental statement. More quantitative investigations are beyond the scope of this thesis. Future work could comprise the calculation of exchange coupling constants at differently terminated interfaces, simulations of thermal spin fluctuations near the interface, and possibly the setup and evaluation of an inelastic transport model according to Fig. 5.18, which should also take into account the transferred momentum of the interface magnons.

Dieses Werk ist copyrightgeschützt und darf in keiner Form vervielfältigt werden noch an Dritte weitergegeben werden.
Es gilt nur für den persönlichen Gebrauch.

Dieses Werk ist copyrightgeschützt und darf in keiner Form vervielfältigt werden noch an Dritte weitergegeben werden.
Es gilt nur für den persönlichen Gebrauch.

Chapter 6

Summary and Outlook

The preceding three chapters addressed three different major topics from the fields of semiconductor and metal-based spintronics, each time combining transition metals (TMs) and Si in different ways: (i) the growth of ferromagnetic (FM) 3*d* TM silicide layers on the semiconductor Si, which could serve as spin injectors, (ii) the doping of Si with 3*d* TM impurities and the detection of their interaction properties with spin-polarized (SP) STM, and (iii) magnetic tunnel junctions (MTJs) with half-metallic electrodes made from TM-Si Heusler alloys and their spincaloric properties. Eventually, the aim was to provide an understanding of magnetism on the atomic scale in these materials systems in order to exploit them in future spintronics devices. To this end, other aspects had to be considered as well: On the one hand, the magnetic behavior of a material is usually closely related to its structural properties, which can depend on the growth protocol. On the other hand, different magnetic states can lead to different transport and spincaloric properties. In the following, the contents of this thesis are recapitulated and its central statements are summarized.

Chapter 3 treated several topics concerning different 3*d* TM silicides as bulk material and as film structure of different thickness grown epitaxially on the Si(111) surface. After a collection of information about Si and the Si(111) surface, fundamental properties of bulk 3*d* TM monosilicides, which largely crystallize in the B20 structure, were presented. Simulations of the Heisenberg model on the TM trillium sublattice of the B20 structure showed significant differences to the equally coordinated simple cubic lattice. Analysis of the electronic structure revealed the universality of the band gap in B20 3*d* TM monosilicides and its interdependence with the sevenfold coordination. Detailed investigations of the orbital structure in FeSi showed that this band gap actually separates two opposing groups of bands with different predominant Fe 3*d* orbital character. MnSi and FeSi were also studied in the rock-salt and zinc-blende crystal structures, which are closely related to the B20 crystal structure.

Calculations for bulk 3*d* TM silicides under biaxial strain provided materials properties in the limit of thick (e.g., several hundred monolayers) epitaxial films on Si(111). For MnSi, a strain-induced volume expansion and an increase of the magnetic moments and of the Curie temperature were found. This unusual behavior points to the insufficiency of a Heisenberg-type description and underlines the importance of itinerant exchange for the magnetic ordering in MnSi. Moreover, a phonon softening due to biaxial strain was observed in MnSi. FeSi, on the other hand, makes a surprising transition from a nonmagnetic semiconductor to an almost half-metallic ferromagnet if matched epitaxially to Si(111). These interesting theo-

Dieses Werk ist copyrightgeschützt und darf in keiner Form vervielfältigt werden noch an Dritte weitergegeben werden.
Es gilt nur für den persönlichen Gebrauch.

retical findings call for more detailed, carefully performed experimental investigations of the FeSi/Si(111) system. Later in the chapter it was explicitly demonstrated for MnSi/Si(111) heterostructures that the magnetic behavior of thin (e.g., just a few monolayers) 3*d* TM silicide films differs significantly from that of thicker films due to quantum confinement and/or interface/surface effects.

The next part of the chapter analyzed the growth mode, the atomic, and the magnetic structure of MnSi/Si(111) in more detail. First of all it was shown that MnSi(111) surfaces prefer to be terminated by a Si-dense layer. Subsequently, interface properties of MnSi/Si(111) and FeSi/Si(111) were presented. Besides, it was noted that Si/MnSi/Si structures are more useful in a spin-filtering context than Si/FeSi/Si structures due to the presumably higher Curie temperature and the FM interface magnetic structure of the former. Afterwards, the atomic structure behind the $\sqrt{3} \times \sqrt{3}$ and 3×3 surface patterns recently observed by atomic-resolution STM imaging of MnSi/Si(111) heterostructures was revealed in close cooperation between experiment and theory. In the $\sqrt{3} \times \sqrt{3}$ case, the coexistence of areas with high and low corrugation in the STM images was exploited to draw conclusions about the internal layer stacking sequence of the films, which is challenging for surface methods like STM. Thus, a subtle analysis of the subsurface layers and their effect on the experimental data was required, and deviations from the MnSi bulk stoichiometry due to enrichment or depletion of one of the elements near the surface had to be accounted for. Performing this detailed analysis for experimental data of films grown by reactive epitaxy (solid-phase epitaxy) and by codeposition of Mn and Si provided evidence that the internal stacking depends on the growth protocol. Since the magnetic properties of MnSi films are closely related to their atomic structure, the occurrence of two possible stacking sequences implies that strict control of the growth conditions is required to reproducibly fabricate MnSi films with specified properties. A similar approach was applied to the case of the 3×3 surface pattern of MnSi/Si(111), and an atomic structure model that exhibits a real reconstruction was suggested in this case. Additionally, the validity of *ab initio* thermodynamics in the case of MnSi thin film growth was assessed, concluding that it can indeed serve as a guideline, even though the structures are metastable.

The *ab initio* results for MnSi/Si(111) agree qualitatively with recent experimental data, and also the structural properties of epitaxially strained FeSi are correctly described. Thus, DFT-GGA is capable of providing a qualitatively correct description of these materials. Aiming for a better *quantitative* agreement (e.g., concerning the size of the magnetic moments), the influence of on-site electronic correlation in a DFT+U formalism was investigated. It was concluded that this methodology yields no improvements of the ground state properties, even though DFT+U provides a possible interpretation of the high experimental magnetic moments derived from paramagnetic susceptibility fits. LDA+DMFT calculations for MnSi could be illuminating and remain as future project.

The chapter closed with the discussion of Mn_5Si_3. After a presentation of surface and interface properties of Mn_5Si_3/Si(111) heterostructures and corresponding simulated STM images, it was demonstrated that STM can discriminate between MnSi and Mn_5Si_3 film growth on the basis of symmetry arguments, and that the competing formation of Mn_5Si_3 can be excluded in the present experiments. It was also found that the surface termination made by a pure Mn layer, which is the usual assignment in the literature based on STM experiments, is highly unstable for both Mn_5Si_3/Si(111) and Mn_5Ge_3/Ge(111). This conflict has to be resolved in future work.

Dieses Werk ist copyrightgeschützt und darf in keiner Form vervielfältigt werden noch an Dritte weitergegeben werden.
Es gilt nur für den persönlichen Gebrauch.

Chapter 4 presented a new strategy, founded on an *ab initio* theoretical basis, to study experimentally the *bulklike* impurity-host interactions (which are responsible for the formation of local magnetic moments) and the impurity-impurity interactions (which cause the emergence of collective order between these moments) of magnetic impurities in semiconductors and insulators on the atomic scale by using *surface* methods like (SP) STM. This strategy will hopefully provide new insights in the field of dilute magnetic semiconductors (DMS), since understanding the interactions in a DMS on a fundamental, atomic level (instead of the common trial-and-error approach) is a prerequisite for rational materials design.

The proof of principle was given by large-scale computer simulations for the specific case of 3*d* TM impurities in Si, but the suggested approach is generalizable to other DMS systems like Co-doped ZnO. It basically relies on the passivation of host surfaces. Consequently, the chapter opened with a discussion of H-passivated Si(111) and GaAs(110) surfaces. It was shown that the topmost H layer removes the surface states near the Fermi energy by passivating the Si dangling bonds. On the basis of DFT total energies it was argued that the application of a H layer from the gas phase is possible and advantageous. Simulated STM images were shown for a structural assignment. Close agreement with the literature supported the employed theoretical methods.

Subsequently, different structural, electronic, and magnetic properties of interstitial and substitutional Cr, Mn, and Fe impurities in bulk Si were presented, and their electronic structure was explained with the Ludwig-Woodbury model and hybridization diagrams. Exemplarily, the spatial influence of Fe impurities in bulk Si was visualized; the deduced wave function extension was found to be much smaller than for Mn in GaAs, thus obstructing ferromagnetism in Si. Formation energies for isolated impurities in their magnetic ground state and in different excited states were shown. The calculations were found to be prone to several numerical pitfalls. By comparing PBE, PBE+U, and hybrid functional (HSE06) results, the reliability of semilocal exchange-correlation functionals was assessed, which is essential for the whole field of first-principles studies of TM-doped Si. It was shown that PBE and HSE06 lead to qualitatively very similar electronic and magnetic structures, which validates the PBE approach and also results obtained in the past *a posteriori*. The spin state of the substitutional Fe impurity was found to be an exception.

In the next section, the mentioned strategy to detect bulklike properties of impurities with surface experiments was demonstrated. To this end, it was shown that the electronic structure of different impurities is preserved below the H-passivated Si(111) surface, whereas an unpassivated surface strongly biases its electronic and magnetic properties. Afterwards, (SP) STM simulations were presented, which demonstrated how the extension of the impurity wave function and the anisotropic spin polarization induced in the host electronic structure can be imaged with (SP) STM. It was found that the magnetic contrast is related to the impurity magnetic moment and sufficiently large to be resolvable in a SP STM experiment. This is especially the case for substitutional Fe, and since SP STM in the proposed setup allows for detection of the impurity site and the magnetic moment *at the same time*, a strategy could be devised to decide about the issue of the substitutional Fe spin state. The answer to this open question is an important benchmark for the applicability of hybrid functionals in DMS simulations, which calls for carefully performed experiments realizing the aforementioned strategy. Finally it was shown that even the impurity-impurity interactions are quantitatively preserved below the passivated surface, which proves that the exchange

Dieses Werk ist copyrightgeschützt und darf in keiner Form vervielfältigt werden noch an Dritte weitergegeben werden.
Es gilt nur für den persönlichen Gebrauch.

coupling constants of impurities in the *bulk* material can be obtained from *surface* experiments.

After kinetic considerations concerning the injection and migration of subsurface 3d TM impurities, the formation of two-dimensional impurity δ layers was addressed. In order to keep these objects accessible to SP STM simulations, they were studied below the H/Si(111) surface. The most notable result here was that (111) δ layers of interstitial Cr in Si exhibit a strong FM interaction and are half-metallic. This surprising behavior was traced back to the position and filling of Cr minority spin t_2 states, which are located in the fundamental band gap of Si and close to the conduction band. More generally, the obtained results suggest that Cr-doped Si, which has received little attention in the literature so far, seems to be an interesting candidate material for a DMS. It is therefore recommended here for intense future investigations. In particular, the interaction of Cr impurities with common dopants like Al and P is of importance.

Besides, it was found that very dense, continuous δ layers of 3d TM impurities [i.e., one TM impurity per Si(111)-(1×1) surface unit cell] destabilize the Si matrix and lead to the formation of nonmagnetic silicide layers. One strategy to circumvent this issue is based on using two-dimensional clusters (i.e., discontinuous layers). As an example, differently shaped and sized clusters of interstitial Fe impurities were discussed. In contrast to the Fe δ layers, FM order was found within the clusters, and a stronger exchange coupling that reduces the internal spin fluctuations. The Fe impurities exhibit an attractive interaction on short length scales, making clustering advantageous. A FM semiconductor can be constructed if the total magnetic moments of neighboring clusters align parallel.

The last part of the chapter was devoted to the experimentally motivated question whether or not it is possible to generate subsurface Fe impurities by deposition of organic molecules (e.g., iron phthalocyanine, FePc) on the H/Si(111) surface. It was concluded that the implantation is possible, but the necessary steps in the reaction are quite improbable due to the high binding energy of Fe in FePc. Gas phase calculations of phthalocyanine molecules with different TM centers employing different exchange-correlation functionals underlined that the high binding energies are reasonable. It was shown that van-der-Waals corrections to semilocal DFT are very important for the correct description of the FePc adsorption on H/Si(111), which makes it an useful benchmark system in the field of modern electronic structure theory. Besides, silicon phthalocyanine was found to be an interesting example of d_0 magnetism in molecules, since its delocalized spin density can facilitate the magnetic interaction with a substrate or with neighboring molecules through a substrate, e.g., graphene.

Chapter 5 focused on electronic transport and spincaloric properties of epitaxial MTJs with half-metallic Co_2MnSi Heusler electrodes and MgO tunneling barriers. Possible applications are magnetoresistive random access memory (MRAM) or the suggested “thermo-MRAM” modules, in which the magneto-Seebeck effect is exploited to read out the magnetic state of a MTJ without an applied voltage (electric field) or a flowing charge current. Moreover, a Co_2MnSi/MgO/semiconductor setup with an applied voltage or temperature gradient can be used as spin injector and should lead to a very high spin polarization of the injected carriers while at the same time avoiding the conductivity mismatch problem.

For the case of parallel electrode magnetization, electronic transport, spincaloric properties, and the dependence of both on the interface atomic structure were analyzed. While almost no transmission occurs in the minority spin channel due to the half-metallicity of the Co_2MnSi electrodes, the majority spin transmission shows a strong dependence on the

Dieses Werk ist copyrightgeschützt und darf in keiner Form vervielfältigt werden noch an Dritte weitergegeben werden.
Es gilt nur für den persönlichen Gebrauch.

interface termination. It was attempted to capture this dependence by a simple model: Close to the Fermi energy, tunneling through a potential barrier, whose height is influenced by the interface termination, is indeed able to explain the observations. However, by inspecting the transmission over a larger energy interval and its structure within the two-dimensional Brillouin zone it was also demonstrated that the interface termination influences the transport properties far beyond such modeling.

A consequence of perfect half-metallicity is that the entire voltage generated under a temperature gradient is converted into a spin accumulation. The conductance was found to be largest (smallest) for the MnMn/O (CoCo/O) interface, whereas the absolute value of the Seebeck coefficient was found to be largest (smallest) for the CoCo/O (MnMn/O) interface. In addition, the interface termination influences the sign of the Seebeck coefficient. Hence, a targeted growth control of the MTJs can be used to tailor their spincaloric properties (e.g., magnitude and sign of the thermally induced voltage). Subsequently, a more general route to spincaloric properties than the Sivan-Imry approach was presented that circumvents the linear response approximation inherent in the Seebeck coefficient and directly provides the response of the system (current or voltage) to arbitrary thermal gradients. It was demonstrated that the conventional Seebeck coefficient can be understood as first-order Taylor expansion coefficient of the voltage response. Moreover, thermal variations of the chemical potential in the leads and finite-bias effects can be readily included in this method, but were found to be negligible for this specific MTJ.

Entirely different questions arise in the case of antiparallel electrode magnetization. While this configuration should ideally block any electronic transport, a parasitic current flows in room-temperature experiments that reduces the tunnel magnetoresistance ratio. It was shown by using a statistical approach to the electron-phonon interaction involving randomly distorted structures that the excitation of phonons has no relevant effect on the electronic structure of Co_2MnSi at room temperature and therefore cannot account for the strong decrease of the tunnel magnetoresistance ratio. On the other hand, it was argued that inelastic tunneling involving thermally activated interface magnons is among the most probable explanations for the observed behavior. First-principles calculations revealed that interface magnons are much more easy to excite than bulk magnons. Future work on this subject could comprise a more detailed investigation of lattice vibrations at the interfaces, the influence of structural distortions on the magnetic coupling, and the application of a band structure unfolding scheme to the randomly distorted supercells on the one hand, and the calculation of exchange coupling constants at differently terminated interfaces, simulations of thermal spin fluctuations near the interface, and possibly the setup and evaluation of an inelastic transport model on the other hand.

Dieses Werk ist copyrightgeschützt und darf in keiner Form vervielfältigt werden noch an Dritte weitergegeben werden.
Es gilt nur für den persönlichen Gebrauch.

Selected results

Some of the results that have been presented in this thesis stand out due to their fundamental nature, widespread applicability in modern research, or creative use of the numerical methodology beyond standard procedures.

Chapter 3: Despite the complex crystal structure of epitaxial TM monosilicide thin films on Si(111), a careful surface/subsurface analysis (exploiting two different coexisting surface terminations) and a thorough combinatorial matching of simulated and experimental STM images made it possible to draw conclusions about the internal layer stacking sequence (which is challenging for surface methods such as STM) and its dependence on the growth conditions (which is important in order to reproducibly fabricate films with desired magnetic properties). Semilocal exchange-correlation functionals were found to provide a qualitatively correct description for TM silicides in B20 structure, which are known to exhibit nontrivial electronic correlations.

Chapter 4: A new method to investigate different *bulklike* magnetic interactions in any DMS system (e.g., TM-doped Si, Mn-doped GaAs, Co-doped ZnO) with *surface* methods like (SP) STM on the atomic scale was presented and proven by large-scale first-principles simulations. It can image the extension of wave functions, the anisotropy of the induced spin polarization in the host material, and the exchange coupling between neighboring impurities. The issue of high-spin vs. low-spin ground state of substitutional Fe impurities in Si can be answered by experiments implementing this method and could become a benchmark for the applicability of hybrid functionals in the field of DMS. The technique can also be applied to two-dimensional structures like clusters or δ layers. Of particular interest are (111) δ layers formed by interstitial Cr impurities in Si, which were found to exhibit a strong FM interaction and to be half-metallic. It was possible to plausibly suggest Cr-doped Si as novel DMS. Moreover, it was shown by comparison with hybrid functional results that the conventionally used semilocal exchange-correlation functionals provide a qualitatively correct electronic structure for TM-doped Si structures, which validates many results obtained in the past *a posteriori*.

Chapter 5: An unconventional statistical supercell approach to the electron-phonon interaction (instead of the coherent potential approximation or model theories) showed that the thermal excitation of phonons leaves the half-metallic band gap of Co_2MnSi intact, even far beyond the Curie temperature. A new route to spincaloric properties was presented that circumvents the linear response approximation inherent in the Seebeck coefficient and can readily include thermal variations of the chemical potential in the leads and finite-bias effects. Application to Co_2MnSi/MgO(001)/Co_2MnSi MTJs showed that their spincaloric properties can be tailored by a targeted growth control, which can be used in a suggested, thermally operated MRAM module.

Dieses Werk ist copyrightgeschützt und darf in keiner Form vervielfältigt werden noch an Dritte weitergegeben werden.
Es gilt nur für den persönlichen Gebrauch.

Appendix A

Computational details

This appendix contains details about the numerical procedures, which are provided in order to facilitate a reproduction of the results. All *ab initio* results presented in this thesis have been obtained by the author, unless explicit reference to the literature is made. If not indicated otherwise, the results have been obtained in the plane wave framework using USPPs (cf. Sec. 2.2.4 on page 31) and the PBE exchange-correlation functional (cf. Sec. 2.2.3 on page 25). The employed DFT programs were Quantum ESPRESSO [78] in the first place, but also VASP [80,81], WIEN2k [82], and FHI-aims [83] (cf. Sec. 2.2.5 on page 37). The latter two programs allow for an all-electron treatment and are the reference against which the USPP and the PAW approaches can be compared (for small systems).

Generated pseudopotentials

The largest part of the results presented in this thesis have been obtained within a plane wave USPP framework. The pseudopotentials had to be generated in advance for every element of interest and with the envisaged exchange-correlation functional.[1] This has been accomplished by using version 7.3.6 of the USPP generation code from the group of D. Vanderbilt, Rutgers University. Some details about the pseudopotentials are collected in Table A.1. After the generation, each pseudopotential had to be tested thoroughly; for instance, it has to provide results for different materials (different chemical environments) that approximate the corresponding all-electron reference as good as possible (transferability). Moreover, convergence properties have to be checked (i.e., the required/minimal wave function and density cutoff energies, cf. Sec. 2.2.4 on page 31).

[1] Only for V and Ni the pseudopotential files “V.pbe-sp-van.UPF” and “Ni.pbe-nd-rrkjus.UPF” from *http://www.quantum-espresso.org* have been used.

Dieses Werk ist copyrightgeschützt und darf in keiner Form vervielfältigt werden noch an Dritte weitergegeben werden.
Es gilt nur für den persönlichen Gebrauch.

Table A.1 – Details (i.e., included orbitals and NLCC [77]) about the USPPs that have been generated by the author of this thesis in order to obtain the presented results.

Chemical element			Orbitals	NLCC
Number	Symbol	Name		
1	H	hydrogen	$1s$	no
6	C	carbon	$2s$, $2p$	no
7	N	nitrogen	$2s$, $2p$	no
8	O	oxygen	$2s$, $2p$	no
12	Mg	magnesium	$2p$, $3s$, $3p$	no
14	Si	silicon	$3s$, $3p$	yes
22	Ti	titanium	$3s$, $3p$, $3d$, $4s$, $4p$	no
24	Cr	chromium	$3p$, $3d$, $4s$, $4p$	yes
25	Mn	manganese	$3p$, $3d$, $4s$, $4p$	yes
26	Fe	iron	$3p$, $3d$, $4s$, $4p$	yes
27	Co	cobalt	$3d$, $4s$, $4p$	yes
29	Cu	copper	$3d$, $4s$, $4p$	yes
31	Ga	gallium	$3d$, $4s$, $4p$	yes
32	Ge	germanium	$3d$, $4s$, $4p$	yes
33	As	arsenic	$4s$, $4p$	yes

Transition metal silicide bulk compounds and films on Si(111)

Pure Si structures

Since Si is quite simple to simulate, only two interesting cases are described here.

The PAW-HSE06 ($\omega \approx 0.2$ Å^{-1}, $\alpha = 1/4$) calculations of bulk Si were performed using a $11 \times 11 \times 11$ Monkhorst-Pack $\vec{k}$-point grid [107] including the Γ point and a plane wave cutoff energy of 19 Ry.

The Si(111)-(7×7) reconstruction was simulated using a hexagonal supercell with a slab of 445 atoms in total and a vacuum region of about 20 Å. Below the reconstructed surface, 6 additional layers of Si were terminated by a H-passivated backside. The plane wave cutoffs for wave functions and densities were 35 and 250 Ry, respectively. The Brillouin zone was sampled using a $2 \times 2 \times 1$ Monkhorst-Pack $\vec{k}$-point grid including the Γ point and a Fermi-Dirac smearing with a very small smearing parameter, so that the Fermi distribution function almost resembled a step function. The atomic positions were accurately optimized (forces ≤ 1 mRy/bohr, energy changes ≤ 0.1 mRy).

Transition metal silicide bulk structures

The spin-polarized bulk calculations of B20 TM silicides were carried out using simple cubic unit cells with 8 atoms. In [111] direction, a rhombohedral unit cell (as used, for instance, in Ref. [196]) comprising 8 atoms does not allow for more complex magnetic configurations than ferromagnetism. Thus, hexagonal cells with 24 atoms were used for the strained-bulk

Dieses Werk ist copyrightgeschützt und darf in keiner Form vervielfältigt werden noch an Dritte weitergegeben werden.
Es gilt nur für den persönlichen Gebrauch.

calculations. The plane wave cutoffs for wave functions and densities were 35 and 350 Ry, respectively. The author used a $16\times16\times16$ Monkhorst-Pack $\vec{k}$-point grid for cubic unit cells and a $6\times6\times4$ grid for hexagonal unit cells, always in conjunction with a Methfessel-Paxton smearing [350] of 5 mRy. All grids were chosen in such a way that they did not include the Γ point. The DOS post-processing was performed with denser $\vec{k}$-point grids that did include the Γ point. The atomic positions were accurately optimized (forces ≤ 1 mRy/bohr, energy changes ≤ 0.1 mRy). Constrained total moment calculations were carried out using two separate Fermi energies, one for each spin channel. Noncollinear spin configurations, as they arise, for example, in MnSi, were approximated to be collinear (see also Sec. 3.3.3).

As a reference, all-electron calculations employing the LAPW technique [82] were performed. Muffin-tin radii of 1.06 – 1.11 Å for both the TM and Si atoms, an interstitial plane wave cutoff of $E_{\rm cut}^{\rm WF} = 20$ Ry, and wave function and density expansions up to $l_{\rm max}^{\rm WF} = 12$ and $G_{\rm max} = 14$ were used.

Surfaces and interfaces

MnSi(111) surfaces were simulated using a hexagonal supercell with a MnSi slab, a vacuum region of about 20 Å, a $6\times6\times1$ Monkhorst-Pack $\vec{k}$-point grid without the Γ point, and a Methfessel-Paxton smearing of 5 mRy.

The MnSi/FeSi interfaces to Si(111) were simulated using a long hexagonal cell containing the (fully periodic) Si(111)/TM-Si(111)/Si(111) structures. A $4\times4\times2$ Monkhorst-Pack $\vec{k}$-point grid without the Γ point in conjunction with a Methfessel-Paxton smearing of 5 mRy was used for the sampling of the Brillouin zone.

In all cases, the atomic positions were accurately optimized (forces ≤ 1 mRy/bohr, energy changes ≤ 0.1 mRy), and the plane wave cutoffs for wave functions and densities were 35 and 350 Ry, respectively.

MnSi thin film structures

The spin-polarized calculations for the $\sqrt{3}\times\sqrt{3}$ MnSi film structures were carried out using a supercell approach. A hexagonal Si(111)-$(\sqrt{3}\times\sqrt{3})$ unit cell containing 6 layers of Si, the MnSi films, and a vacuum region of about 20 Å was used. The lower side of the Si substrate was passivated by H atoms. The lateral cell size was fixed to the calculated Si(111)-$(\sqrt{3}\times\sqrt{3})$ surface lattice constant. The plane wave cutoffs for wave functions and densities were chosen as 35 Ry and 350 Ry, respectively. Brillouin zone sampling was done using $4\times4\times1$, $6\times6\times1$, and $8\times8\times1$ Monkhorst-Pack $\vec{k}$-point grids in conjunction with a Methfessel-Paxton smearing of 5 mRy, accounting for the fact that only results obtained with equal grid density and smearing parameter can be reliably compared. All grids were chosen in such a way that they did not include the Γ point. The DOS post-processing was performed with denser $\vec{k}$-point grids that did include the Γ point. The atomic positions were accurately optimized (forces ≤ 1 mRy/bohr, energy changes ≤ 0.1 mRy). A dipole correction scheme was included [208, 209], but found to be of minor importance. For the 3×3 supercells a $2\times2\times1$ Monkhorst-Pack $\vec{k}$-point grid was used. The Mn_5Si_3/Si(111) heterostructures were simulated in complete analogy, but using an $8\times8\times1$ Monkhorst-Pack $\vec{k}$-point grid including the Γ point. From the obtained electronic structure, STM images were simulated (in all cases) according to Sec. 2.3.2.

Dieses Werk ist copyrightgeschützt und darf in keiner Form vervielfältigt werden noch an Dritte weitergegeben werden.
Es gilt nur für den persönlichen Gebrauch.

Transition metal impurities in Si

Isolated impurities in bulk Si

Spin-polarized calculations for isolated impurities in bulk Si were performed within the USPP and PAW frameworks together with semilocal PBE and the hybrid functional HSE06, respectively. Bulk results were obtained from cubic 216/217-atom Si supercells.

For the USPP-PBE calculations, cutoff energies of 35 Ry for the wave functions and 250 Ry for the densities were used. The Brillouin zone was sampled using a $5 \times 5 \times 5$ Monkhorst-Pack $\vec{k}$-point grid including the Γ point. A Fermi-Dirac smearing with a very small smearing parameter was employed, so that the Fermi distribution function almost resembled a step function. The atomic positions were accurately optimized (forces ≤ 1 mRy/bohr, energy changes ≤ 0.1 mRy).

For the PAW-HSE06 calculations the author used the (VASP-recommended) value of 19 Ry as cutoff energy. The Brillouin zone was sampled using a $2 \times 2 \times 2$ Monkhorst-Pack $\vec{k}$-point grid that included the Γ point. Gaussian smearing with a very small smearing parameter was employed. Optimized PBE structural parameters were used.

Subsurface impurities

Impurity wave functions are very sensitive objects that converge much slower with increasing system size as, for instance, the total energy. Even if the latter is already well converged, STM images of the former still show the influence of periodic images (periodic boundary conditions). Thus, very large supercells had to be used. Si(111)-(9×9) slabs with 10 layers of Si and two passivating H layers were employed (972/973 atoms in total). The slabs were separated in [111] direction by a vacuum region of 20 Å. Cutoff energies of 35 Ry for the wave functions and 250 Ry for the densities were used. Brillouin zone sampling was performed using a $2 \times 2 \times 1$ Monkhorst-Pack $\vec{k}$-point grid that included the Γ point. A Fermi-Dirac smearing with a very small smearing parameter was employed, so that the Fermi distribution function almost resembled a step function. From the obtained electronic structure, (SP) STM images were simulated according to Secs. 2.3.2 and 2.3.3.

For the Fe-Fe interactions in bulk material, which are used as reference, a hexagonal Si cell with 434 atoms in total was employed. The Brillouin zone was sampled using a $2 \times 2 \times 2$ Monkhorst-Pack $\vec{k}$-point grid without the Γ point.

Two-dimensional impurity clusters and layers

Here the procedure was analogous to the case of subsurface impurities, only that smaller Si(111) unit cells were used. For the subsurface impurity δ layers, the unit cell size (and thus also the corresponding Monkhorst-Pack $\vec{k}$-point grid that always included the Γ point) was chosen according to the desired doping density: Si(111)-(6×6) with $2 \times 2 \times 1$, Si(111)-(4×4) with $4 \times 4 \times 1$, and Si(111)-(2×2) with $8 \times 8 \times 1$. For the subsurface impurity clusters, a Si(111)-(6×6) unit cell with a $2 \times 2 \times 1$ Monkhorst-Pack $\vec{k}$-point grid was used.

Dieses Werk ist copyrightgeschützt und darf in keiner Form vervielfältigt werden noch an Dritte weitergegeben werden.
Es gilt nur für den persönlichen Gebrauch.

Organic molecules on Si(111)

All-electron calculations for isolated organic molecules (gas phase) were performed with FHI-aims using a "tight, second tier" basis set. The atomic structure was accurately optimized. For the hybrid functional calculations, the expansion of the Coulomb potential of basis function products was localized to two centers. With this approximation, the computational effort scales linearly with the electron number.

The adsorption of FePc on Si(111) was simulated within the USPP framework using a Si(111)-(6×6) unit cell (as described above) with a vacuum region of 20 Å. Cutoff energies of 35 Ry for the wave functions and 250 Ry for the densities were used. Brillouin zone sampling was performed with a $2 \times 2 \times 1$ Monkhorst-Pack $\vec{k}$-point grid that included the Γ point. A Fermi-Dirac smearing with a very small smearing parameter was employed, so that the Fermi distribution function almost resembled a step function. An empirical vdW energy correction to the PBE exchange-correlation functional (also known as "dispersive forces" or DFT-D) was included [123,124] in order to strongly improve the description of the vdW-dominated (physisorbed) system.

Magnetic tunnel junctions with Heusler electrodes

The spin-polarized calculations were performed within the USPP framework using plane wave cutoffs for wave functions and densities of 35 Ry and 350 Ry, respectively. A Methfessel-Paxton smearing of 10 mRy and different Monkhorst-Pack $\vec{k}$-point grids, all without the Γ point, were used: $12 \times 12 \times 12$ for bulk calculations with 4-atom fcc cells, $4 \times 4 \times 4$ together with 32-atom fcc cells for the random frozen phonons, and $16 \times 16 \times 2$ for the tetragonal MTJ cells with two atoms per layer.

Transport calculations were carried out within the formalism described in Sec. 2.4 on page 42. The 2D-BZ was sampled using a 401×401 Monkhorst-Pack $\vec{k}_\perp$-point grid for each energy point. For the energy integration in Eqs. (5.1) and (5.2), spin-resolved transmission curves $T_\sigma(E)$ were calculated on a regular E mesh with 25-meV spacing followed by an interpolation of $T_\sigma(E)$ on a denser E mesh with 1.36-meV (0.1-mRy) spacing.

Dieses Werk ist copyrightgeschützt und darf in keiner Form vervielfältigt werden noch an Dritte weitergegeben werden.
Es gilt nur für den persönlichen Gebrauch.

Dieses Werk ist copyrightgeschützt und darf in keiner Form vervielfältigt werden noch an Dritte weitergegeben werden.
Es gilt nur für den persönlichen Gebrauch.

List of Figures

2.1 DFT-SCF flowchart for solving the Kohn-Sham equations 22
2.2 Illustration of the pseudopotential principle 32
2.3 Two selected all-electron and pseudo wave functions of a Mn USPP 34
2.4 STM working principle 39
2.5 Ballistic conductance setup 43

3.1 Atomic structure of bulk Si and its valence charge density 49
3.2 Electronic Kohn-Sham band structures and DOS for Si in diamond structure . 51
3.3 Silicene 53
3.4 Unreconstructed, but relaxed Si(111) surfaces 55
3.5 Si(111)-(7×7) surface reconstruction 58
3.6 Atomic models of the rock-salt, the B20, and the zinc-blende structure 60
3.7 Illustration of the three- and five-atom loops in the trillium lattice 61
3.8 Heat capacity and magnetic susceptibility for the trillium lattice and the simple cubic lattice 62
3.9 Wyckoff parameters, cohesive energies, and total magnetic moments of different TM monosilicides in B20 structure 64
3.10 Spin-resolved DOS for different TM monosilicides in B20 structure 66
3.11 Electronic structure of FeSi 68
3.12 TiSi and NiSi 69
3.13 Cohesive energies as functions of the lattice constant for MnSi and FeSi 70
3.14 Electronic structure of MnSi and FeSi in different crystal structures 71
3.15 Structural transformations between B20, B1, and B3 structures in MnSi 72
3.16 Relation between cubic and hexagonal unit cells for B20 TM-Si compounds . . 74
3.17 Effect of strain on the total energy and magnetic properties of MnSi and FeSi . 75
3.18 DOS of biaxially strained CrSi, MnSi, and FeSi 78
3.19 Different metastable antiparallel magnetic configurations in MnSi 79
3.20 MnSi phonon dispersion relations 82
3.21 MnSi phonon thermodynamics 83
3.22 Correlation effects in MnSi and FeSi 85
3.23 Phase diagram of Mn-Si compounds 87
3.24 MnSi(111) surface atomic and magnetic structures 88
3.25 MnSi(111) surface energies 89
3.26 Optimized interfaces of MnSi and FeSi with Si(111) 90

Dieses Werk ist copyrightgeschützt und darf in keiner Form vervielfältigt werden noch an Dritte weitergegeben werden.
Es gilt nur für den persönlichen Gebrauch.

3.27 Side views of the atomic structure of MnSi/Si(111) films 92
3.28 STM images of MnSi thin films on Si(111) for higher Mn coverage 94
3.29 Coexistence of HC and LC surface areas within one and the same QL for MnSi/Si(111) films 95
3.30 Surface and film formation energies of MnSi/Si(111) heterostructures 96
3.31 Comparison of experimental STM images and theoretical STM simulations for different MnSi/Si(111) surfaces 97
3.32 Visualization of different dense/sparse Mn/Si layers within MnSi 98
3.33 STM images of MnSi thin films on Si(111) formed by codeposition of Mn and Si 99
3.34 Top and side views of Mn and Si adatom layers on different MnSi/Si(111) surface terminations 101
3.35 STM images of Mn nanoclusters and MnSi islands forming on a clean Si(111)-(7×7) surface for low Mn coverage 105
3.36 The 3×3 two-Si-trimer model 106
3.37 Atomic and magnetic structure of MnSi films of successively increasing thickness in up and down stacking 108
3.38 Atomic structures and magnetic configurations of MnSi thin films 109
3.39 Atomic structure of Mn_4Si_7 112
3.40 Atomic structure of Mn_5Si_3 114
3.41 Surface and interface energies of Mn_5Si_3(001) and Mn_5Si_3/Si(111) 115
3.42 Mn_5Si_3/Si(111) interface atomic structures I 116
3.43 Mn_5Si_3/Si(111) interface atomic structures II 117
3.44 Simulated STM images of different Mn_5Si_3/Si(111) surfaces 118
3.45 Surface energies of Mn_5Ge_3(001) 119

4.1 The H/Si(111) and H/GaAs(110) surfaces 123
4.2 Surface band structures of H/Si(111) and H/GaAs(110) 124
4.3 Simulated STM images of H/Si(111) 126
4.4 Formation energies as functions of the magnetic moment for different isolated interstitial and substitutional TM impurities in bulk Si 128
4.5 Atomic and electronic structure (PBE) of isolated TM impurities in bulk Si . . 129
4.6 Schematic hybridization diagram for interstitial and substitutional Fe impurities in Si 131
4.7 Influence of isolated Fe impurities on different ILDOS in bulk Si 133
4.8 Possible DFT error in the description of impurities 134
4.9 Electronic structure (PBE+U) of isolated TM impurities in bulk Si 135
4.10 Electronic structure (HSE06) of isolated TM impurities in bulk Si 136
4.11 Application of (SP) STM to TM impurities below a H passivated surface 138
4.12 Atomic and electronic structure of different isolated TM impurities close to the H/Si(111) surface 139
4.13 Simulated STM images of interstitial Cr, Mn, and Fe impurities below the H/Si(111) surface 141
4.14 Simulated SP STM magnetic-contrast images of interstitial Cr, Mn, and Fe impurities below the H/Si(111) surface 142
4.15 Simulated STM and SP STM magnetic-contrast images of a substitutional Fe impurity below the H/Si(111) surface 143

Dieses Werk ist copyrightgeschützt und darf in keiner Form vervielfältigt werden noch an Dritte weitergegeben werden.
Es gilt nur für den persönlichen Gebrauch.

4.16 Experimental STM images for a potential substitutional Fe impurity below the H/Si(111) surface . . . 143
4.17 Tip-induced band bending . . . 145
4.18 Simulated STM and SP STM magnetic-contrast images of two interacting subsurface interstitial Fe impurities . . . 147
4.19 Formation energies for Cr, Mn, and Fe atoms entering the H/Si(111) structure 149
4.20 Kinetic migration barrier between two different subsurface interstitial sites for Cr, Mn, and Fe . . . 150
4.21 Formation energies of two-dimensional subsurface δ layers . . . 151
4.22 Atomic structure and PDOS of a two-dimensional δ layer of interstitial Cr, Mn, and Fe impurities below the H/Si(111) surface . . . 152
4.23 Simulated STM and SP STM images of an interstitial Fe δ layer . . . 153
4.24 Magnetization and magnetic susceptibility of the two-dimensional, hexagonal, classical Heisenberg model . . . 153
4.25 Destabilization of the Si matrix by a dense TM δ layer . . . 155
4.26 Atomic and magnetic structure of several subsurface interstitial-Fe clusters . . 156
4.27 Cluster formation energies and DOS plots . . . 156
4.28 Atomic structure of Pc rings with different centers . . . 158
4.29 Silicon phthalocyanine . . . 161
4.30 Adsorption of FePc on H/Si(111) . . . 162
4.31 Illustration of different scenarios for the Fe injection into the H/Si(111) subsurface layers from the organic molecule FePc . . . 165

5.1 Magnetic tunnel junction and spin injection device . . . 168
5.2 Structural and electronic properties of bulk Co_2MnSi . . . 170
5.3 All-electron band structure plots of bulk Co_2MnSi . . . 171
5.4 Fermi surface sheets of bulk Co_2MnSi . . . 172
5.5 Structural and electronic properties of MgO . . . 173
5.6 Calculated phonon dispersion relations of bulk Co_2MnSi . . . 175
5.7 Response of the spin-resolved electronic structure of bulk Co_2MnSi to differently intense structural distortions, and its thermal evolution . . . 176
5.8 Atomic structure of different epitaxial Co_2MnSi/MgO(001) interfaces . . . 178
5.9 Interface band structure of different Co_2MnSi/MgO(001) interfaces . . . 179
5.10 Dependence of the majority spin transmission $T_\uparrow(E)$ for $E = E_F$ on the MgO barrier thickness and on the interface termination . . . 180
5.11 Majority spin Kohn-Sham potentials of Co_2MnSi/MgO/Co_2MnSi MTJs . . . 181
5.12 Spin-resolved transmission through bulk Co_2MnSi and through MTJs . . . 182
5.13 Conductance and Seebeck coefficient for Co_2MnSi/MgO/Co_2MnSi MTJs . . . 184
5.14 Thermal variation of the chemical potential in bulk Co_2MnSi and finite-bias influence on the transmission through a MTJ . . . 185
5.15 Alternatively calculated thermocurrent and -voltage I . . . 186
5.16 Alternatively calculated thermocurrent and -voltage II . . . 188
5.17 Schematic illustration of a suggested thermo-MRAM module . . . 188
5.18 Schematic illustration of magnon-assisted tunneling through a MTJ . . . 189
5.19 Mn (001) sublattices used to study the effect of reversed local moments . . . 190

Dieses Werk ist copyrightgeschützt und darf in keiner Form vervielfältigt werden noch an Dritte weitergegeben werden.
Es gilt nur für den persönlichen Gebrauch.

Dieses Werk ist copyrightgeschützt und darf in keiner Form vervielfältigt werden noch an Dritte weitergegeben werden.
Es gilt nur für den persönlichen Gebrauch.

List of Tables

3.1 Structural properties of bulk Si 50
3.2 Width of the Kohn-Sham band gap of bulk Si 52
3.3 Lattice constants and magnetic moments of TM silicides in B20 structure . . . 63
3.4 Bulk moduli and Wyckoff parameters of TM silicides in B20 structure 63
3.5 Space and point groups of MnSi in different crystal structures 73
3.6 Volume expansion and total magnetic moment of different TM monosilicides epitaxially grown on Si(111) 77
3.7 Interface magnetic moments of MnSi/Si(111) and FeSi/Si(111) 91
3.8 Adsorption energies of two Mn layers on the up-Si-dense surface 101
3.9 Adsorption energies of a single Si layer on the down-Mn-dense surface 101
3.10 Adsorption energies of different Si adatom configurations on MnSi/Si(111) . . 106
3.11 Energy differences of different FIM configurations with respect to FM configurations in MnSi thin films on Si(111) 110

4.1 Optimized TM-Si nearest-neighbor bond lengths for isolated impurities in bulk Si 132
4.2 Energy differences (FM/AFM) of interacting interstitial Fe impurities below the H/Si(111) surface and in bulk Si 148
4.3 Binding energies and magnetic moments of different central atoms in an empty Pc molecule (PBE) 160
4.4 Binding energies of a central Fe atom or two H atoms in FePc and Pc, respectively, calculated with different exchange-correlation functionals 160
4.5 Different scenarios for the Fe injection into the H/Si(111) subsurface layers from organic FePc and FePc-2H molecules 164

5.1 Structural, electronic, and magnetic properties of bulk Co_2MnSi 171
5.2 Results of MTJ transmission data fitting 181
5.3 Magnetic excitation energies in bulk Co_2MnSi and in MTJ devices 191

A.1 Pseudopotential details 200

Dieses Werk ist copyrightgeschützt und darf in keiner Form vervielfältigt werden noch an Dritte weitergegeben werden.
Es gilt nur für den persönlichen Gebrauch.

Dieses Werk ist copyrightgeschützt und darf in keiner Form vervielfältigt werden noch an Dritte weitergegeben werden.
Es gilt nur für den persönlichen Gebrauch.

List of Abbreviations

General abbreviations

- TM — transition metal
- NM — nonmagnetic
- FM — ferromagnetic
- AFM — antiferromagnetic
- FIM — ferrimagnetic
- f.u. — formula unit
- fcc — face-centered cubic
- bcc — body-centered cubic
- hcp — hexagonal close-packed
- VB(M) — valence band (maximum)
- CB(M) — conduction band (minimum)
- SDB (TDB) — single (triple) dangling bond [Si(111) surface]
- ML, QL — monolayer, quad-layer
- HC, LC — high corrugation, low corrugation
- TIBB — tip-induced band bending
- vdW — van der Waals
- HOMO (LUMO) — highest occupied (lowest unoccupied) molecular orbital
- TMR — tunnel magnetoresistance
- MTJ — magnetic tunnel junction
- MRAM — magnetoresistive random access memory
- 2D-BZ — two-dimensional Brillouin zone

Dieses Werk ist copyrightgeschützt und darf in keiner Form vervielfältigt werden noch an Dritte weitergegeben werden.
Es gilt nur für den persönlichen Gebrauch.

Experimental methods

- ARPES — angle-resolved photoemission spectroscopy
- EPR — electron paramagnetic resonance
- PCAR — point contact Andreev reflection
- (SP) STM — (spin-polarized) scanning tunneling microscopy / microscope
- XMCD — x-ray magnetic circular dichroism

DFT-related abbreviations

- DFT — density functional theory
- USPP — ultrasoft pseudopotential
- NLCC — nonlinear core correction
- LAPW — linearized augmented plane wave (and related methods)
- PAW — projector augmented wave
- KKR — Korringa-Kohn-Rostocker
- SCF — self-consistent field
- DOS — density of states
- PDOS — projected density of states (onto atomic orbitals; element and site specific)
- LDOS — local density of states
- ILDOS — integrated local density of states (over a certain energy interval)
- DFPT — density functional perturbation theory (used for phonons here)
- DMFT — dynamical mean field theory

DFT exchange-correlation functionals

- L(S)DA — local (spin) density approximation
- GGA — generalized gradient approximation
- PBE, PW91 — different GGA functionals
- PBE0 — a hybrid functional based on PBE
- HSE, HSE06 — a hybrid functional based on PBE, with screened Coulomb operator
- B3LYP — a hybrid functional frequently used in chemistry
- HF — Hartree-Fock, which can be seen in a DFT context as extreme case of a hybrid functional without correlation and containing pure exact exchange

Dieses Werk ist copyrightgeschützt und darf in keiner Form vervielfältigt werden noch an Dritte weitergegeben werden.
Es gilt nur für den persönlichen Gebrauch.

References

[1] G. A. Prinz, Science **282**, 1660 (1998).

[2] S. A. Wolf, D. D. Awschalom, R. A. Buhrman, J. M. Daughton, S. von Molnár, M. L. Roukes, A. Y. Chtchelkanova, and D. M. Treger, Science **294**, 1488 (2001).

[3] I. Žutić, J. Fabian, and S. Das Sarma, Rev. Mod. Phys. **76**, 323 (2004).

[4] R. Winkler and M. Oestreich, Physik Journal **11**, 39 (2004).

[5] R. Jansen, Nat. Mater. **11**, 400 (2012).

[6] J. Åkerman, Science **308**, 508 (2005).

[7] C. Chappert, A. Fert, and F. N. Van Dau, Nat. Mater. **6**, 813 (2007).

[8] A. Ney, C. Pampuch, R. Koch, and K. H. Ploog, Nature (London) **425**, 485 (2003).

[9] D. D. Awschalom and M. E. Flatté, Nat. Phys. **3**, 153 (2007).

[10] D. E. Nikonov and G. I. Bourianoff, J. Supercond. Novel Magn. **21**, 479 (2008).

[11] J. H. Jiang and M. W. Wu, Phys. Rev. B **79**, 125206 (2009).

[12] J. L. Cheng, M. W. Wu, and J. Fabian, Phys. Rev. Lett. **104**, 016601 (2010).

[13] S. P. Dash, S. Sharma, R. S. Patel, M. P. de Jong, and R. Jansen, Nature (London) **462**, 491 (2009).

[14] T. Suzuki, T. Sasaki, T. Oikawa, M. Shiraishi, Y. Suzuki, and K. Noguchi, Appl. Phys. Express **4**, 023003 (2011).

[15] B. Geisler, P. Kratzer, T. Suzuki, T. Lutz, G. Costantini, and K. Kern, Phys. Rev. B **86**, 115428 (2012).

[16] B. Geisler and P. Kratzer, Phys. Rev. B **88**, 115433 (2013).

[17] T. Suzuki, T. Lutz, B. Geisler, P. Kratzer, K. Kern, and G. Costantini, Surf. Sci. **617**, 106 (2013).

Dieses Werk ist copyrightgeschützt und darf in keiner Form vervielfältigt werden noch an Dritte weitergegeben werden.
Es gilt nur für den persönlichen Gebrauch.

[18] B. Geisler, P. Kratzer, and V. Popescu, Phys. Rev. B **89**, 184422 (2014).

[19] D. Comtesse, B. Geisler, P. Entel, P. Kratzer, and L. Szunyogh, Phys. Rev. B **89**, 094410 (2014).

[20] M. Born and R. Oppenheimer, Ann. Phys. **84**, 457 (1927).

[21] G. Czycholl, *Theoretische Festkörperphysik*, Springer, Berlin, Heidelberg (2008).

[22] R. M. Martin, *Electronic Structure: Basic Theory and Practical Methods*, Cambridge University Press (2004).

[23] R. P. Feynman, Phys. Rev. **56**, 340 (1939).

[24] X.-Z. Li, M. I. J. Probert, A. Alavi, and A. Michaelides, Phys. Rev. Lett. **104**, 066102 (2010).

[25] M. Ceriotti, J. Cuny, M. Parrinello, and D. E. Manolopoulos, Proc. Natl. Acad. Sci. U.S.A. **110**, 15591 (2013).

[26] M. E. Gruner, G. Rollmann, P. Entel, and M. Farle, Phys. Rev. Lett. **100**, 087203 (2008).

[27] G. Rollmann, M. E. Gruner, A. Hucht, R. Meyer, P. Entel, M. L. Tiago, and J. R. Chelikowsky, Phys. Rev. Lett. **99**, 083402 (2007).

[28] P. Hohenberg and W. Kohn, Phys. Rev. **136**, B864 (1964).

[29] R. Parr and W. Yang, *Density-Functional Theory of Atoms and Molecules*, Oxford University Press, New York, USA (1989).

[30] M. Levy, Phys. Rev. A **26**, 1200 (1982).

[31] E. H. Lieb, Int. J. Quantum Chem. **24**, 243 (1983).

[32] W. Kohn and L. J. Sham, Phys. Rev. **140**, A1133 (1965).

[33] A. Görling, Phys. Rev. A **54**, 3912 (1996).

[34] M. Levy, J. P. Perdew, and V. Sahni, Phys. Rev. A **30**, 2745 (1984).

[35] W. G. Aulbur, L. Jönsson, and J. W. Wilkins, *Quasiparticle Calculations in Solids*, volume 54 of *Solid State Phys.*, Academic Press (1999).

[36] D. M. Ceperley and B. J. Alder, Phys. Rev. Lett. **45**, 566 (1980).

[37] S. H. Vosko, L. Wilk, and M. Nussair, Can. J. Phys. **58**, 1200 (1980).

[38] U. von Barth and L. Hedin, J. Phys. C **5**, 1629 (1972).

[39] J. P. Perdew and A. Zunger, Phys. Rev. B **23**, 5048 (1981).

[40] P. Haas, F. Tran, and P. Blaha, Phys. Rev. B **79**, 085104 (2009).

[41] P. S. Svendsen and U. von Barth, Phys. Rev. B **54**, 17402 (1996).

Dieses Werk ist copyrightgeschützt und darf in keiner Form vervielfältigt werden noch an Dritte weitergegeben werden.
Es gilt nur für den persönlichen Gebrauch.

[42] F. Herman, J. P. Van Dyke, and I. B. Ortenburger, Phys. Rev. Lett. **22**, 807 (1969).

[43] J. P. Perdew, *Unified theory of exchange and correlation beyond the local density approximation*, in *Electronic Structure of Solids '91*, edited by P. Ziesche and H. Eschrig, Akademie Verlag, Berlin (1991).

[44] J. P. Perdew, J. A. Chevary, S. Vosko, K. Jackson, M. R. Pederson, D. J. Singh, and C. Fiolhais, Phys. Rev. B **64**, 6671 (1992).

[45] J. P. Perdew, K. Burke, and M. Ernzerhof, Phys. Rev. Lett. **77**, 3865 (1996).

[46] A. E. Mattsson, R. Armiento, P. A. Schultz, and T. R. Mattsson, Phys. Rev. B **73**, 195123 (2006).

[47] E. H. Lieb and S. Oxford, Int. J. Quantum Chem. **19**, 427 (1981).

[48] M. J. Lucero, T. M. Henderson, and G. E. Scuseria, J. Phys.: Condens. Matter **24**, 145504 (2012).

[49] O. Madelung, *Semiconductors: Data Handbook*, Springer, Berlin, Heidelberg (2004).

[50] A. D. Becke, J. Chem. Phys. **98**, 5648 (1993).

[51] J. P. Perdew, M. Ernzerhof, and K. Burke, J. Chem. Phys. **105**, 9982 (1996).

[52] J. Heyd, G. E. Scuseria, and M. Ernzerhof, J. Chem. Phys. **118**, 8207 (2003).

[53] J. Heyd, G. E. Scuseria, and M. Ernzerhof, J. Chem. Phys. **124**, 219906 (2006).

[54] A. V. Krukau, O. A. Vydrov, A. F. Izmaylov, and G. E. Scuseria, J. Chem. Phys. **125**, 224106 (2006).

[55] K. Terakura, T. Oguchi, A. R. Williams, and J. Kübler, Phys. Rev. B **30**, 4734 (1984).

[56] P. Dufek, P. Blaha, V. Sliwko, and K. Schwarz, Phys. Rev. B **49**, 10170 (1994).

[57] M. Cococcioni and S. de Gironcoli, Phys. Rev. B **71**, 035105 (2005).

[58] V. I. Anisimov and O. Gunnarsson, Phys. Rev. B **43**, 7570 (1991).

[59] V. I. Anisimov, J. Zaanen, and O. K. Andersen, Phys. Rev. B **44**, 943 (1991).

[60] V. I. Anisimov, I. V. Solovyev, M. A. Korotin, M. T. Czyżyk, and G. A. Sawatzky, Phys. Rev. B **48**, 16929 (1993).

[61] I. V. Solovyev, P. H. Dederichs, and V. I. Anisimov, Phys. Rev. B **50**, 16861 (1994).

[62] A. I. Liechtenstein, V. I. Anisimov, and J. Zaanen, Phys. Rev. B **52**, R5467 (1995).

[63] S. L. Dudarev, G. A. Botton, S. Y. Savrasov, C. J. Humphreys, and A. P. Sutton, Phys. Rev. B **57**, 1505 (1998).

[64] J. P. Perdew, R. G. Parr, M. Levy, and J. L. Balduz, Phys. Rev. Lett. **49**, 1691 (1982).

Dieses Werk ist copyrightgeschützt und darf in keiner Form vervielfältigt werden noch an Dritte weitergegeben werden.
Es gilt nur für den persönlichen Gebrauch.

[65] J. F. Janak, Phys. Rev. B **18**, 7165 (1978).

[66] D. A. Scherlis, M. Cococcioni, P. Sit, and N. Marzari, J. Phys. Chem. B **111**, 7384 (2007).

[67] A. M. P. Sena, V. Brázdová, and D. R. Bowler, Phys. Rev. B **79**, 245404 (2009).

[68] F. Küwen, R. Leitsmann, and F. Bechstedt, Phys. Rev. B **80**, 045203 (2009).

[69] H. C. Kandpal, G. H. Fecher, C. Felser, and G. Schönhense, Phys. Rev. B **73**, 094422 (2006).

[70] D. R. Hamann, M. Schlüter, and C. Chiang, Phys. Rev. Lett. **43**, 1494 (1979).

[71] A. M. Rappe, K. M. Rabe, E. Kaxiras, and J. D. Joannopoulos, Phys. Rev. B **41**, 1227 (1990).

[72] N. Troullier and J. L. Martins, Phys. Rev. B **43**, 1993 (1991).

[73] L. Kleinman and D. M. Bylander, Phys. Rev. Lett. **48**, 1425 (1982).

[74] D. Vanderbilt, Phys. Rev. B **41**, 7892 (1990).

[75] K. Laasonen, A. Pasquarello, R. Car, C. Lee, and D. Vanderbilt, Phys. Rev. B **47**, 10142 (1993).

[76] P. Giannozzi, F. D. Angelis, and R. Car, J. Chem. Phys. **120**, 5903 (2004).

[77] S. G. Louie, S. Froyen, and M. L. Cohen, Phys. Rev. B **26**, 1738 (1982).

[78] P. Giannozzi *et al.*, J. Phys.: Condens. Matter **21**, 395502 (2009).

[79] P. E. Blöchl, Phys. Rev. B **50**, 17953 (1994).

[80] G. Kresse and D. Joubert, Phys. Rev. B **59**, 1758 (1999).

[81] G. Kresse and J. Furthmüller, Phys. Rev. B **54**, 11169 (1996).

[82] P. Blaha, K. Schwarz, G. K. H. Madsen, D. Kvasnicka, and J. Luitz, *WIEN2k, an Augmented Plane Wave + Local Orbitals Program for Calculating Crystal Properties*, K. Schwarz, Technische Universität Wien, Austria (2001).

[83] V. Blum, R. Gehrke, F. Hanke, P. Havu, V. Havu, X. Ren, K. Reuter, and M. Scheffler, Comput. Phys. Commun. **180**, 2175 (2009).

[84] H. Ebert, D. Ködderitzsch, and J. Minár, Rep. Prog. Phys. **74**, 096501 (2011).

[85] G. Binnig, H. Rohrer, C. Gerber, and E. Weibel, Phys. Rev. Lett. **49**, 57 (1982).

[86] G. Binnig, H. Rohrer, C. Gerber, and E. Weibel, Phys. Rev. Lett. **50**, 120 (1983).

[87] G. Binnig and H. Rohrer, IBM J. Res. Dev. **30**, 355 (1986).

[88] M. F. Crommie, C. P. Lutz, and D. M. Eigler, Science **262**, 218 (1993).

Dieses Werk ist copyrightgeschützt und darf in keiner Form vervielfältigt werden noch an Dritte weitergegeben werden.
Es gilt nur für den persönlichen Gebrauch.

[89] R. Berndt, R. Gaisch, J. K. Gimzewski, B. Reihl, R. R. Schlittler, W. D. Schneider, and M. Tschudy, Science **262**, 1425 (1993).

[90] X. H. Qiu, G. V. Nazin, and W. Ho, Science **299**, 542 (2003).

[91] E. Ćavar, M.-C. Blüm, M. Pivetta, F. Patthey, M. Chergui, and W.-D. Schneider, Phys. Rev. Lett. **95**, 196102 (2005).

[92] C. Chen, P. Chu, C. A. Bobisch, D. L. Mills, and W. Ho, Phys. Rev. Lett. **105**, 217402 (2010).

[93] G. Reecht, F. Scheurer, V. Speisser, Y. J. Dappe, F. Mathevet, and G. Schull, Phys. Rev. Lett. **112**, 047403 (2014).

[94] R. Wiesendanger, Rev. Mod. Phys. **81**, 1495 (2009).

[95] J. Bardeen, Phys. Rev. Lett. **6**, 57 (1961).

[96] J. Tersoff and D. R. Hamann, Phys. Rev. Lett. **50**, 1998 (1983).

[97] J. Tersoff and D. R. Hamann, Phys. Rev. B **31**, 805 (1985).

[98] C. J. Chen, Phys. Rev. Lett. **65**, 448 (1990).

[99] C. J. Chen, Phys. Rev. B **42**, 8841 (1990).

[100] M. Tsukada, K. Kobayashi, and N. Isshiki, Surf. Sci. **242**, 12 (1991).

[101] R. Wiesendanger, H.-J. Güntherodt, G. Güntherodt, R. J. Gambino, and R. Ruf, Phys. Rev. Lett. **65**, 247 (1990).

[102] R. A. de Groot, Physica B **172**, 45 (1991).

[103] D. K. Ferry, S. M. Goodnick, and J. Bird, *Transport in Nanostructures*, Cambridge University Press (2009).

[104] M. Büttiker, Y. Imry, R. Landauer, and S. Pinhas, Phys. Rev. B **31**, 6207 (1985).

[105] H. Joon Choi and J. Ihm, Phys. Rev. B **59**, 2267 (1999).

[106] A. Smogunov, A. Dal Corso, and E. Tosatti, Phys. Rev. B **70**, 045417 (2004).

[107] H. J. Monkhorst and J. D. Pack, Phys. Rev. B **13**, 5188 (1976).

[108] E. A. Karhu, S. Kahwaji, T. L. Monchesky, C. Parsons, M. D. Robertson, and C. Maunders, Phys. Rev. B **82**, 184417 (2010).

[109] E. A. Karhu, S. Kahwaji, M. D. Robertson, H. Fritzsche, B. J. Kirby, C. F. Majkrzak, and T. L. Monchesky, Phys. Rev. B **84**, 060404 (2011).

[110] N. A. Porter, G. L. Creeth, and C. H. Marrows, Phys. Rev. B **86**, 064423 (2012).

[111] D. Shinoda and S. Asanabe, J. Phys. Soc. Jpn. **21**, 555 (1966).

Dieses Werk ist copyrightgeschützt und darf in keiner Form vervielfältigt werden noch an Dritte weitergegeben werden.
Es gilt nur für den persönlichen Gebrauch.

[112] H. Wu, P. Kratzer, and M. Scheffler, Phys. Rev. B **72**, 144425 (2005).

[113] H. Wu, M. Hortamani, P. Kratzer, and M. Scheffler, Phys. Rev. Lett. **92**, 237202 (2004).

[114] M. Hortamani, P. Kratzer, and M. Scheffler, Phys. Rev. B **76**, 235426 (2007).

[115] F. Carbone, M. Zangrando, A. Brinkman, A. Nicolaou, F. Bondino, E. Magnano, A. A. Nugroho, F. Parmigiani, T. Jarlborg, and D. van der Marel, Phys. Rev. B **73**, 085114 (2006).

[116] V. V. Mazurenko, A. O. Shorikov, A. V. Lukoyanov, K. Kharlov, E. Gorelov, A. I. Lichtenstein, and V. I. Anisimov, Phys. Rev. B **81**, 125131 (2010).

[117] X.-P. Li, D. M. Ceperley, and R. M. Martin, Phys. Rev. B **44**, 10929 (1991).

[118] C. Kittel, *Introduction to Solid State Physics*, Wiley, New York (1986).

[119] A. G. Beattie and J. E. Schirber, Phys. Rev. B **1**, 1548 (1970).

[120] M. Hortamani, PhD thesis, Freie Universität Berlin (2006).

[121] N. Moll, M. Bockstedte, M. Fuchs, E. Pehlke, and M. Scheffler, Phys. Rev. B **52**, 2550 (1995).

[122] F. D. Murnaghan, Proc. Natl. Acad. Sci. U.S.A. **30**, 244 (1944).

[123] S. Grimme, J. Comput. Chem. **27**, 1787 (2006).

[124] V. Barone, M. Casarin, D. Forrer, M. Pavone, M. Sambi, and A. Vittadini, J. Comput. Chem. **30**, 934 (2009).

[125] M. Shishkin and G. Kresse, Phys. Rev. B **75**, 235102 (2007).

[126] A. A. Stekolnikov, J. Furthmüller, and F. Bechstedt, Phys. Rev. B **65**, 115318 (2002).

[127] J. E. Peralta, J. Heyd, G. E. Scuseria, and R. L. Martin, Phys. Rev. B **74**, 073101 (2006).

[128] K. S. Novoselov, A. K. Geim, S. V. Morozov, D. Jiang, Y. Zhang, S. V. Dubonos, I. V. Grigorieva, and A. A. Firsov, Science **306**, 666 (2004).

[129] A. K. Geim and K. S. Noselov, Nat. Mater. **6**, 183 (2007).

[130] A. K. Geim, Science **324**, 1530 (2009).

[131] K. Takeda and K. Shiraishi, Phys. Rev. B **50**, 14916 (1994).

[132] G. G. Guzmán-Verri and L. C. Lew Yan Voon, Phys. Rev. B **76**, 075131 (2007).

[133] S. Cahangirov, M. Topsakal, E. Aktürk, H. Şahin, and S. Ciraci, Phys. Rev. Lett. **102**, 236804 (2009).

[134] P. Vogt, P. De Padova, C. Quaresima, J. Avila, E. Frantzeskakis, M. C. Asensio, A. Resta, B. Ealet, and G. Le Lay, Phys. Rev. Lett. **108**, 155501 (2012).

Dieses Werk ist copyrightgeschützt und darf in keiner Form vervielfältigt werden noch an Dritte weitergegeben werden.
Es gilt nur für den persönlichen Gebrauch.

[135] K. R. Knox, S. Wang, A. Morgante, D. Cvetko, A. Locatelli, T. O. Mentes, M. A. Niño, P. Kim, and R. M. Osgood, Phys. Rev. B **78**, 201408 (2008).

[136] S. Zhou, G.-H. Gweon, A. Fedorov, P. N. First, W. A. de Heer, D.-H. Lee, F. Guinea, A. H. C. Neto, and A. Lanzara, Nat. Mater. **6**, 770 (2007).

[137] S. Kokott, L. Matthes, and F. Bechstedt, Phys. Status Solidi RRL **7**, 538 (2013).

[138] K. Reuter, C. Stampfl, and M. Scheffler, *Ab initio atomistic thermodynamics and statistical mechanics of surface properties and functions*, in *Handbook of Materials Modeling*, edited by D. Yip, Kluwer, Dordrecht (2004).

[139] E. Penev, P. Kratzer, and M. Scheffler, Phys. Rev. Lett. **93**, 146102 (2004).

[140] F. Bechstedt, *Principles of Surface Physics*, Springer, Berlin, Heidelberg (2003).

[141] C. B. Duke, Chem. Rev. **96**, 1237 (1996).

[142] K. C. Pandey, Phys. Rev. Lett. **47**, 1913 (1981).

[143] R. Seiwatz, Surf. Sci. **2**, 473 (1964).

[144] Y.-N. Yang and E. D. Williams, Phys. Rev. Lett. **72**, 1862 (1994).

[145] K. Takayanagi, Y. Tanishiro, S. Takahashi, and M. Takahashi, Surf. Sci. **164**, 367 (1985).

[146] K. D. Brommer, M. Needels, B. Larson, and J. D. Joannopoulos, Phys. Rev. Lett. **68**, 1355 (1992).

[147] I. Štich, M. C. Payne, R. D. King-Smith, J.-S. Lin, and L. J. Clarke, Phys. Rev. Lett. **68**, 1351 (1992).

[148] F. Bechstedt, A. A. Stekolnikov, J. Furthmüller, and P. Käckell, Phys. Rev. Lett. **87**, 016103 (2001).

[149] R. M. Tromp, R. J. Hamers, and J. E. Demuth, Science **234**, 304 (1986).

[150] Y. L. Wang, H.-J. Gao, H. M. Guo, H. W. Liu, I. G. Batyrev, W. E. McMahon, and S. B. Zhang, Phys. Rev. B **70**, 073312 (2004).

[151] J.-Z. Wang, J.-F. Jia, Z.-H. Xiong, and Q.-K. Xue, Phys. Rev. B **78**, 045424 (2008).

[152] R. J. Hamers, R. M. Tromp, and J. E. Demuth, Phys. Rev. Lett. **56**, 1972 (1986).

[153] D. J. Eaglesham, A. E. White, L. C. Feldman, N. Moriya, and D. C. Jacobson, Phys. Rev. Lett. **70**, 1643 (1993).

[154] T. Jeong and W. E. Pickett, Phys. Rev. B **70**, 075114 (2004).

[155] M. Vočadlo, G. D. Price, and I. G. Wood, Acta Crystallogr. Sec. B **55**, 484 (1999).

[156] J. M. Hopkinson and H.-Y. Kee, Phys. Rev. B **74**, 224441 (2006).

[157] S. V. Isakov, J. M. Hopkinson, and H.-Y. Kee, Phys. Rev. B **78**, 014404 (2008).

Dieses Werk ist copyrightgeschützt und darf in keiner Form vervielfältigt werden noch an Dritte weitergegeben werden.
Es gilt nur für den persönlichen Gebrauch.

[158] N. Metropolis, A. W. Rosenbluth, M. N. Rosenbluth, A. H. Teller, and E. Teller, J. Chem. Phys. **21**, 1087 (1953).

[159] M. Matsumoto and T. Nishimura, ACM Trans. Model. Comput. Simul. **8**, 3 (1998).

[160] R. G. Brown and M. Ciftan, Phys. Rev. Lett. **76**, 1352 (1996).

[161] Z. Z. Zhang, B. Partoens, K. Chang, and F. M. Peeters, Phys. Rev. B **77**, 155201 (2008).

[162] D. van der Marel, A. Damascelli, K. Schulte, and A. A. Menovsky, Physica B **244**, 138 (1998).

[163] B. Borén, Ark. Kemi, Mineral. Geol. **11A**, 1 (1933).

[164] D. Hobbs and J. Hafner, J. Phys.: Condens. Matter **13**, L681 (2001).

[165] D. Hobbs, J. Hafner, and D. Spišák, Phys. Rev. B **68**, 014407 (2003).

[166] W. Gale and T. Totemeier, editors, *Smithells Metals Reference Book*, Elsevier Science, 8th edition (2004).

[167] M. Ekman and V. Ozoliņš, Phys. Rev. B **57**, 4419 (1998).

[168] O. Madelung, editor, *Landolt-Börnstein, New Series*, volume IV/5J, Springer, Berlin, Heidelberg (1998).

[169] S. Mühlbauer, B. Binz, F. Jonietz, C. Pfleiderer, A. Rosch, A. Neubauer, R. Georgii, and P. Böni, Science **323**, 915 (2009).

[170] A. Hamann, D. Lamago, T. Wolf, H. v. Löhneysen, and D. Reznik, Phys. Rev. Lett. **107**, 037207 (2011).

[171] Y. Ishikawa, K. Tajima, D. Bloch, and M. Roth, Solid State Commun. **19**, 525 (1976).

[172] P. Bak and M. H. Jensen, J. Phys. C **13**, L881 (1980).

[173] O. Nakanishi, A. Yanase, A. Hasegawa, and M. Kataoka, Solid State Commun. **35**, 995 (1980).

[174] Y. Ishikawa and M. Arai, J. Phys. Soc. Jpn. **53**, 2726 (1984).

[175] S. V. Grigoriev, S. V. Maleyev, A. I. Okorokov, Y. O. Chetverikov, and H. Eckerlebe, Phys. Rev. B **73**, 224440 (2006).

[176] S. M. Stishov, A. E. Petrova, S. Khasanov, G. K. Panova, A. A. Shikov, J. C. Lashley, D. Wu, and T. A. Lograsso, Phys. Rev. B **76**, 052405 (2007).

[177] J. Wernick, G. Wertheim, and R. Sherwood, Mater. Res. Bull. **7**, 1431 (1972).

[178] M. Fäth, J. Aarts, A. A. Menovsky, G. J. Nieuwenhuys, and J. A. Mydosh, Phys. Rev. B **58**, 15483 (1998).

[179] S. Paschen, E. Felder, M. A. Chernikov, L. Degiorgi, H. Schwer, H. R. Ott, D. P. Young, J. L. Sarrao, and Z. Fisk, Phys. Rev. B **56**, 12916 (1997).

Dieses Werk ist copyrightgeschützt und darf in keiner Form vervielfältigt werden noch an Dritte weitergegeben werden.
Es gilt nur für den persönlichen Gebrauch.

[180] V. Jaccarino, G. K. Wertheim, J. H. Wernick, L. R. Walker, and S. Arajs, Phys. Rev. **160**, 476 (1967).

[181] T. E. Mason, G. Aeppli, A. P. Ramirez, K. N. Clausen, C. Broholm, N. Stücheli, E. Bucher, and T. T. M. Palstra, Phys. Rev. Lett. **69**, 490 (1992).

[182] Z. Fisk, J. Sarrao, S. Cooper, P. Nyhus, G. Boebinger, A. Passner, and P. Canfield, Physica B **223-224**, 409 (1996).

[183] M. Klein, D. Zur, D. Menzel, J. Schoenes, K. Doll, J. Röder, and F. Reinert, Phys. Rev. Lett. **101**, 046406 (2008).

[184] K. Ishizaka, T. Kiss, T. Shimojima, T. Yokoya, T. Togashi, S. Watanabe, C. Q. Zhang, C. T. Chen, Y. Onose, Y. Tokura, and S. Shin, Phys. Rev. B **72**, 233202 (2005).

[185] M. Arita, K. Shimada, Y. Takeda, M. Nakatake, H. Namatame, M. Taniguchi, H. Negishi, T. Oguchi, T. Saitoh, A. Fujimori, and T. Kanomata, Phys. Rev. B **77**, 205117 (2008).

[186] L. F. Mattheiss and D. R. Hamann, Phys. Rev. B **47**, 13114 (1993).

[187] V. I. Anisimov, S. Y. Ezhov, I. S. Elfimov, I. V. Solovyev, and T. M. Rice, Phys. Rev. Lett. **76**, 1735 (1996).

[188] H. L. Zhang, S. Lu, M. P. J. Punkkinen, Q.-M. Hu, B. Johansson, and L. Vitos, Phys. Rev. B **82**, 132409 (2010).

[189] E. Magnano, F. Bondino, C. Cepek, F. Parmigiani, and M. C. Mozzati, Appl. Phys. Lett. **96**, 152503 (2010).

[190] H. von Känel, N. Onda, H. Sirringhaus, E. Müller-Gubler, S. Goncalves-Conto, and C. Schwarz, Appl. Surf. Sci. **70-71**, 559 (1993).

[191] K. Schwinge, C. Müller, A. Mogilatenko, J. Paggel, and P. Fumagalli, J. Appl. Phys. **97**, 103913 (2005).

[192] S. Higashi, Y. Ikedo, P. Kocan, and H. Tochihara, Appl. Phys. Lett. **93**, 013104 (2008).

[193] S. Higashi, P. Kocán, and H. Tochihara, Phys. Rev. B **79**, 205312 (2009).

[194] J. Hirvonen Grytzelius, H. M. Zhang, and L. S. O. Johansson, Phys. Rev. B **78**, 155406 (2008).

[195] J. Hirvonen Grytzelius, H. M. Zhang, and L. S. O. Johansson, Phys. Rev. B **80**, 235324 (2009).

[196] E. A. Karhu, U. K. Rößler, A. N. Bogdanov, S. Kahwaji, B. J. Kirby, H. Fritzsche, M. D. Robertson, C. F. Majkrzak, and T. L. Monchesky, Phys. Rev. B **85**, 094429 (2012).

[197] L. T. Vinh, J. Chevrier, and J. Derrien, Phys. Rev. B **46**, 15946 (1992).

[198] S. Picozzi, A. Continenza, and A. J. Freeman, Phys. Rev. B **66**, 094421 (2002).

Dieses Werk ist copyrightgeschützt und darf in keiner Form vervielfältigt werden noch an Dritte weitergegeben werden.
Es gilt nur für den persönlichen Gebrauch.

[199] D. Lamago, E. S. Clementyev, A. S. Ivanov, R. Heid, J.-M. Mignot, A. E. Petrova, and P. A. Alekseev, Phys. Rev. B **82**, 144307 (2010).

[200] S. Baroni, S. de Gironcoli, A. Dal Corso, and P. Giannozzi, Rev. Mod. Phys. **73**, 515 (2001).

[201] H. Schulz, *Statistische Physik beruhend auf Quantentheorie. Eine Einführung*, Verlag Harri Deutsch, Frankfurt (2005).

[202] E. Wohlfarth, J. Magn. Magn. Mater. **7**, 113 (1978).

[203] T. Moriya, *Spin fluctuations in itinerant electron magnetism*, Springer, Berlin (1985).

[204] A. E. Petrova, V. N. Krasnorussky, A. A. Shikov, W. M. Yuhasz, T. A. Lograsso, J. C. Lashley, and S. M. Stishov, Phys. Rev. B **82**, 155124 (2010).

[205] H. Okamoto, J. Phase Equilib. **12**, 505 (1991).

[206] S. Azatyan, O. Utas, N. Denisov, A. Zotov, and A. Saranin, Surf. Sci. **605**, 289 (2011).

[207] N. Chetty and R. M. Martin, Phys. Rev. B **45**, 6089 (1992).

[208] L. Bengtsson, Phys. Rev. B **59**, 12301 (1999).

[209] B. Meyer and D. Vanderbilt, Phys. Rev. B **63**, 205426 (2001).

[210] S. V. Grigoriev, D. Chernyshov, V. A. Dyadkin, V. Dmitriev, E. V. Moskvin, D. Lamago, T. Wolf, D. Menzel, J. Schoenes, S. V. Maleyev, and H. Eckerlebe, Phys. Rev. B **81**, 012408 (2010).

[211] S. V. Grigoriev, D. Chernyshov, V. A. Dyadkin, V. Dmitriev, S. V. Maleyev, E. V. Moskvin, D. Menzel, J. Schoenes, and H. Eckerlebe, Phys. Rev. Lett. **102**, 037204 (2009).

[212] M. Hortamani, H. Wu, P. Kratzer, and M. Scheffler, Phys. Rev. B **74**, 205305 (2006).

[213] E. Magnano, E. Carleschi, A. Nicolaou, T. Pardini, M. Zangrando, and F. Parmigiani, Surf. Sci. **600**, 3932 (2006).

[214] C. T. Foxon, J. Vac. Sci. Technol. **B1**, 293 (1983).

[215] W. Theis and R. M. Tromp, Phys. Rev. Lett. **76**, 2770 (1996).

[216] E. J. Tarsa, B. Heying, X. H. Wu, P. Fini, S. P. DenBaars, and J. S. Speck, J. Appl. Phys. **82**, 5472 (1997).

[217] H. Wang and Z.-Q. Zou, Appl. Phys. Lett. **88**, 103115 (2006).

[218] C.-Y. Niu, J.-T. Wang, E. Wang, and C. Chen, J. Chem. Phys. **138**, 164705 (2013).

[219] C. Pfleiderer, J. Bœuf, and H. v. Löhneysen, Phys. Rev. B **65**, 172404 (2002).

[220] D. B. Migas, V. L. Shaposhnikov, A. B. Filonov, V. E. Borisenko, and N. N. Dorozhkin, Phys. Rev. B **77**, 075205 (2008).

Dieses Werk ist copyrightgeschützt und darf in keiner Form vervielfältigt werden noch an Dritte weitergegeben werden.
Es gilt nur für den persönlichen Gebrauch.

[221] Y. Miyazaki, D. Igarashi, K. Hayashi, T. Kajitani, and K. Yubuta, Phys. Rev. B **78**, 214104 (2008).

[222] S. Yabuuchi, H. Kageshima, Y. Ono, M. Nagase, A. Fujiwara, and E. Ohta, Phys. Rev. B **78**, 045307 (2008).

[223] S. Caprara, E. Kulatov, and V. Tugushev, Eur. Phys. J. B **85**, 149 (2012).

[224] C. Zeng, S. C. Erwin, L. C. Feldman, A. P. Li, R. Jin, Y. Song, J. R. Thompson, and H. H. Weitering, Appl. Phys. Lett. **83**, 5002 (2003).

[225] S. Picozzi, A. Continenza, and A. J. Freeman, Phys. Rev. B **70**, 235205 (2004).

[226] J. H. Grytzelius, H. M. Zhang, and L. S. O. Johansson, Phys. Rev. B **84**, 195306 (2011).

[227] W. Ndiaye, M. C. Richter, O. Heckmann, P. De Padova, J.-M. Mariot, A. Stroppa, S. Picozzi, W. Wang, A. Taleb-Ibrahimi, P. Le Fèvre, F. Bertran, C. Cacho, M. Leandersson, T. Balasubramanian, and K. Hricovini, Phys. Rev. B **87**, 165137 (2013).

[228] A. Spiesser, I. Slipukhina, M.-T. Dau, E. Arras, V. Le Thanh, L. Michez, P. Pochet, H. Saito, S. Yuasa, M. Jamet, and J. Derrien, Phys. Rev. B **84**, 165203 (2011).

[229] C. Sürgers, M. Gajdzik, G. Fischer, H. v. Löhneysen, E. Welter, and K. Attenkofer, Phys. Rev. B **68**, 174423 (2003).

[230] C. Sürgers, K. Potzger, T. Strache, W. Moller, G. Fischer, N. Joshi, and H. v. Löhneysen, Appl. Phys. Lett. **93**, 062503 (2008).

[231] P. J. Brown and J. B. Forsyth, J. Phys.: Condens. Matter **7**, 7619 (1995).

[232] J. M. Higgins, R. Ding, and S. Jin, Chem. Mater. **23**, 3848 (2011).

[233] P. J. Brown, J. B. Forsyth, V. Nunez, and F. Tasset, J. Phys.: Condens. Matter **4**, 10025 (1992).

[234] H. M. Zhang, J. H. Grytzelius, and L. S. O. Johansson, Phys. Rev. B **88**, 045311 (2013).

[235] C. Zeng, W. Zhu, S. C. Erwin, Z. Zhang, and H. H. Weitering, Phys. Rev. B **70**, 205340 (2004).

[236] M. Ciorga, A. Einwanger, U. Wurstbauer, D. Schuh, W. Wegscheider, and D. Weiss, Phys. Rev. B **79**, 165321 (2009).

[237] G. Schmidt, D. Ferrand, L. W. Molenkamp, A. T. Filip, and B. J. van Wees, Phys. Rev. B **62**, R4790 (2000).

[238] T. Dietl, H. Ohno, F. Matsukura, J. Cibert, and D. Ferrand, Science **287**, 1019 (2000).

[239] A. Zunger, S. Lany, and H. Raebiger, Physics **3**, 53 (2010).

[240] K. Ueda, H. Tabata, and T. Kawai, Appl. Phys. Lett. **79**, 988 (2001).

Dieses Werk ist copyrightgeschützt und darf in keiner Form vervielfältigt werden noch an Dritte weitergegeben werden.
Es gilt nur für den persönlichen Gebrauch.

[241] D. P. Norton, M. E. Overberg, S. J. Pearton, K. Pruessner, J. D. Budai, L. A. Boatner, M. F. Chisholm, J. S. Lee, Z. G. Khim, Y. D. Park, and R. G. Wilson, Appl. Phys. Lett. **83**, 5488 (2003).

[242] C. Song, K. W. Geng, F. Zeng, X. B. Wang, Y. X. Shen, F. Pan, Y. N. Xie, T. Liu, H. T. Zhou, and Z. Fan, Phys. Rev. B **73**, 024405 (2006).

[243] K. R. Kittilstved, D. A. Schwartz, A. C. Tuan, S. M. Heald, S. A. Chambers, and D. R. Gamelin, Phys. Rev. Lett. **97**, 037203 (2006).

[244] M. Bouloudenine, N. Viart, S. Colis, J. Kortus, and A. Dinia, Appl. Phys. Lett. **87**, 052501 (2005).

[245] A. Barla, G. Schmerber, E. Beaurepaire, A. Dinia, H. Bieber, S. Colis, F. Scheurer, J.-P. Kappler, P. Imperia, F. Nolting, F. Wilhelm, A. Rogalev, D. Müller, and J. J. Grob, Phys. Rev. B **76**, 125201 (2007).

[246] A. Ney, K. Ollefs, S. Ye, T. Kammermeier, V. Ney, T. C. Kaspar, S. A. Chambers, F. Wilhelm, and A. Rogalev, Phys. Rev. Lett. **100**, 157201 (2008).

[247] A. Ney, T. Kammermeier, K. Ollefs, S. Ye, V. Ney, T. C. Kaspar, S. A. Chambers, F. Wilhelm, and A. Rogalev, Phys. Rev. B **81**, 054420 (2010).

[248] H. Ohno, A. Shen, F. Matsukura, A. Oiwa, A. Endo, S. Katsumoto, and Y. Iye, Appl. Phys. Lett. **69**, 363 (1996).

[249] G. S. Higashi, Y. J. Chabal, G. W. Trucks, and K. Raghavachari, Appl. Phys. Lett. **56**, 656 (1990).

[250] M. Gruyters, Surf. Sci. **515**, 53 (2002).

[251] M. Gruyters, T. Pingel, and R. Berndt, Phys. Rev. B **87**, 165405 (2013).

[252] B. Cordero, V. Goméz, A. E. Platero-Prats, M. Revés, J. Echeverría, E. Cremades, F. Barragán, and S. Alvarez, Dalton Trans., 2832 (2008).

[253] J. L. A. Alves, J. Hebenstreit, and M. Scheffler, Phys. Rev. B **44**, 6188 (1991).

[254] Y. Li and G. Galli, Phys. Rev. B **82**, 045321 (2010).

[255] K. Hricovini, R. Günther, P. Thiry, A. Taleb-Ibrahimi, G. Indlekofer, J. E. Bonnet, P. Dumas, Y. Petroff, X. Blase, X. Zhu, S. G. Louie, Y. J. Chabal, and P. A. Thiry, Phys. Rev. Lett. **70**, 1992 (1993).

[256] H. Lim, K. Cho, I. Park, J. D. Joannopoulos, and E. Kaxiras, Phys. Rev. B **52**, 17231 (1995).

[257] S. J. Blanksby and G. B. Ellison, Acc. Chem. Res. **36**, 255 (2003).

[258] P. Dumas, Y. J. Chabal, and G. S. Higashi, Phys. Rev. Lett. **65**, 1124 (1990).

[259] A. Zunger and U. Lindefelt, Phys. Rev. B **26**, 5989 (1982).

Dieses Werk ist copyrightgeschützt und darf in keiner Form vervielfältigt werden noch an Dritte weitergegeben werden.
Es gilt nur für den persönlichen Gebrauch.

[260] F. Beeler, O. K. Andersen, and M. Scheffler, Phys. Rev. Lett. **55**, 1498 (1985).

[261] F. Beeler, O. K. Andersen, and M. Scheffler, Phys. Rev. B **41**, 1603 (1990).

[262] M. Shaughnessy, C. Y. Fong, R. Snow, L. H. Yang, X. S. Chen, and Z. M. Jiang, Phys. Rev. B **82**, 035202 (2010).

[263] M. C. Qian, C. Y. Fong, K. Liu, W. E. Pickett, J. E. Pask, and L. H. Yang, Phys. Rev. Lett. **96**, 027211 (2006).

[264] H. Wu, P. Kratzer, and M. Scheffler, Phys. Rev. Lett. **98**, 117202 (2007).

[265] M. M. Otrokov, A. Ernst, V. V. Tugushev, S. Ostanin, P. Buczek, L. M. Sandratskii, G. Fischer, W. Hergert, I. Mertig, V. M. Kuznetsov, and E. V. Chulkov, Phys. Rev. B **84**, 144431 (2011).

[266] E. R. Weber, Appl. Phys. A **30**, 1 (1983).

[267] D. A. van Wezep and C. A. J. Ammerlaan, J. Electron. Mater. **14A**, 863 (1985).

[268] G. Ludwig and H. Woodbury, Solid State Phys. **13**, 223 (1962).

[269] M. Bolduc, C. Awo-Affouda, A. Stollenwerk, M. B. Huang, F. G. Ramos, G. Agnello, and V. P. LaBella, Phys. Rev. B **71**, 033302 (2005).

[270] W. F. Su, L. Gong, J. L. Wang, S. Chen, Y. L. Fan, and Z. M. Jiang, J. Cryst. Growth **311**, 2139 (2009).

[271] C. Panse, R. Leitsmann, and F. Bechstedt, Phys. Rev. B **82**, 125205 (2010).

[272] P. M. Koenraad and M. E. Flatté, Nat. Mater. **10**, 91 (2011).

[273] A. M. Yakunin, A. Y. Silov, P. M. Koenraad, J.-M. Tang, M. E. Flatté, J.-L. Primus, W. Van Roy, J. De Boeck, A. M. Monakhov, K. S. Romanov, I. E. Panaiotti, and N. S. Averkiev, Nat. Mater. **6**, 512 (2007).

[274] A. M. Yakunin, A. Y. Silov, P. M. Koenraad, J. H. Wolter, W. Van Roy, J. De Boeck, J.-M. Tang, and M. E. Flatté, Phys. Rev. Lett. **92**, 216806 (2004).

[275] A. M. Yakunin, A. Y. Silov, P. M. Koenraad, J.-M. Tang, M. E. Flatté, W. V. Roy, J. De Boeck, and J. H. Wolter, Phys. Rev. Lett. **95**, 256402 (2005).

[276] D. Kitchen, A. Richardella, J.-M. Tang, M. E. Flatté, and A. Yazdani, Nature (London) **442**, 436 (2006).

[277] J. K. Garleff, C. Çelebi, W. Van Roy, J.-M. Tang, M. E. Flatté, and P. M. Koenraad, Phys. Rev. B **78**, 075313 (2008).

[278] J. K. Garleff, A. P. Wijnheijmer, A. Y. Silov, J. van Bree, W. Van Roy, J.-M. Tang, M. E. Flatté, and P. M. Koenraad, Phys. Rev. B **82**, 035303 (2010).

[279] A. A. Khajetoorians, B. Chilian, J. Wiebe, S. Schuwalow, F. Lechermann, and R. Wiesendanger, Nature (London) **467**, 1084 (2010).

Dieses Werk ist copyrightgeschützt und darf in keiner Form vervielfältigt werden noch an Dritte weitergegeben werden.
Es gilt nur für den persönlichen Gebrauch.

[280] S. Loth, K. von Bergmann, M. Ternes, A. F. Otte, C. P. Lutz, and A. J. Heinrich, Nat. Phys. **6**, 340 (2010).

[281] J.-M. Jancu, J.-C. Girard, M. O. Nestoklon, A. Lemaître, F. Glas, Z. Z. Wang, and P. Voisin, Phys. Rev. Lett. **101**, 196801 (2008).

[282] F. Meier, L. Zhou, J. Wiebe, and R. Wiesendanger, Science **320**, 82 (2008).

[283] K. Teichmann, M. Wenderoth, S. Loth, R. G. Ulbrich, J. K. Garleff, A. P. Wijnheijmer, and P. M. Koenraad, Phys. Rev. Lett. **101**, 076103 (2008).

[284] A. P. Wijnheijmer, J. K. Garleff, K. Teichmann, M. Wenderoth, S. Loth, R. G. Ulbrich, P. A. Maksym, M. Roy, and P. M. Koenraad, Phys. Rev. Lett. **102**, 166101 (2009).

[285] V. Madhavan, W. Chen, T. Jamneala, M. F. Crommie, and N. S. Wingreen, Science **280**, 567 (1998).

[286] P. Wahl, L. Diekhöner, M. A. Schneider, L. Vitali, G. Wittich, and K. Kern, Phys. Rev. Lett. **93**, 176603 (2004).

[287] L. Vitali, R. Ohmann, S. Stepanow, P. Gambardella, K. Tao, R. Huang, V. S. Stepanyuk, P. Bruno, and K. Kern, Phys. Rev. Lett. **101**, 216802 (2008).

[288] Y. Wang, B. Meyer, X. Yin, M. Kunat, D. Langenberg, F. Traeger, A. Birkner, and C. Wöll, Phys. Rev. Lett. **95**, 266104 (2005).

[289] A. S. Foster, M. A. Gosálvez, T. Hynninen, R. M. Nieminen, and K. Sato, Phys. Rev. B **76**, 075315 (2007).

[290] D. Wortmann, S. Heinze, P. Kurz, G. Bihlmayer, and S. Blügel, Phys. Rev. Lett. **86**, 4132 (2001).

[291] S. Blügel, M. Weinert, and P. H. Dederichs, Phys. Rev. Lett. **60**, 1077 (1988).

[292] N. D. Mermin and H. Wagner, Phys. Rev. Lett. **17**, 1133 (1966).

[293] M. Bander and D. L. Mills, Phys. Rev. B **38**, 12015 (1988).

[294] J. M. Kosterlitz and D. J. Thouless, J. Phys. C **6**, 1181 (1973).

[295] A. Hirth, U. Michelsen, and D. Wöhrle, Chemie in unserer Zeit **33**, 84 (1999).

[296] V. G. Ruiz, W. Liu, E. Zojer, M. Scheffler, and A. Tkatchenko, Phys. Rev. Lett. **108**, 146103 (2012).

[297] M. Gruyters, T. Pingel, T. G. Gopakumar, N. Néel, C. Schütt, F. Köhler, R. Herges, and R. Berndt, J. Phys. Chem. C **116**, 20882 (2012).

[298] J. Repp, G. Meyer, S. M. Stojković, A. Gourdon, and C. Joachim, Phys. Rev. Lett. **94**, 026803 (2005).

Dieses Werk ist copyrightgeschützt und darf in keiner Form vervielfältigt werden noch an Dritte weitergegeben werden.
Es gilt nur für den persönlichen Gebrauch.

[299] M. Bernien, J. Miguel, C. Weis, M. E. Ali, J. Kurde, B. Krumme, P. M. Panchmatia, B. Sanyal, M. Piantek, P. Srivastava, K. Baberschke, P. M. Oppeneer, O. Eriksson, W. Kuch, and H. Wende, Phys. Rev. Lett. **102**, 047202 (2009).

[300] N. Atodiresei, J. Brede, P. Lazić, V. Caciuc, G. Hoffmann, R. Wiesendanger, and S. Blügel, Phys. Rev. Lett. **105**, 066601 (2010).

[301] S. Bhandary, S. Ghosh, H. Herper, H. Wende, O. Eriksson, and B. Sanyal, Phys. Rev. Lett. **107**, 257202 (2011).

[302] H. Wende *et al.*, Nat. Mater. **6**, 516 (2007).

[303] Y.-S. Fu, S.-H. Ji, X. Chen, X.-C. Ma, R. Wu, C.-C. Wang, W.-H. Duan, X.-H. Qiu, B. Sun, P. Zhang, J.-F. Jia, and Q.-K. Xue, Phys. Rev. Lett. **99**, 256601 (2007).

[304] U. G. E. Perera, H. J. Kulik, V. Iancu, L. G. G. V. Dias da Silva, S. E. Ulloa, N. Marzari, and S.-W. Hla, Phys. Rev. Lett. **105**, 106601 (2010).

[305] N. Marom and L. Kronik, Appl. Phys. A **95**, 165 (2009).

[306] A. Mugarza, R. Robles, C. Krull, R. Korytár, N. Lorente, and P. Gambardella, Phys. Rev. B **85**, 155437 (2012).

[307] J. Åhlund, K. Nilson, J. Schiessling, L. Kjeldgaard, S. Berner, N. Mårtensson, C. Puglia, B. Brena, M. Nyberg, and Y. Luo, J. Chem. Phys. **125** (2006).

[308] G. Bouzerar and T. Ziman, Phys. Rev. Lett. **96**, 207602 (2006).

[309] H. Wu, A. Stroppa, S. Sakong, S. Picozzi, M. Scheffler, and P. Kratzer, Phys. Rev. Lett. **105**, 267203 (2010).

[310] Y.-L. Wang, J. Ren, C.-L. Song, Y.-P. Jiang, L.-L. Wang, K. He, X. Chen, J.-F. Jia, S. Meng, E. Kaxiras, Q.-K. Xue, and X.-C. Ma, Phys. Rev. B **82**, 245420 (2010).

[311] J. Ren, S. Meng, Y.-L. Wang, X.-C. Ma, Q.-K. Xue, and E. Kaxiras, J. Chem. Phys. **134**, (2011).

[312] A. Tkatchenko, R. A. DiStasio, R. Car, and M. Scheffler, Phys. Rev. Lett. **108**, 236402 (2012).

[313] A. Tkatchenko and M. Scheffler, Phys. Rev. Lett. **102**, 073005 (2009).

[314] M. Dion, H. Rydberg, E. Schröder, D. C. Langreth, and B. I. Lundqvist, Phys. Rev. Lett. **92**, 246401 (2004).

[315] R. A. de Groot, F. M. Mueller, P. G. v. Engen, and K. H. J. Buschow, Phys. Rev. Lett. **50**, 2024 (1983).

[316] G. Reiss, J. Schmalhorst, A. Thomas, A. Hütten, and S. Yuasa, *Magnetic tunnel junctions*, in *Magnetic Heterostructures*, edited by H. Zabel and S. D. Bader, volume 227 of *Springer Tracts in Modern Physics*, pages 291–333, Springer, Berlin, Heidelberg (2008).

Dieses Werk ist copyrightgeschützt und darf in keiner Form vervielfältigt werden noch an Dritte weitergegeben werden.
Es gilt nur für den persönlichen Gebrauch.

[317] T. Ishikawa, N. Itabashi, T. Taira, K. Matsuda, T. Uemura, and M. Yamamoto, J. Appl. Phys. **105** (2009).

[318] H. Liu, Y. Honda, T. Taira, K. Matsuda, M. Arita, T. Uemura, and M. Yamamoto, Appl. Phys. Lett. **101**, (2012).

[319] B. Hülsen, PhD thesis, Universität Duisburg-Essen (2009).

[320] P. Mavropoulos, M. Ležaić, and S. Blügel, Phys. Rev. B **72**, 174428 (2005).

[321] B. Hülsen, M. Scheffler, and P. Kratzer, Phys. Rev. Lett. **103**, 046802 (2009).

[322] Y. Miura, K. Abe, and M. Shirai, J. Phys.: Condens. Matter **21**, 064245 (2009).

[323] M. Ležaić, P. Mavropoulos, J. Enkovaara, G. Bihlmayer, and S. Blügel, Phys. Rev. Lett. **97**, 026404 (2006).

[324] M. Walter, J. Walowski, V. Zbarsky, M. Münzenberg, M. Schäfers, D. Ebke, G. Reiss, A. Thomas, P. Peretzki, M. Seibt, J. S. Moodera, M. Czerner, M. Bachmann, and C. Heiliger, Nat. Mater. **10**, 472 (2011).

[325] U. Sivan and Y. Imry, Phys. Rev. B **33**, 551 (1986).

[326] A. Slachter, F. L. Bakker, J. P. Adam, and B. J. van Wees, Nat. Phys. **6**, 879 (2010).

[327] G. X. Miao, J. Y. Chang, M. J. van Veenhuizen, K. Thiel, M. Seibt, G. Eilers, M. Münzenberg, and J. S. Moodera, Appl. Phys. Lett. **93**, (2008).

[328] K.-R. Jeon, B.-C. Min, I.-J. Shin, C.-Y. Park, H.-S. Lee, Y.-H. Jo, and S.-C. Shin, Appl. Phys. Lett. **98**, (2011).

[329] G. Li, T. Taira, K. Matsuda, M. Arita, T. Uemura, and M. Yamamoto, Appl. Phys. Lett. **98**, (2011).

[330] P. J. Webster, J. Phys. Chem. Solids **32**, 1221 (1971).

[331] I. Galanakis, P. H. Dederichs, and N. Papanikolaou, Phys. Rev. B **66**, 174429 (2002).

[332] I. Galanakis, P. Mavropoulos, and P. H. Dederichs, J. Phys. D: Appl. Phys. **39**, 765 (2006).

[333] M. Meinert, C. Friedrich, G. Reiss, and S. Blügel, Phys. Rev. B **86**, 245115 (2012).

[334] M. Jourdan, J. Minár, J. Braun, A. Kronenberg, S. Chadov, B. Balke, A. Gloskovskii, M. Kolbe, H. J. Elmers, G. Schönhense, H. Ebert, C. Felser, and M. Kläui, Nat. Commun. **5**, 3974 (2014).

[335] H. K. Mao and P. M. Bell, J. Geophys. Res. **84**, 4533 (1979).

[336] A. N. Baranov, V. S. Stepanyuk, W. Hergert, A. A. Katsnelson, A. Settels, R. Zeller, and P. H. Dederichs, Phys. Rev. B **66**, 155117 (2002).

[337] V. Musolino, A. Selloni, and R. Car, J. Chem. Phys. **108**, 5044 (1998).

Dieses Werk ist copyrightgeschützt und darf in keiner Form vervielfältigt werden noch an Dritte weitergegeben werden.
Es gilt nur für den persönlichen Gebrauch.

[338] L. Chioncel, Y. Sakuraba, E. Arrigoni, M. I. Katsnelson, M. Oogane, Y. Ando, T. Miyazaki, E. Burzo, and A. I. Lichtenstein, Phys. Rev. Lett. **100**, 086402 (2008).

[339] N. H. Long, M. Ogura, and H. Akai, Phys. Rev. B **85**, 224437 (2012).

[340] L. Chioncel, M. I. Katsnelson, R. A. de Groot, and A. I. Lichtenstein, Phys. Rev. B **68**, 144425 (2003).

[341] H. Ebert, S. Mankovsky, D. Ködderitzsch, and P. J. Kelly, Phys. Rev. Lett. **107**, 066603 (2011).

[342] V. Popescu and A. Zunger, Phys. Rev. B **85**, 085201 (2012).

[343] P. V. C. Medeiros, S. Stafström, and J. Björk, Phys. Rev. B **89**, 041407 (2014).

[344] S. J. Hashemifar, P. Kratzer, and M. Scheffler, Phys. Rev. Lett. **94**, 096402 (2005).

[345] Y. Miura, H. Uchida, Y. Oba, K. Abe, and M. Shirai, Phys. Rev. B **78**, 064416 (2008).

[346] M. Jullière, Phys. Lett. A **54**, 225 (1975).

[347] C. Heiliger, P. Zahn, B. Y. Yavorsky, and I. Mertig, Phys. Rev. B **73**, 214441 (2006).

[348] A. I. Liechtenstein, M. I. Katsnelson, and V. A. Gubanov, J. Phys. F: Met. Phys. **14**, L125 (1984).

[349] A. I. Liechtenstein, M. I. Katsnelson, V. P. Antropov, and V. A. Gubanov, J. Magn. Magn. Mater. **67**, 65 (1987).

[350] M. Methfessel and A. T. Paxton, Phys. Rev. B **40**, 3616 (1989).

Dieses Werk ist copyrightgeschützt und darf in keiner Form vervielfältigt werden noch an Dritte weitergegeben werden.
Es gilt nur für den persönlichen Gebrauch.

Dieses Werk ist copyrightgeschützt und darf in keiner Form vervielfältigt werden noch an Dritte weitergegeben werden.
Es gilt nur für den persönlichen Gebrauch.

Danksagungen

Zunächst möchte ich mich bei Herrn Prof. Dr. Peter Kratzer für die Aufnahme in seine Arbeitsgruppe, die sorgsame Betreuung dieser Dissertation und für zahlreiche Diskussionen, die oft auch nichtwissenschaftliche Themen behandelten, bedanken.

Meinen Kollegen und Gästen der Arbeitsgruppe, die mich in den Jahren begleitet haben, danke ich ebenfalls: Dr. Matthias Zuchowski, Dr. Sung Sakong, Dr. Volker Pankoke, Prof. Dr. Vladimir Fomin, Prof. Dr. Seyed Javad Hashemifar, Dr. Johann Gutjahr, Dr. Yaojun Du, Dr. Igor Bejenari, Gregor Fiedler und Hendrik Eilken. Besonders möchte ich Herrn Dr. Voicu Popescu danken für die kritische Durchsicht dieser Dissertation, die gute Zusammenarbeit, die vielen interessanten Gespräche und seine offene und direkte Art, die eine angenehme Atmosphäre verbreitete.

Für die fruchtbare Zusammenarbeit bezüglich der MnSi-Schichten auf Si(111) danke ich Herrn Prof. Dr. Giovanni Costantini, University of Warwick, sowie Herrn Prof. Dr. Takayuki Suzuki, Fukuoka University. Ebenfalls danke ich Herrn PD Dr. Markus Gruyters, Christian-Albrechts-Universität zu Kiel, für umfassende Diskussionen zu STM-Untersuchungen von Eisendefekten unter der H/Si(111)-Oberfläche. Herrn Prof. Dr. Peter Entel und Herrn Dr. Denis Comtesse danke ich für die gute Zusammenarbeit bezüglich der Heuslerlegierungen zwischen Pt-Elektroden.

Weiterer Dank geht an Herrn Prof. Dr. Ole Krogh Andersen, Max-Planck-Institut Stuttgart, der seine unveröffentlichten Ergebnisse zur Orbitalstruktur von FeSi zur Verfügung gestellt hat. Herrn PD Dr. Alfred Hucht danke ich für Diskussionen zur Monte-Carlo-Simulation von Heisenbergmodellen.

Unserem Sekretariat, bestehend aus Frau Barbara Sacha, Frau Kay Eibl und Frau Sabine Lukas, sei ebenso gedankt wie Herrn Dr. Rüdiger Oberhage für die Beantwortung aller Fragen rund um Computertechnik und Linux.

Ohne die Bereitstellung und Pflege des Opterox-Linuxclusters und insbesondere der Cray der Universität Duisburg-Essen durch das „Center for Computational Sciences and Simulation“ (CCSS) wären die extrem aufwändigen Rechnungen, die im Rahmen dieser Arbeit durchgeführt wurden, nicht möglich gewesen. Daher ergeht hier ein ausdrücklicher Dank an die Betreuer dieser Maschinen. Zusätzliche Rechenzeit wurde vom „John von Neumann-Institut für Computing“ (NIC) auf dem Supercomputer JUROPA im „Jülich Supercomputing Centre“ (JSC) gewährt und für einige Rechnungen in Anspruch genommen.

Dieses Werk ist copyrightgeschützt und darf in keiner Form vervielfältigt werden noch an Dritte weitergegeben werden.
Es gilt nur für den persönlichen Gebrauch.

Die Finanzierung meiner Forschungstätigkeit erfolgte weitgehend durch die Deutsche Forschungsgemeinschaft (DFG) im Rahmen des SFB 491 „Magnetische Heteroschichten: Spinstruktur und Spintransport“ sowie des SPP 1538 „Spin Caloric Transport (SpinCaT)“. An dieser Stelle möchte ich mich auch bei allen (ehemaligen) Mitgliedern und Doktoranden des SFB 491 bedanken.

Abschließend bedanke ich mich von Herzen bei meinen Freunden, die mir auch über die Distanz treu geblieben sind, und bei meinen Eltern, die mich auf meinem bisherigen Lebensweg stets unterstützt haben.

Dieses Werk ist copyrightgeschützt und darf in keiner Form vervielfältigt werden noch an Dritte weitergegeben werden.
Es gilt nur für den persönlichen Gebrauch.

Dieses Werk ist copyrightgeschützt und darf in keiner Form vervielfältigt werden noch an Dritte weitergegeben werden.
Es gilt nur für den persönlichen Gebrauch.

Dieses Werk ist copyrightgeschützt und darf in keiner Form vervielfältigt werden noch an Dritte weitergegeben werden.
Es gilt nur für den persönlichen Gebrauch.